

Innovative Therapeutic Strategy Targeting Neurons with Cholesterol in Huntington's Disease: From Preclinical Studies to Clinical Trial Readiness

A thesis submitted in fulfillment of the requirements for the degree of Doctor of
Philosophy in Life and Biomolecular Sciences at the Open University, UK

Alice PASSONI

Personal identifier: H8411601

Laboratory of Mass Spectrometry

Istituto di Ricerche Farmacologiche "Mario Negri" IRCCS - Milan, Italy

Director of Studies: Dr Renzo Bagnati

Supervisor: Prof Pietro Ghezzi

October, 2022

ABSTRACT

The current pharmacological treatment of Huntington's disease (HD) is palliative, and therapies to restore functions in patients are needed. One of the pathways affected in HD involves brain cholesterol (Chol) synthesis, which is essential for optimal synaptic transmission. Given these bases, the presented thesis proposes three different mass spectrometric strategies to support the study of cholesterol involvement in HD.

Firstly, we evaluated nose-to-brain delivery as a non-invasive strategy to deliver Chol to the adult brain. We treated wild-type (WT) and R6/2 mice with intranasal (IN) doses of liposomes loaded with Chol in single and repeated doses trials. The results indicated the effectiveness of IN Chol-loaded liposomes to deliver Chol in different brain regions. In parallel, we investigated the levels of Chol metabolites in the brain after chronic IN treatment. The results highlighted a reduction in brain Chol synthesis, mostly involving the astrocytes, with a significant reduction of desmosterol levels in R6/2 mice. Moreover, the significantly lower levels of 24S-hydroxycholesterol in R6/2 mice with higher levels of desmosterol suggested the use of administered Chol to maintain the steady state of Chol synthesis in the whole brain. The analysis of Chol metabolites in plasma and brain samples from R6/2 mice showed how the reduction of Chol synthesis related to the disease was significant only at 12 weeks of age when the disease led definitely to death. Finally, we evaluated the distribution of Chol metabolites using imaging mass spectrometry (IMS). In conclusion, the presented thesis explored the study of HD, focusing on the development of different mass spectrometric strategies to study the pharmacokinetics of the administered Chol, the alteration of Chol metabolism, and the spatial distribution of Chol metabolites in brain slices of a mouse model of the disease. The proposed methods paved the way to further investigations on the alteration of brain Chol metabolism related to HD.

“Ho capito: Bontà, Fiducia e Resistenza”

“Hai dimenticato Lealtà”

.....

A mio nonno, uomo di poche parole ma essenziali

GRAZIE

Laboratory of Mass Spectrometry
Laboratory of Biochemistry and Protein Chemistry

Istituto di Ricerche Farmacologiche Mario Negri IRCCS, Milan
(Italy)



ISTITUTO DI RICERCHE
FARMACOLOGICHE
MARIO NEGRI · IRCCS

TABLE OF CONTENTS

ABSTRACT.....	ii
LIST OF ABBREVIATIONS	xv
1. INTRODUCTION.....	1
1.1. Huntington's disease	1
1.1.1. Clinical features of Huntington's Disease.....	3
1.1.2. Huntingtin protein and its role in disease progression	7
1.1.3. Central Nervous system pathology in Huntington's Disease.....	9
1.1.4. Peripheral pathology in Huntington's disease.....	10
1.1.5. Epidemiology	12
1.1.6. Cell and animal models of Huntington's disease	14
1.1.7. Therapeutic Treatments.....	16
1.2. Cholesterol	18
1.2.1. Cholesterol metabolism.....	19
1.2.2. Cerebral cholesterol metabolism.....	22
1.2.3. Cholesterol metabolism regulation	27
1.2.4. Cholesterol metabolism in Huntington's Disease	29
1.2.5. Cholesterol administration	32
1.3. The intranasal administration as a strategy for delivering drugs to the CNS.....	33
1.4. Mass spectrometry as analytical technique in biological investigations.....	35
1.4.1. Theoretical principles.....	36
1.4.2. Liquid chromatography coupled to mass spectrometry (LC-MS)	37
1.4.2.1. Tandem mass spectrometry.....	38
1.4.3. Imaging Mass Spectrometry	40
1.4.3.1 MALDI-IMS	42
1.4.3.2. Quantitative IMS	44
1.4.5. Analysis of cholesterol metabolites by mass spectrometry	45
1.4.5.1. Hydrolysis methods in literature	50
1.5. Analytical method validation	53
1.5.1. Lower limit of quantitation	54
1.5.2. Calibration curve	54
1.5.3. Carry over.....	55
1.5.4. Accuracy	55
1.5.5. Precision.....	56

1.5.6. Matrix Effect	57
1.5.7. Recovery	57
1.5.8. Freeze and thaw stability.....	58
1.5.9. Validation of analytical methods for endobiotics	59
2. RATIONALE AND AIM	64
2.1 RATIONALE.....	64
2.2. AIM	65
3. MATERIALS AND METHODS	68
3.1. Standards and Chemicals	68
3.2. Liposomes	69
3.3. Animal model and treatment schedules	70
3.4. LC-MS analysis of exogenously administered cholesterol	72
3.4.1. Sample preparation.....	73
3.4.2. Validation scheme for Chol-D6 analysis	74
3.5. LC-MS analysis of cholesterol metabolites	76
3.5.1. Sample preparation.....	76
3.5.3. Instrument set-up.....	78
3.5.4. Validation scheme for Chol metabolites	80
3.6. Imaging Experiments	81
3.6.1. Sample Preparation	81
3.6.2. Sample derivatization.....	82
3.6.3. Instrumental analysis.....	84
3.7. Statistical Analysis	85
4. RESULTS AND DISCUSSION.....	86
4.1. Validation of the LC-MS method for D6-Chol quantitation.....	86
4.1.1. Calibration curves	86
4.1.2. Carry-over	89
4.1.3. Accuracy and precision	89
4.1.4. Recovery	92
4.1.5. Stability	92
4.2. I trial: Single Treatment of 8-week-old WT mice.....	94
4.3. II trial: Single Treatment of 8-week-old WT and R6/2 mice.....	96
4.4. III Trial: Repeated Treatments in WT and R6/2 mice	98
4.5. IV Trial: evaluation of D6-Chol levels 42 days after a single dose	101
4.6. Cholesterol metabolites analysis	104

4.6.1 Method optimization	104
4.6.2. MRM transitions	105
4.6.3 Chromatographic separation optimization	110
4.7. Optimization of sample preparation.....	114
4.8. Hydrolysis reaction set up	115
4.8.1 KOH concentration and temperature of the reaction	115
4.8.2 Optimization of incubation time for hydrolysis reaction	119
4.8.3. Validation of the optimized hydrolysis reaction with a commercial kit	121
4.9. Validation of the method.....	123
4.9.1 Calibration curves	123
4.9.1.1. Brain calibration range.....	124
4.9.1.2. Plasma calibration range	126
4.9.2 Recovery from plasma matrices.....	129
4.9.3 Recovery from brain matrices	130
4.10. Chronic treatment with D6-Chol: metabolism analysis in striatum samples...	131
4.11. Cholesterol metabolism analysis: WT and R6/2 mice	136
4.12. Clinical Longitudinal Study	138
4.13 Imaging mass spectrometry.....	142
4.13.1 Evaluation of derivatization reaction on desmosterol, 24-hydroxycholesterol, and cholesterol.....	142
4.13.2. Source parameters optimization.....	146
4.13.3. Imaging experiment on WT and R6/2 mice.....	148
4.13.4. Cholesterol Quantitative Imaging Mass Spectrometry	153
5. CONCLUSIONS	156
6. BIBLIOGRAPHY	160
7.1. List of publications related to the presented Ph.D. project.....	168

Table 1. HD symptoms grouped in motor, cognitive and psychiatric fields.....	5
Table 2. Derivatization methods used for Chol metabolites analyses in literature	48
Table 3. Basic hydrolysis conditions present in literature.	50
Table 4 Method validation steps for endobiotics and their similarities with method validation for xenobiotics	60
Table 5. Validation scheme proposed for Chol metabolites quantitation in biological matrices	63
Table 6. Scheme of temperature and solvent gradient of the developed UHPLC-MRM method	78
Table 7. Graphical representation of the segmented gradient used for oxysterols and Chol precursors	79
Table 8. Selected MRM transitions and related Collision Energy (CE)	79
Table 9. Validation scheme for Chol metabolites method	80
Table 10. Calibration range for chol metabolites analysis in plasma and brain matrices	80
Table 11. Linearity and LLOQ of D6-Chol in plasma.....	1
Table 12. Linearity and LLOQ of D6-Chol in brain	1
Table 13. Intra-day accuracy and precision of D6-Chol in plasma.....	90
Table 14. Intra-day accuracy and precision of D6-Chol in mouse homogenates	90
Table 15. Inter-day accuracy and precision of D6-Chol in plasma.....	91
Table 16. Inter-day accuracy and precision of D6-Chol in brain homogenates.....	91
Table 17. Recovery of D6-Chol in plasma and brain matrices	92
Table 18. Stability of D6-Chol in plasma in different analytical conditions: benchtop stability, long-term storage and freeze and thaw stability	93
Table 19. Stability of D6-Chol in brain homogenate in different analytical conditions: benchtop stability, long-term storage and freeze and thaw stability.....	93
Table 20. D6-Chol levels in plasma, striatum, cortex, and cerebellum of WT mice following single intranasal treatment expressed as average (\pm SD); (ND: not detectable; N=3/time point)	95
Table 21. II trial. Calculated concentrations of D6-Chol in plasma samples, bulbs, striatum, cortex, and cerebellum in WT and R6/2 mice expressed as average (\pm SD);	97
Table 22. . D6-Chol levels in striatum, cortex, cerebellum, kidney, liver, plasma and bulbs of WT and R6/2 mice 42 days after a single treatment (N=4/experimental group).	102

Table 23. Optimized MRM transitions (quantifier and qualifier) and relative CE (V)	108
Table 24. Chromatographic gradient for oxysterols separation (Villani et al.).....	110
Table 25. Final chromatographic method for the separation of oxysterols and Chol precursors	111
Table 26. Hydrolysis conditions tested for method setup	115
Table 27. 24SOHC and 27OHC levels in plasma samples after hydrolysis with KOH 1M (N=3/experimental group)	116
Table 28. Oxysterols and relative IS peak areas under different hydrolysis conditions	118
Table 29. Experimental conditions tested for the identification of the best time of incubation	119
Table 30. Quantified Chol levels using Commercial kit and in-house developed and validated method based on LC-MS	121
Table 31. Back-calculated concentrations of lanosterol over five different analytical sessions	124
Table 32. Back-calculated concentrations of desmosterol over five different analytical sessions	125
Table 33. Back-calculated concentrations of 7-dehydrocholesterol over five different analytical sessions	125
Table 34. Back-calculated concentrations of 24SOHC over five different analytical sessions	126
Table 35. Back-calculated concentrations of lanosterol over five different analytical sessions	126
Table 36. Back-calculated concentrations of desmosterol over five different analytical sessions	127
Table 37. Back-calculated concentrations of 7-dehydrocholesterol over five different analytical sessions	127
Table 38. Back-calculated concentrations of 24S-hydroxycholesterol over five different analytical sessions	128
Table 39. Back-calculated concentrations of 27-hydroxycholesterol over five different analytical sessions	128
Table 40. Back-calculated concentrations of 7 α -phadihydroxycholesterol over five different analytical sessions	128
Table 41. Recovery from plasma matrix. (N=3/experimental group).....	129

Table 42. Recovery from brain matrix. (N=3/experimental group).....	130
---------------------------------------------------------------------	-----

Figure 1. Overview of George Huntington first article in which he described the disease for the first time, 1872.....	2
Figure 2. HD symptoms divided for different phases of the disease: from the initial phases characterized by involuntary movements, across middle phase characterized by cognitive disorders up to the final phase characterized by loss of bowel and bladder control (from (13)).	6
Figure 3. Functions of huntingtin and effects of abnormal CAG repeats in disease development	7
Figure 4. Comparison between Huntington Disease Brain and Normal Brain (from (23))	9
Figure 5. Scheme of peripheral symptoms of HD, modified from (25).....	11
Figure 6. Longer CAG repeats in individuals of European descent are thought to result in higher rates of CAG repeat expansion and de novo HTT mutation (from (6)).....	13
Figure 7. Overview of HD: list of principal aspects discussed in chapter 1.1.	15
Figure 8. Resume of possible HD treatments.	17
Figure 9. Structure of Chol (created with Chems sketch)	18
Figure 10. Simplified scheme of Chol synthesis.....	20
Figure 11. Representative scheme of Chol metabolism (created with BioRender).	21
Figure 12. Scheme of brain Chol synthesis and transport.....	25
Figure 13. Scheme of Chol metabolism (created with Biorender).....	28
Figure 14. Scheme of Chol role in disease development.....	31
Figure 15. Example of MS/MS spectra from chol metabolites analyses (Shimadzu LCMS8060, Product ion scan, positive mode)	36
Figure 16. Scheme for the easy representation of various scan modes of triple quadrupole (modified from (92))	39
Figure 17. Block Scheme of an imaging mass spectrometry experiment.	41
Figure 18 IMS experiment workflow (created with BioRender).	42
Figure 19 Number of published articles/year relating GC-MS to oxysterols (Panel A) or LC-MS to oxysterols (Panel B).....	45

Figure 20. Number of articles/year published in the field of cholesterol imaging mass spectrometry.....	49
Figure 21. Comparison of three different hydrolysis methods from literature.	52
Figure 22. LC–MS/MS chromatograms showing (A) background peak of an endogenous analyte in blank matrix, (B) a surrogate matrix with known concentration of the target analyte, (C) the same matrix after spiking with a standard of a known concentration (method of background subtraction), (D) method of the standard addition: one study sample is split into several aliquots, each spiked with a standard (Std.) of different concentration, (E) a standard of a surrogate analyte spiked into the same original matrix (surrogate analyte method).	61
Figure 23. Chemical structure of 24SOHC with and without Girard’s T (GT) derivatization. ..	82
Figure 24. Chemical structure of desm with and without Girard’s T (GT) derivatization.....	82
Figure 25. Chemical structure of Chol with and without Girard’s T derivatization	83
Figure 26A. Representative calibration curve in plasma, from 0.05 to 5 µg/mL 26B. Representative calibration curve in brain homogenate, from 0.03 ng/mg and 10 ng/mg	88
Figure 27. D6-Chol levels in plasma, striatum, cortex, and cerebellum of WT mice following single intranasal treatment (connecting lines with error bars, average ± SD; N=3/time point)..	94
Figure 28 II trial. Calculated concentrations of D6-Chol in plasma samples (A), bulbs (B), striatum (C), cortex (D,) and cerebellum (E) in WT and R6/2 mice (connecting lines with error bars, average ± SD; N=3/time point)	96
Figure 29. D6-Chol levels in striatum, cortex and cerebellum of WT and R6/2 mice following intranasal acute or sub-chronic treatments. BL: D6-Chol basal level.....	100
Figure 30. D6-Chol levels in striatum, cortex, cerebellum, kidney, liver, plasma and bulbs of WT and R6/2 mice 42 days after a single treatment (N=4/experimental group). Statistical analysis: one-way ANOVA	102
Figure 31. Parent ions selected for Chol precursors analysis.....	105
Figure 32. Parent ions selected for oxysterols analysis.....	106
Figure 33. MS/MS experiments using product ion scan in the analysis of standard mix solution (10 ng/µL; 5 µL injected).....	109
Figure 34. Complete LC-MRM chromatogram obtained from the analysis of a standard mix	112

Figure 35. Challenging separation of 24SOHC and 25OHC: LC-MRM chromatogram obtained from the analysis of a standard mix	113
Figure 36. 24SOHC and 27OHC levels in plasma samples after hydrolysis (N=3/experimental group).....	116
Figure 37. Oxysterols and relative IS peak areas under different hydrolysis condition (N=3/experimental group)s. Statistics: One-way ANOVA	117
Figure 38. Results of the optimization of the incubation time with KOH 1M.....	120
Figure 39. Comparison between the chol analysis using a commercial kit and in-house developed hysrolysis method (Spearman correlation)	122
Figure 40. Upper panel: Block scheme of Chol metabolic pathway; Lower panel: Lanosterol, Desmosterol, 7-dehydrocholesterol and 24SOHC levels in striatum area in WT, R6/2 mice and R6/2 mice treated with liposomes (n>=5 mice/group). Data are expressed as mean ± standard error of the mean. Each dot correspond to the value obtained from each animal. Statistics: one-way ANOVA with Kruskal-Wallis test (*p < 0.05; **p < 0.01; ***p < 0.001).....	133
Figure 41. 7-alpha dihydroxycholesterol, 24SOHC, 27OHC, Lanosterol, Desmosterol and 7-dehydrocholesterol levels in striatum area in WT and R6/2 (n>=3 mice/group). Data are expressed as mean ± standard error of the mean. Each dot correspond to the value obtained from each animal. Statistics: one-way ANOVA with Kruskal-Wallis test (*p < 0.05; **p < 0.01; ***p < 0.001).135	135
Figure 42. Desmosterol, 7-dehydrocholesterol and 24SOHC levels in striatum area in WT and R6/2 (n>=6 mice/group). Data are expressed as mean ± standard error of the mean. Each dot correspond to the value obtained from each animal. Statistics: one-way ANOVA with Kruskal-Wallis test (*p < 0.05; **p < 0.01; ***p < 0.001).....	137
Figure 43. Block scheme of the proposed longitudinal study	139
Figure 44. 24SOHC plasma levels in control, Pre-HD, HD-I and HD-II-III groups. (N>=20/experimental group). Statistics: one-way ANOVA with Kruskal-Wallis test (*p < 0.05; **p < 0.01; ***p < 0.001).....	141
Figure 45. Total Ion Current (TIC), MS, and MS/MS spectra obtained from the analysis of a derivatized Chol spot (0.2 ng/spot).....	143

Figure 46. Total Ion Current (TIC), MS, and MS/MS spectra obtained from the analysis of a derivatized 24SOHC spot (0.2 ng/spot)	144
Figure 47. Total Ion Current (TIC), MS, and MS/MS spectra obtained from the analysis of a derivatized desmosterol spot (0.2 ng/spot)	145
Figure 48. The ramp of spray voltage optimization (kV) using m/z 498.4402 as a reference peak	146
Figure 49. The ramp of capillary temperature optimization using m/z 498.4402 as a reference peak.....	147
Figure 50. Mean spectra (450 scans) of WT brain slice obtained during an IMS experiment..	148
Figure 51. Comparison of IMS analysis of sagittal brain slice from a WT and R6/2 mice, highlighting a lower level of Chol in R6/2 mice. The figures show the Chol distribution and the intensity is proportional to its abundance in the different brain areas (arbitrary units).	150
Figure 52. Comparison of IMS analysis of sagittal brain slice from a WT and R6/2 mice, highlighting a lower level of m/z 514.5357 in R6/2 mice. The figures show the distribution and the intensity is proportional to its abundance in the different brain areas (arbitrary units).	151
Figure 53. Comparison of IMS analysis of sagittal brain slice from a WT and R6/2 mice, highlighting a lower level of m/z 496.4268 in R6/2 mice. The figures show the distribution and the intensity is proportional to its abundance in the different brain areas (arbitrary units).	152
Figure 54 Results obtained from the quantitative IMS experiment of Chol on brain slices from WT and R6/2 mice. Panel A. shows the linearity obtained from the calibration curve. Panel B. shows the quantified Chol level in WT and R6/2 slices expressed as ng/mm ² , highlighting a reduction of free Chol level in whole the whole brain area of R6/2 with respect to WT mice. Panel C. shows the results of IMS experiment acquiring Chol standard.....	154

LIST OF ABBREVIATIONS

24SOHC: 24S-hydroxycholesterol

25OHC: 25-hydroxycholesterol

27OHC: 27-hydroxycholesterol

7 α HC: 7- α hydroxycholesterol

7-dehydrochol: 7-dehydrocholesterol

ABCA1: ATP-binding cassette transporter A1

ACAT: acyl-CoA: cholesterol acyl-transferase

AD: Alzheimer Disease

AP-MALDI: Atmospheric Pressure MALDI

ApoE: apolipoprotein E

BBB: blood-brain barrier

BDNF: Brain-derived neurotrophic factor

BHT: Butylated hydroxytoluene

CE: collision energy

CHCA: α -cyano-4-hydroxy-cinnamic acid

Chol: cholesterol

CNS: central nervous system

CSF: cerebral spinal fluid

CV: coefficient of variation

CYP51: sterol 14 α -demethylase

CYP7A1: cholesterol 7 α -hydroxylase

CYP27A1: sterol 27-hydroxylase

CYP46A1: cholesterol 24-hydroxylase

DCM: dichloromethane

DESI: Desorption electrospray ionization

desm: desmosterol

DHB: 2,5-dihydroxybenzoic acid

DHCR7: 7-dehydrocholesterol 7-reductase

DHCR24: 3 β -hydroxysterol delta-24-reductase

ER: endoplasmic reticulum

FDA: Food Drug Administration

GC-MS: Gas chromatography-Mass spectrometry

HD: Huntington's disease

HMGCoA: 3-hydroxy-3-methylglutaryl-coenzyme A

HMGCoAR: 3-hydroxy-3-methylglutaryl-coenzyme A reductase

HMGCoAS: 3-hydroxy-3-methylglutaryl-coenzyme A synthase

HTT: huntingtin protein

IMS: imaging mass spectrometry

iPSC: induced pluripotent stem cells

IS: internal standard

IV: intravenous

LC-MS: liquid chromatography-mass spectrometry

lan: lanosterol

Lat: lathosterol

LLOQ: lower limit of quantitation

LXR: liver X receptor

MALDI: matrix-assisted laser desorption/ionization

MF: matrix factor

MRI: magnetic resonance imaging

MRM: multiple reaction monitoring

MS/MS: tandem mass spectrometry

mHTT: mutated huntingtin protein

NMDA: N-methyl-D-aspartate

PBS: phosphate-buffered saline

PreHD: pre - Huntington's disease

Q-IMS: quantitative imaging mass spectrometry

QC: quality control

SA: sinapinic acid

SD: standard deviation

SIM: selected ion monitoring

SPE: Solid-phase extraction

SQS: squalene

SREBP: sterol-regulatory element-binding protein

TG: transgenic mice

ULOQ: upper limit of quantitation

WT: wild type mice

1. Introduction

1. INTRODUCTION

1.1. Huntington's disease

Huntington's disease (HD) is an autosomal dominant neurodegenerative disorder caused by a CAG repeat expansion in exon 1 of the huntingtin (HTT) gene on chromosome 4¹. This protein is widely expressed throughout the body and various roles in different intracellular functions have been attributed to it, such as protein trafficking, vesicular transport, endocytosis, synaptic post-transmission, transcriptional regulation, and an anti-apoptotic function². The triplet CAG translates to the amino acid glutamine and the increase of its repetitions in the gene causes the production of a mutated protein with an abnormal polyglutamine chain at the N-terminal end¹. The maximum number of repetitions normally present in the first exon of the gene of the HTT is 35; in the patients with HD the polymorphic region is long because of the increase of these repetitions³. The mutation is completely penetrating at 40 or more repetitions; between 36 and 39 the mutation penetrance is reduced and carriers may develop symptoms later in time or not develop them at all. An inverse correlation has been found between the number of CAGs and the age of onset of the disease: as the number of triplets of CAG increases, the onset of the disease is anticipated. In addition, cases of juvenile onset have been reported in patients with more than 60 repetitions⁴. Patients are affected by a combination of symptoms, ranging from movement disorders to psychiatric disturbances, with death occurring 15-20 years after symptom onset⁵. The disease affects approximately 10.6-13.7 individuals per 100,000 in western populations⁶; however, there is considerable variability between different regions and ethnic groups⁷.

Among the main symptoms of the disease is listed chorea (from the latin *chorēa*, dance), namely the sudden onset of involuntary, irregular and asymmetrical movements⁸. The original discovery of this disease was due to the manifestation of this symptom which is the most recognizable. Several physicians throughout the 19th century noted a chorea of hereditary nature, but the more detailed account was written in 1872 by the newly graduated George Huntington from whom the disease is named⁸.

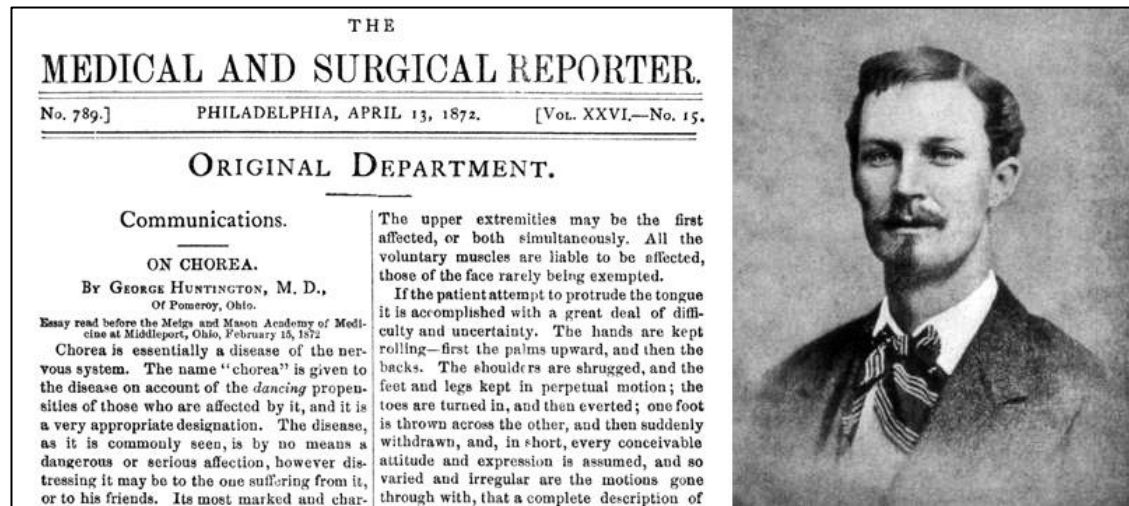


Figure 1. Overview of George Huntington first article in which he described the disease for the first time, 1872

In his essay entitled "On chorea" he talked about a hereditary chorea confined to a few families, transmitted by past generations, which manifested itself in a serious form only in adult life. Furthermore, he wrote that, as the disease progressed, the mind was compromised, leading many patients to insanity and, often, to a marked tendency to suicide. Initially the disorder was called Huntington's chorea, but at the moment the terminology Huntington's disease is preferred, because it is the motor coordination skills, such as walking and posture, that directly harm the patient's functions, being compromised with the advancement of the disease ⁸.

1.1.1. Clinical features of Huntington's Disease

HD typically affects patients in middle age but can occur at any time in life, both in childhood and in old age. Before the symptomatic phase of the disease, the patients do not show any particular clinical abnormality. After HD starts, the function abilities of patients gradually worsen over time. The disease progression is slow and leads to death in 17-20 years from the first onset of symptoms ⁹. The symptoms related to HD include motor, cognitive and psychiatric disorders ⁸. Which symptoms appear first varies greatly from person to person, as well as the timing of disease progression. After the first phase of a healthy life, the first symptoms begin to emerge without patient awareness ¹⁰, the first symptoms involve some imperceptible personality changes, mild cognitive decline, and movement control skills. During this stage individuals can become irritable, uninhibited, or unreliable at work, they become unable to perform multiple actions simultaneously, feeling increased anxiety, forgetfulness and restlessness even during the night ⁸. The diagnosis of the disease occurs when it is impossible to find other explanations for the occurrence of symptoms and it is characterized by the appearance of the most serious symptoms, such as chorea.

The motor decline begins with occasional, labile, and low-amplitude movements of the face and distal extremities; over time the decline involves more proximal muscles and generates amplified movements of the entire body. Impairments due to involuntary movements — rather than voluntary movements — may have a greater impact on a person's ability to work, perform daily activities, communicate and remain independent. During the disease progression, other more disabling motor symptoms may emerge, such as dysphagia, dystonia, stiffness, and ataxia. In particular, dysphagia in patients could cause weight loss and respiratory difficulties ¹¹, while dystonia is caused by an inappropriate and prolonged muscle contraction that leads to abnormal postures. Moreover, motor disorders can lead to walking problems and a higher risk of falls that can lead to serious injuries and complications. The onset of the disease affects the long-term memory, while the worsening of the disease over time affects the executive functions, like the organization, the planning, the control, and the acquisition of new motor functions ⁸. Cognitive

disorders involve the alteration of visual-spatial and executive functions, recognition of emotions, and altered processing speeds (12).

There are several neuropsychiatric symptoms that can arise in HD such as apathy, anxiety, irritability, depression, obsessive-compulsive behaviours and psychosis. Depression is the most common with a prevalence of 40% in HD (12); it is estimated that the number of suicides among patients is about 5-10 times higher than the general population ¹². Depression isn't simply a reaction to receiving a diagnosis of HD but appears to occur because of injury to the brain and subsequent changes in brain function. George Huntington wrote in his article "On chorea" about the patients' marked tendency to madness that often can lead to their suicide. Apathy appears to be the only psychiatric symptom that has been shown to worsen as the disease progresses (13); it is characterized by loss of interest, difficulty starting activities and passive behaviour. Table 1 summarizes the main symptoms of HD, classifying them in the three main categories (motor, cognitive, psychiatric).

Table 1. HD symptoms grouped in motor, cognitive and psychiatric fields.

HD Symptoms		
<i>Motor disorders</i>	<i>Cognitive disorders</i>	<i>Psychiatric disorders</i>
- Involuntary jerking or writhing movements (chorea)	- Difficulty organizing, prioritizing, or focusing on tasks	- Depression is the most common psychiatric disorder
- Slow or abnormal eye movements	- Lack of impulse control, acting without thinking	- Sadness, irritability, or apathy
- Impaired gait, posture, and balance	- Lack of awareness of one's own behavior and abilities	- Social withdrawal
- Difficulty with speech	- Slowness in processing thoughts	- Insomnia
- Impairments in voluntary movements	- Difficulty in learning information	- Fatigue and loss of energy
- Muscle problems, such as rigidity or muscle contracture (dystonia)		- Frequent thoughts of death, dying, or suicide

Figure 2 shows the subdivision of symptoms from the onset of the disease and during its worsening, highlighting how psychiatric disorders arise in the early stages of the disease whereas the cognitive ones occur during the worsening of the disease.

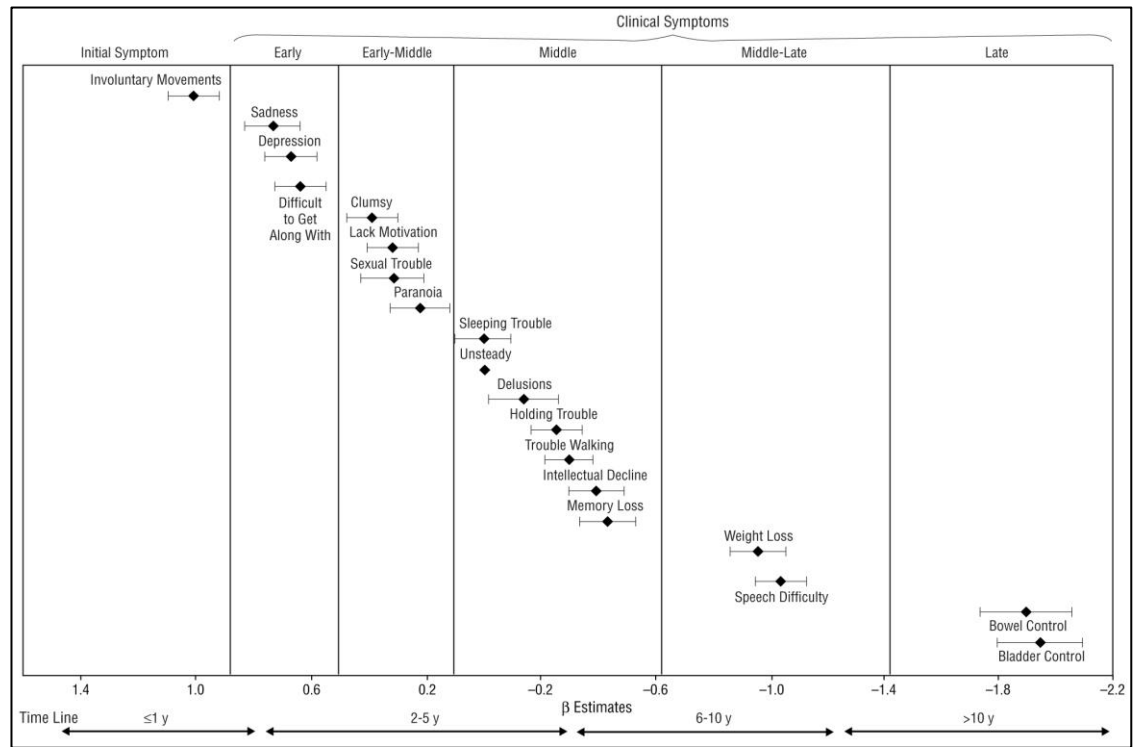


Figure 2. HD symptoms divided for different phases of the disease: from the initial phases characterized by involuntary movements, across middle phase characterized by cognitive disorders up to the final phase characterized by loss of bowel and bladder control (from ¹³).

1.1.2. Huntingtin protein and its role in disease progression

Huntingtin (HTT) is the protein coded by the *htt* gene, also known as the IT15 ("interesting transcript 15") gene, expressed in many tissues in humans and mammals. The role of the native HTT is not yet fully known but it seems to be involved in several cellular processes, including axonal transport and transcriptional events. HTT is essential for the development of many tissues in mammals, and its absence is lethal in mice ¹⁴. HTT has no sequence homology with other proteins and it has the highest concentration in the brain and testicles; small amounts are also present in the liver, heart, and lungs ¹⁵. HTT upregulates the expression of brain-derived neurotrophic factor (BDNF) at the transcription level, but the mechanism by which huntingtin regulates gene expression has not been determined. The localisation of HTT in the mitochondrial membrane further suggests that HTT is involved in the regulation of energy metabolism ¹⁶.

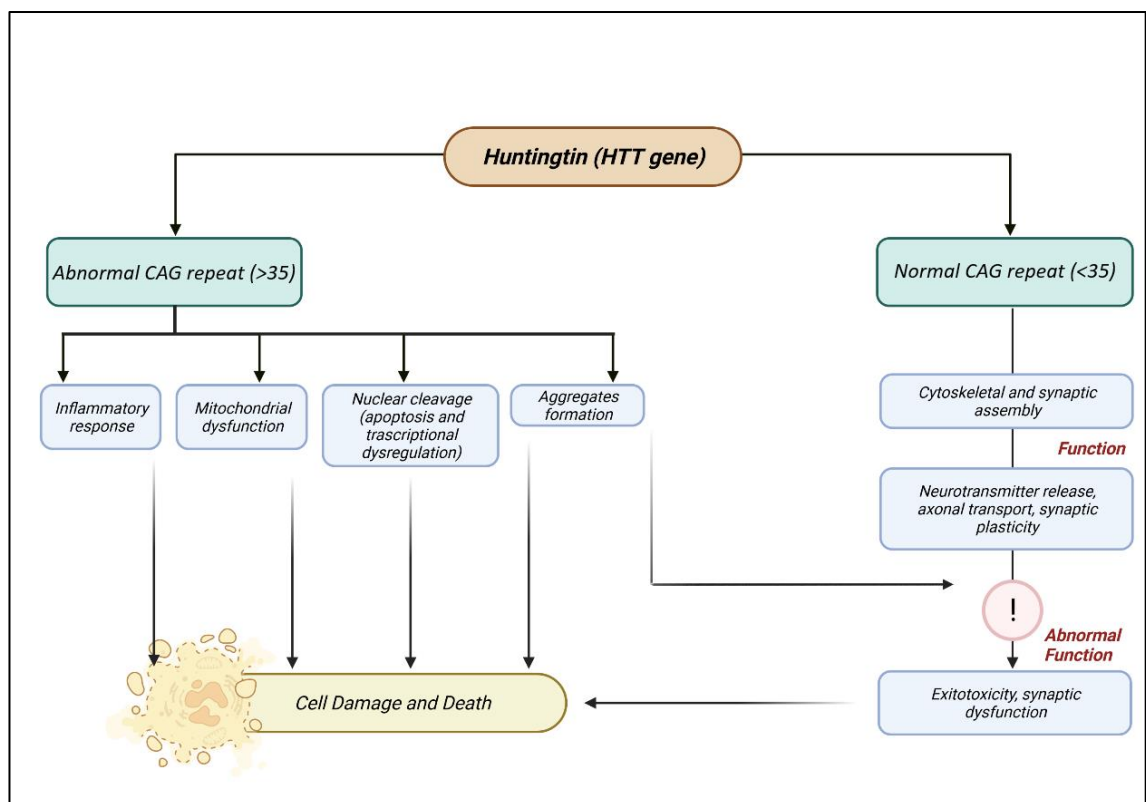


Figure 3. Functions of huntingtin and effects of abnormal CAG repeats in disease development

Although not all mechanisms of action of HTT are clearly explained by literature, it is well known that mutated HTT (mHTT) is the cause of HD and it has been investigated for its involvement in long-term memory alteration and disease progression. Data present in literature confirmed that the expression of normal and mHTT protein forms are similar ¹⁷. Interestingly, the cellular localisation of mHTT differ from the wild-type since the first one forms inclusions in the nucleus whereas the HTT is primarily cytoplasmatic ¹⁵.

Evidences from the literature suggest that HD arises predominantly from the gain of a toxic function due to an abnormal conformation of mHTT. The presence of an expanded polyQ tract causes a number of structural and conformational changes in the mHTT protein that play a key role in HD pathogenesis ⁵. Although the exact toxicity mechanism of mHTT remain elusive, N-terminal fragments containing the polyQ tract have been shown to be fundamental for the pathology ¹⁸. While wildtype HTT is largely α -helical, toxic mHTT has parts forming a compact β -sheet secondary structure and this lead to the formation of aggregates that are homologous to aggregates seen in other protein misfolding diseases ⁵.

1.1.3. Central Nervous system pathology in Huntington's Disease

The CNS degeneration caused by HD is widespread, with a post-mortem reduction of total brain volume of 19 % ¹⁹ (Figure 4). The most prominently affected site is the striatum in the basal ganglia, where 95 % of GABAergic medium spiny neurons (MSNs) are lost ²⁰. This results in a total striatal volume loss of approximately 50%. Striatal pathology is crucial for disease progression and studies in the literature confirmed that it correlates to motor impairment ²¹.

It is important to note that while neuronal death is the hallmark of HD, dysfunction probably occurs earlier ²². CNS pathology in HD is not merely neuronal, as the mutant protein is also expressed in glial cells (23).

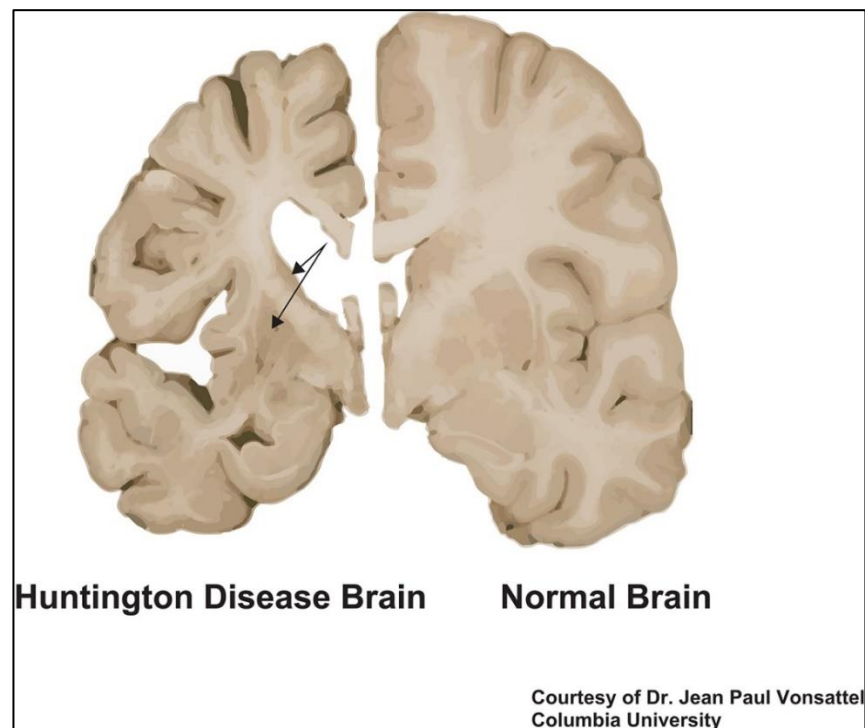


Figure 4. Comparison between Huntington Disease Brain and Normal Brain (from ²³)

1.1.4. Peripheral pathology in Huntington's disease

In recent years, it has emerged that HD is a disease of the whole body, not only related to CNS. Most of these changes are described in animal models of HD, but is gradually becoming evident that similar abnormalities occur in peripheral tissues of patients. The mHTT protein is expressed in all cells and tissues ²⁴, resulting in a range of pathologies as diverse as the tissues affected ²⁵. This is easily understandable if we take into account that wild-type HTT has a role also in non-neuronal cells. The peripheral pathology is not a response to CNS pathology but it is an own response.

In addition to the classic symptoms, HD is complicated by other disorders, such as weight loss and skeletal-muscle wasting, which are not necessarily directly associated with changes in brain functions (Figure 5). These problems sometimes appear early in the disease course and can eventually contribute substantially to both morbidity and mortality.

One of the most important aspects of peripheral pathology relates to an abnormal immune system function, which causes, in HD patients of all disease stages, elevated levels of circulating proinflammatory cytokines and chemokines in their peripheral blood ^{26,27}. Further peripheral changes include endocrine dysfunction, osteoporosis and testicular atrophy ²⁵. These data confirm that the ubiquitous expression of mHTT has intrinsic negative effects on peripheral tissues and not only in the CNS.

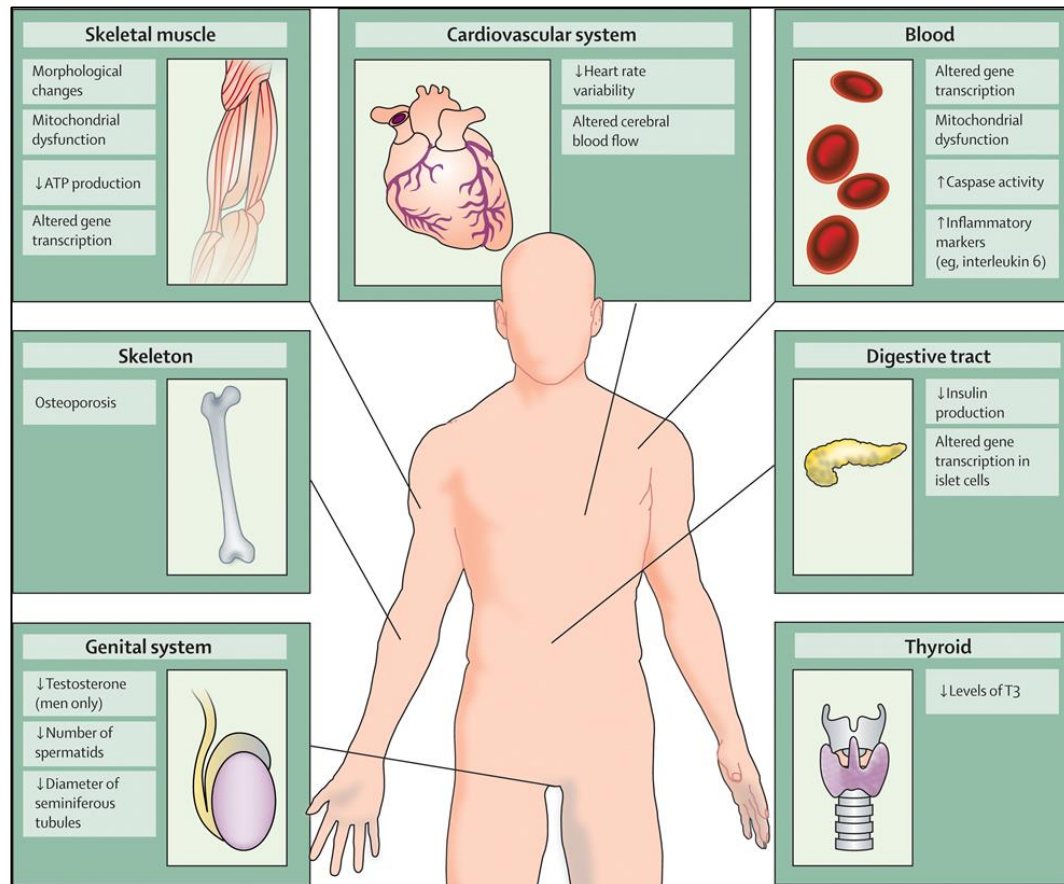


Figure 5. Scheme of peripheral symptoms of HD, modified from ²⁵.

Direct measurements of peripherally manifested symptoms could possibly translate into potential biomarkers. The idea that the effects of mHTT in peripheral cells can be used to track the disease progression is appealing. Moreover, this could integrate the monitoring of other promising biomarkers, such as 24-hydroxycholesterol that, as reported in literature, can reflect the neurodegeneration at plasma level.

1.1.5. Epidemiology

The prevalence of HD is different depending on the geographical area considered. In addition, since the introduction of genetic tests, there has been a reported increase in the prevalence of the disease²⁸. The most affected population is the western one and according to recent studies people affected are 12.3 per 100000²⁹.

In Venezuela, among the communities living near Lake Maracaibo, the incidence of the disease is higher, up to 700 per 100000. On this population, conducive to few founders, were made the genetic studies that led, in 1993, to the discovery of the mutation that causes HD^{30 1}.

In Asia, on the other hand, the prevalence is very low³¹ while in Western Europe the prevalence is 9.71 per 100000 inhabitants²⁹. Interestingly, Bates *et al.* highlighted differences in mean CAG repeat length prevalence in world populations. Average CAG repeat lengths are longer in populations with a high prevalence of the disease, from 18.4–18.7 repeats in people of European descent, to only 17.5–17.7 in East Asian and 16.9–17.4 in African populations⁶ (Figure 6).

In northern Italy, a study on the prevalence of the disease, carried out before the HTT gene was detected and the genetic test was created, reported an incidence of HD between 1.8 and 4.8 per 100000 people³². A more recent study, carried out instead on the population of Molise, reported a prevalence of 10.85 per 100000 inhabitants, more than double that identified before the creation of the genetic test³³.

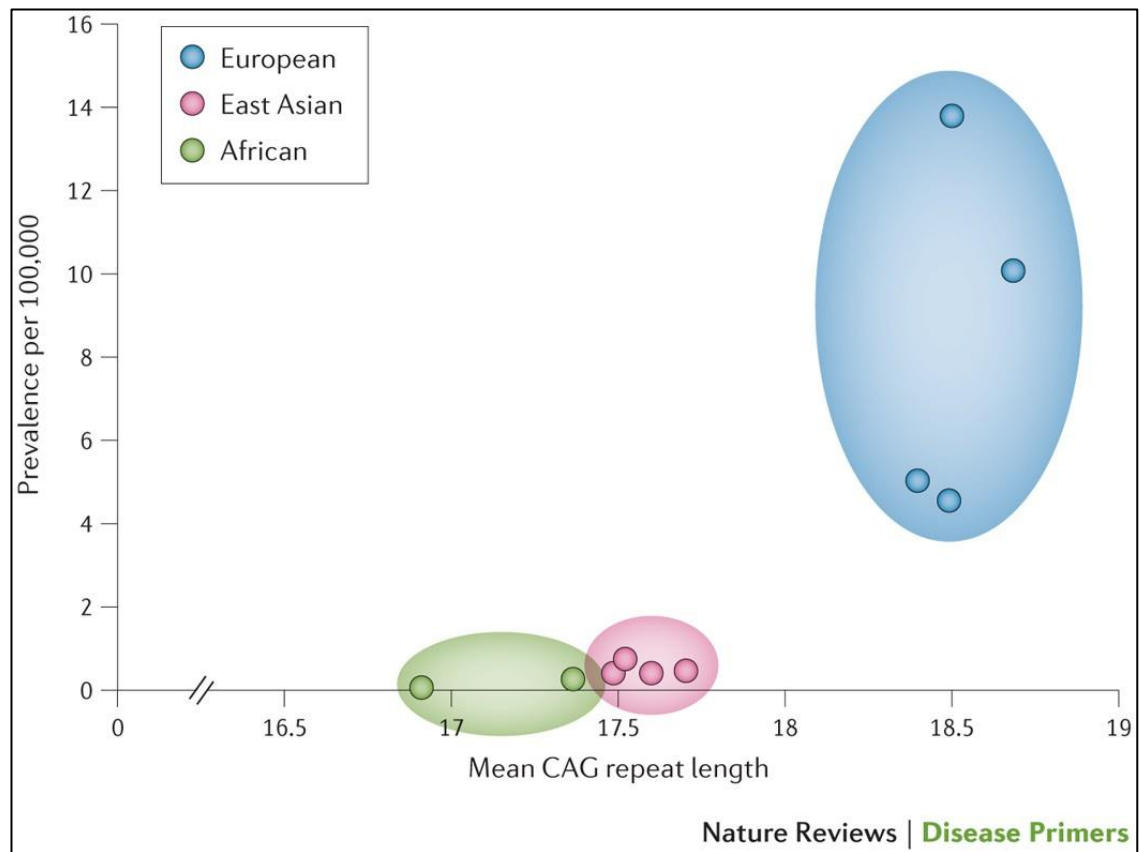


Figure 6. Longer CAG repeats in individuals of European descent are thought to result in higher rates of CAG repeat expansion and de novo HTT mutation (from (6))

1.1.6. Cell and animal models of Huntington's disease

Numerous cell models exist to study HD in the laboratories, from *ex vivo* patient cells to neuronal cell lines with CAG repeat knock-ins, with a recent avenue of investigation focusing on the development of induced pluripotent stem cells (iPSCs). However, it is important to remember that HD pathogenesis is complex, and studying individual cell lines in isolation is therefore unlikely to provide a complete picture of the disease.

Animal models of HD range from invertebrate models to mammals such as primates, sheep, mice and rats (33). Invertebrate models like *Caenorhabditis Elegans* and *Drosophila Melanogaster* allow a rapid and high-throughput testing of specific hypotheses and novel therapeutic strategies. The *C. Elegans* model expresses expanded polyglutamine repeats in the worm nervous system³⁴. Long CAG repeats result in the formation of polyglutamine aggregates in muscle cells and overall decreased motility. The *Drosophila* model of HD expresses expanded polyglutamine repeats in the eye of the fly³⁵ and the photoreceptors progressively develop inclusions and subsequently degenerate. Invertebrates' short life spans make it easy and inexpensive to generate large numbers of animals. However, thorough evaluation of disease processes and research to develop novel therapeutics ultimately require models with more complexity. Murine models are the most commonly used, and are available in a variety of different types. With the discovery of the *htt* mutation in 1993, it became possible to create animal models with a similar genetic background of the disease seen in humans with HD (35). Genetic mice created to express the mutant *htt* gene, or a portion of it, have been the most commonly used models to answer basic biological questions about the disease and to investigate potential therapies. There are two main categories of genetic mouse models: transgenic and knock-in. Transgenic mice result from the random insertion of a portion of the human *htt* gene, containing the polyglutamine repeat, in the mouse genome, the expression of which can be driven by different promoters. Alternatively, “knocking in” a portion of the human *htt* gene in the mouse *htt* gene locus on chromosome 7 results in the creation of knock-in mice.

In this thesis project, all the experiments were carried out on R6/2 mice, a type of transgenic model of HD. R6/2 mice originates from a random insertion of 90 amino acids (a.a.) of human htt into mouse genome ³⁶.

The mutation results in mice individuals with a significant neuronal loss and neuronal atrophy in striatum ³⁷ and with a significant loss of enkephalin positive neurons in the striatum within 12 weeks.

Figure 7 summarizes all the principal aspects of HD discussed in chapter 1.1..

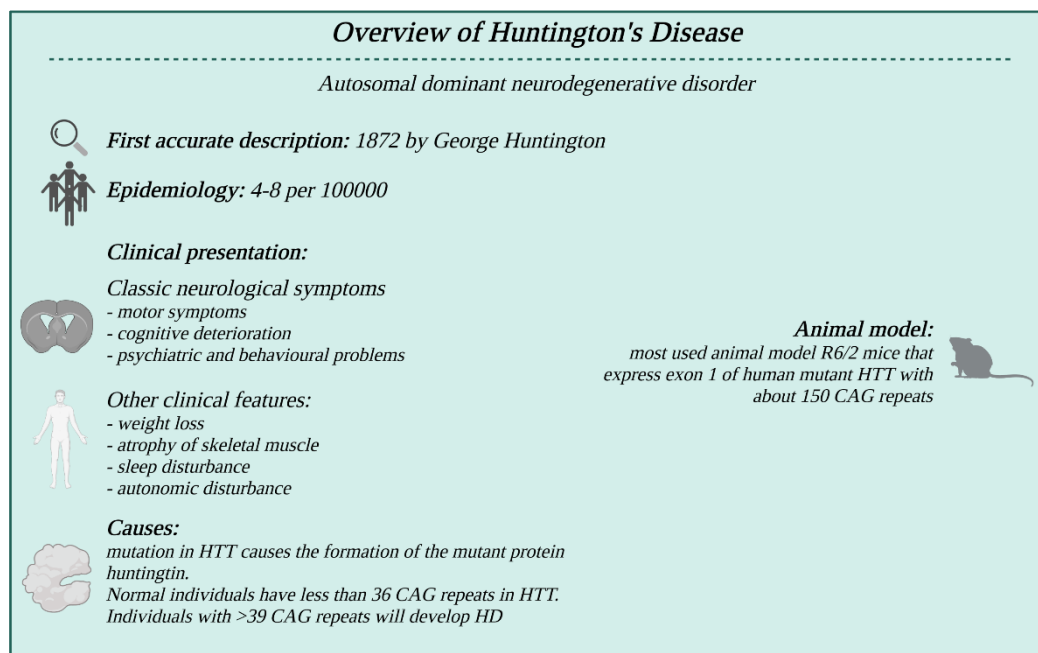


Figure 7. Overview of HD: list of principal aspects discussed in chapter 1.1.

1.1.7. Therapeutic Treatments

Currently there is no cure for HD, however there are palliative treatments focussing on symptomatic relief³⁸. Symptomatic relief, rehabilitation, and support are used to treat the disease's various symptoms of motor, mental, and cognitive decline. Excitotoxicity, the dopamine pathway, caspase inhibitors, mHTT aggregation, mitochondrial dysfunction, transcriptional dysregulation, and nutrition are among the current treatment targets for HD.

The treatment of excitotoxicity (excessive stimulation of receptors in nerve cells), is necessary when chorea becomes bothersome and it is aimed at decreasing the severity of involuntary movements. The only drug approved by the US Food and Drug Administration (FDA) for the treatment of motor symptoms is tetrabenazine, an anti-choreic agent. However, this drug is used with caution due to concerns about its proclivity to cause depression and suicidality in a population which is already at risk for these factors. Memantine, an antagonist of extrasynaptic N-methyl-D-aspartate (NMDA) receptors, is used for the treatment of moderate-severe dementia in Alzheimer's disease (AD). It reduces striatal cell death, slows disease development, and boosts cognitive performance, all of which are linked to HD and other neurodegenerative diseases³⁹. The combination of memantine and risperidone prevented the expected progression of motor symptoms, cognitive decline, and psychosis over a 6-month study period⁴⁰. However, memantine dosing may be critical, since mice on low-dose of memantine had reduced pathology, but mice on high-dose had impairing outcomes and may have encouraged cell death⁴¹. Psychiatric manifestations are treated conventionally, for example with selective serotonin reuptake inhibitors for depression. Various studies indicate that a Mediterranean-type diet may delay the onset of other neurodegenerative diseases, like AD, PD, dementia, and cognitive impairment⁴². Recently a study highlighted that a Mediterranean-type diet affects the time of HD phenoconversion. In fact, eating high amounts of dairy products was associated with an increased risk of phenoconversion. This may be due to a lower level of urate, which leads to a faster progression and manifestation of HD but these types of diet-related studies need further investigation^{43,44}. Interestingly, the intermittent fasting promotes autophagy and cleared the mHTT⁴⁵.

Other pharmacological treatments involve the mHTT as therapeutic target, inducing proteolysis, reducing mHTT aggregation or targeting the transcriptional dysregulation. Minocycline, an analogue of tetracycline, was used as a neuroprotector and showed an efficiency in reducing motor and cognitive decline in a human trial study (100 mg for 24 months). Moreover, a decrease of psychiatric symptoms was also highlighted after 24 months of treatment. The treatment of R6/2 mice with Congo-Red or Compound C2-8 showed a decrease of polyglutamine aggregation, improving motor functions.

More recent evidences highlighted how neurodegeneration is related to altered brain cholesterol metabolism. More details about the metabolic alteration and cholesterol administration will be discussed in the next chapters.

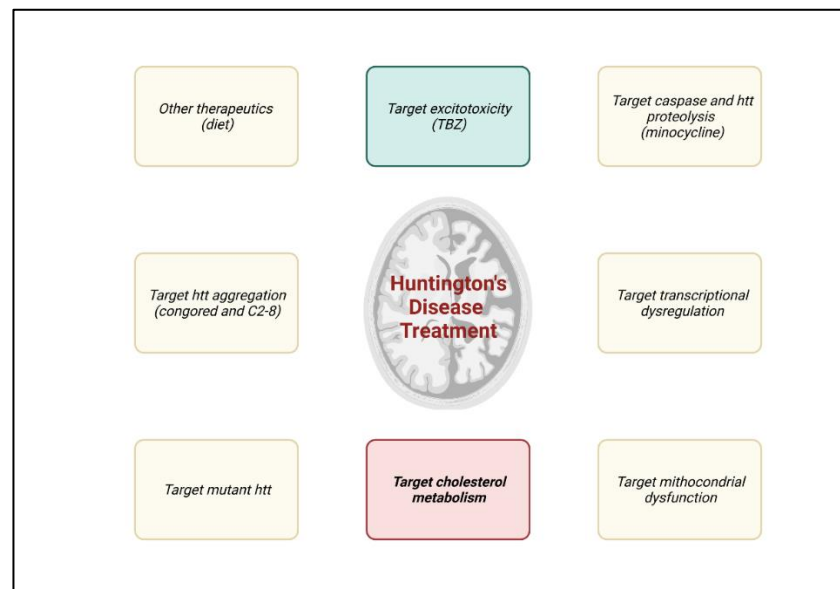


Figure 8. Resume of possible HD treatments.

1.2. Cholesterol

Cholesterol (Chol) is the most abundant member of the family of polycyclic compounds known as sterols in animal tissues. It is distributed in all tissues and mainly in the brain and spinal cord. It was first recognized in 1769 as a component of gallstones and was isolated from animal fat in 1815 by the French chemist Chevreul, father of lipid chemistry. Its structure was completely defined by German chemist Heinrich Wieland, in 1917 ⁴⁶.

It is a fundamental component of all mammalian cell membranes ⁴⁷ and its tetracyclic structure makes it the most rigid lipid among those of the double lipid layer. It is the precursor of other important steroids, fundamental for the functioning of the whole organism, such as hormones or bile acids ⁴⁷⁴⁸.

However, an excess of Chol can contribute to the onset of cardiovascular problems, so it is necessary to keep plasma levels under control and ensure that there is no excessive supply ⁴⁹⁵⁰.

Chol consists of a tetracyclic nucleus, a cyclopentaperhydrophenanthrene, with an iso-octyl side chain linked to carbon 17. In its structure there are 8 asymmetric carbon atoms and therefore 256 stereoisomers

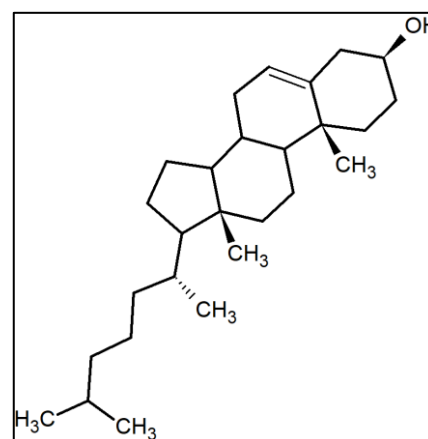


Figure 9. Structure of Chol (created with Chems sketch)

are possible, but in nature we can find only one stereoisomer (see figure 9).

Since an excess of free Chol is toxic to cells, it is exported by lipoproteins, preserved in an esterified form or released after being oxidized into oxysterols ⁴⁷. In animal tissues there are several forms of Chol esterified with different fatty acids. The enzyme responsible for esterification is sterol O-acyltransferase and by LCAT in lipoprotein particles in the circulation and CSF; the esterified Chol is then stored within the cell in the form of lipid droplets ⁴⁸.

1.2.1. Cholesterol metabolism

The daily human requirement of Chol is covered by both cell synthesis (60%) and nutrition, thanks to its absorption at the intestinal level and its transport linked to lipoproteins⁴⁷. Within the body, all cells are able to synthesize, release or take Chol from lipoproteins, in order to maintain the organism's homeostasis. The synthesis capacities of the different cells are variable, i.e.: astrocytes produce enough Chol to maintain their physiological activities while neurons need to acquire exogenous Chol to maintain homeostatic levels⁴⁷.

The first step of Chol biosynthesis is the conversion of three units of acetyl-coenzyme A to 3-hydroxy-3-methylglutaryl-coenzyme A (HMG-CoA), this involves two successive steps. In the first phase, the first two units are condensed thanks to the β -ketothiolase, then the HMG-CoA synthetase condense the third unit. The second phase consists on the reduction of HMG-CoA by Hmgcoa reductase (HMGCR), a microsomal NADPH dependent enzyme, with the formation of mevalonate. Unlike the first reactions, this is irreversible and it is considered the rate limiting step of Chol synthesis pathway. HMGCR is located in the smooth endoplasmic reticulum (ER) which becomes the main regulation site of the process. The following step involves the phosphorylation of mevalonate and a series of chain elongation reactions until the formation of farnesyl-pyrophosphate, formed by fifteen carbon atoms. Squalene synthetase (SQS) condenses two units of farnesyl pyrophosphate leading to the formation of squalene, the last linear precursor of Chol, formed by 30 carbon atoms. The cyclization of squalene leads to the formation of lanosterol (Lan), the first cyclic steroid produced in the biosynthesis of Chol. Starting from Lan, the biosynthesis can follow two different pathways: the Bloch pathway or the Kandutsch-Russel pathway. The first one leads to the synthesis of Chol through the precursor desmosterol (desm), while the second one passes through the formation of lathosterol (lat) and then 7-dehydrocholesterol (7-dehydroChol). Overall, the synthesis involves NADPH dependent enzymes and phosphorylation which therefore requires ATP. The total energy balance highlights the consumption of 4(NADPH + H⁺) and 3ATP for the production of a single Chol molecule. The subsequent metabolism of Chol proceeds with the formation of several metabolites.

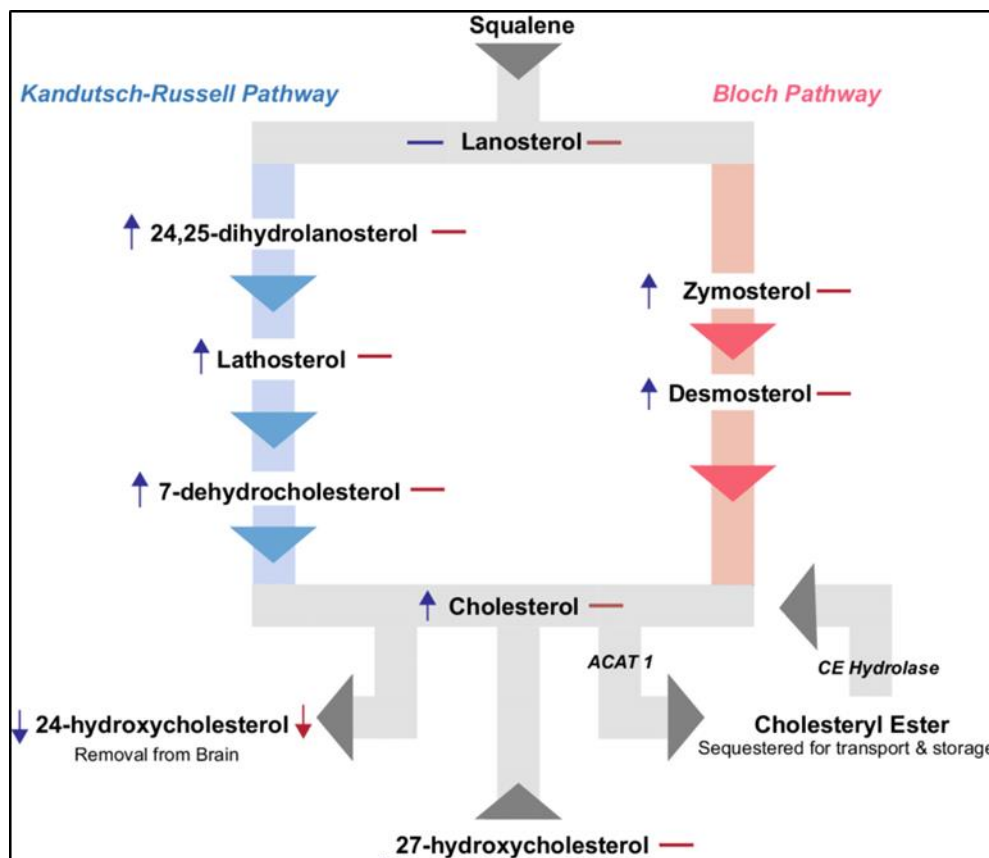


Figure 10. Simplified scheme of Chol synthesis

In hepatocytes the enzyme cholesterol 7 α -hydroxylase (CYP7A1) hydroxylates Chol in the 7 α position. This pathway is prevalent in healthy adult humans and leads to the formation of bile acids via neutral pathway⁵¹. If the levels of Chol present in the organism are high, the sterol 27-hydroxylase (CYP27A1) is activated to maintain the Chol homeostasis. CYP27A1 is expressed in all cells and the 27-hydroxycholesterol (27OHC) obtained is involved in bile acids synthesis. Unlike the peripheral metabolism, in the brain, the cholesterol 24-hydroxylase (CYP46A1) regulates the conversion of Chol to 24S-hydroxycholesterol (24SOHC), which, unlike Chol, is able to pass the blood-brain barrier (BBB). The final elimination of Chol occurs through the synthesis of bile acids, starting from the synthesized oxysterols. Chol may be esterified with different fatty acids producing molecules that are less polar than the free form. These forms are used for transport in plasma, for excess buffering and for storage as inert reserves.

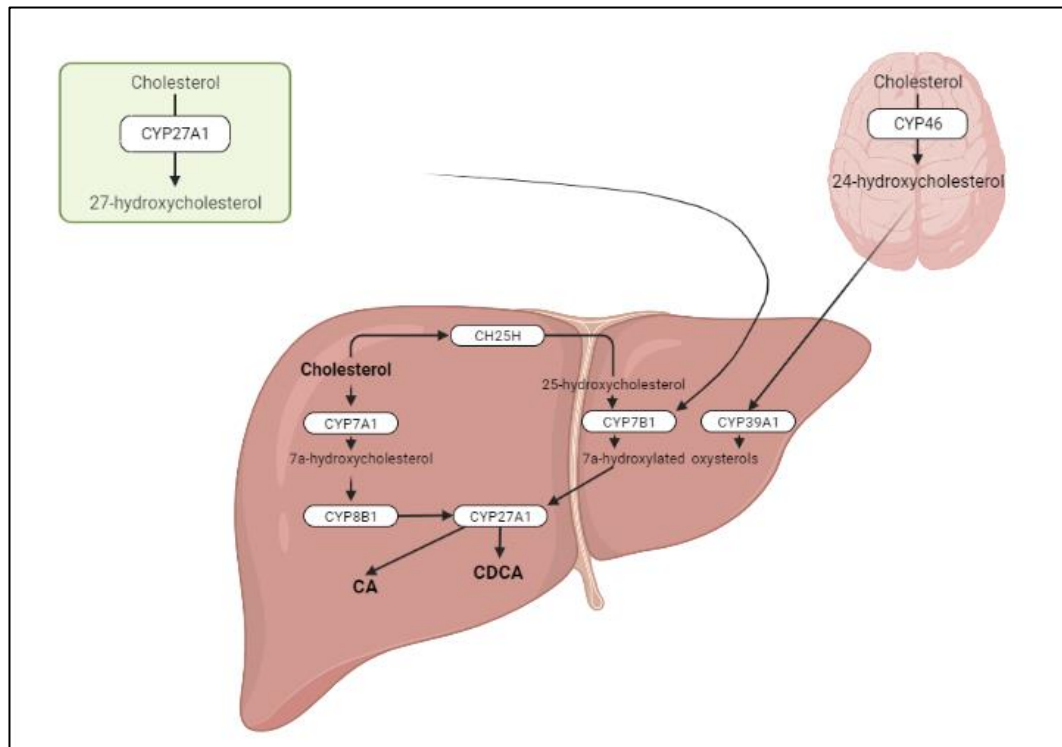


Figure 11. Representative scheme of Chol metabolism (created with BioRender).

1.2.2. Cerebral cholesterol metabolism

The importance of Chol in the CNS is well known since many years: in 1834 Couerbe wrote an essay entitled "*Du Cerveau, considéré sous le point du vue chimique et physiologique*" on the *Annales de Chimie et de Physique*, in which he defines Chol as the "*principal élément*" of the CNS. In recent years, we obtained more informations about its role in the maintenance of CNS physiology, confirming the idea of Couerbe.

Although the brain is only 2.1% of the total weight of the human body, it contains 25% of the total Chol present in the body ⁵², mainly in non-esterified form (>99.5%).

It represents a structural element of the cell membrane and it is distributed in myelin (70%), glial cells (20%) and neurons (10%) ⁵³. As a component of membranes it is involved in the maintenance of the three-dimensional conformation and it is organized in micro domains that allow the maintenance of the properties of proteins present in the double layer, such as receptors and ion channels. Its turnover in the brain is much slower (250-300 times) than in the peripheral metabolism ⁵², confirming its important structural role in the CNS. Its presence is fundamental also for the transmission of the impulses that are facilitated by the presence of myelin, repeatedly rolled around the axons. The myelin sheets are rich in Chol which reduces its permeability to ions, regulating the transmission of signal and avoiding the spread through the membrane ⁵⁴. The rate of Chol synthesis is very high during brain maturation and gradually decreases over time. It is also high in areas with a high fraction of myelin and white matter, such as the midbrain and spinal cord. The progressive increase of Chol ends in adulthood, when myelin formation is completed ⁴⁷.

The presence of BBB does not allow the passage of Chol bound to lipoproteins from the circulation to the brain, therefore more than 95% of the steroid present in CNS and in the peripheral nervous system is produced *in situ* by de novo synthesis. There are several reports in literature, since 1940, about the impermeability of BBB to Chol.

In 1943, Bloch et al. studied the conversion of Chol into cholic acid and decided to administer deuterated Chol to some dogs, and, by analyzing the different tissues, they noted the complete

absence of deuterated Chol in the brain and spinal cord. Similar studies have also been conducted in humans to verify the Chol behaviour in human organism. In 1962, Chobanian et al. administered an intravenous dose of 4- ^{14}C -Chol to terminally ill patients in a range of days before death between 1 and 226. The radioactivity of the different tissues due to the presence of ^{14}C was measured at the death of the patients: the brain samples showed low radioactivity, confirming the lack of Chol exchange from the circulatory system to the nervous system ⁵⁵. A 2001 study by Meaney et al. brought further evidence of the presence of two distinct pools of Chol in the body. The experimental design involved two different experiments. A male volunteer was exposed to air enriched with $^{18}\text{O}_2$ and blood samples were taken before and up to 60 minutes after treatment. A significant plasma enrichment of 7 α -hydroxycholesterol (7 α -HC) and 27OHC containing ^{18}O atoms was observed after 15 minutes, while the levels of these steroids decreased rapidly over the next 45 minutes. On the other hand, 24SOHC and Chol did not show any significant enrichment and this has led to the hypothesis that the first two have a very short half-life in circulation, while the second have a considerably long one. The second part of the experiment consisted of intravenous administration of liposomes containing deuterated Chol over a total of 55 hours. Blood sample were taken from the volunteers daily from 9 days before the infusion and then every two days from the eleventh until 31 days after the administration. The experiment did not demonstrate a significant enrichment of 24SOHC with deuterium at any stage. On the fourth day of treatment, the maximum plasma enrichment of deuterated Chol was obtained, resulting in a percentage of 13%; analysis of CSF, on the other hand, showed an incorporation of deuterium of less than 0.5%. These results reinforced the idea of the presence of two different metabolism, one of which is located in the brain and does not exchange with the peripheral one ⁵⁶.

The study conducted by Thelen et al. on the hippocampus of 20 individuals, post-mortem, without evidences of neurodegeneration during life showed no differences in levels of sex-dependent sterols, but different concentrations of sterols were found related to age. In younger subjects, significantly higher levels of Chol precursors, Lan and Lat (respectively, $P=0.036$ and 0.005) were found. Moreover, Lat levels showed a significant negative correlation with the age of subjects ($r=-0.505$, $P=0.023$) ⁵⁷.

In brain, there are several cells that can synthesize Chol; according to some *in vitro* studies on cell cultures, astrocytes synthesize 2 or 3 times more Chol than neurons and fibroblasts. The sterols derived from the Kandutsch-Russel pathway are mainly found in neurons, whereas the predominant synthetic pathway of astrocytes is the Bloch pathway ⁵⁸. A study by Nieweg et al. has observed the lower synthesis capacity of neurons compared to astrocytes, highlighting the low levels of the enzymes that catalyse the transformation of Lan (24-dehydrohydrohrolacholesterol reductase and lanosterol-14 α demethylase), suggesting that this type of cells cannot effectively convert Lan ⁵⁹.

In conclusion, neurons can produce enough Chol to survive, differentiate axons and dendrites, and form a few inefficient synapses. For massive synapse production, their smooth operation and maintenance require an additional intake of Chol provided by astrocytes, by means of lipoproteins, such as apolipoprotein E (ApoE), the main lipid transporter of CNS ⁶⁰. Moreover, oligodendrocytes, which appear to be the largest sterol-producing brain cells, supply sterols to neurons and astrocytes via ApoE ⁶¹. In this way, neurons can concentrate on generating electrical activity instead of spending energy on expensive synthesis, since more than 100 moles of ATP are required to synthesize a mole of Chol.

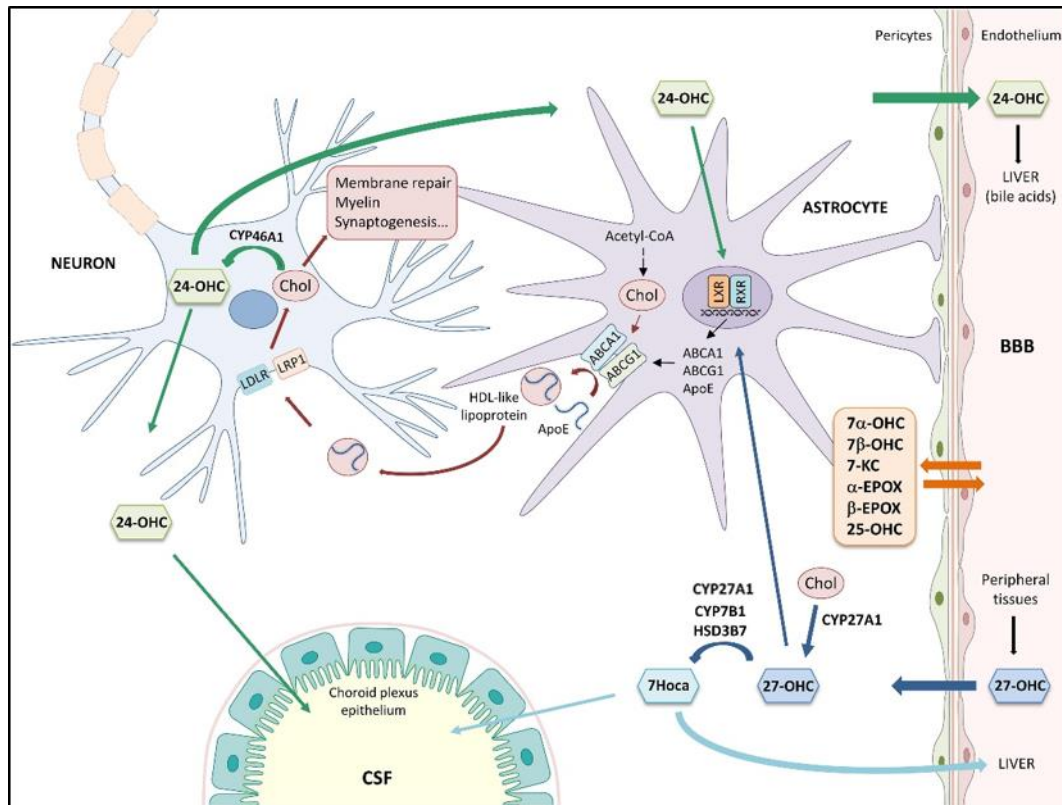


Figure 12. Scheme of brain Cholesterol synthesis and transport

The synthesized Cholesterol is inserted into apoE particles by the ATP binding cassette conveyor A1 (ABCA1). ApoE particles are recognized by LDL receptors⁶² and the apo-cholesterol-receptor complex LDL is finally formed. This is internalized in the neurons and then hydrolysed, releasing Cholesterol, which is then distributed to the plasma membrane and the ER, activating the negative feedback mechanism for the genes involved in the synthesis of Cholesterol⁶³. The excess steroid, instead, is esterified in the ER by the enzyme acyl-coA:cholesterol acyl transferase (ACAT) and is stored in cytoplasmic lipid drops as a reserve⁶⁴. A part of the Cholesterol is eliminated thanks to the conversion to 24SOHC, a more polar metabolite, by the CYP46A1 enzyme expressed only in neuronal cells. This metabolite is able to pass BBB, either by diffusion, or through the transport polypeptide of organic anions (OATP 2) in humans. Over the course of 24 hours there are about 6-8 mg of Cholesterol released into the circulation from the brain in the form of 24SOHC. A further outpouring of Cholesterol from CNS, albeit of a smaller magnitude, occurs through CSF in the form of ApoE-containing lipoproteins⁶⁵.

24SOHC is to induce and regulate the expression of enzymes associated with Chol homeostasis in the brain. In addition, 24SOHC derived from neurons appears to act as a neuronal Chol sensor in astrocytes. Although in very small quantities, 27OHC is also produced by neurons, astrocytes and oligodendrocytes by the enzyme CYP27A1. This metabolite is then removed from the brain via the BBB.

1.2.3. Cholesterol metabolism regulation

Chol and oxysterols are directly involved in a negative feedback mechanism of enzyme regulation, at protein and transcriptional levels ⁴⁷. Key element of the regulation of steroid synthesis is the protein SREBP (sterol-Regulatory element-binding protein). It is a transcriptional factor that regulates lipid homeostasis in cells by activating more than thirty genes involved in the synthesis and uptake of Chol ⁶⁶. SREBP-2 is anchored to the ER membrane and is capable of binding to the SCAP (SREBP Cleavage-activating protein) which has the function of detector of Chol, thanks to its sterol-sensitive domain ⁶². SREBPs are expressed as inactive precursors (pSREBPs) and, when the intracellular levels of Chol are low, pSREBP is translocated from the ER to Golgi thanks to SCAP. Here, they are transformed into active transcription factors (mSREBP) that are able to cross into the nucleus. In the nucleus, mSREBPs are able to modulate the transcription of genes that contain the sterol regulator element in the promoter region ⁶⁷.

If the intracellular levels of Chol are in excess, SCAP binds the INSIG-1 and 2 (insulin induced gene) proteins, then the SREBP-SCAP-INSIG complex stays in ER thereby reducing Chol synthesis.

A study by Suzuki et al. in mice knockout for the SCAP gene showed a reduction in enzymes in the synthetic pathway of Chol, accompanied by a 50% reduction in the total steroid content per gram of brain tissue ⁶⁸. According to Camargo et al. the suppression of SCAP in astrocytes significantly reduces cerebral lipid levels leading progressively to motor deficits, behavioural dysfunctions, and premature death ⁶⁹. Verheijen et al. conducted a study in mice with a suppression of the SCAP gene in Schwann cells showing congenital hypomyelination, walking disorders and tremors ⁷⁰.

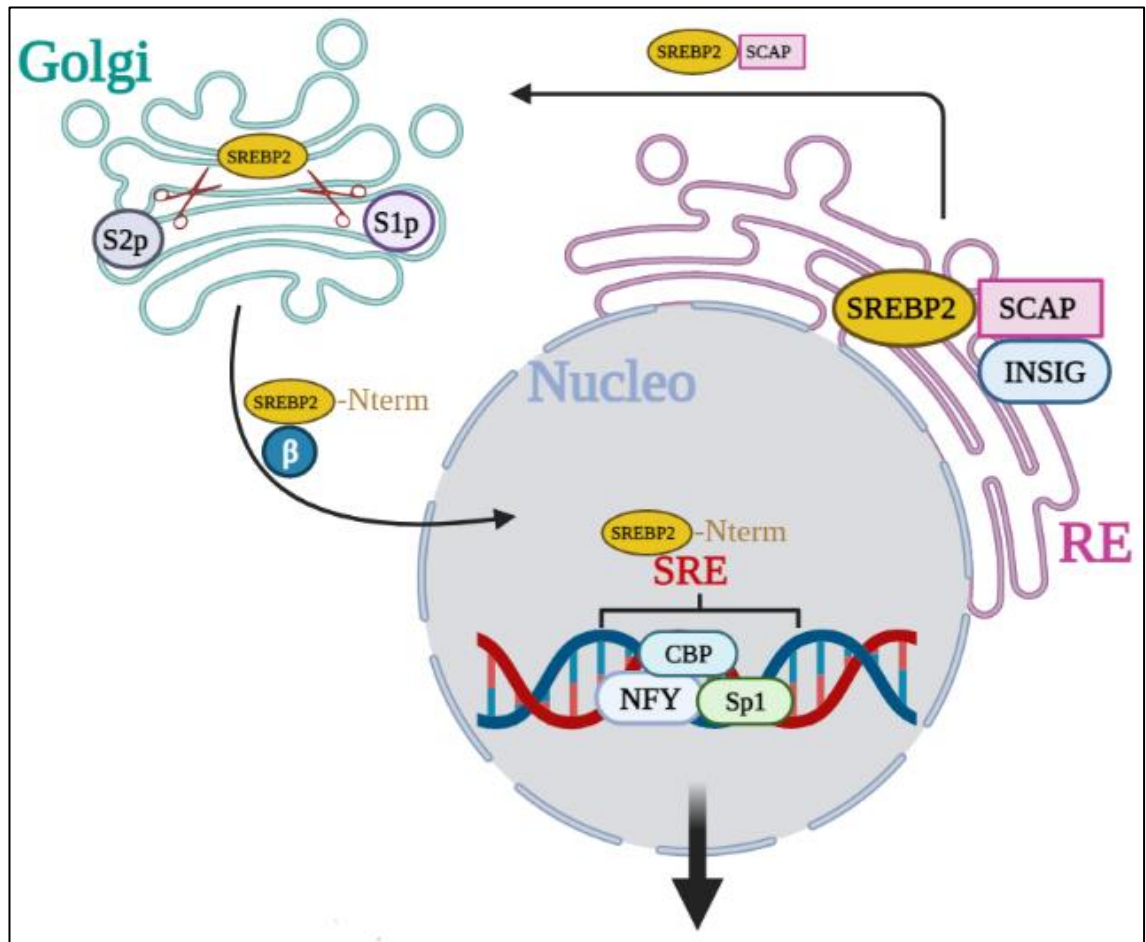


Figure 13. Scheme of Chol metabolism (created with Biorender)

1.2.4. Cholesterol metabolism in Huntington's Disease

Several studies in the literature highlighted that Chol metabolism is altered and reduced in HD, both in mouse models of the disease and in humans^{71 72 47}. Valenza et al. showed that a reduced expression of several genes involved in the Chol synthetic pathway, such as *Hmgcr*, CYP51 and 7-dehydrocholesterol 7-reductase (DHCR7), was found both in cell lines and in the striatum and cortex of transgenic mice⁷¹⁷³. A study by Samara et al. reported a reduction in the expression of 3 β -hydroxysterol delta-24-reductase (DHCR24), in cell lines, animal models and in post-mortem brain samples of HD patients⁷².

In different HD mouse models has been reported a significant reduction of brain Chol levels. Brain levels of Lan and Lat, considered markers for Chol synthesis⁶⁵, were reduced in the whole brain, cortex and striatum of different mouse models of the disease. Interestingly, in transgenic mice with artificial yeast chromosome (YAC), the reduction of Chol precursors was directly proportional to the length of CAG repeats⁴⁷.

The synthesis rate of Chol decreases with the maturation of the brain⁵² and therefore also the levels of precursors decrease over time until they reach a plateau⁴⁷: a study by Valenza et al. showed that the reduction observed was greater in the case of HD mice than in wild-type (WT) mice of the same age⁷¹. 24SOHC levels in the whole brain, striatum and cortex of diseased mice were also reduced, suggesting an impairment of Chol elimination by metabolically active neuronal cells⁷⁴.

A molecular explanation for the impairment in Chol synthesis is the decreased levels of active SREBP, due to mHTT⁴⁷. This transcriptional factor regulates the expression of HMGCR, an enzyme used in the rate-limiting step of the synthetic pathway. A reduced SREBP translocation was found by Valenza et al. in cellular models of the disease and in the striatum of HD mice.

An adequate supply of Chol is necessary for neuronal development, for the formation of synapses and dendrites and for the orientation of axons⁷⁵⁷⁶: the loss of dendrites and axons is one of the first evidences in several neurodegenerative diseases, such as HD, in which defects in synaptic activity have been observed together with cerebral morphological alterations⁷⁷⁻⁷⁹. Reduced intake of Chol leads to synaptic degeneration, lack of neurotransmission and decreased synaptic

plasticity⁶⁴. The fluidity of cell membranes and the distribution of lipid microdomains affect the transfer of Chol between cells and the function and structure of the membranes themselves. Another ability of native HTT is to bind to some nuclear receptors involved in lipid metabolism such as LXR, the γ receptor activated by peroxisome proliferators (PPAR γ) and the vitamin D receptor, modulating its transcriptional activity, but the same cannot be said for mHTT. An over-expression of HTT activates LXR, while a lack of HTT leads to an inhibition of LXR-mediated transcription⁸⁰. Another mechanism that would explain the link between HTT mutation and Chol metabolism disturbances would therefore be mHTT's poor ability to regulate LXR and its target genes.

mHTT also affects the release and transport of cerebral neurotrophic factor (BDNF), which is released by neurons and is involved in synaptic plasticity and neuronal survival, and induces Chol synthesis in post-synaptic neurons. The influence of mHTT on BDNF therefore presumably leads to an inhibition of neuronal synthesis of the steroid, enhanced by insufficient removal of it caused by reduced expression of ApoE in astrocytes⁸¹. Reduced levels of mRNA of Chol efflux genes in astrocytes from mouse models of the disease were found in a study by Valenza et al. et al. In the same study, it also emerged that lipoproteins with ApoE present in the brains of transgenic mice are smaller and less lipidated⁴⁷. Overall, in HD there is a reduced transport, and therefore a lower supply, of Chol from astrocytes to neurons via ApoE and at the same time an inefficient removal of Chol from neurons to astrocytes.

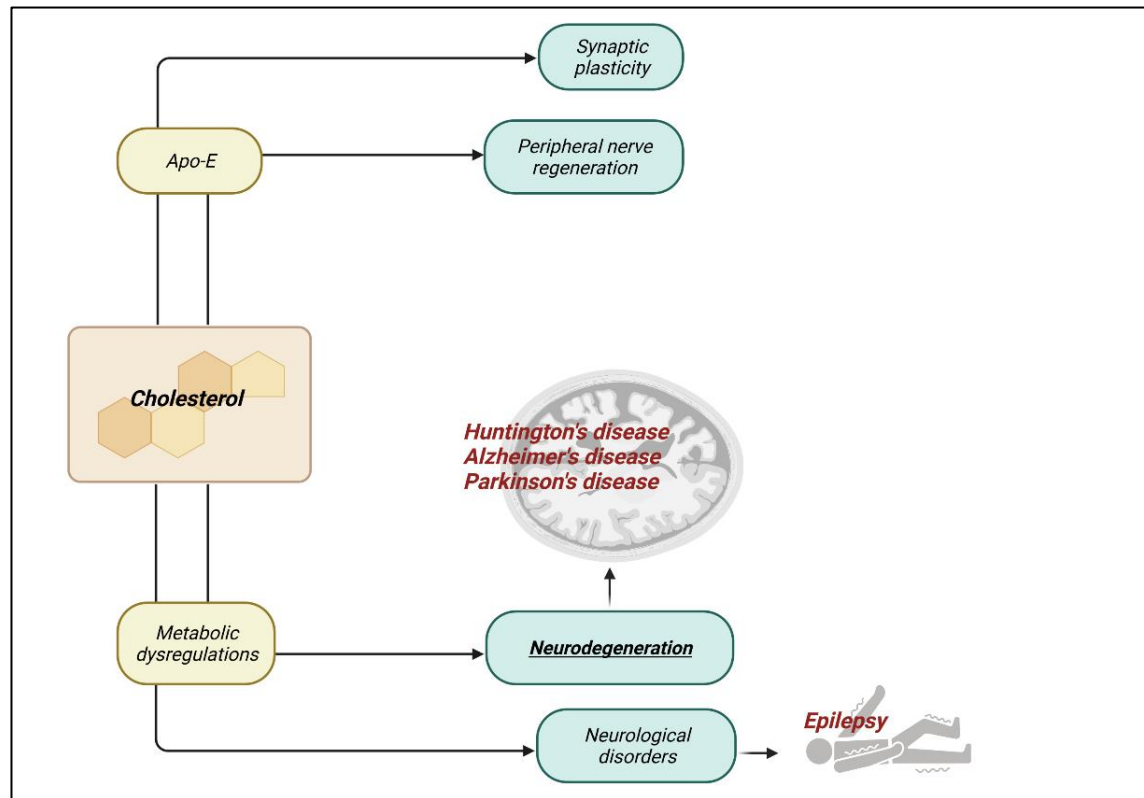


Figure 14. Scheme of Chol role in disease development

1.2.5. Cholesterol administration

Typically human neurodegenerative diseases are devastating illnesses that predominantly affect elderly people, progress slowly, and lead to disability and premature death. However, they may occur at all ages. Despite extensive research and investments, current therapeutic interventions against these disorders are palliative, as they can only alleviate the symptoms. Since in many neurodegenerative diseases the underlying mechanisms of damages to neurons are similar, in spite of heterogeneous etiology and backgrounds, it will be of interest to identify possible trigger points of neurodegeneration that can enable the development of drugs and/or prevention strategies that target many disorders simultaneously. Among the factors that have been identified so far to cause neurodegeneration, failures in Chol homeostasis are indubitably the best investigated, as discussed before. However, delivering Chol to the brain is challenging due to the BBB, which prevents it from reaching, especially, the striatum with therapeutically relevant doses. In literature, there are different works highlighting how the supplement of exogenous Chol could restore the phenotype of the disease. Valenza et al., in 2015, reported that systemic administration of brain-permeable polymeric nanoparticles loaded with Chol (g7-NPs-Chol) reversed synaptic alterations and prevented cognitive defects in a HD transgenic mouse model ⁸². In 2020, the same research group, showed how the direct infusion in the brain of HD mice by the use of osmotic mini-pumps is able to reverse both cognitive and motor abnormalities. They found that cognitive decline was prevented by all the three tested doses, while motor dysfunction was reversed only with the highest dose ⁸³. More recently, they proposed the administration of exogenous Chol throughout an intraperitoneal treatment with poly(lactide-co-glycolide) (PLGA) and Chol nanoparticles which were modified with a heptapeptide (g7) for BBB transit (hybrid-g7-NPs-Chol). They highlighted how, also with Chol loaded NPs, Chol reach the brain and target neural cells, preventing cognitive decline and ameliorating motor defects ⁸². Given these basis, this PhD project discusses the efficacy of an alternative way of administration of Chol, the intranasal delivery, with the aim of reaching target brains of WT and HD model transgenic mice. Mass spectrometry is used as a tool to quantify exogenous administered Chol and to evaluate brain and plasma metabolic state in the mouse model of the disease.

1.3. The intranasal administration as a strategy for delivering drugs to the CNS

The presence of the BBB is one of the main problems encountered when administering drugs to level of the CNS, because it prevents the entry of pathogens or other substances that could be toxic, and simultaneously it is an obstacle for diffusion of drugs from the bloodstream to the nervous tissue.

The BBB is characterized by endothelial cells that exert a reduced process of pinocytosis, a high expression of ABC transporters, such as P-glycoprotein, and numerous tight junctions ⁸⁴. A molecule can cross the BBB only if it has specific characteristics, such as small size and a certain degree of lipophilicity, or if a transporter is present specific at the BEE level, which allows it to pass ⁸⁵. Given these basis, one of the main problems that must be addressed in the treatment of neurological pathologies is precisely the difficulty of reaching the CNS with concentrations enough of the drug. Intranasal administration turned out to be one winning strategy to get around this obstacle. Traditionally, the intranasal route has always been exploited for the administration of medicines with local action, in particular for the treatment of those disorders such as allergies, sinusitis, infections and nasal congestion. In recent decades the attention of many researchers has instead moved to this path as a valid alternative, safe and non-invasive, for administer drugs of different nature, in order to have a faster and higher absorption ⁸⁶. The reasons that have attracted the interest for this route of administration are multiple, including the high vascularity of the nasal mucosa epithelium, the large area of the absorption surface, the rapid onset of action, and direct drug transport to the systemic circulation and al brain. Also not negligible is the avoidance of hepatic metabolism (first effect passage), which thus increases the bioavailability of the drug itself ⁸⁶. In fact intranasal administration may be a valid one alternative for the administration of peptides, proteins or polar drugs, which if administered orally they present gastric instability, insufficient absorption intestinal or

an early elimination caused by the first pass effect in the liver. Neither examples are insulin and growth hormone, whose intranasal formulation is already present in the clinic.

1.4. Mass spectrometry as analytical technique in biological investigations

Mass spectrometry (MS) draws its origins in the first part of the 20th century, from experiences of J. J. Thomson and F. W. Aston, who highlighted the formation of positively charged rays between electrodes placed in a vacuum tube, to which a difference in electrical potential was applied. Thomson observed that this technique could find application to chemistry but, despite its far-sighted observation, the application remained confined to physics for about thirty years ⁸⁷.

Mass spectrometry was used in particular to identify isotopes, to determine their relative abundance and to measure their exact mass. These important findings allowed the creation of the basics for the subsequent developments of mass spectrometry in different fields, ranging from geochronology to biochemical research ⁸⁸. To date, mass spectrometry represents one of the more efficient analytical techniques for the qualitative and quantitative analysis of compounds in different matrices, allowing the elucidation of chemical structures and the study of the properties of molecules.

This technique is based on the separation of ions according to their mass to charge ratio (m/z) through the application of static or dynamic electromagnetic fields. The success of this technique is due to two main advantages: the possibility to determine molecular weights and elemental compositions using very small amount of substances (in the order of 10^{-12} to 10^{-9} g) and the possibility to fragment molecules into smaller ions, obtaining additional information for the identification of their chemical structures. Mass spectrometry is very frequently used for the analysis of complex mixture of compounds, like biological or environmental samples. The analysis of complex mixtures particularly requires the combination of mass spectrometry with an efficient separation technique, such as liquid chromatography (LC) or gas chromatography (GC). The separation technique adds an additional dimension to the analytical measurement. The hyphen used to indicate the coupling of a separation technique to mass spectrometry led to the term hyphenated techniques.

1.4.1. Theoretical principles

The first step of a mass spectrometric analysis is the production of gas phase ions. The molecular ion and its possible fragments are then separated according to the different m/z ratios and measured in proportion to their abundances. The result is a mass spectrum (figure 15).

The x-axis of the spectrum represents the values of m/z ratios. When m is given as a relative mass and z as the number of charges, both are without units of measure, hence the m/z value is dimensionless. The unified atomic mass (u), also called Dalton (Da), is used as the unit of measurement; it is defined as the twelfth part of the mass of the carbon-12 isotope (^{12}C) and is equal to 1.660540×10^{-27} kg. The charge is indicated as multiples of the elementary charge of the electron ($e = 1.602177 \times 10^{-29}$ C).

Molecular and fragment ions provide informations about the nature and the structure of compounds. In mass spectrometry, which is a technique capable to distinguish different isotopes, the masses of ions are measured as monoisotopic values, contrary to stoichiometric calculations, where the masses are calculated using the average atomic weights (which are the weighted averages of the atomic masses of the naturally present isotopes for each element in the molecule).

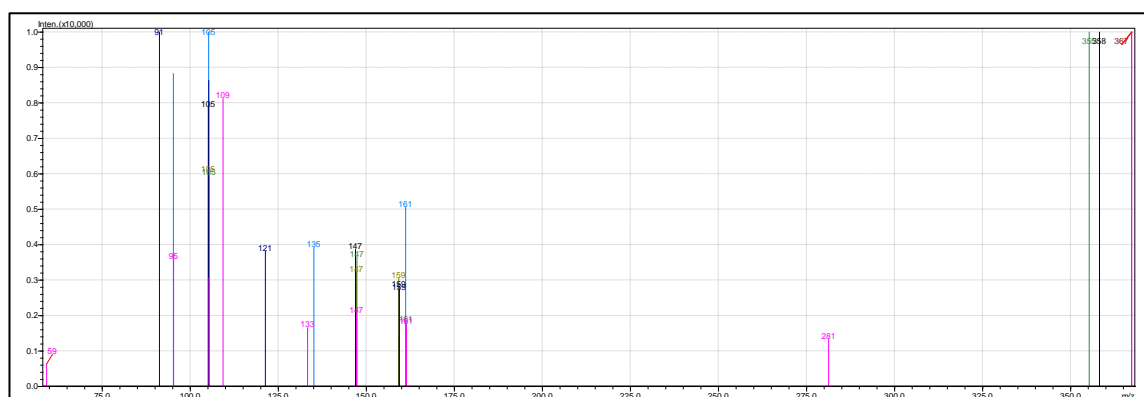


Figure 15. Example of MS/MS spectra from chol metabolites analyses
(Shimadzu LCMS8060, Product ion scan, positive mode)

1.4.2. Liquid chromatography coupled to mass spectrometry (LC-MS)

As mentioned, the use of hyphenated techniques is necessary to allow the analysis of complex mixtures, such as environmental or biological samples. The separation technique allows the introduction of compounds one after the other into the mass spectrometer, either in the gaseous state, for GC-MS, or in the liquid phase, for LC-MS. Modern instruments are manufactured with direct (on-line) interfacing of chromatographs to mass spectrometers and are called hyphenated instruments. Several reviews on the coupling of separation techniques with mass spectrometry have been published with a wide range of application fields, involving environmental applications⁸⁹, new drug discovery⁹⁰ or metabolomics and metabonomics applications⁹¹.

In the environmental, pharmaceutical and biological fields, the most frequently used technique is by far LC-MS, because of its sensitivity and versatility. In pharmacokinetic and metabolic studies, LC-MS is used in the analysis of different samples such as plasma, brain and other peripheral tissues for studying the kinetic and the biological distribution of drugs or candidate drugs. In the metabolomic field, LC-MS allows the identification and the quantitation of metabolites in biological matrices, i.e.: plasma, brain or peripheral tissues. This innovative approach could give important information about metabolism related to administered substances or information about a particular state of a biological system, i.e: the evaluation of the phenotype of a disease in a mouse model. In this thesis, LC-MS methods were developed and validated for different purposes. A first method was developed and validated for the quantitation of administered cholesterol and a second method was developed and validated to study the metabolism of cholesterol in both plasma and brain samples in R6/2 mice, a mouse model of HD.

1.4.2.1. Tandem mass spectrometry

Tandem mass spectrometry (MS/MS) is a method that involves two steps, consisting in the isolation of a precursor ion followed by its fragmentation in a collision cell. Instruments used in a MS/MS analysis have usually two analysers: the first analyser selects one or more precursor ions, the second analyser isolates the fragments formed in the collision cell, which are then measured by the instrument detector.

One of the most frequently used MS/MS instruments is the triple quadrupole, consisting of three sequential quadrupoles in which the middle one acts as a collision cell. In this case the technique can be described as tandem mass spectrometry in space. Other instruments (e.g. ion traps) can perform all the processes using a single analyser, with a process called tandem mass spectrometry in time.

Tandem mass spectrometry is used for the identification of metabolites or unknown substances, for the quantitation of specific analytes in complex samples with high specificity and sensitivity and for structural or fragmentation mechanism studies.

There are four main types of MS/MS experiments:

- Product Ion Scan: consists in the selection of a precursor ion (or parent ion) and the determination of all its fragmentation ions (daughter ions).
- Precursor Ion Scan: consists in the selection of a product ion (or daughter ion) in the second analyser and in the determination, in the first analyser, of all the precursor ions (or parent ions) that give origin to that particular product ion. This scan mode cannot be performed with time-based mass spectrometers.
- Neutral Loss Scan: consists in the selection of a neutral fragment and the detection of all the fragmentations leading to the loss of that neutral. This scan mode is not possible with time-based mass spectrometers.
- Selected Reaction Monitoring (SRM): consists in the continuous measurement of a fragmentation reaction. It is a two-step acquisition method in which a precursor ion is selected in the first stage of a tandem mass spectrometer and one of its product ions is

selected in the second stage. In modern instruments several precursor/product ion pairs can be monitored sequentially in time.

Figure 16 shows a graphical representation of the four different acquisition modes.

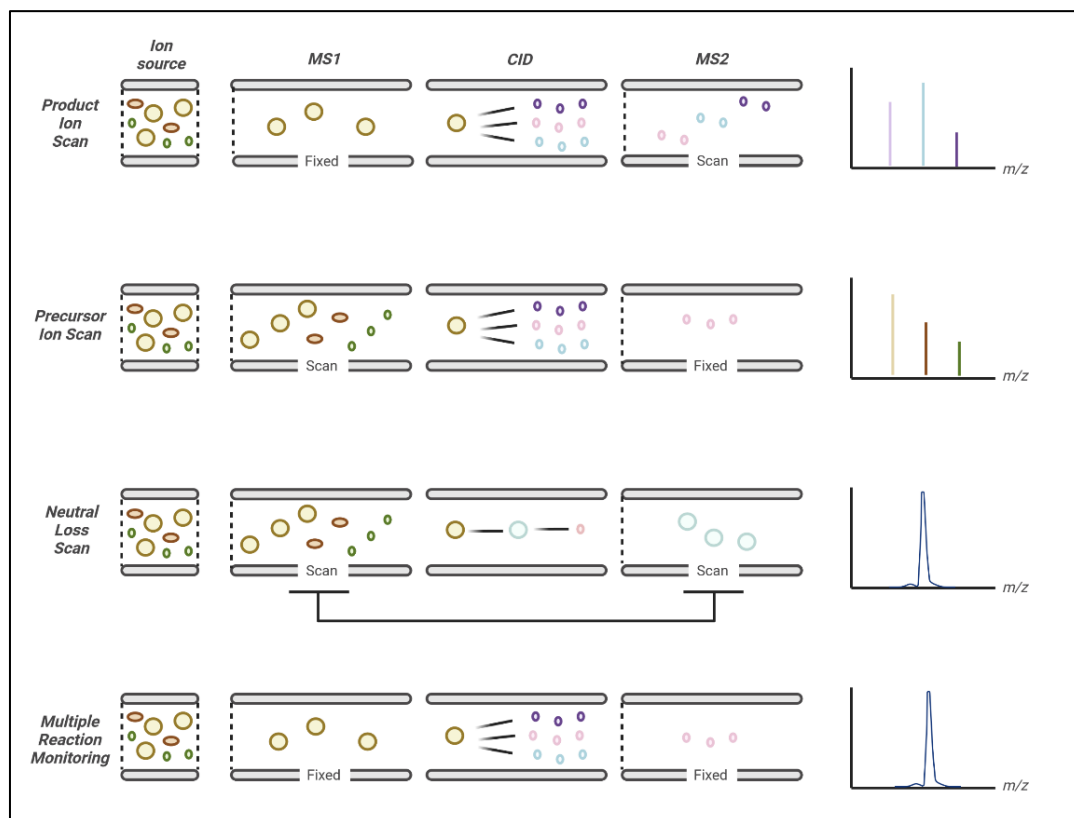


Figure 16. Scheme for the easy representation of various scan modes of triple quadrupole (modified from ⁹²)

1.4.3. Imaging Mass Spectrometry

Mass Spectrometry Imaging (IMS) is a remarkable new technology that allows the study of the distribution of biological molecules present in tissue slices. Initially developed for the localization of peptides and proteins ⁹³, this technique has recently been applied to the study of molecules with lower molecular weights, such as metabolites and drugs. The application of IMS to the study of endogenous metabolites has received considerable attention because endogenous compounds are the result of the interactions of a system's genome with the environment and they are representative of a particular state of a biological system. The spatial study of metabolites in tissue slices could give a more comprehensive view of a phenotype of a disease or of a metabolic state. IMS uses the achievements of traditional mass spectrometry methods to provide informations about the localization of a compound with a higher specificity than conventional methods, such as magnetic resonance imaging (MRI), positron emission tomography (PET) and fluorescence microscopy. The main advantage of IMS is that it can be performed without homogenating, and thus destroying, the structure of a slice of tissue. The IMS results could be integrated with the results obtained from histology, giving more detailed informations on the fine distribution of the analytes of interest in biological tissues. Moreover, the data obtained by IMS experiments could integrate the quantitative data of LC-MS analysis, with spatial information about the analytes of interest. Although IMS was initially developed as a tool for intact protein imaging from the tissue surface using MALDI-MS ⁹³, in current research the target analytes includes drugs ⁹⁴ and low molecular weight metabolites ⁹⁵.

IMS, as all mass spectrometric techniques, can use different ionization techniques, such as Matrix Assisted Laser Desorption Ionisation (MALDI), Desorption Electrospray Ionization (DESI) or Atmospheric Pressure MALDI (AP-MALDI). In general, IMS studies involve the use of thin slices (10 μ m) of tissues that are placed on MALDI targets or other appropriate supports for ionization.

In this thesis project, all imaging experiments are conducted using an AP-MALDI source interfaced with a high-resolution mass spectrometer (Orbitrap Q-Exactive, Thermo Scientific).

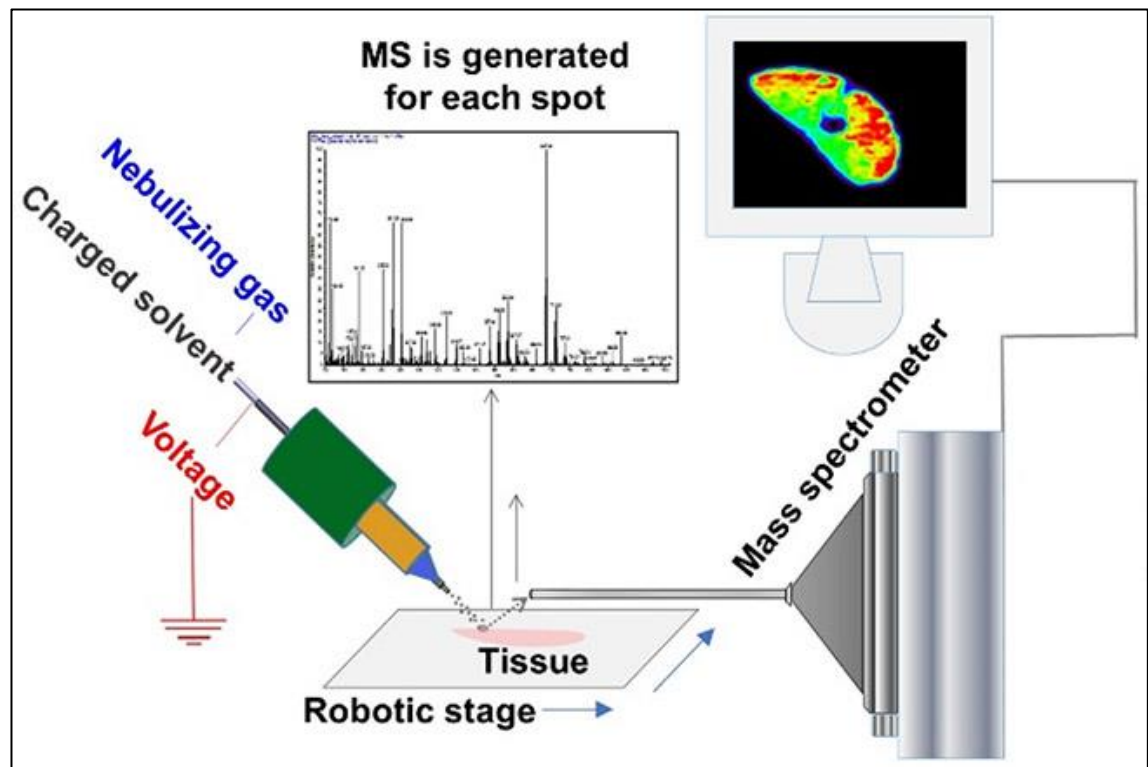


Figure 17. Block Scheme of an imaging mass spectrometry experiment.

1.4.3.1 MALDI-IMS

MALDI is the most used soft ionization method for IMS, coupled with different high resolution mass analysers, such as Time of Flight (TOF) or Orbitrap. There are several factors that improve the quality of the MALDI spectra including choice of matrix and selection of solvent. In any case, the mass of the metabolite of interest is key in determining the preferred method of analysis. For these experiments, slices are placed on MALDI targets and covered with an appropriated MALDI matrix, which has the purpose of “assisting” the ionization process. The MALDI target is hit by a focused laser beam, which moves following predefined coordinates to cover the entire area of the tissue slice. The ions are produced by thermal desorption and are then accelerated and separated according to their m/z ratio by the mass analyser. During the acquisition, thousands of spectra are generated, one for each point of the tissue slice that has been hit by the laser. All the mass spectra obtained are processed by specific software for image elaboration. The result shows the intensity of each analyte of interest with a colour scale, producing an image of the spatial distribution of the compound. Figure 18 shows a scheme of IMS workflow.

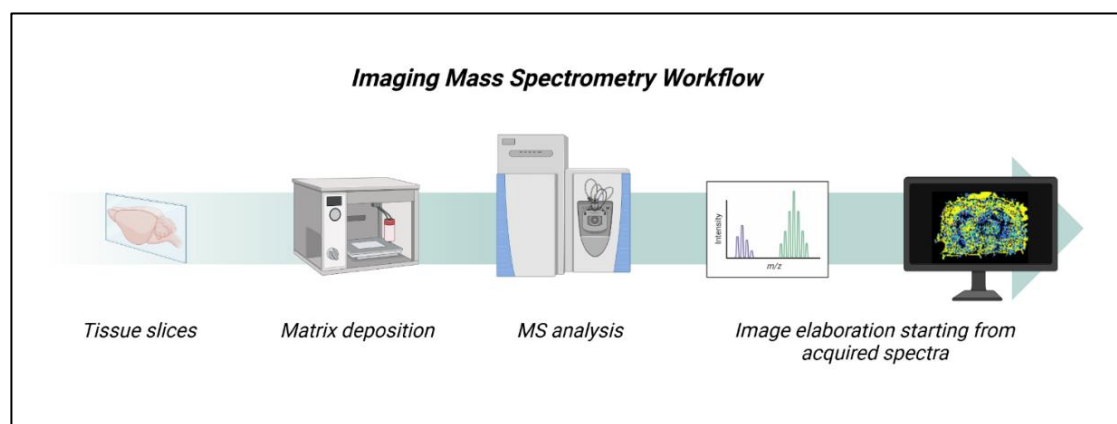


Figure 18 IMS experiment workflow (created with BioRender).

The possibility of analysing several molecules in parallel, based on the different m/z , is a considerable advantage that allows the study of a high number of metabolites on the same tissue slice.

The most critical step in a MALDI IMS experiment is the sample preparation. The collected tissues must be immediately frozen in liquid nitrogen and stored at -80°C until sectioning. This constitutes a limit of the applicability of the technique, because it is currently not possible to

analyse tissues fixed in formalin or paraffin. The frozen tissues are then cut into thin slices (from 3 μ m to 50 μ m), transferred on a stainless steel plate or on a conductive slide and covered with the most appropriate matrix. The choice and technique of matrix deposition are the most critical aspects that determine the success or failure of the experiments. The most widely used matrices are 3,5-dimethoxy-4-hydrocinnamic acid (SA or synapinic acid), 2,5-dihydroxybenzoic acid (DHB) and α -cyano-4-hydroxycinnamic acid (HCCA). These compounds have the property of absorbing the UV radiations produced by the laser (typically 337 nm for a nitrogen laser) and therefore to assist the ionization on the tissue slices by thermal desorption. The choice of the suitable matrix for the imaging of drugs and metabolites is often empirical and requires several attempts to find the most suitable one to obtain the best signal without introducing interferences or a high ion suppression. This field is in continuous development and is leading to the development of new matrices free of interfering ions, such as 1,8-bis(dimethylamino)naphthalene (DMAN) or titanium dioxide nanoparticles (TiO₂). These matrices have the advantage of allowing a high spatial resolution and produce a low background noise, especially in the low molecular weight range, to which many drugs and metabolites belong ⁹⁶. In 2019, Shariatogorji et al. synthesized an innovative MALDI matrix able to derivatize neurotransmitters directly on tissue slices and promote the ionisation at the same time ⁹⁷. In literature there are other studies that describe derivatization procedures directly on tissue slices to improve the ionisation of several analytes. One study of particular interest is that of Angelini et al., that showed how the use of Girard's Reagent P as a derivatizing agent can improve the signal and the imaging of cholesterol on brain slices ⁹⁸. The improvement of the approaches of Angelini and Shariatogorji is that the proposed synthesized molecule has a double function of derivatizing agent and MALDI matrix, reducing the passages of sample preparation (e.g. the number of matrix layers sprayed on tissues), enhancing signal and reducing ion suppression.

1.4.3.2. Quantitative IMS

The quantitation of analytes of interest is important to integrate the spatial information obtained from IMS study. Quantitative IMS (Q-IMS) is one of the hottest topics of the current discussions among the experts of the MS imaging community. If IMS is established as a powerful qualitative tool in drug and biomarker discovery, its reliability for absolute and accurate quantification is still controversial. Indeed, Q-IMS has to deal with several fundamental aspects that are difficult to control, and that must be taken into account for absolute quantification⁹⁹. Several indirect quantitative IMS approaches have been proposed to correlate LC–MS quantifications from serial tissue sections with IMS spatial information^{94 100 101 102}. Early attempts at quantitative IMS used an in-solution approach where the standard solutions are spotted directly onto the sample target. While it is straightforward in practice, this method typically fails to directly account for tissue matrix effects. Several studies have investigated the use of a homogeneously applied stable isotope-labeled internal standard to determine a tissue specific suppression factor, or tissue extinction coefficient, to be used as a normalization factor. The efficiency of extracting the analyte from a biological tissue varies depending on the biological and structural characteristics of the tissue and the experimental conditions, such as matrix characteristics or deposition method. The normalization of the signal using an IS is the most common used technique of quantitation: it consists in the addition of a suitable molecule that is analyzed at the same time as the analyte. The IS can be an endogenous compound, a matrix product or an exogenous compound which must have the same or a similar behaviour of the analyte of interest during the analysis. In the end, knowing exactly the amount of IS, it is possible to normalize the signal of the analyte and to obtain the quantity present in the sample. The internal standard can be sprayed together with the matrix or can be deposited in drops over the sample. To date, there is no standardised protocol for the quantification of analytes, but great efforts are being made to achieve this, especially within the pharmaceutical industry. Quantification through IMS requires the development of a standardized and controlled sample preparation procedure as well as a highly reproducible matrix deposition protocol.

1.4.5. Analysis of cholesterol metabolites by mass spectrometry

The best analytical method for measuring the levels of different analytes in biological samples in a single analysis is the use of hyphenated techniques, such as liquid-chromatography or gas chromatography coupled with mass spectrometry. In particular, Chol metabolites are non-volatile molecules and a derivatization step is necessary for the analysis with gas chromatography. This results in a more complicated procedure, requiring a further step in the sample preparation, with an increase of possible errors resulting from sample handling. Up to date there are several GC-MS methods reported in the literature, but in recent years the number of LC-MS methods has significantly increased. Figure 19 shows the number of publications reporting GC-MS and LC-MS methods for the study of Chol metabolites.

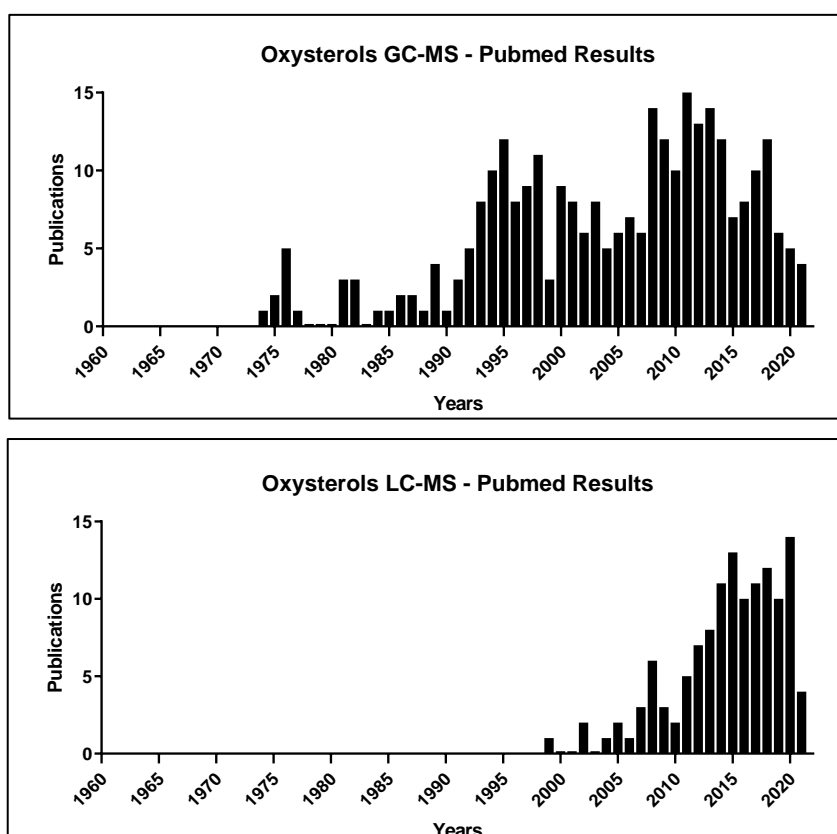


Figure 19 Number of published articles/year relating GC-MS to oxysterols (Panel A) or LC-MS to oxysterols (Panel B)

The classical method used for the measurement of oxysterols is GC-MS. However, this method requires a derivatization that is not applicable to conjugated oxysterols that are present in both esterified and free form in biological matrices. The reference method for this type of analysis is the one created in 1995 by Björkhem and Diczfalusy described in the publication of Dzeletovic et al. The method described included an alkaline hydrolysis with KOH 0.35 M at room temperature for two hours, followed by a liquid liquid extraction with chloroform. The extracted was evaporated and re-suspended in toluene. The method included a solid phase extraction (SPE) step to separate oxysterols from cholesterol. The eluate was derivatized to trimethyl-silyl-ethers with a mixture of pyridine, hexamethyldisilazane and trimethylchlorosilane. The final solution was evaporated and suspended in hexane for the analysis (99). The suspended samples were analysed by GC-MS, generally in selected ion monitoring (SIM) mode on a single quadrupole instrument ¹⁰³.

Leoni and Caccia used a GC-MS method to simultaneously determine Chol, Lat, Lan and 24SOHC. Samples were hydrolysed and extracted with organic solvent. The extracts were evaporated and the steroids were converted to trimethyl-silyl ethers by derivatization with N,O-bis-trimethylsilyl-trifluoroacetamide and trimethylchlorosilane ⁸² The GC oven temperature gradient for chromatographic separation was from 180° C maintained for 1 minute, followed by a linear ramp of 20° C min⁻¹ to a maximum of 270° C and by a ramp of 5° C min⁻¹ up to a maximum of 290° C, maintained then for 10 minutes. ⁸³.

The various methods based on LC-MS reported in the literature differ in sample preparation, i.e.: some methods use derivatization while other methods bypass this step. Nagy et al. proposed an LC-MS method to simultaneously determine phytosterols, Desm and Lat in plasma samples. However, there was no hydrolysis phase in the preparation, allowing the measurement only of the free fraction of sterols. Samples were deproteinized with methanol, the supernatants were diluted and purified by SPE. The eluates were dried and re-suspended in methanol. The chromatographic separation was performed with a reverse phase column at room temperature using a gradient of methanol/water (85:15, v/v), and methanol/acetone/hexane (2:2:1, v/v). APCI was used as ionisation source, while the mass spectrometer was a triple quadrupole used in SRM ¹⁰⁴. A high-throughput LC-MS method for the measurement of oxysterols was proposed by McDonald,

Russell and collaborators ¹⁰⁵. Their study required a single extraction of plasma for the measurement of about 60 sterols but the extracted samples were analysed with three different instruments. The method proposed the use of 200 µl of plasma, firstly hydrolysed with 300 µl of KOH 10 N, at 35 °C for 1.5 hours. The reaction solution was extracted with dichloromethane (DCM), the solvent was evaporated and re-suspended in hexane. After a further SPE purification step, the eluates were re-suspended in 400 µl of 90% methanol. Oxysterol analysis was performed by LC-MS using electrospray ionization and a chromatographic separation with a reversed phase column. The elution gradient used 70% acetonitrile with the addition of 5 mM ammonium acetate and a 1:1 solution of isopropyl alcohol and acetonitrile, with 5 mM ammonium acetate. The other sterols were measured using LC-MS using APCI ionization. In this case, the chromatographic separation was performed on a reversed phase column using a two-step isocratic elution: the first one using 96% methanol, added with 0.1% acetic acid and the second one using methanol containing 0.1% acetic acid. The measurement of Lat alone, however, was carried out by GC-MS ¹⁰⁶. Another method, proposed by McDonald et al. allowed, with a single extraction, the measurement of about 60 sterols by using three different analytical methods, due to the difficulty to obtain a chromatographic separation of all these compounds that have many isomers and/or different polarities.

Among the several LC-MS methods for the analysis of oxysterols that are available in literature, the ones that include a derivatization step are listed in Table 2.

Table 2. Derivatization methods used for Chol metabolites analyses in literature

Literature Reference	Derivatization	Final target analyte
(Honda et al., 2009) ¹⁰⁷	Picolinic Acid	Picoline ester
(Sidhu et al., 2015) ¹⁰⁸	Nicotinic Acid	Nicotine ester
(Jiang et al., 2011) ¹⁰⁹	Dimethylglycine	N, N-dimethylglycine ester
(Karu et al., 2011)		
(Lavrynenko et al., 2013) ¹¹⁰		
(DeBarber et al., 2011) ¹¹¹	Girard's reagent	Hydrazone
(Soroosh et al., 2014) ¹¹²		
(Crick et al., 2015) ¹¹³		

During the last decades, there is an increasing interest in the study of Chol metabolites from a spatial point of view. The methods described above give us quantitative information but, considering the importance of Chol as a critical component of cell membranes and its involvement in human neurodegenerative diseases, there is an unmet need of new methods that allow the imaging study of these molecules in brain sections.

In fact, the ability to map cholesterol distribution and abundance has been the forefront of a growing number of biophysical studies. The following figure shows the number of publications that include IMS of Chol.

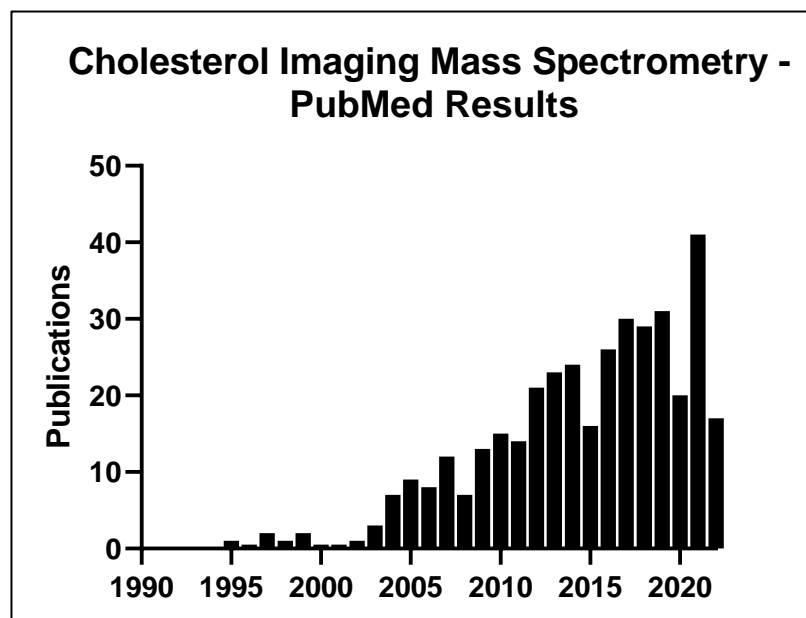


Figure 20. Number of articles/year published in the field of cholesterol imaging mass spectrometry

Studies using MALDI-IMS have increased in the last two decades, as confirmed by the above figure. Zima et al. reported images of Chol esters in atherosclerosis lesions, while Chol sulfate mapping was reported in skin tissue sections. In addition to tissue section mappings, a study by Schober et al. focused on single-cell imaging in which Chol was mapped on individual HeLa cells. Other examples of Chol imaging by MALDI evidenced changes in Chol levels in aortic plaques or in brain after injury due to atherosclerosis.

More recently, Angelini et al. showed for the first time the efficacy of using a Girard's Reagent P derivatisation in imaging study and not only in LC-MS analysis. They proposed a two derivatization steps to map Chol in brain slices from a mouse model of neurodegeneration ⁹⁸.

1.4.5.1. Hydrolysis methods in literature

The analytes of interest are not entirely present in free form in tissues and plasma but are partly in an esterified form; to measure their total concentration it is therefore necessary to hydrolyse the esters before analysis. The hydrolysis reaction can be acid, basic or enzymatic; the more frequently used, found in the literature for the analysis of Chol and Chol metabolites, are the enzymatic and basic (or alkaline) hydrolysis. The efficiency of the alkaline hydrolysis reaction is influenced by the concentration of the base used, the time and the temperature of incubation. In literature there are several different methods of alkaline hydrolysis that differ the reaction conditions. Tab. 3 report some combinations found in the literature.

In general, potassium hydroxide is used as a base in different concentrations, but the most used is 1 M. The temperature of incubation most frequently used is 37 °C with 1 hour of incubation time. A study by Mendiara et al.¹¹⁴ compares the basic hydrolysis method with the enzymatic method.

Table 3. Basic hydrolysis conditions present in literature.

Literature reference	Basic hydrolysis conditions
----------------------	-----------------------------

(Dzeletovic et al., 1995)	Room temperature, 2 hours KOH 0.35 M
(Dieter Lütjohann et al., 1996)	Room temperature, 2 hours KOH 0.35 M
(Lembcke et al., 2005)	68°C, 1 hour KOH 1 M
(DeBarber et al., 2008)	37°C, 1 hours KOH 0.9 M
(McDonald et al., 2012)	35°C, 1.5 hour KOH 10 N
(Y. Xu et al., 2013)	37°C, 45 minutes KOH 1M
(M. Q. Huang et al., 2014)	37°C, 30 minutes KOH 1M
(Kreilaus et al., 2016)	Room temperature, 16 hours NaOH 1 M
(Villani et al., 2016)	100°C, 2 hours KOH 10 M
(Goodenough et al., 2011)	37°C, 1 hour
(Di Natale et al., 2018)	KOH 1 M
(Yamamuro et al., 2020)	37°C, 1 hour KOH 1 N
(Birolini et al., 2020)	Room temperature, 1 hour KOH 1 M

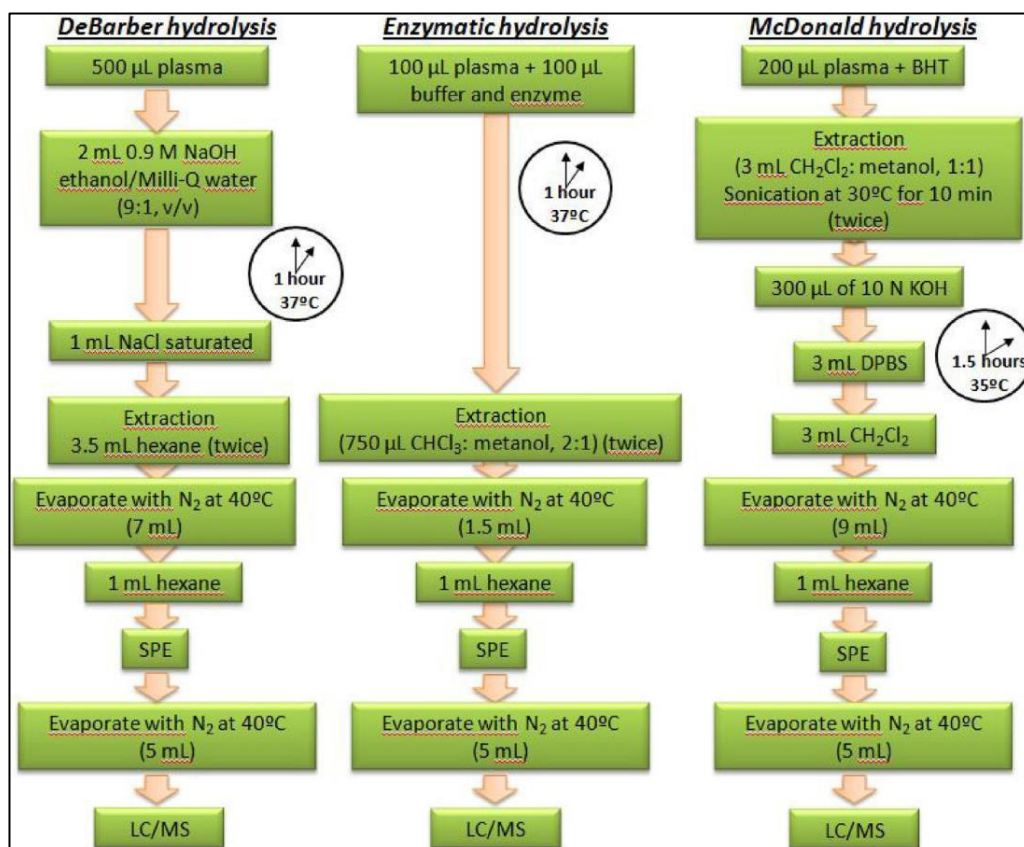


Figure 21. Comparison of three different hydrolysis methods from literature.

The study compared the three hydrolysis techniques in terms of noise signal during the instrumental analysis. Chromatograms obtained from samples that have undergone enzymatic hydrolysis have been found to be cleaner and with fewer unknown compounds than the SPE step. The comparison of the three methods in terms of recovery did not show any significant difference ¹¹⁴.

Considering the elimination of the SPE step, the enzymatic hydrolysis leads to a higher matrix effect due to the presence of the enzyme. The use of alkaline hydrolysis gives the possibility to remove the SPE step with a lower matrix effect.

1.5. Analytical method validation

A bioanalytical method is a set of procedures involved in the collection, processing, storage, and analysis of a biological matrix for a chemical compound. The availability of selective and sensitive bioanalytical methods is a prerequisite for the generation of reliable data on pharmacokinetics, bioavailability and bioequivalence studies of drugs. These methods should allow the quantification of drugs and their metabolites in biological matrices (e.g. plasma, urine, and cerebrospinal fluid) and must be validated with respect to their reliability for the intended use. The validation of a bioanalytical method comprises all the criteria determining data quality, such as selectivity, accuracy, precision, recovery, sensitivity, and stability. As in many other fields of analysis, demonstrating the validity of bioanalytical methods has become increasingly important. Over the past 15 years, bioanalytical method validation has been subject of much debate, and in literature are present many papers, guidelines and commentaries on this topic ¹¹⁵.

In this chapter, the main aspects of bioanalytical method validation are described, with special attention on the validation of bioanalytical methods for the analysis of endobiotics.

1.5.1. Lower limit of quantitation

The lower limit of quantitation (LLOQ) is defined as the lowest analyte concentration in the sample that can be quantified with acceptable accuracy and precision. In general, the lowest calibration standard is considered the LLOQ. The analyte signal in the LLOQ must be at least 10 times that of the blank.

1.5.2. Calibration curve

The calibration curve is necessary to establish the relationship between the instrumental response and the analyte concentration; this is evaluated in a specific concentration range, determined from the concentrations expected by the study. If more than one analyte is evaluated in an analytical run, a calibration curve must be available for each analyte.

The validation of an analytical method requires the definition of the concentration range expected in the samples; it must therefore be covered by the calibration curve, from LLOQ to ULOQ (Upper limit of quantitation). For the construction of this curve a minimum of 6 concentration levels must be used, to which are added a blank (where analyte and IS are absent) and a zero standard (where only the IS is present) for each analytical session.

The parameters of the curve, slope and intercept, must be reported and, having analyzed replicates of each standard, the concentrations calculated retrospectively for each level can be reported as mean with standard deviation. The accuracy and precision for each level must also be indicated. At the end of the validation, all the acceptable curves obtained must be reported (at least three).

The concentrations calculated retrospectively for each standard must be in a range of 15% around the nominal value, except for LLOQ which must be within 20%. At least 75% of the measures, with at least 6 concentration levels, must meet these criteria. If replicates are used, they must be met by 50% of the standards tested for each level, if this is not the case, that calibrator must be eliminated and the curve must be re-evaluated. If all replicates of LLOQ or ULOQ are rejected then the batch should be eliminated from validation and the source of error should be determined, if necessary by reviewing the method.

1.5.3. Carry over

During the method development it is necessary to evaluate and minimize the carry-over, i. e. the transport of an analyte from one sample to another during the analysis. To evaluate the carry-over within an analytical session, blanks are injected after a high concentration sample or a calibration standard at the upper limit of quantification (ULOQ). Carry-over in blank samples must not be greater than 20% of the lower limit of quantitation (LLOQ) for the analyte, while for the internal standard (IS) it must be less than 5%. If carry-over is unavoidable it is therefore necessary to apply the right measures to avoid affecting the accuracy and precision of the method. In particular, it is necessary to determine how many wash samples are needed to reduce carry-over until the levels required by the guidelines are reached.

1.5.4. Accuracy

The accuracy describes the proximity between the concentration determined by the method and the nominal analyte concentration, expressed as a percentage. It is evaluated on fortified samples at known analyte concentration, called quality control (QC) samples. These should be prepared independently of the calibration curve standards using a different starting solution.

Once the concentration has been analysed and determined by means of the calibration curve, the values obtained are related to the nominal values. The accuracy is reported as a percentage of the nominal value and is evaluated both within the same run (within-run) and between different runs (between-run).

QCs are prepared at four different concentrations covering the span of the calibration curve:

LLOQ;

Low QC (LQC) at three-fold LLOQ concentration;

Medium QC (MQC) at about 30-50% of the calibration curve,

High QC (HQC) at least 75% of the highest concentration in the calibration curve.

Within-run accuracy is determined in a single run with a minimum of 5 samples for each of the four concentration levels defined above. The average concentration should be between 15% of the nominal value for QCs, while LLOQs should be within 20%.

To determine the between-run accuracy, samples at LLOQ, LQC, MQC and HQC must be analysed in at least three runs over at least two different days. The average concentration should be within 15% of the nominal value (20% for LLOQ).

1.5.5. Precision

The precision describes the dispersion of repeated measurements of an analyte. It is expressed as the coefficient of variation (CV):

$$CV = \frac{SD}{|media|} \%$$

Where: SD is the standard deviation and |media| is the mean of the repeated measurements.

It must be evaluated for LLOQ, LQC, MQC and HQC, both within-run and between-run.

At least five replicates must be analysed for each concentration level to calculate the within-run CV value. The value obtained must not exceed 15% for QCs and 20% for LLOQs.

The between-run CV value is evaluated at the same levels, in at least three runs in at least two different days; the obtained values must to be under 15%.

1.5.6. Matrix Effect

When mass spectrometry methods are used, the matrix effect must also be evaluated. It is possible, and common, that interfering molecules are present in the sample to be analysed. These interferences, when they have chromatographic retention times similar to those of the analytes, may change the instrumental response that is therefore no longer proportional to the concentration of the analyte.

To verify the extent of this effect, at least six fortified independent analyte matrices after extraction and a solvent solution of the analyte should be analysed in triplicate. For each analyte and for the IS, the matrix factors (MF) shall be calculated as the ratio between the peak area in the presence of matrix and that in the absence of matrix. The normalized MF is then calculated by dividing the MFs of each analyte by that of the IS. The CV of these values, calculated for the 6 lots of matrix must not be greater than 15%. The matrix effect must be determined in this way for both low and high levels of concentration, and therefore at maximum 3 times the LLOQ and close to ULOQ.

It is essential that the normalized MF values tend as much as possible to one, since this is an indication of a very similar matrix effect for analyte and IS and therefore shows that the IS perfectly mimics the target analyte.

1.5.7. Recovery

The recovery determination of the added analyte assesses the extraction efficiency of the analytical method and must be determined for both the analyte and the IS. The peak area obtained from the analysis of a matrix sample fortified at known concentration *_before_* extraction must be compared with that of a matrix sample fortified at the same concentration *_after_* extraction. The calculation used to obtain recovery is as follows:

$$\text{Recovery \%} = \frac{(\text{Analyte extracted from the matrix peak area})}{(\text{Analyte peak area in presence of matrix})} * 100$$

For the determination it is necessary to analyse at least 5 replicates for each level of QC, the average of the values for each concentration must have a CV less than 20%.

1.5.8. Freeze and thaw stability

Freeze-thawing stability (freeze and thaw) of matrix analytes is evaluated at LQC and HQC for a minimum of 5 replicates, as soon as they are prepared and after various freezing and thawing cycles. The mean concentration value found should be within 15% of the nominal value.

In each cycle the samples are frozen for 24 hours, thawed at room temperature, restored for 12-24 hours, finally thawed again at room temperature.

1.5.9. Validation of analytical methods for endobiotics

The quantitative determination of endogenous and endobiotics compounds in biological samples is more complicated, from the analytical and the validation points of view. Endogenous compounds are substances naturally present in biological tissues, while endobiotics are compounds administered to biological systems that are also already present in biological tissues. In these cases, it is often difficult, if not impossible, to obtain analyte-free samples of the authentic biological matrix or samples with known analyte concentrations; so the preparation of reference samples has to be addressed in a different way and the validation of an analytical method becomes less straightforward.

In detail, for these compounds, the accuracy of measurement poses a challenge when the assay cannot distinguish between the therapeutic agent and the same endogenous compound already present. The validation of the method for endobiotics and endogenous compounds has so far been hampered by the absence of official guidelines.

For endobiotics, the validation of an analytical method presents steps in common with the validation of xenobiotics and steps that are difficult to transfer. Table 4 summarizes the steps that are common to method validation for xenobiotics, the steps that need particular attention and the steps that are difficult to transfer.

Table 4 Method validation steps for endobiotics and their similarities with method validation for xenobiotics

Method validation: endobiotics	
Precision	Similar to xenobiotics
Stability	
Carry-over	
Calibration Curve, Linearity	Special attention for endobiotics
Accuracy	
Lower limit of quantitation (LLOQ)	
Matrix effects and extraction recovery	
Limit of detection (LOD)	Difficult to evaluate for endobiotics
Selectivity	

Various approaches are followed to address the lack of blank authentic matrices for the quantitation of endobiotics, including:

- Background subtraction
- The standard addition method
- Surrogate analytes
- Surrogate matrices

In background subtraction, the endogenous background concentrations of analytes in an authentic matrix are subtracted from the concentrations of the added standards, subsequently the subtracted concentrations are used to construct the calibration curves. This approach allows the use of the same matrix for the calibration curves as the one to be analyzed, so that recovery and matrix effect are the same between samples and calibration curves. However, for this method to be reproducible, the increase in background peak area after spiking with standards has to be significantly higher than the reproducibility limits of the method, i.e. at least 15–20% of the background peak areas. Therefore, the critical point for this method is that the different batches of pooled matrices used as blank will have different background levels of endobiotic to subtract, which makes it an irreproducible process over time or between different labs. Furthermore, it is difficult to quantify multiple analytes if they have variable endogenous levels, as in the case of Chol metabolites in plasma and brain samples. Moreover, this method is applicable for endobiotic compounds but not for endogenous ones.

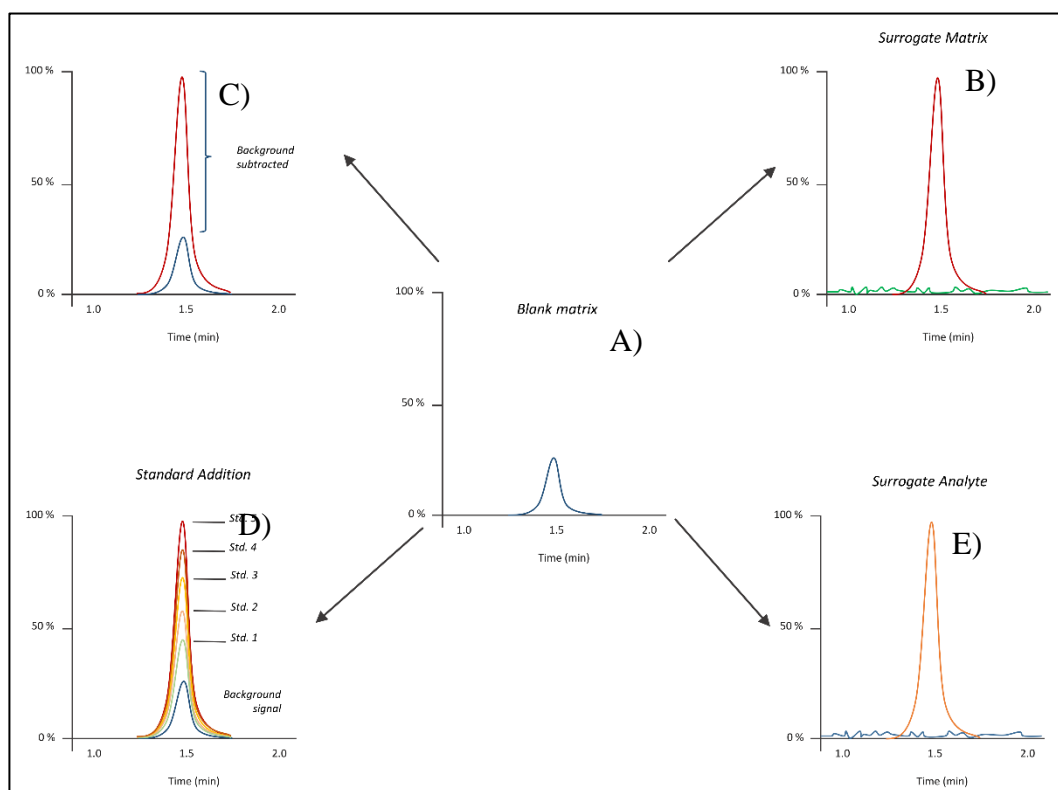


Figure 22. LC-MS/MS chromatograms showing (A) background peak of an endogenous analyte in blank matrix, (B) a surrogate matrix with known concentration of the target analyte, (C) the same matrix after spiking with a standard of a known concentration (method of background subtraction), (D) method of the standard addition: one study sample is split into several aliquots, each spiked with a standard (Std.) of different concentration, (E) a standard of a surrogate analyte spiked into the same original matrix (surrogate analyte method).

In the standard addition method, every sample is divided into aliquots of equal volumes. All aliquots, but one, are separately spiked with known and varying amounts of the analyte to construct a calibration curve for every sample. The standard addition method has the advantage of the use of the exact same matrix of every sample for the construction of its own calibration curve. Furthermore, this approach allows direct quantitation of endogenous analytes without manual subtraction of background peak areas. However, this process generally requires a large amount of samples and can be highly time-consuming and labour intensive.

If no analyte-free samples of the authentic matrix are available, calibration standards can be prepared by spiking the analyte in artificial or surrogate matrix. Surrogate matrices can vary widely in complexity. In its simplest form, a surrogate matrix is pure water or a buffer, such as phosphate-buffered saline (PBS), which is frequently used for plasma and serum analyses because of its similar pH (7.4) and ionic strength (150 mM). Often, bovine (BSA) or human serum albumin (HSA) is added to PBS at a concentration of 40–60 g/l to take into account the protein content of the biological matrix, which can increase the solubility of hydrophobic analytes. A novel and very interesting approach is the application of surrogate analytes. For methods employing the use of MS or MS/MS detection, quantitation of an endogenous analytes can be performed by reference to a calibration curve constructed from samples of the authentic matrix spiked with a stable-isotope-labeled form of the analyte – the surrogate analyte – which does not occur naturally in the matrix. The assumption is that the physico-chemical properties of authentic and surrogate analytes are similar – as they differ in molecular mass only – and that therefore, their analytical response is identical. In this thesis the method for the quantitation of administered Chol-D6 was validated according to the EMA guidelines for the validation of bioanalytical methods, while the method for the analysis of Chol metabolites in plasma and brain was validated using the scheme presented in table 5. Since Chol metabolites are endobiotics we set up a validation scheme that uses a surrogate matrix for all the experiments that need a quantitation of target analytes and a surrogate of the analytes (i.e.: deuterated compounds) for all the validation step that evaluate the influence of the matrix.

Table 5. Validation scheme proposed for Chol metabolites quantitation in biological matrices

Method validation: Chol metabolites	
Matrix effects and extraction recovery	Surrogate analyte
Stability	Surrogate analyte
Carry-over	Surrogate analyte
Calibration Curve, Linearity	Surrogate matrix
Accuracy	Surrogate matrix
Precision	Surrogate matrix



2. Rationale and aim

2. RATIONALE AND AIM

2.1 RATIONALE

Huntington's disease (HD) is a neurodegenerative disorder caused by an expansion of the CAG repeat in the gene coding for the huntingtin protein. The first description of the disease occurred in 1872, and in 1993 the causative role of the gene mutation in the huntingtin protein was discovered. HD is characterized by motor defects, cognitive decline, and psychiatric disorders. Today it is well known that brain cholesterol (Chol) metabolism is a key pathway linked to HD progression. The blood-brain barrier (BBB) prevents the peripheral diffusion of Chol to the brain and, as a consequence, only the Chol synthesized in the brain is involved in synapse formation, maintenance, and activity, as well as optimal neurotransmitters release. Dysfunction in the brain Chol metabolism, observed in HD, means that newly synthesized Chol and its metabolites are less available in the HD brain, which has negative consequences for neuronal and synaptic activities. It is well known from the literature that treatments supplying Chol improve the neurite outgrowth defects observed in HD neurons *in vitro*, and that Chol-loaded brain-permeable nanoparticles prevent cognitive decline and synaptic dysfunction in HD mice. The prevention of the intake by the central nervous system (CNS) of many drugs (such as Chol), due to the BBB, is one of the drawbacks of treatments of CNS disorders by peripheral drug administration. Furthermore, drugs administered through this route undergo first-pass metabolism and systemic clearance, lowering their bioavailability. So innovative, non-invasive, and easy-transferable clinical approaches that overcome this issue are appealing.

2.2. AIM

Given these bases, the presented project, part of a project financed by the Italian Ministry of Health in collaboration with the University of Milan and Istituto Carlo Besta, has the aim to study an innovative route to deliver exogenous Chol into the brain and, in parallel, to deeply investigate the Chol metabolism alterations related to HD. Specifically, we are evaluating the efficacy of an intranasal treatment with exogenous Chol and the metabolic alterations of Chol in the mouse model of the disease (R6/2 mice), using mass spectrometry-based methods. Moreover, we use a validated LC-MS method to quantify peripheral Chol metabolites in patients of a clinical trial, in collaboration with Istituto Carlo Besta. Detailed clinical data and blood samples from patients were collected at baseline and after two years to investigate the changes in Chol metabolism during the longitudinal study. Blood samples were used to measure 24-hydroxycholesterol (24SOHC), the main brain metabolite of Chol (which is capable to pass the BBB), and a panel of other sterols reflecting, instead, peripheral Chol synthesis. We finally expect to verify whether changes in plasma 24SOHC may be a marker of the disease progression and, eventually, of the pheno-conversion from pre-symptomatic to symptomatic stages of HD (in combination with other clinical, cognitive, and imaging parameters). The proposed 24SOHC metabolic-biomarker study has been designed to complement other international observational trials conducted on pre-HD subjects and to integrate with an ongoing clinical-neuropsychological and neuroimaging study initiated at the Istituto Carlo Besta in 2013.

In detail, the presented Ph.D. project is focused on the development, validation, and application of different mass spectrometry methods to assess both the pharmacokinetics of exogenous administered Chol and the Chol metabolic alterations.

The specific aims can be summarized as follow:

- Investigation of the efficacy of nose-to-brain delivery of Chol using mass spectrometry
- Description of the altered metabolic state in a mouse model of the disease and, eventually, the effect of administered Chol in restoring metabolic defects
- Study of the spatial distribution of the Chol metabolites in the brain using mass spectrometry imaging techniques
- Study of Chol metabolic alterations in HD patients

An LC-MS-based method was developed and fully validated to determine exogenous Chol (D6-cholesterol) levels in bulbs, brain, plasma, and peripheral tissues after intranasal administrations in WT and R6/2 mice, to define pharmacokinetic and biological distribution after both single and chronic treatments. A second, LC-MS method, was developed and validated to quantify the main Chol metabolites in plasma and brain from WT and R6/2 mice, in order to confirm the altered Chol metabolic state in R6/2 mice and to investigate if the treatment with exogenous Chol could restore the normal brain Chol metabolism as well as improve the phenotype of the disease.

Finally, an imaging mass spectrometric method was implemented to investigate, in mouse models, the spatial distribution of Chol metabolites in slices of the striatum tissue, the most involved brain area in the disease progress. This experimental approach may provide a new understanding of possible treatments of HD. The obtained results, giving an overview of the Chol metabolic alteration in HD mice and the efficacy of the proposed innovative treatment, can pave the way for further investigations to understand the optimal therapeutic dose of Chol and its efficacy in improving the phenotype of the disease.

3

3. Materials and Methods

3. MATERIALS AND METHODS

3.1. Standards and Chemicals

Deuterated cholesterol (Chol-D6) (isotopic purity: 97 atom % D), phosphatidylcholine (PC), and β -sitosterol were obtained from Sigma-Aldrich (St Louis, MO, U.S.A.). LC-MS grade acetonitrile and formic acid were from Carlo Erba, Milan, Italy. LC-MS grade deionized water was obtained from Milli-Ro 60 Water System, Millipore, Milford, MA, U.S.A. Chol-D6 and β -sitosterol, used as the internal standards (IS), were prepared as stock solutions in ethanol (EtOH) at 1 mg/mL. The Chol-D6 stock solution was diluted in EtOH to obtain a series of seven working solutions for the construction of calibration curves, validation, and sample analysis. The β -sitosterol IS stock solution was diluted to 5 μ g/mL in the same organic solvent. All solutions were stored at -20°C until use. The standards 7- α -hydroxycholesterol, 22(R/S)-hydroxycholesterol, 24(S)-hydroxycholesterol, 25-hydroxycholesterol and 25(S)-27-hydroxycholesterol were purchased from VINCI-BIOCHEM Srl; 24-dehydrohydrocholesterol, 7-dehydrocholesterol, and lanosterol were purchased from CABRU S.A.S. The internal standards used for hydroxysterol analysis were: 24(R/S)-hydroxycholesterol-D7 (SPECTRA 2000 Srl), 25-hydroxycholesterol-D6 (VINCI-BIOCHEM Srl) and desmosterol-D6 (CABRU S.A.S). All standards were dissolved in ethanol (Carlo Erba) and stocked at -20°C as 1 mg/mL solutions.

Butylhydroxytoluene (BHT) was purchased from Acros Organics, potassium hydroxide from Merck Life Science S.r.l., ethanol and dichloromethane from Carlo Erba and Phosphate Buffer Saline (PBS) from Fisher Scientific.

3.2. Liposomes

Chol-D6 was entrapped in oligolamellar, 280-300 nm-wide liposomes, following the dehydration-rehydration method. Briefly, Chol-D6 and PC were dissolved in chloroform at a 1:1 molar ratio. After solvent evaporation, the lipid film was rehydrated with phosphate buffer solution (PBS) and ultracentrifuged at 100,000 g for 35 min at 4°C to separate residual lipids. Liposomes were resuspended with 10 mM phosphate buffered saline, pH 7.4. The concentration of Chol-D6 entrapped in liposomes was determined by HPLC (System Gold instrument – Beckman) equipped with an Eco Cart-LiChrospher® 60 RP-select B column (125 × 3 mm, particle size 5 µm, pore size 60 Å, Merck) at 214 nm. Separation was done with isocratic elution at 100% methanol:isopropanol:NH₄OH (70%:30%, 5mM) for 12 min. The flow rate was 0.6 mL/min. Entrapment efficacy was ±90%, and liposomes were diluted to a final Chol-D6 concentration of 5.6 mg/mL.

3.3. Animal model and treatment schedules

We used an R6/2 colony of mice generated to over-express the first exon of the human mutant huntingtin gene with approximately 144-150 CAG repeats. The R6/2 line was genotyped by polymerase chain reaction (PCR) on DNA from ear samples at weaning ³⁶.

The IRFMN adheres to the principles set out in the following laws, regulations, and policies governing the care and use of laboratory animals: Italian Governing Law (D.lgs 26/2014; Authorisation n.19/2008-A issued March 6, 2008 by Ministry of Health); Mario Negri Institutional Regulations and Policies providing internal authorisation for persons conducting animal experiments (Quality Management System Certificate – UNI EN ISO 9001:2015 – Reg. No. 6121); the NIH Guide for the Care and Use of Laboratory Animals (2011 edition) and EU directives and guidelines (EEC Council Directive 2010/63/UE).

Liposomes were administered to mice by applying 6 μ L of a 5.6 mg/mL solution three times to the inner surface of each nostril for a total of 36 μ L, corresponding to a final dose of 200 μ g of Chol-D6/mouse (Hanson et al, 2013).

For the first acute study (I trial), 8-week-old wild-type (WT) mice were euthanised 1, 3, 6, 24, 48 and 72 hours after a single IN dose (3 mice/time point). While for the second acute study (II trial), 8-week-old WT and R6/2 mice were given two doses of 200 μ g/mouse of Chol-D6, 5 hours apart (5 mice/time point/genotype). Mice were euthanised 3, 24, 48 and 72 hours from the second IN treatment.

The third treatment, III trial, was a repeated-doses treatment, 8-week-old WT and R6/2 mice received 9 or 10 IN doses, once every two days (4 mice/time point). One group of animals was euthanised two days after the ninth IN treatment, while the others received the tenth IN dose and were euthanised 24 and 48 hours later.

The aim of the IV Trial was to evaluate the elimination rate of Chol-D6, through a new acute study. 8-week-old WT and R6/2 mice were treated with a single IN dose (4 mice/time point) and they were euthanized at 42 days after the treatment. Blood samples were collected with the anticoagulant K3EDTA, and plasma samples were obtained by

centrifugation at 2000 g for 15 minutes. Brains were immediately removed and striatum, cortex and cerebellum were collected separately. All samples were stored at -80°C until LC-MS analysis.

3.4. LC-MS analysis of exogenously administered cholesterol

Chol-D6 levels were determined using a 1200 Series HPLC system (Agilent Technologies, Santa Clara, CA, U.S.A.) interfaced to an API 5500 triple quadrupole mass spectrometer (Sciex, Thornhill, Ontario, Canada). The mass spectrometer was equipped with an atmospheric pressure chemical ionization (APCI) source operating in positive ion - multiple reaction monitoring (MRM) mode to measure the product ions obtained, in a collision cell, from the $[MH - H_2O]^+$ ions of the analytes. The transitions identified during the optimization of the method were m/z 375.3–152.1 (quantification transition) and m/z 375.3–167.1 (qualification transition) for Chol-D6; m/z 397.3–147.1 (quantification transition) and m/z 397.3–161.1 (qualification transition) for β -sitosterol (IS). The ion source settings were as follows: nebulizer current (NC) 3; curtain gas (CUR) 30; collision gas (CAD) 7; source temperature 400 °C; ion source gas 1 (GS1) 60 and gas 2 (GS2) 30. Chol-D6 and β -sitosterol were separated on a Gemini C18 column (50 × 2 mm; 5 μ m particle size), using an isocratic gradient of 300 μ L/min in 100 % methanol at 35 °C.

3.4.1. Sample preparation

Plasma

Fifty microliters of plasma were diluted with 200 μ L of ethanol containing 200 ng of β -sitosterol as IS. Samples were vortexed and centrifuged at 13200 rpm for 15 min; 4 μ L aliquots of the supernatants were injected directly into the LC-MS system.

Striatum, Cortex, Cerebellum and peripheral tissues

Almost 100 milligrams of each brain area were homogenized in 1 mL of PBS containing 1 μ g of β -Sitosterol. 200 μ L of PBS homogenate were extracted with 800 μ L of ethanol. Samples were then centrifuged for 15 min at 13200 rpm at 4 °C, and the supernatants were injected into the LC-MS system.

3.4.2. Validation scheme for Chol-D6 analysis

The LC-MS method was validated in mouse plasma and brain tissue following EMA guidelines (22). Accuracy was determined by expressing the calculated concentration as a percentage of the nominal concentration. Accuracy had to be within 15% of the nominal value for each concentration ($\pm 20\%$ of the nominal value for the lower limit of quantification – LLOQ – as an exception); the precision, expressed by the CV (%), had not to exceed 15% for all concentrations, except 20% for the LLOQ. A freshly prepared calibration curve was analyzed during each validation run.

Calibration Curves

All calibration curves during the validation procedure included one zero point and six calibration points at the concentrations of 50, 100, 250, 500, 1000, 2500, and 5000 ng/mL and 0.030, 0.100, 0.300, 1.00, 3.00, and 10.0 ng/mg of Chol-D6 for plasma and brain samples, respectively. The IS concentration was 100 ng/mL in plasma and 0.010 ng/mg in brain homogenates. Responses, expressed as the peak area ratios of the analyte vs the IS, were plotted against the corresponding Chol-D6 concentration, and the data were fitted with a linear regression curve. The quality of a calibration curve was evaluated from the determination coefficient (r^2) and by comparing the back-calculated concentrations of calibrators with the corresponding nominal values.

Carry-over

The carry-over of the analytical instrumentation was checked by injecting Chol-D6 at the highest concentration (upper limit of quantitation, ULOQ), followed by repeated injections of blank samples. The carry-over was considered absent if the Chol-D6 signal measured in the blank samples immediately after the ULOQ was <20% of the LLOQ signal.

Recovery

Recovery was determined by comparing the peak area of Chol-D6 spiked into plasma and brain samples before extraction (C) and the peak area of the analyte spiked into the same samples after extraction (A). The same method was used to calculate the recovery of IS, as follows: % Rec = $C/A \times 100$.

3.5. LC-MS analysis of cholesterol metabolites

Levels of oxysterols and Chol precursors were determined in murine and human plasma samples and in mouse brain tissues. A UHPLC (High-Performance Liquid Chromatography) system was used for the analysis of metabolites interfaced with a triple quadrupole mass spectrometer LCMS 8060 (Shimadzu), equipped with an electrospray source (ESI) and used in Multiple Reaction Monitoring (MRM) mode.

3.5.1. Sample preparation

The extraction method involved the addition of Internal Standards (IS) at the following concentrations: cholesterol precursors (desmosterol-D6 and lathosterol-D7) 100 ng/mg in brain tissues and 1 µg/mL in plasma and cholesterol metabolites (24-hydroxycholesterol-D7 and 25-hydroxycholesterol-D6) 10 ng/mg in tissues and 100 ng/mL in plasma.

- *Plasma*: 250 µL of plasma were spiked with IS. Plasma samples were deproteinized using the slow protein precipitation method by using EtOH (containing 100 µg/mL BHT) in three separate additions of 500 µL each. After each addition samples were stored at 4 °C for 15 minutes and then centrifuged at 13200 rpm for 15 minutes. The main advantage of the slow protein precipitation is the increase of the signal-to-noise ratio of the analytes, without the necessity of an additional solid-phase extraction step. After deproteinization, the supernatant was recovered and hydrolysed by the addition of 175 µL of KOH 1 M in water. The reaction, optimized in terms of KOH concentration, time, and temperature of incubation, was carried out under controlled temperature conditions (40 °C) for 1 hour. After hydrolysis, 500 µL of water and 2 mL of dichloromethane were added to samples for liquid-liquid extraction. Samples were mechanically mixed, sonicated for 30 minutes, and finally centrifuged for 15 minutes at 2400 rcf at room temperature. The extraction was repeated twice and at each step the organic phase was recovered and gently dried under nitrogen flow. The extracts were re-suspended in 40 µL EtOH for the analysis.

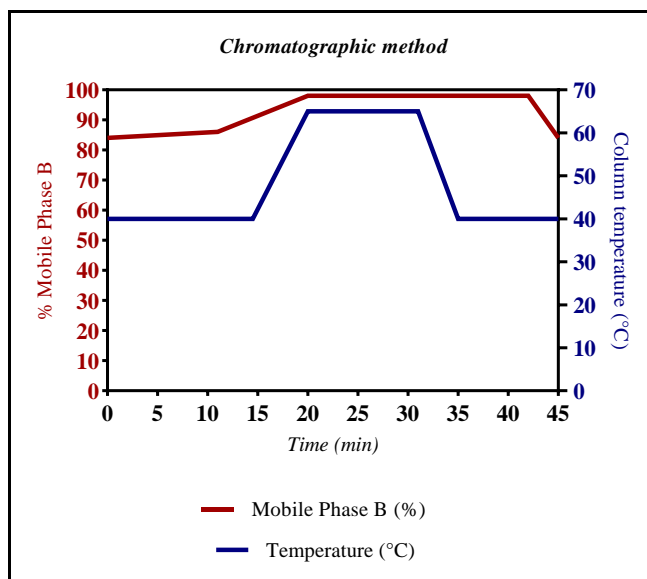
- *Brain tissues:* 100 mg of tissue were homogenated in a 1:10 ratio with a PBS solution, after the addition of the IS. Tissue homogenization was carried out with the Precellys system by using 2 mL screw-cap tubes containing 0.5 g of ceramic beads (zirconium oxide) with a diameter of 1.4 mm. The homogenizer, through a three-dimensional rotation movement, which increases its speed from 4000 to 6800 rpm in two 45-second cycles separated by a 1-minute break, is able to develop high energy and to fully homogenate tissues. 200 μ L of the homogenates were then transferred to a 2 mL tubes and extracted with 800 μ L of a solution of BHT 100 μ g/mL in EtOH. The solutions were vortexed and centrifuged at 13200 rpm at 4 °C for 15 minutes. The supernatant (1 mL) was recovered and hydrolyzed by the addition of 125 μ L of KOH 1 M in water. The reaction was carried out under controlled temperature conditions (40 °C) for 1 hour. The hydrolyzed sample were added with 500 μ L of water and 2 mL of dichloromethane for the liquid-liquid extraction. Samples were mechanically mixed, sonicated for 30 minutes, and centrifuged for 15 minutes at 2400 rcf at room temperature. The extraction was repeated twice and at each step, the organic phase was recovered and gently dried under nitrogen flow. The extracts were suspended in 100 μ L EtOH for the analysis.

3.5.3. Instrument set-up

A Shim-pack XR-ODS III column (200 x 2.1 mm) was used for chromatographic separation of all Chol metabolites. In order to measure metabolites and cholesterol precursors in a single chromatographic run, the developed method consisted of a segmented gradient, slower in the first phase to efficiently separate the oxysterols isomers and faster in the second phase to guarantee an efficient elution of Chol precursors within 30 minutes. The chromatographic gradient was integrated with a temperature ramp to facilitate the elution of precursors in the second phase and to improve the peak shape. A flow rate of 0.30 mL/min was used. Table 6. resumes the chromatographic and temperature gradients.

Table 6. Scheme of temperature and solvent gradient of the developed UHPLC-MRM method

Time		Phase B % (HCOOH 0.1% in methanol) / Phase A% (HCOOH 0.1% in water)	Column Temperature (°C)
0	min	84/16	40 °C
11	min	86/14	
14.5	min		40 °C
20	min	98/2	65 °C
31	min		65 °C
35	min		40 °C
42	min	98/2	
43	min	84/16	40 °C

Table 7. Graphical representation of the segmented gradient used for oxysterols and Chol precursors

During the optimization of the method, we chose the best transitions for the identification and the accurate quantification of the analytes of interest. The monitored transitions included in the MRM method are shown in the table together with the optimized collision energies (CE).

Table 8. Selected MRM transitions and related Collision Energy (CE)

Analyte	Quantifier	CE	Qualifier	CE
7 α HC	383.5 \rightarrow 159.3	27	383.5 \rightarrow 105.1	45
24SOHC	367.3 \rightarrow 159.1	28	363.3 \rightarrow 133.1	25
24SOHC-D ₇	374.1 \rightarrow 159.1	23	374.1 \rightarrow 147.1	25
Lat-D ₇	376.3 \rightarrow 161.1	24	376.3 \rightarrow 105.1	45
25OHC	367.1 \rightarrow 147.1	25	367.1 \rightarrow 159.2	25
25OHC-D ₆	373.3 \rightarrow 147.1	24	373.3 \rightarrow 161.1	23
27OHC	385.2 \rightarrow 161.1	21	385.2 \rightarrow 135.1	24
Desm	367.2 \rightarrow 147.1	24	367.2 \rightarrow 95.1	30
Desm-D ₆	373.2 \rightarrow 147.1	24	373.2 \rightarrow 161.1	23
Lan	409.2 \rightarrow 95.1	35	409.2 \rightarrow 109.2	25
22(R/S)OHC	367.3 \rightarrow 159.3	25	367.3 \rightarrow 91.2	54
7-dehydro	367.2 \rightarrow 159.1	21	367.2 \rightarrow 95.3	34

3.5.4. Validation scheme for Chol metabolites

The LC-MS method was validated using the previously described parameters, ensuring the precision/accuracy of each analytical session within 15%.

As described in the chapter 1.5 of the introduction, the method for Chol metabolites quantitation was validated following the scheme reported in the following table.

Table 9. Validation scheme for Chol metabolites method

Method validation: Chol metabolites	
Matrix effects and extraction	Surrogate analyte
Recovery	
Calibration Curve, Linearity	Surrogate matrix
Accuracy	Surrogate matrix
Precision	Surrogate matrix

The selected calibration ranges for oxysterols, including 24SOHC, 25OHC and 27OHC, 22OHC, and Chol precursor, including Desm, Lan, 7dehydro, in both plasma and brain matrices are reported in the following Table:

Table 10. Calibration range for chol metabolites analysis in plasma and brain matrices

Analyte	Range in plasma (ng/mL)	Range in brain (ng/mg)
Oxysterols	3 ng/mL - 1000 ng/mL	10 ng/mg - 3000 ng/mg
Chol Precursor	10 ng/mL - 3000 ng/mL	30 ng/mg - 10000 ng/mg

3.6. Imaging Experiments

3.6.1. Sample Preparation

In the present study, adult WT and R6/2 mice were employed. Frozen brains were cut into 10 μm thick sections using a cryo-microtome (Leica Microsystems, Wetzlar, Germany) at -20°C . Three to five sagittal sections were cut from the whole brain of both WT and R6/2 mice at 12 weeks and were mounted on a -20°C pre-cooled MALDI plate by standard thaw-mounting techniques (gently touching the back of the frozen MALDI plate with a finger) and stored at -80°C until further analysis. For each section, two adjacent slices were cut, one to be imaged in MS/MS mode and the other (10 μm thickness) placed on a glass slide for hematoxylin and eosin (HE) staining. The plate with the tissue sections was dried in a vacuum drier at room temperature for 1 h. A solution of Chol-D6 at 5 $\text{ng}/\mu\text{L}$, used as IS, was sprayed from a SunCollect automated pneumatic sprayer (SunChrom supplied by KR Analytical, Ltd) at a flow rate of 20 $\mu\text{L}/\text{min}$ at a linear velocity of 900 mm/min with a 2-mm line distance and Z position of 30 mm in a series of 18 layers.

3.6.2. Sample derivatization

Since all Chol metabolites loss one or more water molecule during ionization, we decided to use a sample derivatization step to discriminate them. In particular, desm and 24SOHC loss one and two molecule of water, respectively. After derivatization step they acquired different m/z : 496.4261 and 514.4367, respectively, as shown in figure 23 and 24.

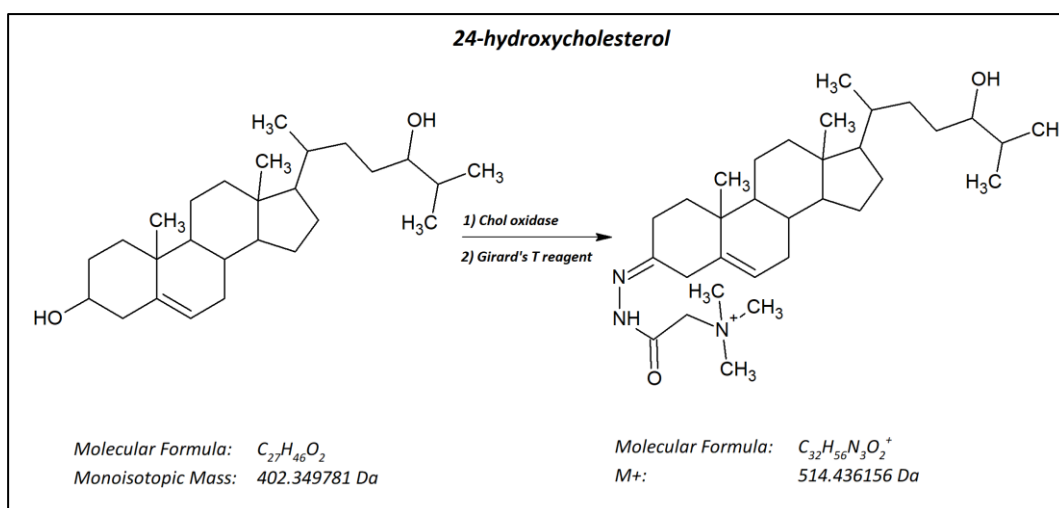


Figure 23. Chemical structure of 24SOHC with and without Girard's T (GT) derivatization.

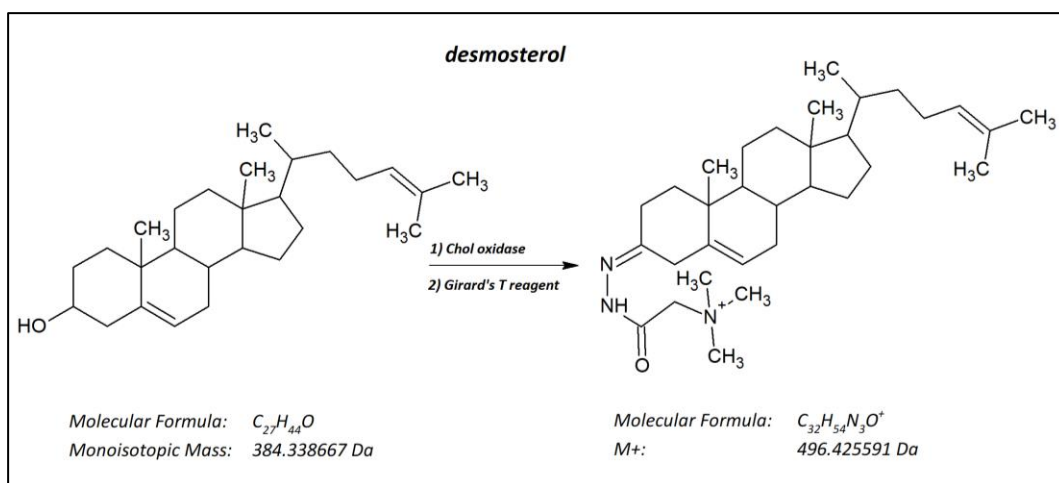


Figure 24. Chemical structure of desm with and without Girard's T (GT) derivatization

Figure 25 shows the result of Chol derivatization using GT reagent.

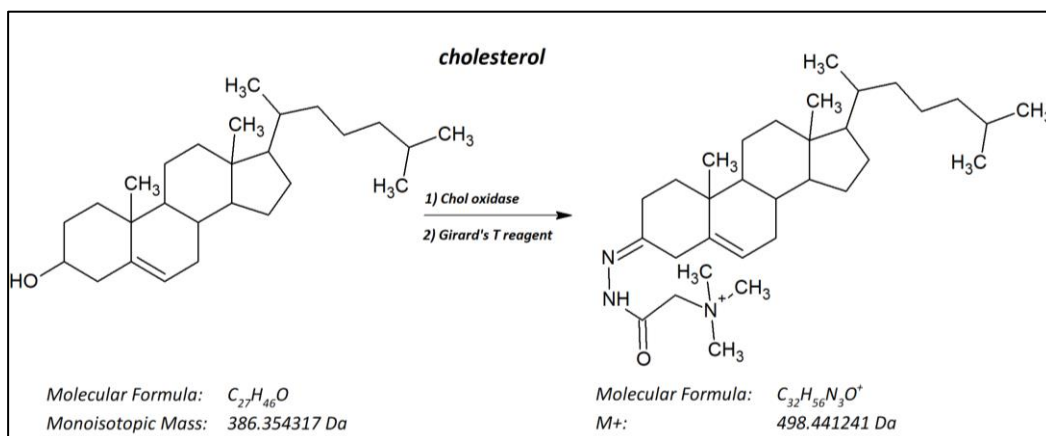


Figure 25. Chemical structure of Chol with and without Girard's T derivatization

The sprayer was thoroughly flushed with about 2 mL of methanol after which cholesterol oxidase (0.264 units/mL in 5 mM KH_2PO_4 , pH7) was sprayed in 18 layers. The first layer was applied at 10 $\mu\text{L}/\text{min}$, the second at 15 $\mu\text{L}/\text{min}$, and then all of the subsequent layers at 20 $\mu\text{L}/\text{min}$ to give an enzyme density of 0.05 munits/ mm^2 . Thereafter, the enzyme-coated slide was placed on a flat dry bed above 30 mL of warm water (37 °C) in a closed pipette-tip box (11.9 cm×8.2 cm×8.5 cm) and then incubated at 37 °C for 1 h, after which, the slide was removed and dried in a vacuum desiccator for 15 min.

Girard's T reagent (GT) (6.3 mg/mL bromide salt, in 70% methanol with 5% acetic acid) was sprayed on the dried slide with the same spray parameters as used for spraying cholesterol oxidase. The resulting GT density was 1.21 $\mu\text{g}/\text{mm}^2$. The slide was then placed on a flat dry bed above 30 mL of pre-warmed (37 °C) 50% methanol, and 5% acetic acid in a covered glass chamber (12 cm×12 cm×7.2 cm) and incubated in a water bath at 37 °C for 1 h. The slide was removed and dried in a vacuum desiccator until IMS analysis.

3.6.3. Instrumental analysis

A Q Exactive Hybrid Quadrupole-Orbitrap mass spectrometer (Thermo Fisher Scientific Waltham, Massachusetts) was used for IMS experiments, coupled with an AP-MALDI-ng-UHR ion source (MassTech Inc., Columbia, MD), controlled by Target-ng software (MassTech Inc., Columbia, MD). Tune software (Thermo Fisher Scientific Waltham, MA, USA) was used to control the mass spectrometer parameters and to manage the MS acquisition. Parameters used, unless otherwise specified, were: laser energy, 12,5%; voltage applied to the plate, 2kV; capillary temperature, 250 °C and S-lens RF, 80 %. In preliminary experiments, each metabolite was co-spotted, after derivatization, with the matrix on the plate and acquired using spiral motion to study the ionization and the fragmentation pattern of each one of them. For MSI experiments, constant speed raster motion was used, with 100 µm spatial resolution and plate velocity dependent on the scan time. Acquisitions were performed in full scan with a positive polarity, a mass range of m/z 100–1000 and a resolution of 70000. Automatic gain control (AGC) was set at 5e6, with 150 ms maximum injection time. The chosen AGC value was high enough to guarantee that all scans reached a maximum injection time, ensuring equal scan times for each pixel. The instrument was calibrated with a standard cal mix before each analysis.

Data were exported as imzML files from Image Quest (Thermo) and imported into MSiReader v1.20. The metabolite ion signal (tolerance 5 ppm) was normalized in each pixel to the signal of the IS.

3.7. Statistical Analysis

Prism 8 (GraphPad software) was used to perform statistical analyses. G-power software was used to pre-determine group allocation, data collection and all related analyses. For animal studies, mice were assigned randomly, and sex was balanced in the various experimental groups; animals from the same litter were divided in different experimental groups; blinding of the investigator was applied to *in vivo* procedures and all data collection. Grubbs' test was applied to identify outliers. For each set of data to be compared, we determined whether data were normally distributed or not to select parametric or not parametric statistical tests. The specific statistical test used is indicated in the legend of all results figures.

4

4. Results and discussion

4. RESULTS AND DISCUSSION

4.1. Validation of the LC-MS method for D6-Chol quantitation

To assure the robustness of the proposed strategy, we developed a rapid LC-MS analytical method for the quantitation of administered D6-Chol and we validated it using EMA guidelines. Chapter 4.1 is focused on the discussion of the validation process and the results obtained.

4.1.1. Calibration curves

We defined a wide calibration range that allowed the quantitation of D6-Chol after single and repeated doses. The calibration curve was linear in the selected range of D6-Chol concentrations. In five different analytical sessions, the determination coefficients (r^2), for linear regression analysis, gave averages of 0.998 and 0.997 in plasma and brain, respectively. The slope values were highly reproducible among different analytical sessions (Tables 11 and 12). The mean accuracy of the back-calculated concentrations ranged from 99% to 102% in plasma samples. The mean accuracy was slightly more variable in brain samples, ranging from 93% to 108%. The precision of back-calculated concentrations was expressed as coefficient of variation (CV%) and was acceptable for all calibration points in both matrices. Figure 1 shows a representative calibration curve in plasma (26A) and brain (26B). To obtain a good accuracy in quantitation through a wide range of concentrations we used weighted values ($1/x^2$) that resulted in lower r^2 scores without affecting the accuracy of low concentrations.

Table 11. Linearity and LLOQ of D6-Chol in plasma

Linearity and LLOQ (0.05 µg/mL) of D6-Chol in mouse plasma									
Mouse plasma	5 runs	Nominal concentration (µg/mL)							Calibration curve
		0.05	0.1	0.25	0.5	1.0	2.5	5.0	slope r ²
		Calculated concentration (µg/mL)							
	Mean	0.05	0.10	0.25	0.49	1.01	2.47	5.12	0.00014 0.9980
	± SD	0.00	0.00	0.01	0.02	0.06	0.09	0.54	0.00002 0.0031
	Accuracy (%)	101%	98%	100%	99%	101%	99%	102%	
	Precision (CV%)	2%	2%	3%	4%	6%	4%	10%	

Table 12. Linearity and LLOQ of D6-Chol in brain

Linearity and LLOQ (0.03 ng/mg) of D6-Chol in mouse brain									
Mouse brain	5 runs	Nominal concentration (ng/mg)						Calibration curve	
		0.03	0.1	0.3	1	3	10	slope	r ²
		Calculated concentration (ng/mg)							
	Mean	0.03	0.10	0.30	1.00	2.78	10.79	0.09286	0.9971
	± SD	0.00	0.00	0.02	0.05	0.16	0.66	0.01633	0.0020
	Accuracy (%)	100%	101%	99%	100%	93%	108%		
	Precision (CV%)	2%	5%	6%	5%	6%	6%		

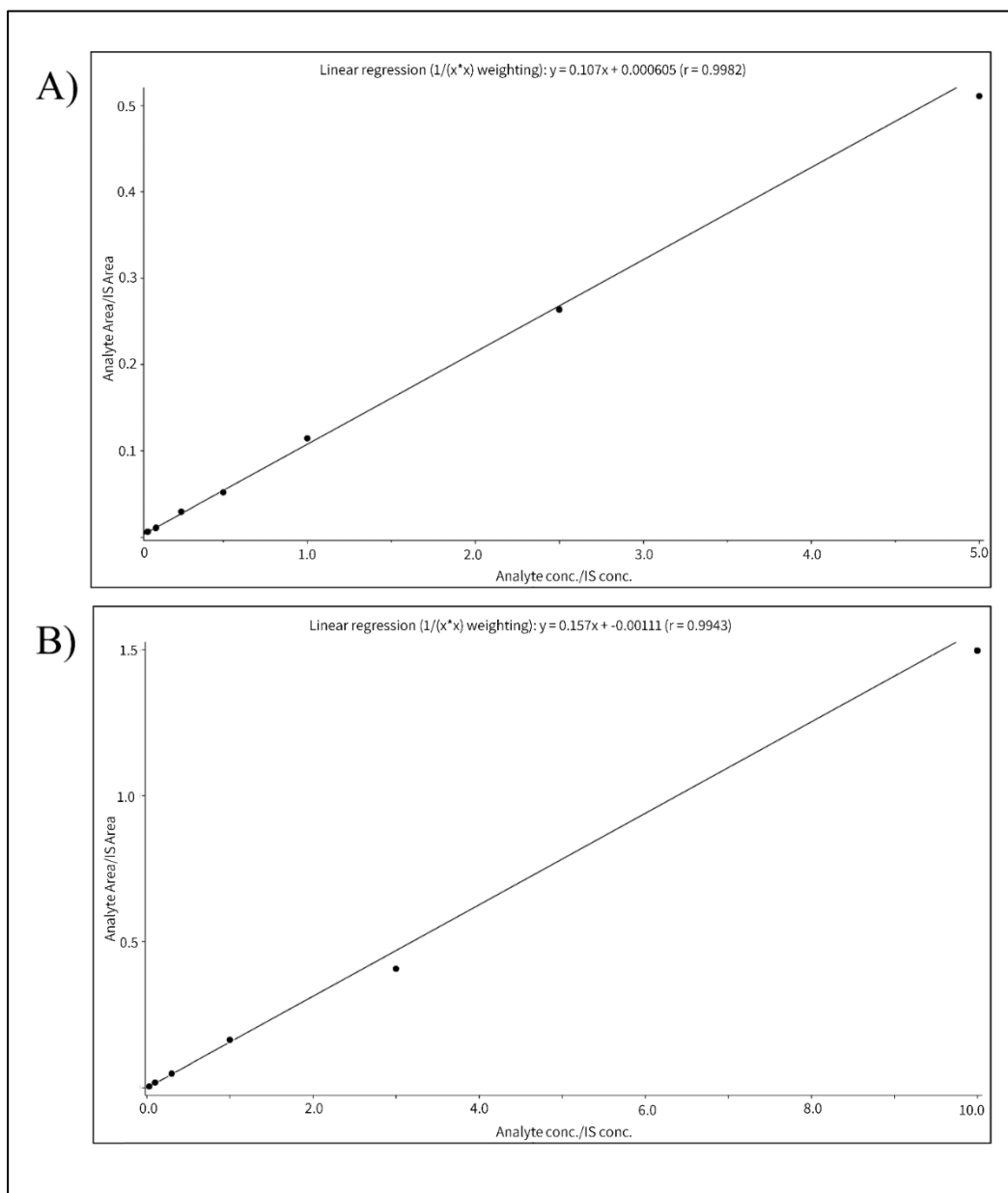


Figure 26A. Representative calibration curve in plasma, from 0.05 to 5 $\mu\text{g/mL}$ **26B.** Representative calibration curve in brain homogenate, from 0.03 ng/mg and 10 ng/mg

4.1.2. Carry-over

The carry-over phenomenon was investigated by examining the D6-Chol signal in blank plasma and brain samples after injection of the highest concentration. The residual signals were about 4% and 40% of the LLOQ signal in plasma and brain samples, respectively. After the injection of samples containing concentrations higher than 3 ng/mg for the brain, blank samples were injected to reduce interference (up to 10%).

4.1.3. Accuracy and precision

In mouse plasma, the mean intra-day accuracy ranged from 87 to 95%, with a mean precision of 5% (Table 13). Intra-day accuracy for brain homogenates ranged from 93% and 98%, with a slightly higher mean precision (7.5 %) (Table 14). The mean inter-day accuracy for plasma samples was similar to the mean intra-day accuracy (from 93% to 98%) with the same mean inter-day precision (Table 15). The mean inter-day accuracy and precision of brain homogenates were higher than intra-day values but within EMA guideline limits for all concentrations (Table 16).

Table 13. Intra-day accuracy and precision of D6-Chol in plasma

Intra-day accuracy and precision of D6-Chol in mouse plasma											
Nominal concentration ($\mu\text{g/mL}$)		Calculated concentration ($\mu\text{g/mL}$)						Mean ($\mu\text{g/mL}$) \pm SD		Accuracy (%)	Precision (CV%)
Mouse Plasma											
	0.05	0.046	0.048	0.049	0.048	0.051	0.050	0.049	0.002	97%	4%
	0.15	0.142	0.138	0.153	0.143	0.157	0.145	0.146	0.007	98%	5%
	1.00	0.897	0.897	0.886	0.772	0.920	0.857	0.872	0.053	87%	6%
	3.00	2.970	2.870	3.010	2.720	2.780	2.730	2.847	0.124	95%	4%

Table 14. Intra-day accuracy and precision of D6-Chol in mouse homogenates

Intra-day accuracy and precision of D6-Chol in mouse brain											
Nominal concentration (ng/mg)		Calculated concentration (ng/mg)						Mean (ng/mg) \pm SD		Accuracy (%)	Precision (CV%)
Mouse Brain											
	0.03	0.032	0.025	0.034	0.030	0.025	0.029	0.029	0.004	97%	12%
	0.20	0.182	0.202	0.178	0.214	0.161	0.183	0.187	0.019	93%	10%
	2.00	1.930	1.800	2.060	2.050	2.000	1.880	1.953	0.102	98%	5%
	6.00	5.780	5.670	6.140	6.000	5.820	5.700	5.852	0.183	98%	3%

Table 15. Inter-day accuracy and precision of D6-Chol in plasma

Inter-day accuracy and precision of D6-Chol in mouse plasma											
Nominal concentration (ng/mL)		Calculated concentration (µg/mL)						Mean (µg/mL)	± SD	Accuracy (%)	Precision (CV%)
		day 1		day 2		day 3					
Mouse Plasma	0.05	0.048	0.048	0.046	0.051	0.052	0.049	0.049	0.002	98%	4%
	0.15	0.157	0.145	0.141	0.138	0.149	0.152	0.147	0.007	98%	5%
	1.00	0.897	0.900	0.883	0.970	0.948	0.980	0.930	0.042	93%	4%
	3.00	3.010	2.720	2.480	2.700	2.860	2.930	2.783	0.191	93%	7%

Table 16. Inter-day accuracy and precision of D6-Chol in brain homogenates

Inter-day accuracy and precision of D6-Chol in mouse brain											
Nominal concentration (ng/mg)		Calculated concentration (ng/mg)						Mean (ng/mg)	± SD	Accuracy (%)	Precision (CV%)
		day 1		day 2		day 3					
Mouse Brain	0.03	0.032	0.032	0.030	0.030	0.024	0.037	0.031	0.004	102%	14%
	0.20	0.182	0.202	0.238	0.237	0.228	0.177	0.211	0.027	105%	13%
	2.00	1.930	1.800	1.980	2.440	1.730	1.920	1.967	0.250	98%	13%
	6.00	5.780	5.670	5.820	6.010	6.130	5.410	5.803	0.254	97%	4%

4.1.4. Recovery

The analyte recovery of the extraction procedure was evaluated for D6-Chol in six independent plasma samples and brain homogenates at LQC and HQC concentrations. In plasma, recoveries of D6-Chol were 98% and 95% for LQC and HQC samples, respectively. In brain homogenates, the recoveries were slightly lower (57% and 43% for LQC and HQC samples) because of the more complicated extraction procedure and the higher matrix effect (Table 17).

Table 17. Recovery of D6-Chol in plasma and brain matrices

Recovery of D6-Chol in plasma and brain matrices							
Recovery (%)							
Nominal conc. (µg/mL)	D6-Chol in plasma			Nominal conc. (ng/mg)	D6-Chol in brain		
	Mean	SD	CV (%)		Mean	SD	CV (%)
LQC (0.15 µg/mL)	98%	4%	4%	LQC (0.2 ng/mg)	57%	8%	14%
HQC (3 µg/mL)	95%	3%	4%	HQC (6 ng/mg)	43%	6%	13%

4.1.5. Stability

We examined D6-Chol stability in plasma and brain homogenates under three conditions, to simulate the working conditions of the analytical sessions. We evaluated the bench-top stability, long-term storage stability, and stability after freeze-thaw cycles. These studies were done on the mouse plasma QC samples at LQC (0.05 µg/mL) and HQC (3 µg/mL) in six replicates; QC sample concentrations were obtained against a freshly prepared calibration curve. All the results indicated D6-Chol stability in plasma and brain homogenates in the conditions used (Tables 18 and 19).

Table 18. Stability of D6-Chol in plasma in different analytical conditions: benchtop stability, long-term storage and freeze and thaw stability

Stability of cholesterol-D6 in mouse plasma										
Stability test conditions	LQC - 0.150 µg/mL					HQC - 3 µg/mL				
	Mean (ng/mL)	± SD	Mean Accuracy (%)	Deviation (%)	CV (%)	Mean (ng/mL)	± SD	Mean Accuracy (%)	Deviation (%)	CV (%)
Freshly prepared	0.146	0.007	98%		5%	2.847	0.124	95%		4%
Benchtop (2h RT)	0.146	0.008	97%	-0.6%	6%	3.037	0.249	101%	6.7%	8%
2 weeks (-20° C)	0.144	0.007	96%	-1.9%	5%	2.762	0.119	92%	-3.0%	4%
Freeze-thaw 1st cycle	0.147	0.008	98%	0.1%	5%	2.860	0.078	95%	0.5%	3%

Table 19. Stability of D6-Chol in brain homogenate in different analytical conditions: benchtop stability, long-term storage and freeze and thaw stability

Stability of D6-Chol in mouse brain										
Stability test conditions	LQC - 0.2 ng/mg					HQC - 6 ng/mg				
	Mean (ng/mg)	± SD	Mean Accuracy (%)	Deviation (%)	CV (%)	Mean (ng/mg)	± SD	Mean Accuracy (%)	Deviation (%)	CV (%)
Freshly prepared	0.190	0.026	95%		14%	5.788	0.414	96%		7%
Bench top (2h RT)	0.220	0.011	110%	15.8%	5%	6.550	0.226	109%	13.2%	3%
2 weeks (-20° C)	0.187	0.019	93%	-1.8%	10%	5.852	0.183	98%	1.1%	3%
Freeze-thaw 1st cycle	0.223	0.026	111%	17.1%	12%	5.983	0.491	100%	3.4%	8%

4.2. I trial: Single Treatment of 8-week-old WT mice¹

To evaluate the efficacy of intranasal delivery of Chol, we initially performed an acute treatment in 8-week-old WT mice with D6-Chol-loaded liposomes (200 µg/mouse). Animals were sacrificed after 1, 3, 6, 24, 48 and 72 hours (3 animals/time-point), and D6-Chol concentrations were measured in plasma and in three brain areas using the in-house developed and validated method (Figure 27 and Table 20).

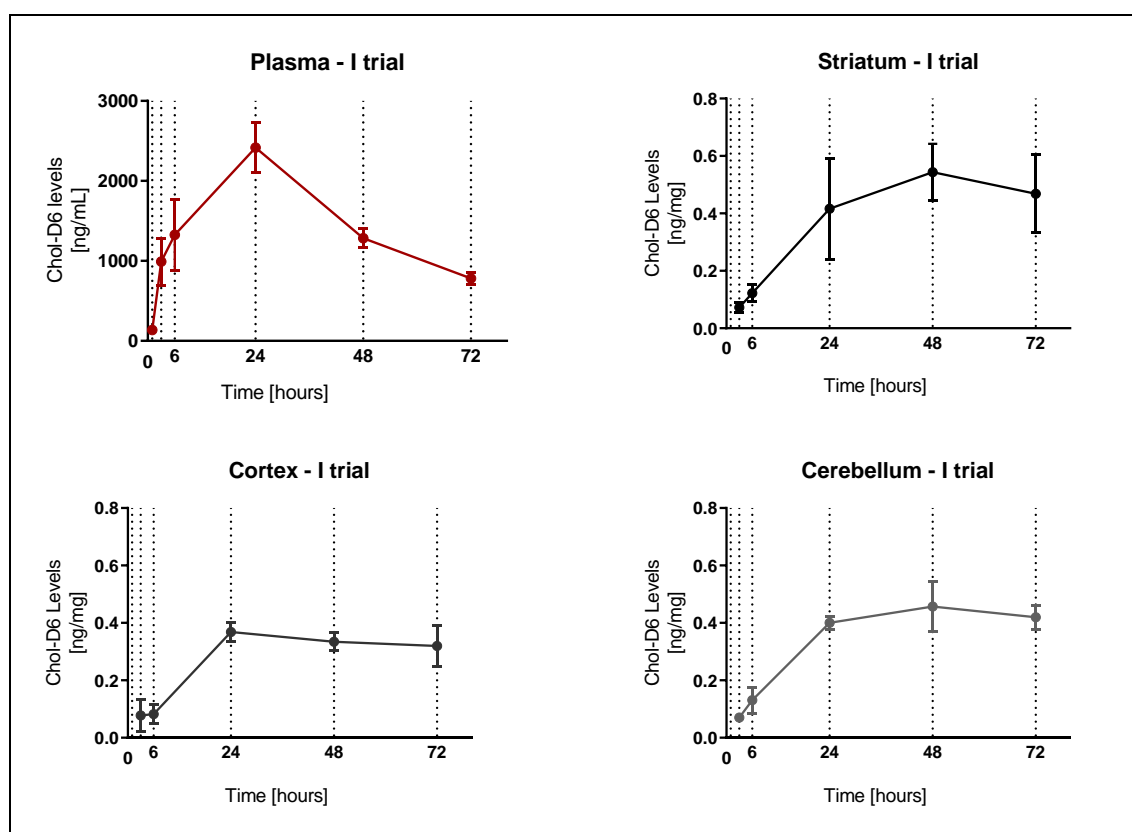


Figure 27. D6-Chol levels in plasma, striatum, cortex, and cerebellum of WT mice following single intranasal treatment (connecting lines with error bars, average \pm SD; N=3/time point)

¹ Protein Chemistry and Biochemistry Laboratory performed the animal treatments and sacrifices. (Dr. Laura Colombo, Dr. Monica Favagrossa – Lab. Head: Dr. Mario Salmons)

Plasma concentrations reached a maximum level of 2417 ng/mL (mean \pm 313 ng/mL SD, N=3), 24 hours after administration, declining thereafter to 839 ng/mL (mean \pm 76 ng/mL SD, N=3) after 72 hours. In the brain areas, D6-Chol levels increased in the first 24 hours but, differently from plasma, no decline was observed, remaining stable until 72 hours. These data, therefore, suggested a slow elimination rate from all the brain areas.

Table 20. D6-Chol levels in plasma, striatum, cortex, and cerebellum of WT mice following single intranasal treatment expressed as average (\pm SD); (ND: not detectable; N=3/time point)

I trial - D6-Chol levels					
Time (hours)	Plasma (ng/mL)	Striatum (ng/mg)	Cortex (ng/mg)	Cerebellum (ng/mg)	
1	137.3 (\pm 23.09)	ND	ND	ND	
3	990.3 (\pm 295.6)	0.0727 (\pm 0.0176)	0.0780 (\pm 0.0560)	0.0707 (\pm 0.0072)	
6	1326 (\pm 444.7)	0.1227 (\pm 0.0290)	0.0827 (\pm 0.0344)	0.1312 (\pm 0.0458)	
24	2417 (\pm 313.4)	0.4163 (\pm 0.1761)	0.368 (\pm 0.0344)	0.4000 (\pm 0.0220)	
48	1283 (\pm 120.6)	0.5437 (\pm 0.0984)	0.3347 (\pm 0.0323)	0.4567 (\pm 0.0883)	
72	781.0 (\pm 76.10)	0.4683 (\pm 0.1363)	0.3197 (\pm 0.0700)	0.4200 (\pm 0.0426)	

4.3. II trial: Single Treatment of 8-week-old WT and R6/2 mice²

In a second trial, we investigated the differences between WT and R6/2 mice after a single treatment with D6-Chol. The obtained results indicated the absence of differences in the two animal models: in each analysed tissue D6-Chol had the same time-course profile in both experimental groups without significant differences in calculated concentrations (Fig. 28 and Table 21).

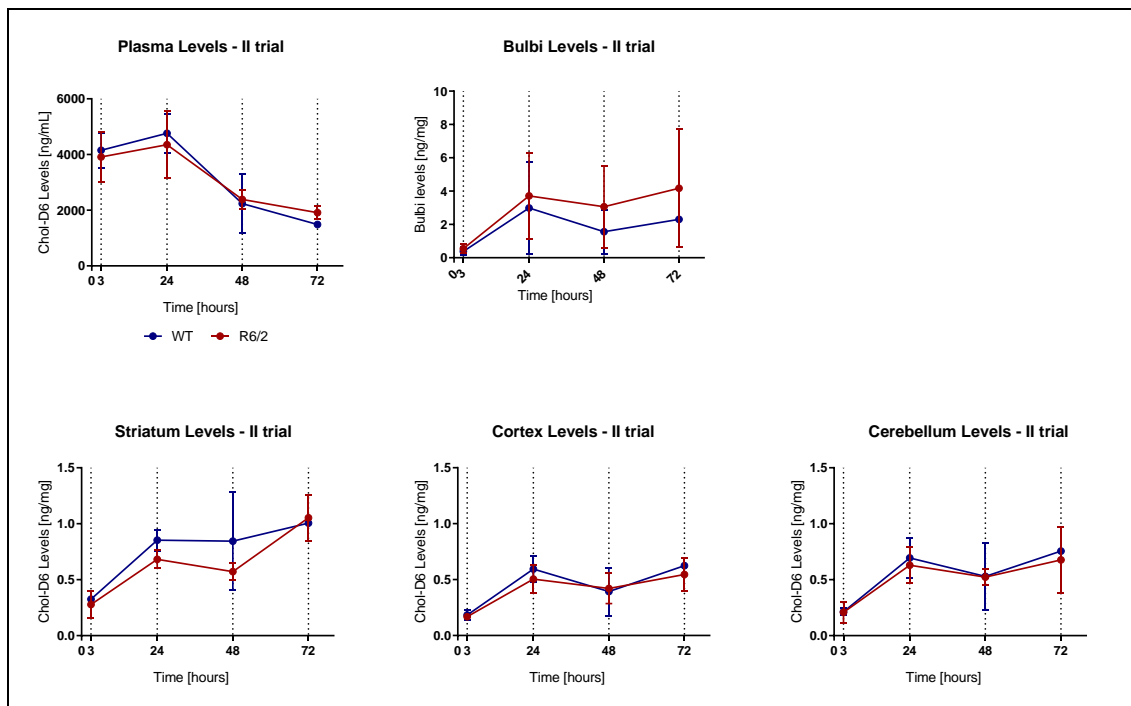


Figure 28 II trial. Calculated concentrations of D6-Chol in plasma samples (A), bulbs (B), striatum (C), cortex (D,) and cerebellum (E) in WT and R6/2 mice (connecting lines with error bars, average \pm SD; N=3/time point)

² Protein Chemistry and Biochemistry Laboratory performed the animal treatments and sacrifices. (Dr. Laura Colombo, Dr. Monica Favagrossa – Lab. Head: Dr. Mario Salmons)

Table 21. *II trial. Calculated concentrations of D6-Chol in plasma samples, bulbs, striatum, cortex, and cerebellum in WT and R6/2 mice expressed as average (\pm SD);*

Time-point hours	II Trial - D6-Chol Levels									
	Plasma (ng/mL)		Bulbs (ng/mg)		Striatum (ng/mg)		Cortex (ng/mg)		Cerebellum (ng/mg)	
	WT	R6/2	WT	R6/2	WT	R6/2	WT	R6/2	WT	R6/2
3	4150 (\pm 635.0)	3910 (\pm 914.8)	0.3760 (\pm 0.2408)	0.5423 (\pm 0.2892)	0.3252 (\pm 0.0105)	0.2785 (\pm 0.1185)	0.1828 (\pm 0.0437)	0.1680 (\pm 0.0161)	0.2135 (\pm 0.0303)	0.2080 (\pm 0.0910)
24	4760 (\pm 703.5)	4350 (\pm 1206)	2.984 (\pm 2.769)	3.7100 (\pm 2.604)	0.8526 (\pm 0.0949)	0.6824 (\pm 0.0805)	0.5944 (\pm 0.1177)	0.5040 (\pm 0.1236)	0.6942 (\pm 0.1790)	0.6294 (\pm 0.1596)
48	2236 (\pm 1053)	2386 (\pm 345.0)	1.560 (\pm 1.315)	3.066 (\pm 2.473)	0.8446 (\pm 0.4397)	0.5718 (\pm 0.0744)	0.3928 (\pm 0.2159)	0.4202 (\pm 0.1354)	0.5296 (\pm 0.2969)	0.5226 (\pm 0.0726)
72	1485	1912 (\pm 247.1)	2.305	4.171 (\pm 3.550)	1.006	1.0526 (\pm 0.2043)	0.624	0.5462 (\pm 0.1502)	0.756	0.6774 (\pm 0.2923)

Moreover, no differences were observed in the selected brain areas of the two mice genotypes. Statistical analysis did not show significant differences in D6-Chol levels between the analyzed brain areas, confirming a homogeneous distribution of D6-Chol in the whole brain and suggesting the use of both olfactory and trigeminal pathways. The connection between the nasal cavity and the CNS through olfactory and trigeminal neurons had already been shown in the literature ¹¹⁶⁸⁶¹¹⁷. In particular, from the nasal olfactory epithelium, drugs are taken up into neuronal cells and transported to the olfactory bulb and the cerebrospinal fluid through the olfactory nerve pathways. The trigeminal nerve innervates both olfactory and respiratory epithelium and enters the CNS in the pons, leading to the distribution of drugs in the rostral brain ¹¹⁸. Together these two pathways allow the distribution of drugs to all brain areas. These preliminary observations definitely confirmed the efficacy of nose-to-brain Chol delivery as a possible strategy to increase Chol availability in the brain using a non-invasive approach.

4.4. III Trial: Repeated Treatments in WT and R6/2 mice³

³ Protein Chemistry and Biochemistry Laboratory performed the animal treatments and sacrifices. (Dr. Laura Colombo, Dr. Monica Favagrossa – Lab. Head: Dr. Mario Salmons)

To evaluate the accumulation of D6-Chol in the brain after multiple IN administrations, we performed repeated treatments of WT and R6/2 mice with D6-Chol-loaded liposomes (200 µg/dose). Both WT and R6/2 mice were treated every two days for 19 days. Two days after the ninth administration, 4 animals/experimental group were sacrificed before the tenth treatment (pre-IN level of D6-Chol). The remaining mice received the tenth IN and were sacrificed at 24 and 48 hours after the treatment (time-points 24h and 48h).

Figure 29 reports the levels of D6-Chol determined in the striatum, cortex, and cerebellum. After repeated treatments, the levels of D6-Chol were remarkably higher than those measured after a single dose, highlighting the accumulation in the brain. D6-Chol levels were at least 1.5 ng/mg tissue in all the brain areas. No differences were observed between the selected brain areas of the two mice genotypes, with the only exception of the levels in the striatum of R6/2 transgenic mice 48h after the last administration. Interestingly, the levels of D6-Chol in cortex and cerebellum after 10 repeated doses were comparable between WT and R6/2 mice while in the striatum the level of D6-Chol after 10 repeated doses were 3 and 1.5 ng/mg in WT and R6/2 mice, respectively. This evidence suggested that R6/2 mice used administered Chol to restore the altered metabolic state in the striatum tissue that is the most affected tissue by the neurodegeneration in HD. Statistical analysis did not show significant differences in D6-Chol levels between different brain areas, confirming an homogeneous distribution of D6-Chol in the whole brain, as previously discussed for acute treatments.

Taken together our observations confirmed the efficacy of nose-to-brain Chol delivery as a possible strategy to increase Chol availability in the HD brain using a non-invasive approach.

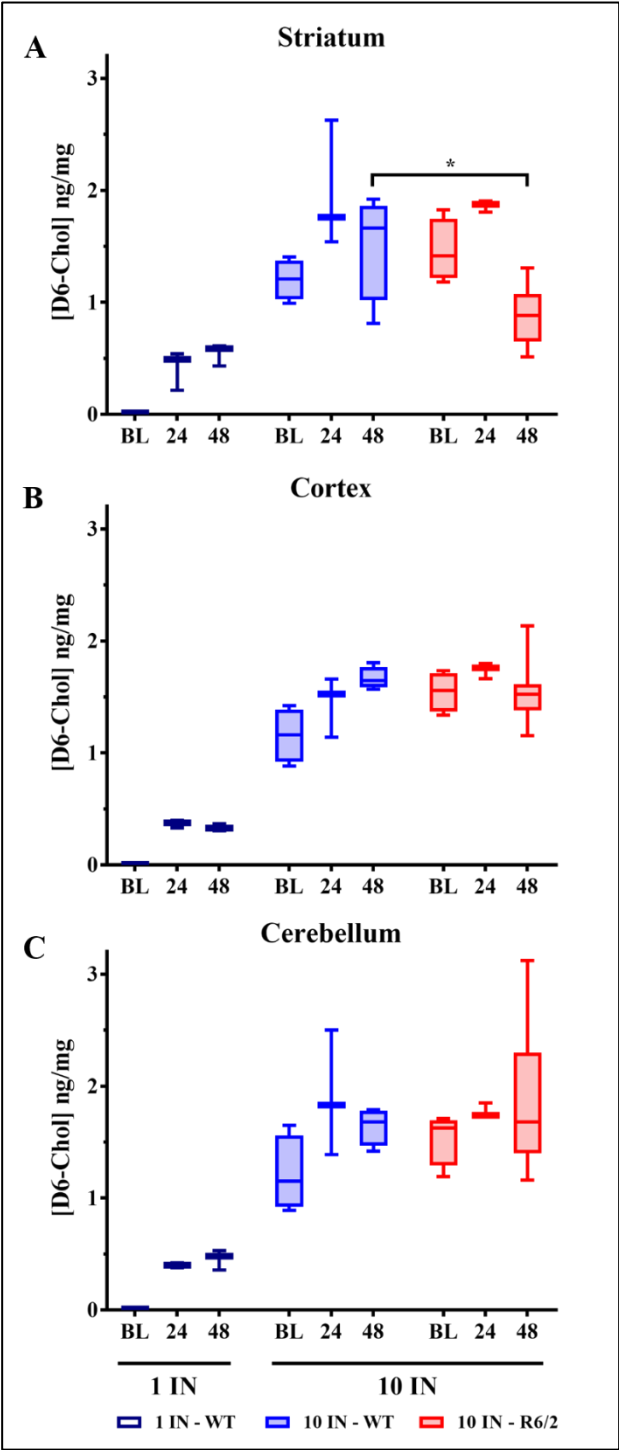


Figure 29. D6-Chol levels in striatum, cortex and cerebellum of WT and R6/2 mice following intranasal acute or sub-chronic treatments. BL: D6-Chol basal level

4.5. IV Trial: evaluation of D6-Chol levels 42 days after a single dose⁴

In the last trial, we investigated the long term distribution and accumulation of D6-Chol after a single intranasal administration (200 µg) in WT (n=4) and R6/2 mice (n=4), measuring D6-Chol levels in cerebral and peripheral tissues 42 days after treatment. The aim was to study the fate of administered D6-Chol and its accumulation in brain areas for long time after a single dose treatment. Figure 30 resumes the results obtained in IV trial, highlighting how the levels of exogenous D6-Chol were lower in R6/2 mice in all analysed tissues, both cerebral and peripheral ones. Interestingly, the levels of D6-Chol were significantly lower in the striatum tissue from R6/2 mice, suggesting the use of Chol in the mouse model of the disease to restore the altered Chol metabolism. The differences in striatum levels between WT and R6/2 mice confirmed the results obtained from the repeated dose trial. The statistical significance of the levels of D6-Chol found in the striatum tissue is consistent with the involvement of this tissue in HD, which is the most affected by HD. All in all, the results from the whole brain, striatum, cortex and cerebellum suggested that R6/2 mice use D6-Chol to restore the Chol metabolism and this is more statistically evident in the striatum area.

⁴ Protein Chemistry and Biochemistry Laboratory performed the animal treatments and sacrifices. (Dr. Laura Colombo, Dr. Monica Favagrossa – Lab. Head: Dr. Mario Salmons)

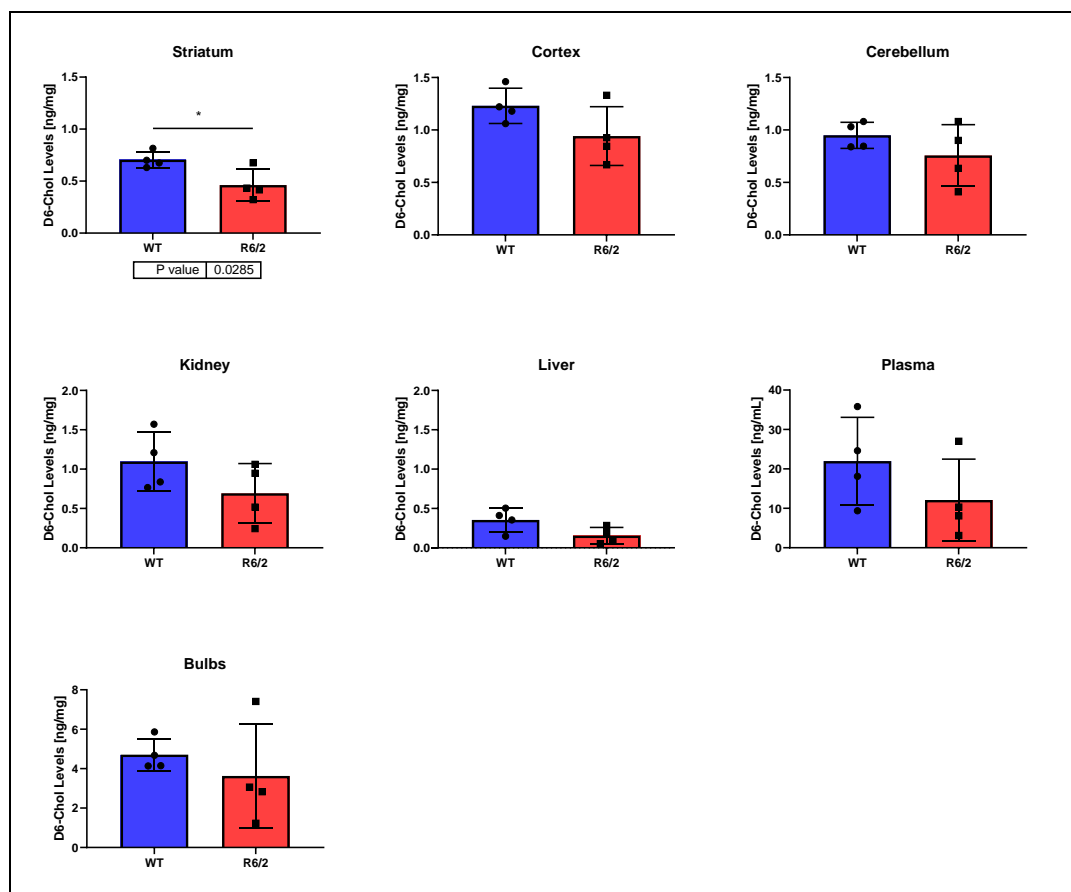


Figure 30. D6-Chol levels in striatum, cortex, cerebellum, kidney, liver, plasma and bulbs of WT and R6/2 mice 42 days after a single treatment ($N=4$ /experimental group). Statistical analysis: one-way ANOVA

Table 22. D6-Chol levels in striatum, cortex, cerebellum, kidney, liver, plasma and bulbs of WT and R6/2 mice 42 days after a single treatment ($N=4$ /experimental group).

IV trial - D6-Chol Levels (42 days after treatment)		
	WT	R6/2
Striatum (ng/mg)	0.7050 (± 0.0787)	0.4615 (± 0.1505)
Cortex (ng/mg)	1.230 (± 0.168)	0.9422 (± 0.2801)
Cerebellum (ng/mg)	0.9488 (± 0.1244)	0.7565 (± 0.2943)
Kidney (ng/mg)	1.096 (± 0.371)	0.6922 (± 0.3792)
Liver (ng/mg)	0.3545 (± 0.1507)	0.1544 (± 1.049)
Plasma (ng/mL)	21.97 (± 11.12)	12.12 (± 10.37)
Bulbs (ng/mg)	4.707 (± 0.808)	3.632 (± 2.646)

The results obtained in bulbs (the site of administration of intranasal treatment) showed higher variability in R6/2 mice with respect to WT mice, suggesting that both WT and R6/2 mice stored D6-Chol in bulbs, but R6/2 mice were using the stored D6-Chol in bulbs to increase the levels in the cerebral areas.

All the results obtained from the explorative trials confirmed the efficacy of intranasal nose-to-brain delivery of Chol. Moreover, the administration through liposomes, completely made of Chol-D6 ensured that all the Chol measured using our developed LC-MS method is effectively bioavailable to use. The experiment with a single dose treatment showed the accumulation of D6-Chol in cerebral areas until 72 hours, and the experiment with repeated dose treatments confirmed the effective accumulation of D6-Chol in all brain areas. Finally, the results obtained 42 days after a single dose treatment showed lower D6-Chol levels in R6/2 mice, suggesting a possible use of administered Chol to restore the altered Chol metabolism in R6/2 mice. Starting from these results, we decided to investigate more deeply the altered metabolic state of Chol by developing and validating a UHPLC-MRM method for the study of Chol metabolism in WT and R6/2 mice.

4.6. Cholesterol metabolites analysis

4.6.1 Method optimization

The mass spectrometric method was optimized through the direct infusions of each analytical standard to identify the best MRM transitions to be used. The optimization process took into account the sensitivity and matrix effect due to both plasma and brain matrices. During the method development, a full scan acquisition was performed to identify the most intense precursor ion for each Chol metabolite and to set up the best source conditions to increase the ionization efficiency for each analyte. Once the precursor ion was defined, we identified at least four fragments for each analyte, through a Product Ion Scan experiment. Finally, a ramp of collision energies (CE) was carried out for each product ion and the CE corresponding to the highest peak intensity was selected.

After the analysis of some brain and plasma samples, we defined two MRM transitions that gave the best signal-to-noise ratio and were the least affected by the matrix, in terms of ion enhancement or suppression. The maintenance of the ratio between the selected transitions was used as an internal control of the robustness of the analysis.

4.6.2. MRM transitions

As expected all target analytes, including IS, ionized with a loss of water in the source. In particular, $[M+H-2H_2O]^+$ ions, corresponding to the loss of 36 Da, have been selected as the precursor ion for oxysterols, while for 27OHC and Chol precursors $[M+H-H_2O]^+$ ions, corresponding to the loss of 18 Da, have been selected. In Fig. 31 and 32 are reported the chemical structures of selected metabolites for targeted study.

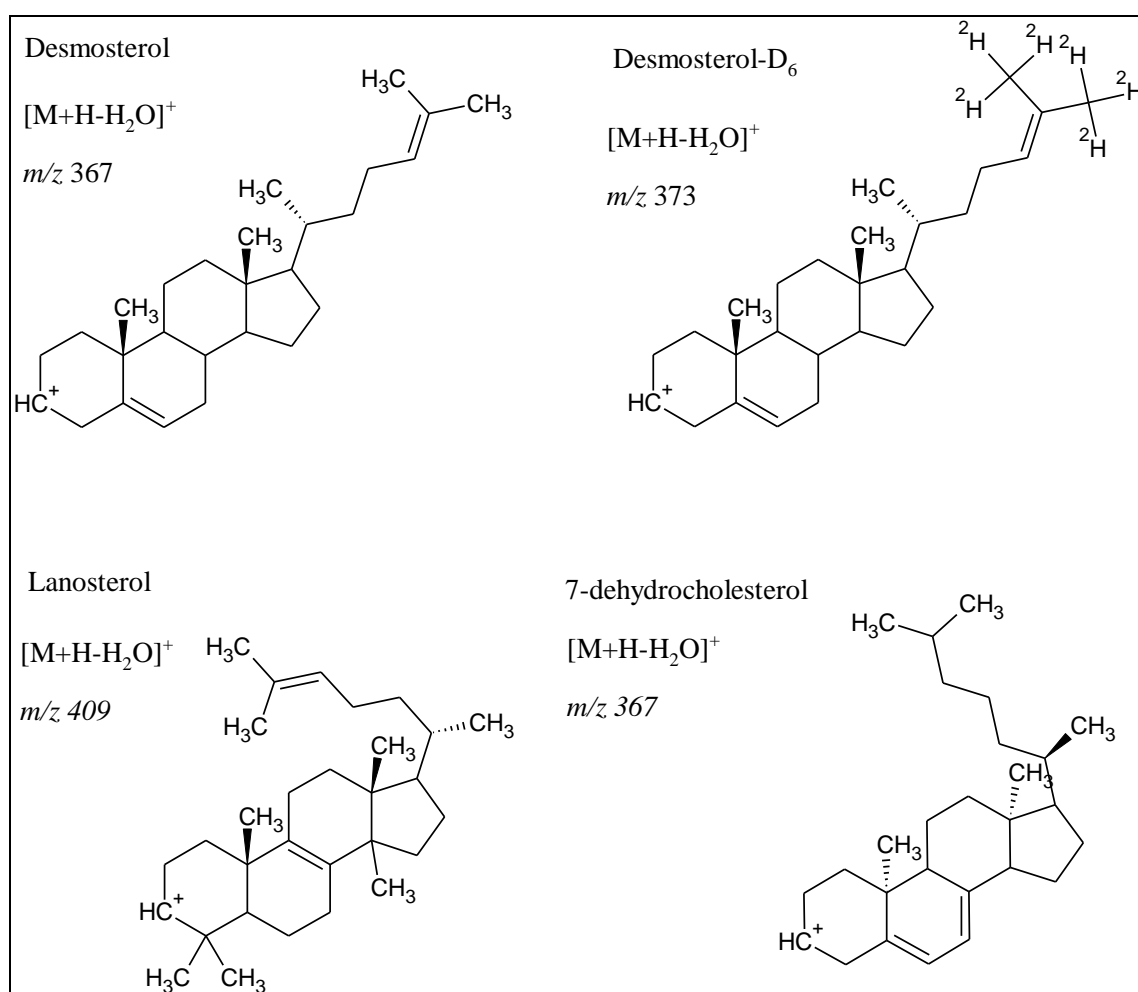


Figure 31. Parent ions selected for Chol precursors analysis

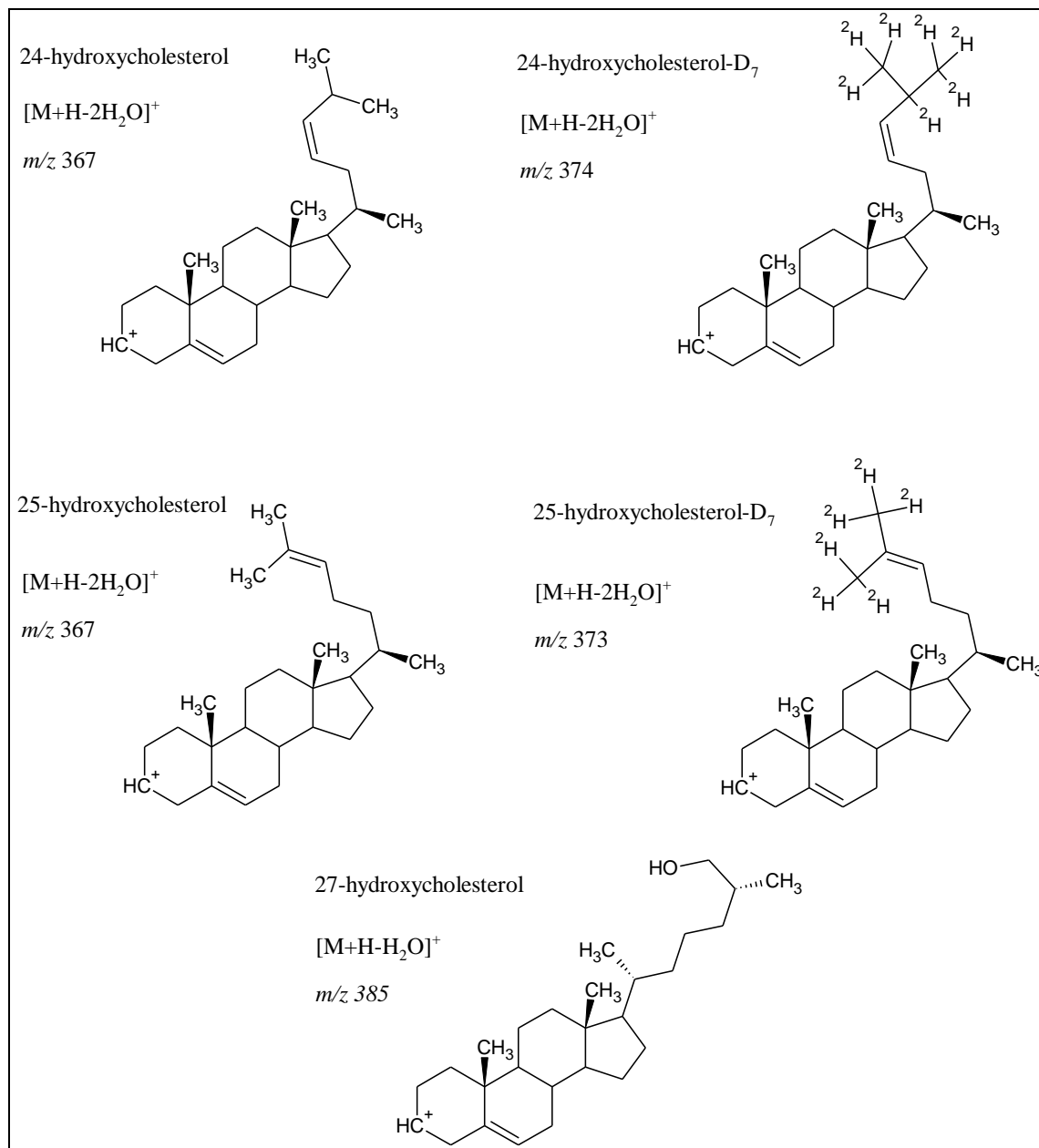


Figure 32. Parent ions selected for oxysterols analysis

The study of the fragmentation pattern of this class of molecules represents a challenging interpretation of the results, since almost all the metabolites show the same characteristic fragments. The transitions selected for the MRM method originate from several breaks and rearrangements involving the tetracyclic steroidal nucleus. The fragments were not specific for each metabolite and often the MRM transitions were the same among the target analytes. The specificity of the proposed strategy must be guaranteed by the setup of an accurate chromatographic separation and the internal control on the peak area ratio between quantifier and qualifier for each metabolite. The product ions obtained from the fragmentation of the internal standard precursor ions were the same as the native metabolite, confirming our initial hypothesis of fragmentation, since the deuterated atoms were on the aliphatic part of the molecule.

24SOHC, 25OHC and Desm, losing water in the source, resulted in a precursor ion with the same m/z . The fragment pattern did not show specific fragments to discriminate them. While the discrimination between oxysterols and desmo is easy, due to the different nature and polarity of the molecules, the separation of 24SOHC and 25OHC is the most critical point of the development of the proposed method. 24SOHC and 25OHC presented the same precursor ion and common fragments, the chromatographic separation is challenging because of the very similar polarity but it is essential since they have a different metabolic origin. 24SOHC is mainly synthesized in the brain while 25OHC derives from hepatic metabolism.

Table 23. Optimized MRM transitions (quantifier and qualifier) and relative CE (V)

Analyte	Quantifier	CE	Qualifier	CE
24SOHC	367.3 → 95.1	28	363.3 → 133.1	25
24SOHC-D ₇	374.1 → 159.1	25	374.1 → 147.1	23
25OHC	367.1 → 95.1	28	367.1 → 133.1	25
25OHC-D ₆	373.2 → 147.1	24	373.2 → 159.1	23
27OHC	385.2 → 95.1	34	385.2 → 109.1	30
Desm	367.2 → 147.1	25	367.2 → 95.1	31
Desm-D ₆	373.2 → 147.1	24	373.2 → 161.1	23
Lan	409.2 → 107.1	35	409.2 → 109.2	30
7-dehydrochol	369.2 → 185.1	35	369.2 → 219.1	16

In Fig. 33 are reported the spectra relative to different fragmentation experiments obtained from the analysis of the standard mix of all target analytes. As mentioned above, the fragmentation pattern was not specific for the analytes and resulted in similar MS/MS spectra for all target analytes. The use of a low-resolution instrument did not allow speculation about the possible chemical structures of fragments and rearrangements during the fragmentation.

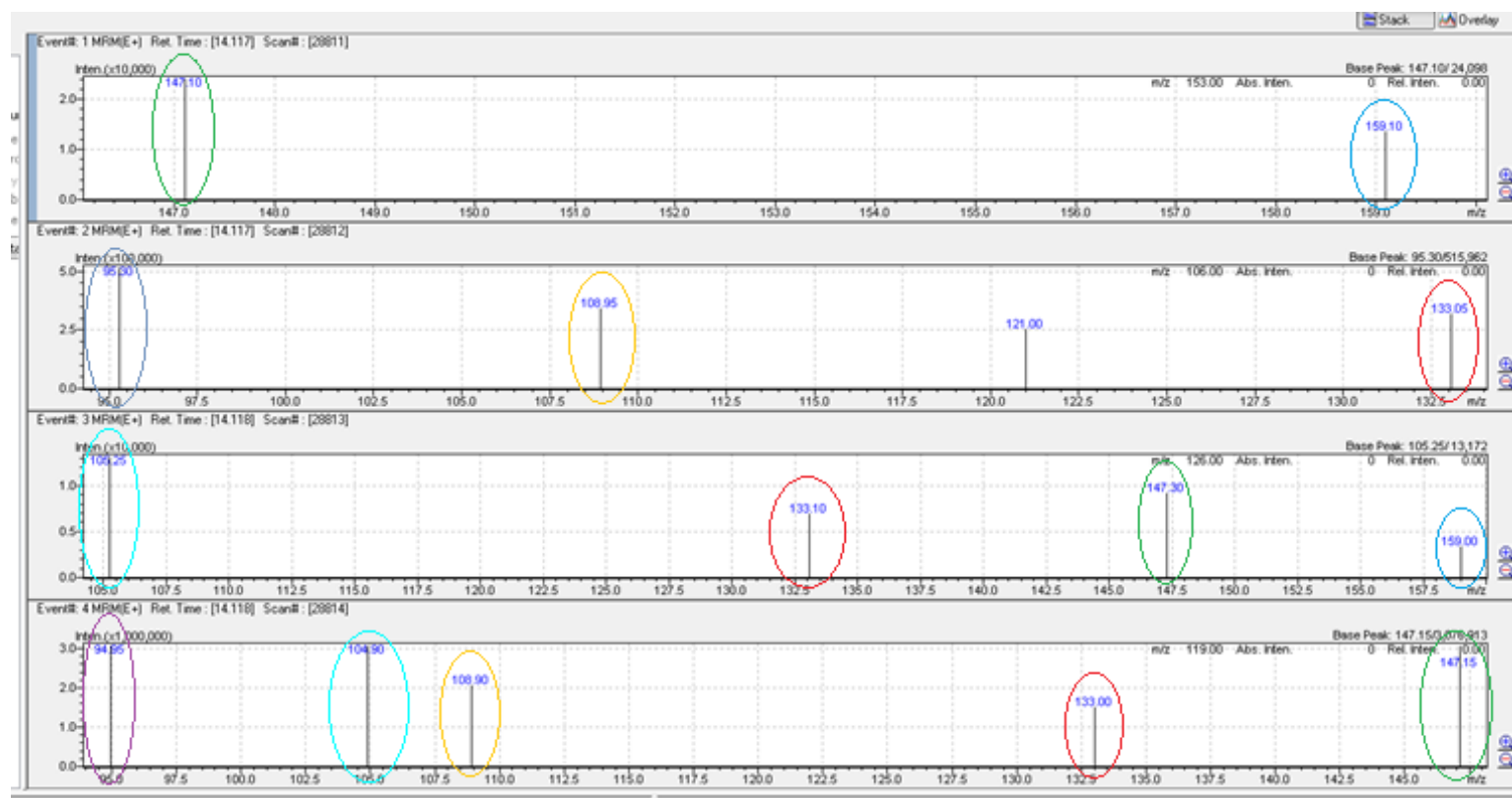


Figure 33. MS/MS experiments using product ion scan in the analysis of standard mix solution (10 ng/ μ L; 5 μ L injected)

4.6.3 Chromatographic separation optimization

Since the mass spectrometric optimization highlighted that many target analytes had the same m/z for both precursor and product ions, we decided to improve the chromatographic separation obtained in a previously published method from our laboratory.

The previous method guaranteed, in 38 minutes, the separation of all oxysterols using a linear gradient on a C18 column at a controlled temperature of 37 °C. The biggest issue with measuring oxysterols is the presence of multiple isomers that differ only by the placement of the hydroxyl group but have the same isotopic mass and fragmentation. For the proper measurement of single oxysterols, effective chromatographic separation is required, which requires special care because all isomers of position have identical polarity and hence the interactions with the phase Stationary are comparable among them.

To efficiently separate compounds with extremely similar polarities, a very slow eluent gradient is required to restrict the co-elution of the isomers. The above mentioned approach was developed using an Ascentis Express C18 column (150x2.1 mm, 2.7 μ m) at 37°C with a gradient of water and methanol, both added with ammonium acetate at 5 mM ¹¹⁹. Table 24 resumes the chromatographic gradient for oxysterols separation.

Table 24. *Chromatographic gradient for oxysterols separation (Villani et al.)*

Time	Mobile Phase B (%)
0 minutes	80%
20 minutes	88%
28 minutes	100%
38 minutes	100%
39 minutes	80%

The Chol precursors are much less polar than the oxysterols and present a higher affinity to the stationary phase of the column. For this reason, under the same chromatographic conditions, they would elute with much longer times than the oxysterols. To detect both Chol metabolites and precursors in a single chromatographic run, it is essential to set up a gradient that guarantees both the oxysterols separation and Chol precursor elution using a

high level of organic solvent. For this reason, the new developed chromatographic method consists of a segmented gradient, slower in the first phase to efficiently separate the oxysterols, and quicker in the second phase to elute the Chol precursors in a reasonable amount of time. A temperature ramp has been added to the chromatographic gradient to help the elution of Chol precursors in the second phase of the analysis. Tab. 25 shows the column's elution gradient and oven temperature ramp.

Table 25. Final chromatographic method for the separation of oxysterols and Chol precursors

Time	Mobile Phase B (HCOOH 0,1% in MeOH)
0 minutes	84%
11 minutes	86%
20 minutes	98%
42 minutes	98%
43 minutes	84%
Time	Oven Temperature (°C)
0 minutes	40°C
12.5 minutes	40°C
20 minutes	65°C
38 minutes	65°C
39 minutes	40°C

In the first 15 minutes all the oxysterols are eluted and separated, in the second phase of the chromatographic run, in which the eluent is almost totally formed by the organic fraction, the precursors are eluted. Fig. 34 shows the complete chromatogram obtained from a fortified plasma sample, while Fig. 35 shows the magnification of the first part of the chromatogram where the peaks of the different oxysterols are clearly visible.

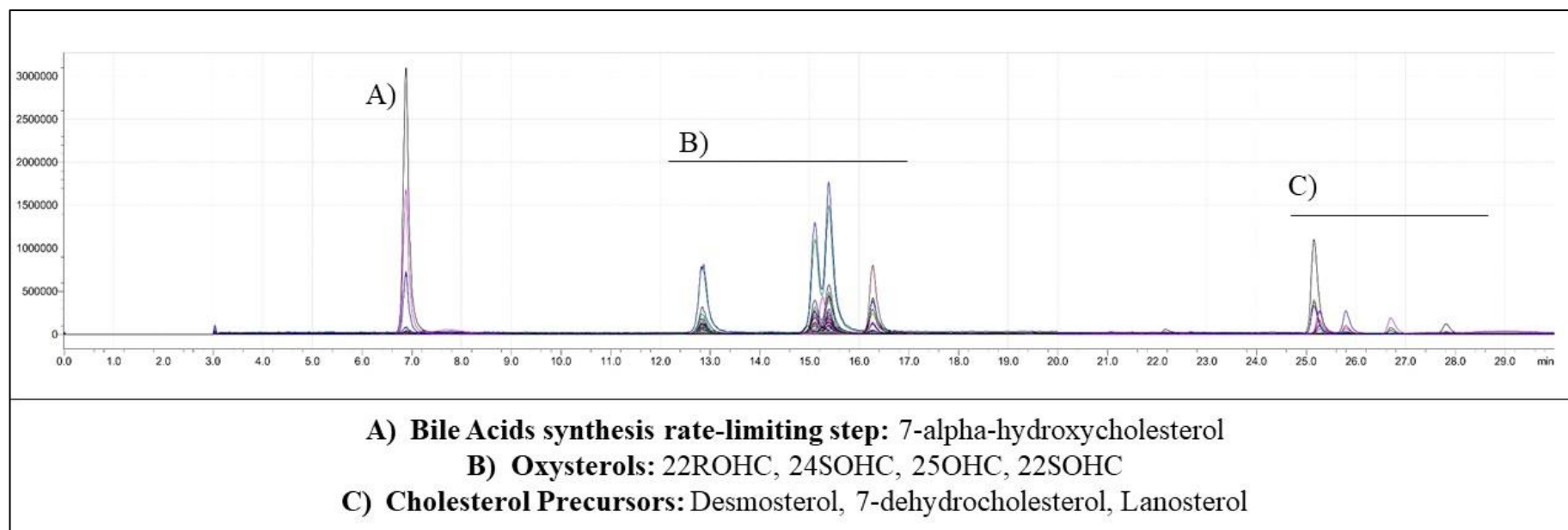


Figure 34. Complete LC-MRM chromatogram obtained from the analysis of a standard mix

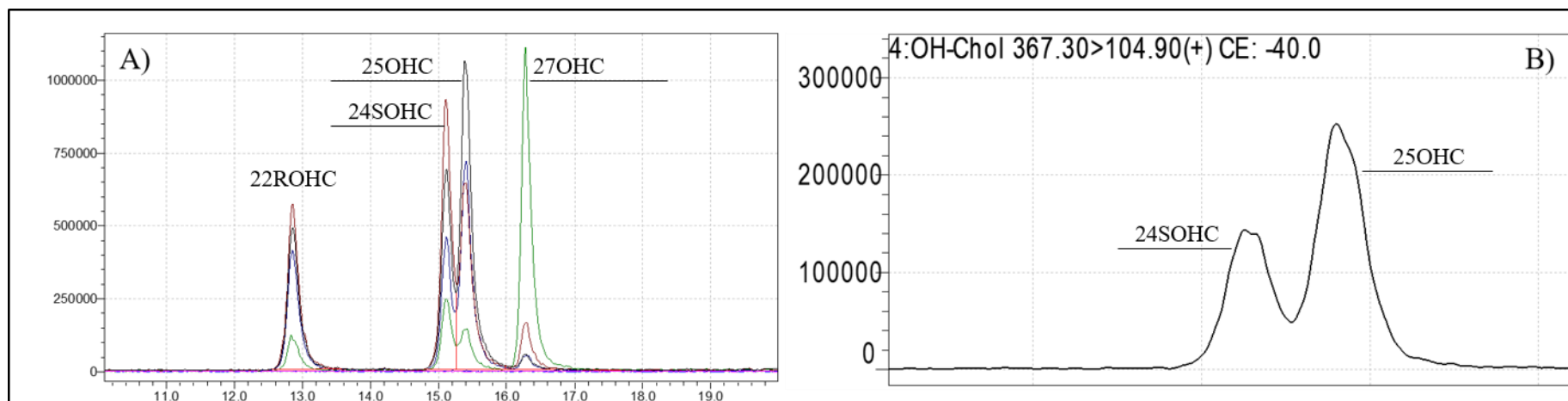


Figure 35. Challenging separation of 24SOHC and 25OHC: LC-MRM chromatogram obtained from the analysis of a standard mix

4.7. Optimization of sample preparation

Two different procedures involving the use of ethanol as a solvent for deproteinization were tested. The first approach involved combining a volume of ethanol (containing 100 µg mL⁻¹ BHT) equal to four times the amount of plasma, followed by mixing the two components and centrifugation for 15 minutes at 4 °C for protein deposition. However, a bibliographical search yielded a process known as slow protein precipitation, which allowed for a higher signal-to-noise ratio. This procedure, published in a research by Karuna et al., consists of a deproteinization of 200 µL of plasma, to which BHT has been added, with a total of 1.8 mL of ethanol, added in four 200 µL and two 400 µL aliquots. After each step, samples were stored for 15 minutes at 4 °C leading to a slow process of deproteinization. This process led to a better signal to noise ratio, thanks to the lower matrix effect. The final result was an increased sensitivity of the instrumental method that was essential for the analysis of underivatized oxysterols in plasma matrix.

4.8. Hydrolysis reaction set up

4.8.1 KOH concentration and temperature of the reaction

After a literature review (see “State of the art of hydrolysis methods” chapter) we found that the conditions for basic hydrolysis varied in terms of base concentration, temperature and incubation time of the reaction. To optimize the hydrolysis reaction, which is necessary for the measurement of the analytes in their total form (ester bound plus free), we tested different conditions, using plasma and spiked plasma samples starting from the more common conditions found in the literature.

Initially, two different concentrations of KOH (10M and 1M) were tested, combined with three different temperatures (100 °C, 50° C and 37° C). The concentrations chosen are the most common in the literature and one was used in the method previously set up in our Institute ¹¹⁹. Tab. 26 summarizes the hydrolysis conditions tested. For each experimental group a biological triplicate was analyzed.

Table 26. *Hydrolysis conditions tested for method setup*

Experimental group	KOH Concentration (M)	Temperature (°C)
1	10 M	100 °C
2	10 M	50 °C
3	10 M	37°C
4	1 M	100°C
5	1 M	50°C
6	1 M	37°C

Analysis of samples hydrolysed with KOH 10M showed low signals corresponding to oxysterols. In the case of samples incubated with KOH 1M, however, the signals were well quantifiable and the quantification showed no significant differences at different temperatures (One-way ANOVA test). This result highlighted how a higher concentration of KOH led to degradation or to a significant ion suppression, resulting in an insufficient sensitivity for oxysterols detection. Figure 36 and Table 27 showed the results obtained with the use of different concentration of KOH.

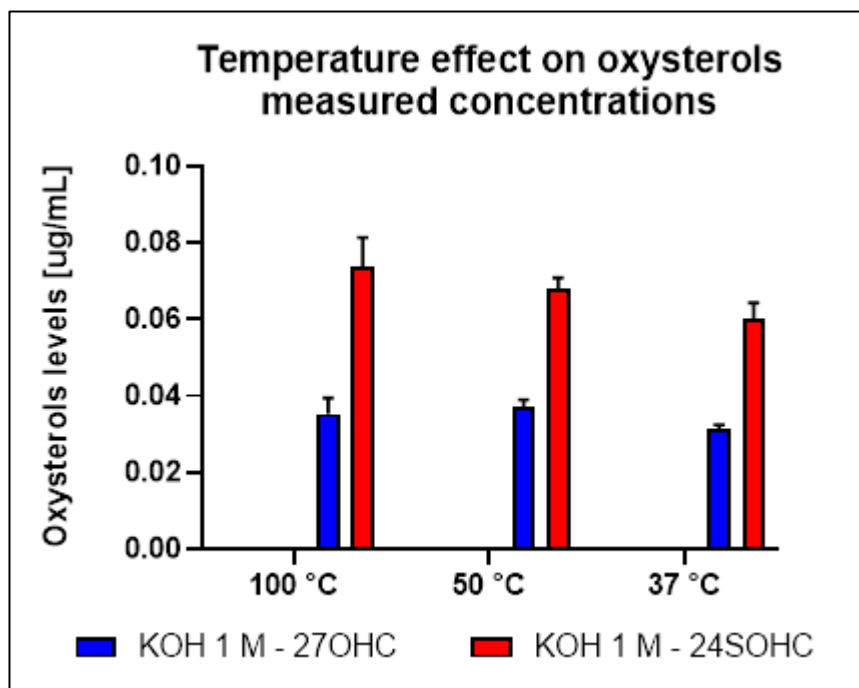


Figure 36. 24SOHC and 27OHC levels in plasma samples after hydrolysis ($N=3/\text{experimental group}$)

Table 27. 24SOHC and 27OHC levels in plasma samples after hydrolysis with KOH 1M ($N=3/\text{experimental group}$)

Analyte		KOH 1 M		
		100°C	50°C	37°C
24SOHC	µg/mL	0.074	0.068	0.06
	SD	0.01	0.003	0.004
	CV	11%	4%	7%
27OHC	µg/mL	0.035	0.037	0.031
	SD	0.004	0.002	0.001
	CV	12%	5%	4%

After identifying the best KOH concentration, the effect of the different temperatures were evaluated. Although there was no significant difference in the calculated concentrations using different temperature of incubation (see figure 29), the evaluation of analytes peak areas showed clear differences. Peak areas for oxysterols and relative IS were double after incubation at 37 °C. Figure 37 and Table 28 showed the peak areas of the oxysterols and the relative IS, under different experimental conditions.

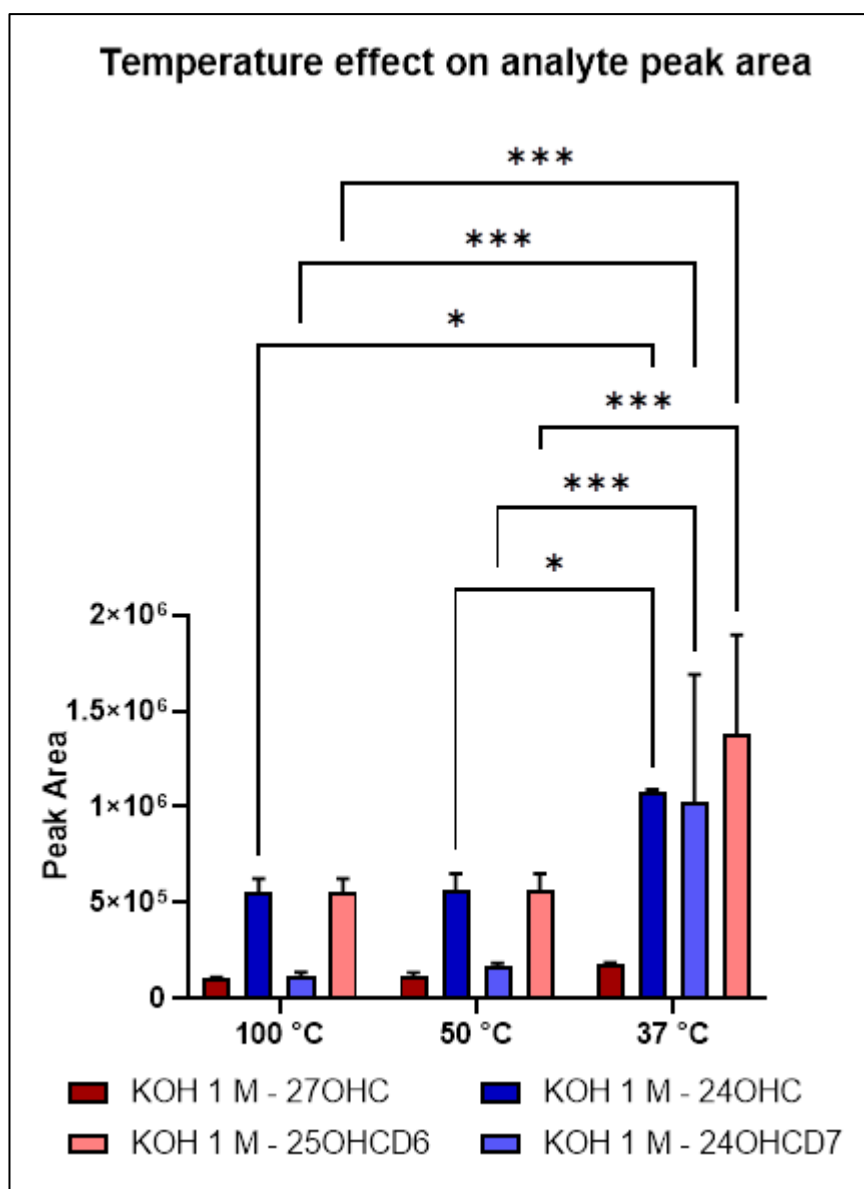


Figure 37. Oxysterols and relative IS peak areas under different hydrolysis condition (N=3/experimental group)s. Statistics: One-way ANOVA

Table 28. Oxysterols and relative IS peak areas under different hydrolysis conditions

Analyte		100°C	50°C	37°C
24-OHC-D7	Mean Peak Area	1.16E+05	1.64E+05	1.03E+06
	SD	1.98E+04	1.96E+04	6.64E+05
	CV (%)	17%	12%	65%
24-OHC	Mean Peak Area	5.51E+05	5.68E+05	1.08E+06
	SD	7.32E+04	8.30E+04	1.11E+04
	CV (%)	13%	15%	1%
25-OHC-D6	Mean Peak Area	5.51E+05	5.68E+05	1.38E+06
	SD	7.32E+04	8.30E+04	5.19E+05
	CV (%)	13%	15%	38%
27-OHC	Mean Peak Area	1.06E+05	1.17E+05	1.78E+05
	SD	3.44E+03	1.79E+04	7.29E+03
	CV (%)	3%	15%	4%

4.8.2 Optimization of incubation time for hydrolysis reaction

After the identification of the best conditions in terms of KOH concentration and temperature of incubation, further tests were carried out to identify the best reaction time. In the literature, hydrolysis was carried out mainly for 1 hour, but there were studies in which a shorter or longer time were used. We set up an experiment with four different incubation times, starting from 15 minutes up to 120 minutes.

Table 29. Experimental conditions tested for the identification of the best time of incubation

Experimental group	[KOH]	Temperature	Time of incubation
1	1 M	37°C	15 minutes
2			30 minutes
3			60 minutes
4			120 minutes

The results obtained from the measurement of Desm and Desm-D6 are reported in the following figure (Figure 38) as an example of the effects of the time of incubation on analytes peak area. It is evident that the areas of analytes and IS decrease if the sample is incubated for a period of 2 hours, while up to an hour the areas were comparable.

Therefore, we confirmed 1 hour as the best incubation time to obtain the total hydrolysis of the analytes and the best signal to noise.

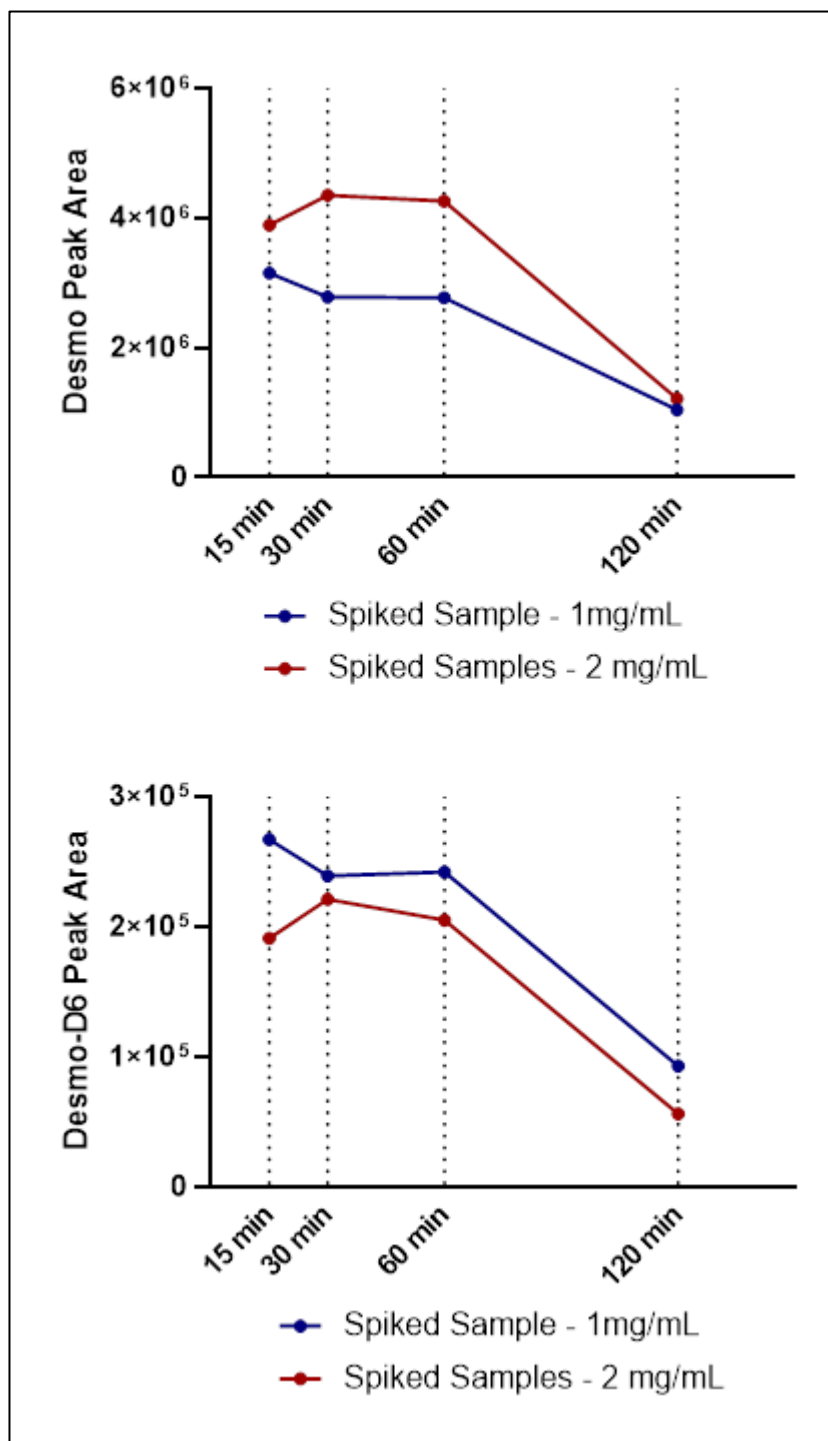


Figure 38. Results of the optimization of the incubation time with KOH 1M using desmo (upper panel) and desmo-D6 (lower panel) as reference metabolite. Peak area intensity was evaluated at 15,30,60 and 120min at two different concentrations (1 mg/mL, 2 mg/mL)

4.8.3. Validation of the optimized hydrolysis reaction with a commercial kit

To evaluate the optimized hydrolysis reaction we tested the performance by comparing the results obtained on the measurement of free and total Chol in plasma samples using our analytical method and the Amplex™ Red Cholesterol Assay Kit (Thermo Scientific). The Amplex™ Red Cholesterol Assay Kit provides a sensitive, rapid, and simple fluorometric method for detecting very low concentrations of cholesterol using a fluorescence microplate reader. We compared the results using different independent plasma samples, evaluating the correlation between the quantified Chol levels (N=15). All plasma samples were split in two different aliquots: one for the in-house developed extraction method and the following LC-MS analysis and one for the analysis using the commercial kit and the following fluorometric detection.

Table 30. resumes the results obtained, highlighting a high grade of accordance of the results obtained.

Table 30. Quantified Chol levels using Commercial kit and in-house developed and validated method based on LC-MS

Chol measured Level (mg/mL)	Commercial Kit	LC-MS
Sample 1	1.51	1.79
Sample 2	1.16	1.47
Sample 3	0.99	0.96
Sample 4	1.33	1.64
Sample 5	1.35	1.74
Sample 6	1.14	1.66
Sample 7	1.18	1.29
Sample 8	1.34	1.69
Sample 9	1.21	1.14
Sample 10	1.31	1.28
Sample 11	1.48	1.37
Sample 12	1.53	2.11
Sample 13	1.15	1.34
Sample 14	1.37	1.78
Sample 15	1.38	1.52

The statistical analysis, Spearman correlation, confirmed the significant correlation between the results obtained with the two different methods (Figure 39). The validation of our extraction and hydrolysis method gave us the confidence of the good performance of our method. To evaluate the robustness of the analytical method we set up a brief method validation, taking into account the limit of the method validation for endobiotic compounds, such as Chol metabolites.

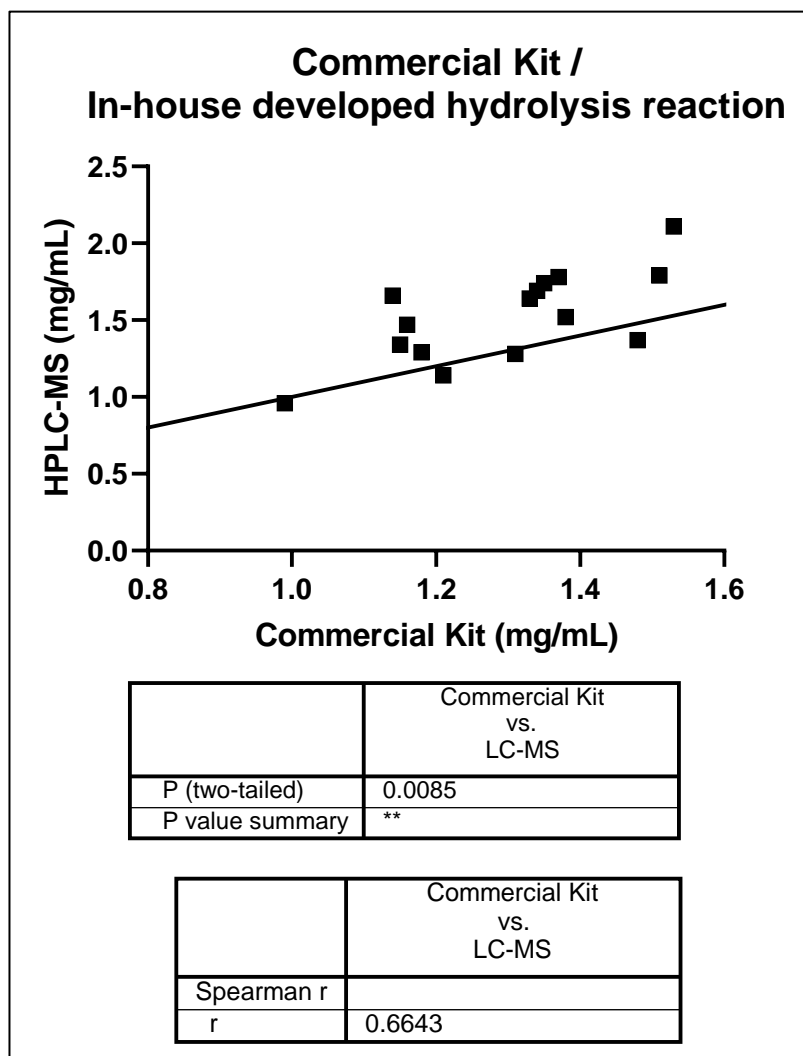


Figure 39. Comparison between the chol analysis using a commercial kit and in-house developed hydrolysis method (N=15) (Spearman correlation)

4.9. Validation of the method

4.9.1 Calibration curves

After a literature review, we defined the concentration ranges expected for each analyte in plasma and brain samples. For each range, calibration curves were prepared in a surrogate matrix simulating the extraction process of the sample, including the addition of KOH and the incubation for one hour at 37 °C. All the calibration curves were analysed in several analytical sessions; the mean measured concentration, SD, accuracy and precision for each analyte were calculated and evaluated. Since the selected ranges were wide, each curve was weighed by $1/x^2$ to avoid the loss of accuracy in the first part of the calibration curve. The tables in the following sections resume the results obtained during the evaluation of the linearity and robustness of the defined calibrants.

4.9.1.1. Brain calibration range

We defined the calibration range for lanosterol in mice brain, starting from data in which lanosterol was found from 1 up to 10 ng/mg ^{120 121} [unpublished data]. In five different analytical sessions, the calibration curve was linear in the selected range and the mean accuracy of the back-calculated concentrations ranged from 94% to 110%. The precision over five different analytical sessions was from 3% up to 15%. Interestingly the precision is lower on higher concentrations with respect to lower ones. This result is due to the use of weighted calibration curves ($1/x^2$) that guarantees a higher accuracies in back-calculated concentrations at lower levels ¹²².

Table 31. Back-calculated concentrations of lanosterol over five different analytical sessions

Lanosterol								
Nominal concentration (ng mg⁻¹)								
	0.1	0.3	1	3	10	30	100	
Back calculated concentration (ng mg⁻¹)								
Mean	0.101	0.323	0.944	3.263	9.491	32.94	102.1	
SD	0.004	0.009	0.051	0.198	0.944	4.861	15.00	
Accuracy (%)	101%	108%	94%	109%	95%	110%	102%	
Precision (CV%)	4%	3%	5%	6%	10%	15%	15%	

Data from literature show that the mean concentration of desmosterol in mice brain was 200 ng/mg ¹²³, with a dynamic range from 10 up to 200 ng/mg ¹²¹ [unpublished data]. Considering the possible reduction of desmosterol levels in brain during neurodegeneration we defined the calibration range from 1 up to 1000 ng/mg. In five different analytical sessions, the calibration curve was linear in the selected range and the mean accuracy of the back-calculated concentrations ranged from 99% to 111%. The precision over five different analytical sessions was from 3% up to 8%.

Table 32. Back-calculated concentrations of desmosterol over five different analytical sessions

Desmosterol								
		Nominal concentration (ng mg⁻¹)						
		1	3	10	30	100	300	1000
		Back calculated concentration (ng mg⁻¹)						
Mean		0.986	3.110	9.876	33.34	95.93	302.5	890.3
SD		0.025	0.215	0.611	1.705	5.009	10.26	74.96
Accuracy (%)		99%	104%	99%	111%	96%	101%	89%
Precision (CV%)		3%	7%	6%	5%	5%	3%	8%

7-dehydrocholesterol, chosen as representative of Kendutsch-Russel pathway, had a mean concentration in mice brain from 0.5 up to 5 nmol/mg protein in mice brain ¹²⁴. In five different analytical sessions, the calibration curve was linear in the selected range and the mean accuracy of the back-calculated concentrations ranged from 84% to 104%. The precision over five different analytical sessions was from 5% up to 14%.

Table 33. Back-calculated concentrations of 7-dehydrocholesterol over five different analytical sessions

7-dehydrocholesterol								
		Nominal concentration (ng mg⁻¹)						
		1	3	10	30	100	300	1000
		Back calculated concentration (ng mg⁻¹)						
Mean		0.988	2.784	10.43	30.78	92.833	291.1	839.2
SD		0.055	0.402	0.515	1.563	6.478	37.74	92.33
Accuracy (%)		99%	93%	104%	103%	93%	97%	84%
Precision (CV%)		6%	14%	5%	5%	7%	13%	11%

The expected concentrations of 24SOHC in mice brain were from 10 up to 70 ng/mg starting from our preliminary data obtained in a comparison study with Istituto Carlo Besta [*unpublished data*] ¹²¹. In five different analytical sessions, the calibration curve of 24SOHC was linear in the selected range and the mean accuracy of the back-calculated concentrations ranged from 97% to 104%. The precision over five different analytical sessions was from 5% up to 15%.

Table 34. Back-calculated concentrations of 24SOHC over five different analytical sessions

24S-hydroxycholesterol							
	Nominal concentration (ng mg⁻¹)						
	1	3	10	30	100	300	1000
	Back calculated concentration (ng mg⁻¹)						
Mean	0.966	2.909	9.485	30.87	98.29	293.7	1036
SD	0.077	0.348	0.437	2.040	14.19	29.17	159.7
Accuracy (%)	97%	97%	95%	103%	98%	98%	104%
Precision (CV%)	8%	12%	5%	7%	14%	10%	15%

4.9.1.2. Plasma calibration range

We defined the calibration range for lanosterol in mice plasma from 60 up to 150 ng/mL¹²¹, comparing our unpublished data with literature. In five different analytical sessions, the calibration curve was linear in the selected range and the mean accuracy of the back-calculated concentrations ranged from 95% to 111%. The precision over five different analytical sessions was from 2% up to 10%.

Table 35. Back-calculated concentrations of lanosterol over five different analytical sessions

Lanosterol							
	Nominal concentration (ng mL⁻¹)						
	10	30	100	300	1000	3000	10000
	Back calculated concentration (ng mL⁻¹)						
Mean	9.456	31.65	110.9	278.7	996.7	3191	8744
SD	0.226	3.081	7.826	28.00	53.19	214.8	139.3
Accuracy (%)	95%	105%	111%	93%	100%	106%	87%
Precision (CV%)	2%	10%	7%	10%	5%	7%	2%

Data from literature defined the mean concentration of desmosterol in mice plasma was 600 ng/mL with a dynamic range from 10 up to 1500 ng/mL [unpublished data]. In five different analytical sessions, the calibration curve was linear in the selected range and the mean accuracy of the back-calculated concentrations ranged from 99% to 106%. The precision over five different analytical sessions was from 3% up to 10%. We defined the same calibration range for 7-dehydrocholesterol, from 10 up to 10000 ng/mL, with good results in terms of accuracy (93%-106%) and precision (3%-10%).

Table 36. Back-calculated concentrations of desmosterol over five different analytical sessions

Desmosterol							
	Nominal concentration (ng mL⁻¹)						
	10	30	100	300	1000	3000	10000
	Back calculated concentration (ng mL⁻¹)						
Mean	9.904	30.07	94.18	298.8	1011	3174	9345
SD	0.373	2	8.435	10.48	104.4	170.4	299.2
Accuracy (%)	99%	100%	94%	100%	101%	106%	93%
Precision (CV%)	4%	7%	9%	4%	10%	5%	3%

Table 37. Back-calculated concentrations of 7-dehydrocholesterol over five different analytical sessions

7-dehydrocholesterol							
	Nominal concentration (ng mL⁻¹)						
	10	30	100	300	1000	3000	10000
	Back calculated concentration (ng mL⁻¹)						
Mean	9.773	31.28	92.18	312.2	996.4	3166	8976
SD	0.349	2.581	4.889	22.32	92.93	115.4	537.2
Accuracy (%)	98%	104%	92%	104%	100%	106%	90%
Precision (CV%)	4%	8%	5%	7%	9%	4%	6%

Considering that oxysterols levels in mice plasma have a wide range of concentrations starting from 10-60 ng/mL for 24SOHC up to 100 ng/mL for 27OHC, we set up the same calibration range for 24SOHC, 27OHC and 7 α HC (3-3000 ng/mL). The use of a weighted calibration curve ($1/x^2$) gave us a good linearity for all the compounds over five different and independent analytical sessions.

Table 38. Back-calculated concentrations of 24S-hydroxycholesterol over five different analytical sessions

24S-hydroxycholesterol							
	Nominal concentration (ng mL ⁻¹)						
	3	10	30	100	300	1000	3000
Back calculated concentration (ng mL ⁻¹)							
Mean	2.984	10.04	30.69	98.78	324.8	1008	2837
SD	0.044	0.343	2.559	8.968	11.18	140.5	219.1
Accuracy (%)	99%	100%	102%	99%	108%	101%	95%
Precision (CV%)	1%	3%	8%	9%	3%	14%	8%

Table 39. Back-calculated concentrations of 27-hydroxycholesterol over five different analytical sessions

27-hydroxycholesterol							
	Nominal concentration (ng mL ⁻¹)						
	3	10	30	100	300	1000	3000
Back calculated concentration (ng mL ⁻¹)							
Mean	3.474	10.63	28.64	106.0	304.2	1047	2940
SD	0.320	1.117	1.041	7.321	34.34	34.39	345.4
Accuracy (%)	116%	106%	95%	106%	101%	105%	98%
Precision (CV%)	9%	11%	4%	7%	11%	3%	12%

Table 40. Back-calculated concentrations of 7 α -hydroxycholesterol over five different analytical sessions

7- α HC							
	Nominal concentration (ng mL ⁻¹)						
	3	10	30	100	300	1000	3000
Back calculated concentration (ng mL ⁻¹)							
Mean	3.007	8.706	33.90	101.4	277.6	876.3	3011
SD	0.181	2.123	2.022	5.557	20.21	59.40	117.6
Accuracy (%)	100%	87%	113%	101%	93%	88%	100%
Precision (CV%)	6%	24%	6%	5%	7%	7%	4%

4.9.2 Recovery from plasma matrices

The main problem in the calculation of recovery is that Chol metabolites are present in biological matrices as endogenous compounds and it is not possible to obtain a completely blank matrix to do the required tests.

For this reason, the recoveries in plasma samples were calculated only for the deuterated compounds, used as IS, assuming that the analytes of interest have the same chemical properties. The evaluations were carried out using independent plasma matrix, in triplicate biological samples, at two different concentration levels, 100 and 200 ng mL⁻¹.

Table 41. Recovery from plasma matrix. (N=3/experimental group)

24-hydroxycholesterol-D7			
Concentration ng mL ⁻¹	Mean Recovery	SD	CV
100	81%	12%	15%
200	86%	4%	4%
25-hydroxycholesterol-D6			
Concentration ng mL ⁻¹	Mean Recovery	SD	CV
100	60%	12%	20%
200	101%	10%	10%
Desmosterol-D6			
Concentration ng mL ⁻¹	Mean Recovery	SD	CV
100	63%	5%	8%
200	88%	10%	11%

Recoveries for all IS were higher than 60% with a CV (%) lower than 20%, as specified in the guidelines for the method validation. Since we used deuterated compounds as surrogate analytes we assumed that Chol metabolites had the same behaviour in plasma matrix and the same percentage of recovery.

4.9.3 Recovery from brain matrices

Similarly to plasma, the recoveries from brain samples were calculated only for the deuterated compounds, used as IS, assuming that the analytes of interest have the same chemical properties. The evaluations were carried out using independent brain matrices, in triplicate, at two different concentration levels, 50 and 150 ng mg⁻¹.

Recoveries for all IS were higher than 81% with a CV (%) lower than 20%, as specified in the guidelines for the analytical method validation. Since we used deuterated compounds as surrogate analytes we assumed that Chol metabolites had the same behaviour in brain matrix and the same percentage of recovery. We used Lathosterol-D7 as representative of 7-dehydrocholesterol behaviour in brain matrix. The results highlighted the good performance and the robustness of the extraction method. Future implementations of the method will include more deuterated compounds for the accurate quantitation of all Chol metabolites, obtaining a method with a specific deuterated internal standard for each analyte of interest. The final result will be a total normalization of the recovery and the matrix effect for each analysed compound.

Table 42. Recovery from brain matrix. (N=3/experimental group)

24-hydroxycholesterol-D7			
Concentration ng mg ⁻¹	Mean Recovery	SD	CV
50	94%	11%	11%
150	116%	10%	8%
Desmosterol-D6			
Concentration ng mL ⁻¹	Mean Recovery	SD	CV
50	81%	15%	19%
150	101%	1%	1%
Lathosterol-D7			
Concentration ng mL ⁻¹	Mean Recovery	SD	CV
50	102%	11%	11%
150	92%	5%	5%

4.10. Chronic treatment with D6-Chol: metabolism analysis in striatum samples

As discussed in the previous chapters, Chol-loaded liposomes are able to carry a large amount of Chol to the whole brain after a single dose treatment. Moreover, the repeated dose treatment highlighted the significant accumulation of administered Chol.

We sought to test whether the administered Chol was sufficient to stimulate endogenous cholesterol synthesis in the diseased brain. As surrogate markers of cholesterol biosynthesis, we quantified Chol precursors (lan, 7-dehydrochol, desm) and Chol main brain catabolite (24SOHC) by the previously described and validated method in the striata of HD mice after a chronic treatment.

Accordingly, HD mice from 5 to 9 weeks of age were treated with Chol-D6-loaded liposomes. As expected, robust deficits of lan were evident in R6/2 mice (compared to WT) confirming the literature results (106)^{71 74}. After the repeated dose treatment with Chol-loaded liposomes, no significant differences were highlighted in R6/2 mice, where lan levels were still under the LOQ of the method in most of the samples. Interestingly, there was no significant difference in the levels of 7-dehydrochol between WT and R6/2 mice, both treated and untreated but there was a significant difference in the levels of desm, suggesting that Bloch pathway is the most affected by the disease. Moreover, the treatment with Chol-loaded liposomes partially restored the desmosterol levels as elucidated by the statistical analysis which showed no significant difference between WT and R6/2 mice treated with liposomes groups.

Finally, the levels of 24SOHC were significantly different between WT and treated R6/2 mice. Interestingly, this result suggested that although the treatment was with D6-Chol-loaded liposomes it had an influence on Chol metabolites' levels. The result obtained suggested that treated mice could use administered Chol to restore the metabolic deficit in Chol synthesis. In fact, 24SOHC is the final product of brain Chol synthesis and it is synthesized to discard the excess of synthesized brain Chol through the BBB in peripheral circulation. Taken together all these results suggested that the reduction in brain Chol synthesis mostly involved the astrocytes with a significant reduction of desmosterol levels in R6/2 mice. The significant lower levels of

$^{24}\text{SOHC}$ in treated R6/2 mice with the higher levels of desmosterol suggested the use of administered Chol to maintain the steady state of Chol synthesis.

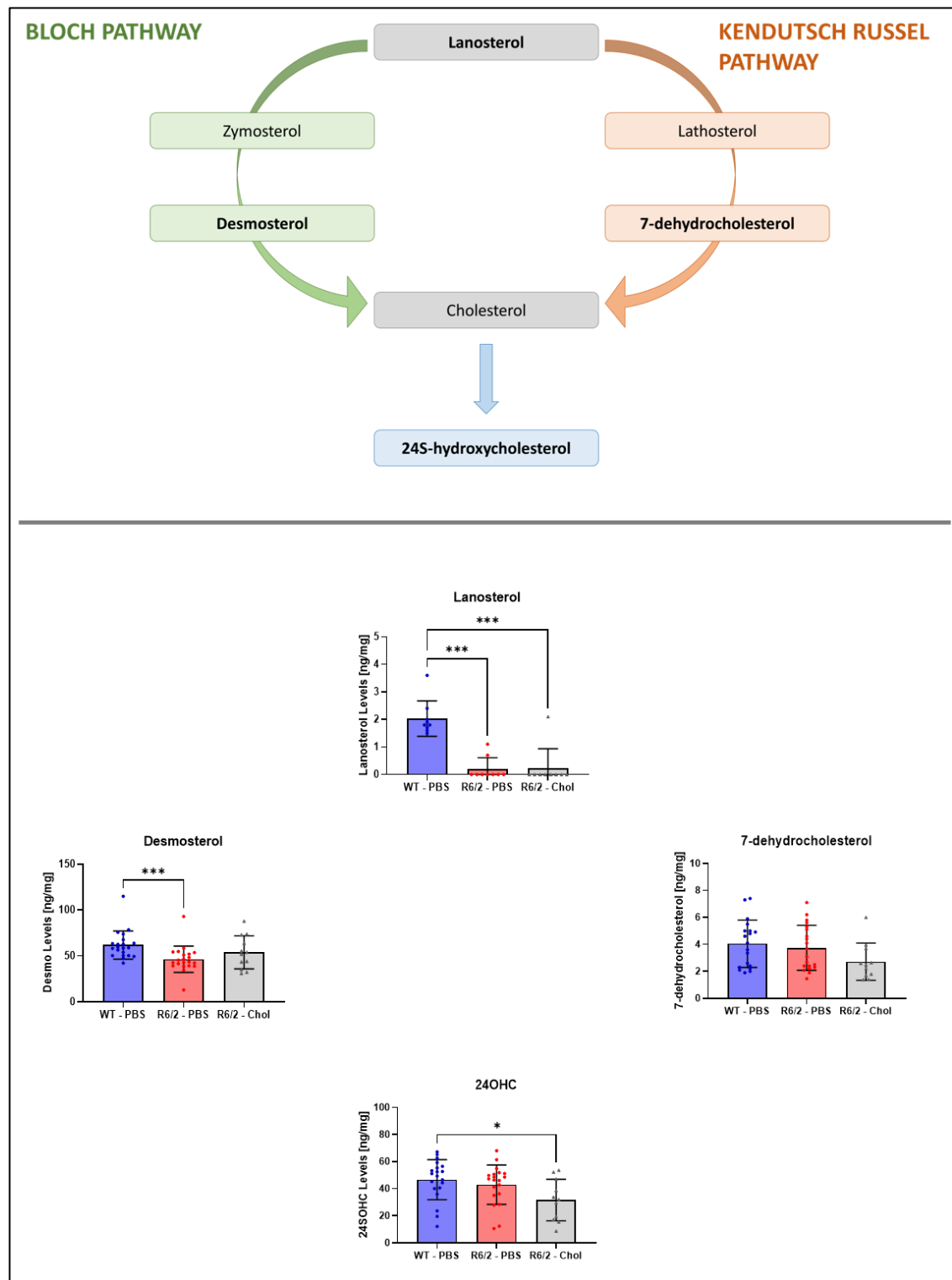


Figure 40. Upper panel: Block scheme of Chol metabolic pathway; Lower panel: Lanosterol, Desmosterol, 7-dehydrocholesterol and 24SOHC levels in striatum area in WT, R6/2 mice and R6/2 mice treated with liposomes ($n \geq 5$ mice/group). Data are expressed as mean \pm standard error of the mean. Each dot correspond to the value obtained from each animal. Statistics: one-way ANOVA with Kruskal-Wallis test (* $p < 0.05$; ** $p < 0.01$; *** $p < 0.001$).

The analysis of plasma samples from chronic treatment did not show significant differences between WT and R6/2 mice, both treated and untreated with D6-Chol-loaded liposomes. 7- α hydroxycholesterol, the precursor of bile acids synthetic pathway, showed lower levels in R6/2 mice treated with PBS with respect to WT mice. Interestingly, the treatment with Chol-loaded liposomes restore 7- α levels in R6/2 mice. This result is consistent with the distribution of administered Chol in peripheral tissues, as discussed in previous chapters. We investigated the levels of 24SOHC in plasma as a marker of brain Chol metabolism but the results did not show statistical differences in WT and R6/2 mice. 27OHC is a catabolite of peripheral metabolism of Chol, it is not strictly related to brain Chol metabolism and its levels were not affected by HD disease or Chol-loaded liposomes treatment. Finally, all precursor Chol metabolites, lan, 7-dehydrochol and desm, showed similar levels in all analysed samples, confirming that the administered Chol did not affect the peripheral metabolic pathway.

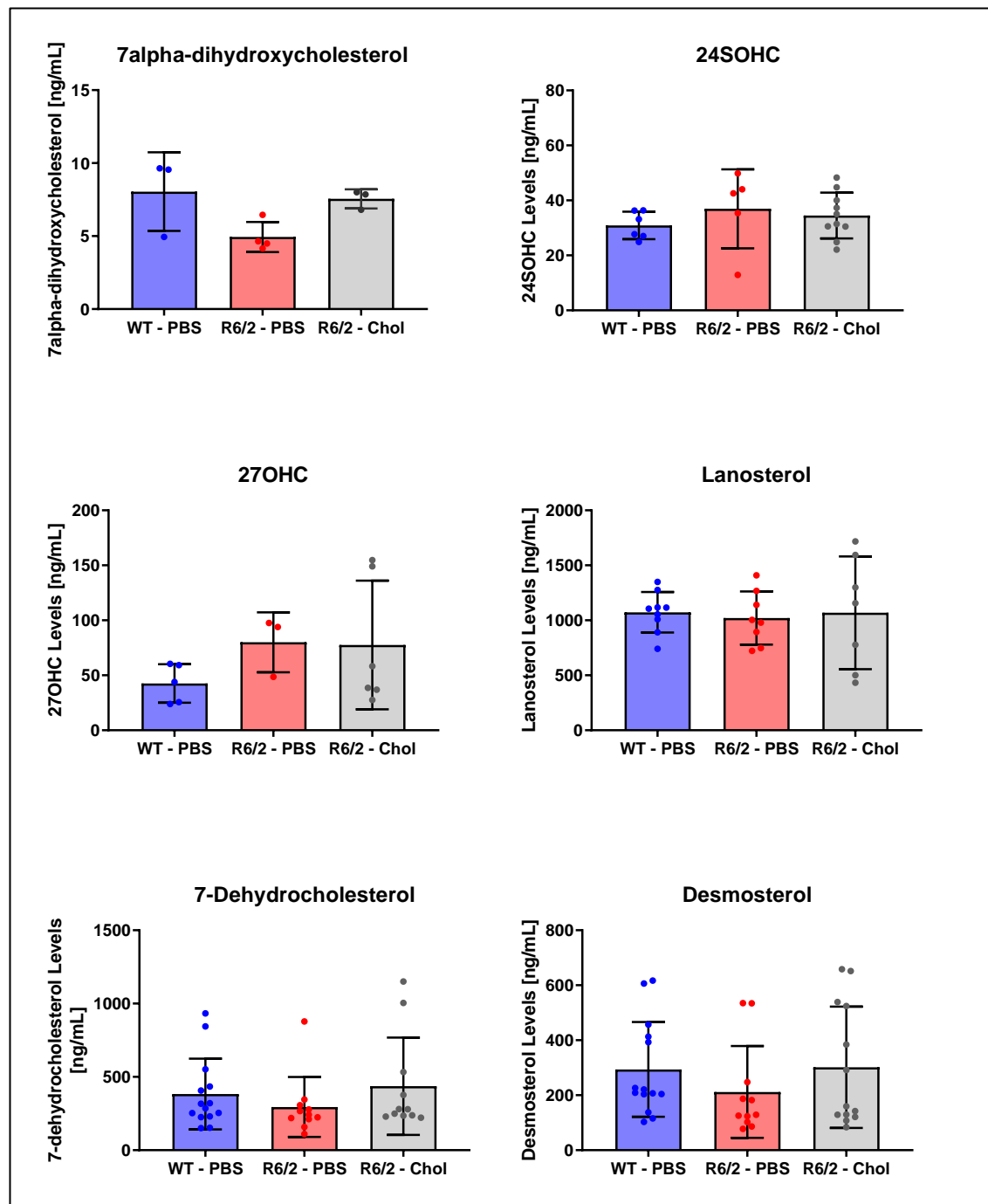


Figure 41. 7- α dihydroxycholesterol, 24SOHC, 27OHC, Lanosterol, Desmosterol and 7-dehydrocholesterol levels in striatum area in WT and R6/2 ($n \geq 3$ mice/group). Data are expressed as mean \pm standard error of the mean. Each dot correspond to the value obtained from each animal. Statistics: one-way ANOVA with Kruskal-Wallis test (* $p < 0.05$; ** $p < 0.01$; *** $p < 0.001$).

4.11. Cholesterol metabolism analysis: WT and R6/2 mice

To understand the changes in Chol metabolites levels during aging in WT and R6/2 mice, we analyzed striatum samples from untreated WT and R6/2 mice starting from 4 weeks old mice. The onset of the disease starts at 6 weeks and the phenotype of the disease is aggressive and leads to animal death within 12 weeks. We evaluated the striatum levels of desmosterol, 7-dehydrocholesterol, and 24SOHC in WT and R6/2 mice ($n \geq 6$ mice/group). As expected the levels of desmosterol and 7-dehydrocholesterol decreased with aging both in WT and R6/2 mice. At 12 weeks R6/2 mice had a significant lower level of desmosterol with respect to WT mice. This result is consistent with the previous result obtained in the chronic study and confirmed the involvement of the astrocyte in disease progression. The levels of 7-dehydrocholesterol were not significantly different between WT and R6/2 mice at all analysed time-point. Interestingly, the levels of 24SOHC did not decrease with aging and did not show significant differences between WT and R6/2 mice until 12 weeks. This result is consistent with the alteration of desmosterol levels at 12 weeks, indicating a significant reduction in Chol synthetic pathway and a subsequent reduction of 24SOHC level, as the main discard product of brain Chol synthesis.

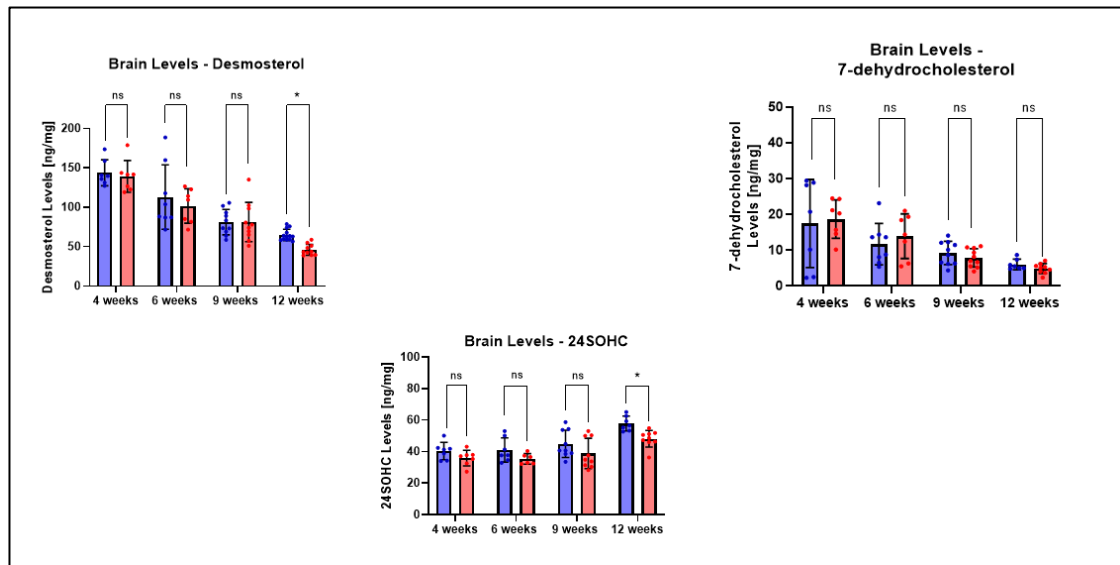


Figure 42. Desmosterol, 7-dehydrocholesterol and 24SOHC levels in striatum area in WT and R6/2 ($n \geq 6$ mice/group). Data are expressed as mean \pm standard error of the mean. Each dot correspond to the value obtained from each animal. Statistics: one-way ANOVA with Kruskal-Wallis test (* $p < 0.05$; ** $p < 0.01$; *** $p < 0.001$).

4.12. Clinical Longitudinal Study

The following chapter is derived from the collaboration with Istituto Carlo Besta and it is still on-going.

We conducted a 2-year observational study in 78 HD patients and 64 healthy controls. Detailed clinical and imaging data and blood samples were collected at baseline, and they will be collected after two years to investigate the rate of changes along the longitudinal study (follow-up starting from October 2022). We measured 24SOHC levels and other Chol metabolites levels in collected plasma samples using the above mentioned validated method. Figure 43 shows the block scheme of the clinical study that includes the collection of clinical and cognitive parameters, the blood sample collection for the analysis of Chol and 24SOHC levels and, finally, the magnetic resonance imaging to monitor brain atrophy related to disease progression.

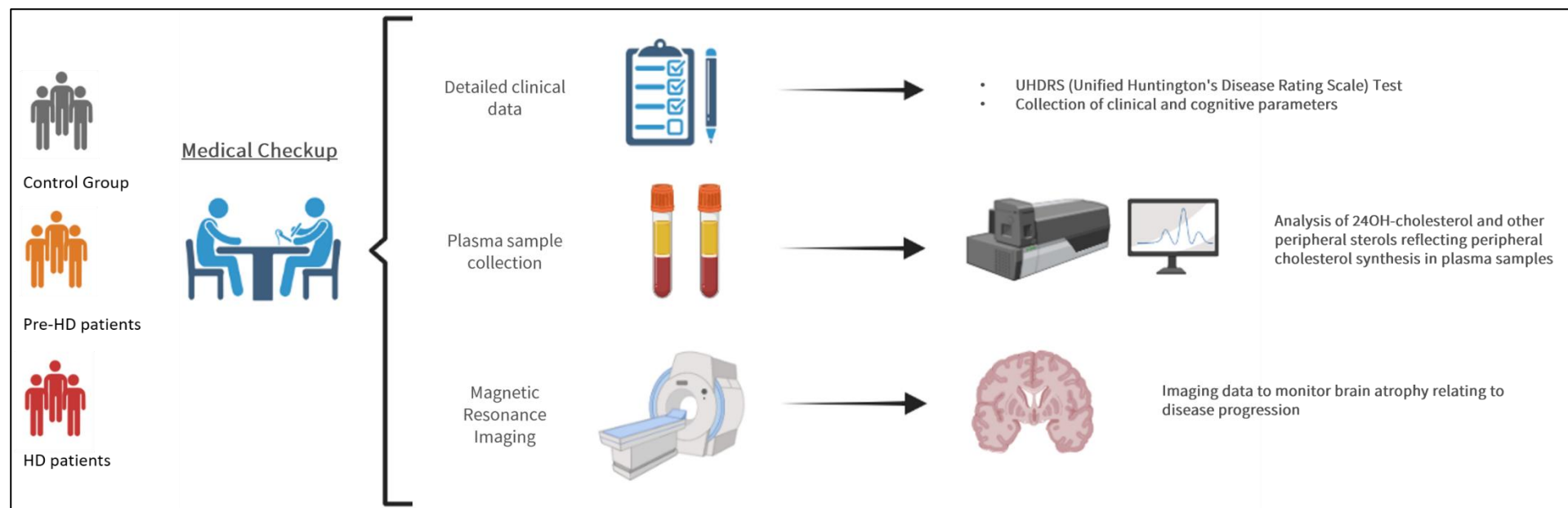


Figure 43.Block scheme of the proposed longitudinal study.

The cohort of patients was divided in control group, patients at the preclinical stage (pre-HD) and HD patients, including patients at phase I (HD-I) and patients at phase II (HD-II). The pre-HD phase can last for 20 years or longer. There are not physical symptoms in this stage but there is already the confirmation of HD thanks to the genetic test. HD-I starts with the onset of physical symptoms. This stage can last for up to eight years. In this phase, patients experience slight emotional, cognitive, or behavioural symptoms. In HD-II, the physical signs of the disease are more noticeable and may begin to affect the daily life of patients. This stage can last for three to 13 years from when the symptoms start. While individual symptoms are similar to those in stage I, they will increase in severity during stage II. Complex movements might become more difficult, and involuntary movements and twitching increase over time. The analysis of plasma samples highlighted significant differences in 24SOHC levels in Pre-HD (30.77 ± 14.52 ng/mL), HD-I (29.15 ± 16.83 ng/mL) and HD-II (29.66 ± 12.19 ng/mL) with respect to the control groups (40.01 ± 14.62 ng/mL). This result is in line with data from literature that confirmed a significant reduction of 24SOHC levels at the onset of the disease, underlying the importance of 24SOHC as possible diagnostic biomarker. These preliminary data will be elaborated by Istituto Carlo Besta for the stratification of the cohort and the integration of the results with the results obtained from the medical check-up.

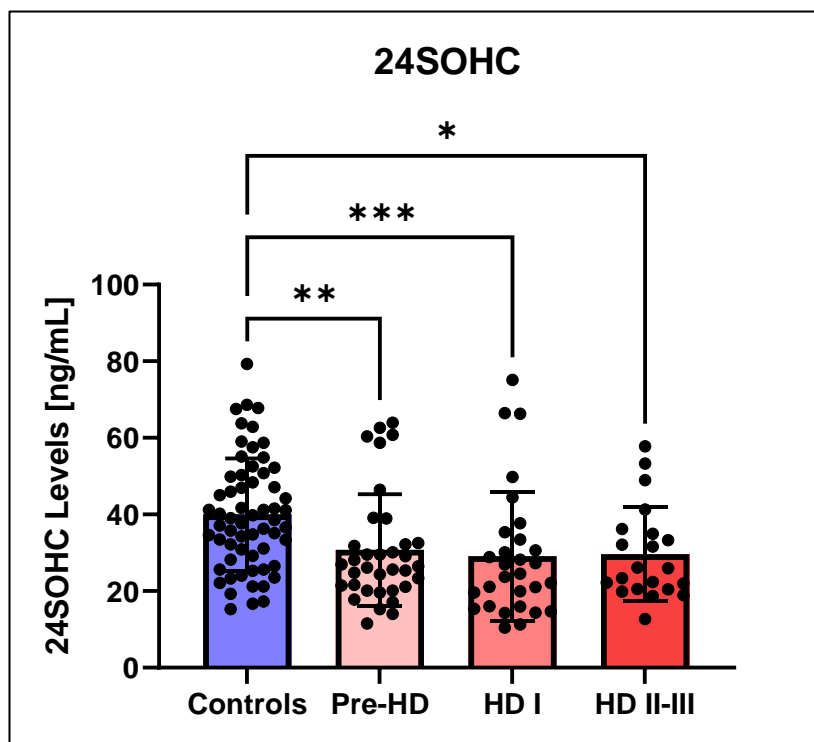


Figure 44. 24SOHC plasma levels in control, Pre-HD, HD-I and HD-II-III groups. ($N \geq 20$ /experimental group). Statistics: one-way ANOVA with Kruskal-Wallis test (* $p < 0.05$; ** $p < 0.01$; *** $p < 0.001$).

Thanks to the longitudinal study, we expect to establish whether changes in plasma 24SOHC mark the disease progression and, eventually, phenoconversion from pre-symptomatic to symptomatic stages in combination with clinical, cognitive and imaging parameters. The proposed 24SOHC metabolic biomarker study has been designed to complement international observational trials conducted on pre-HD subjects to implement an ongoing clinical-neuropsychological and neuroimaging clinical study initiated at the Istituto Carlo Besta in 2013. All recruited patients will continue to be followed in a longitudinal prospective study from the pre-HD to the symptomatic phases of the disease, evaluating the role of 24SOHC in the progression of HD.

4.13 Imaging mass spectrometry

The following chapter is derived from my visiting research period at Swansea University (from May 2022 to July 2022)

4.13.1 Evaluation of derivatization reaction on desmosterol, 24-hydroxycholesterol, and cholesterol

The efficacy of the derivatization reaction, useful for the discrimination of Chol metabolites that have the same m/z (see chapter 3.6.2.) was evaluated on standard spots of the analytes of interest (desmosterol, 24SOHC, and Chol). We set up the derivatization reaction from a previously published method by Angelini et al.⁹⁸.

On a MALDI target, we spotted three replicates of standard solutions at the concentration of 0.2 ng/spot diluted in ethanol/water 7/3, assuring the total dissolution of each analyte.

The cholesterol oxidase (0.264 units/mL in 50 μ M KH_2PO_4 pH 7) was sprayed in 18 layers using the automated sprayer SunCollect (SunChrome). The first layer was applied at 10 μ L/min, the second was applied at 15 μ L/min, and then all the subsequent layers were applied at 20 μ L/min to give an enzyme density of 0.05 munits/ mm^2 . Thereafter, the enzyme-coated slide was placed in a custom-made humidity chamber with 30 mL of warm water (37 °C) and then incubated at 37 °C for 1 h in a cell incubator. The AP-MALDI target was removed, and the spots were dried in a vacuum desiccator for 15 min. Girard's T Reagent (GT) (5 mg/mL in 70% methanol, 5% acetic acid) was sprayed using the automated sprayer SunCollect (SunChrome), resulting in a GT density of 1.00 μ g/ mm^2 .

The slide was then placed in the custom-made humidity chamber as mentioned above containing 10 mL of pre-warmed (37 °C) 50% methanol and 5% acetic acid and incubated at 37 °C for 1 h. Alpha-cyano-4-hydroxy-cinnamic acid (CHCA) was sprayed at 5 mg/mL in water/acetonitrile (3:7, v/v) at a flow rate of 80 μ L/min and a linear velocity of 1200 mm/min, with 2 mm line distance, for a total of 16 lines, with an offset of 1 mm, resulting in a matrix density of 1.33 μ g/ mm^2 .

The following figures showed the obtained results in this first experiment. Figure 45 showed the result obtained from the derivatization of cholesterol: Panel A: extracted ion current of derivatized Chol with GT, Panel B: extracted ion current of underivatized Chol; Panel C: extracted ion current

of oxidated Chol. Taking together all these results showed how the selected reaction conditions, including reagent deposition using an automatic sprayer, led to total derivatization of spotted Chol. Panel D and E showed the full scan MS and MS/MS spectra, respectively.

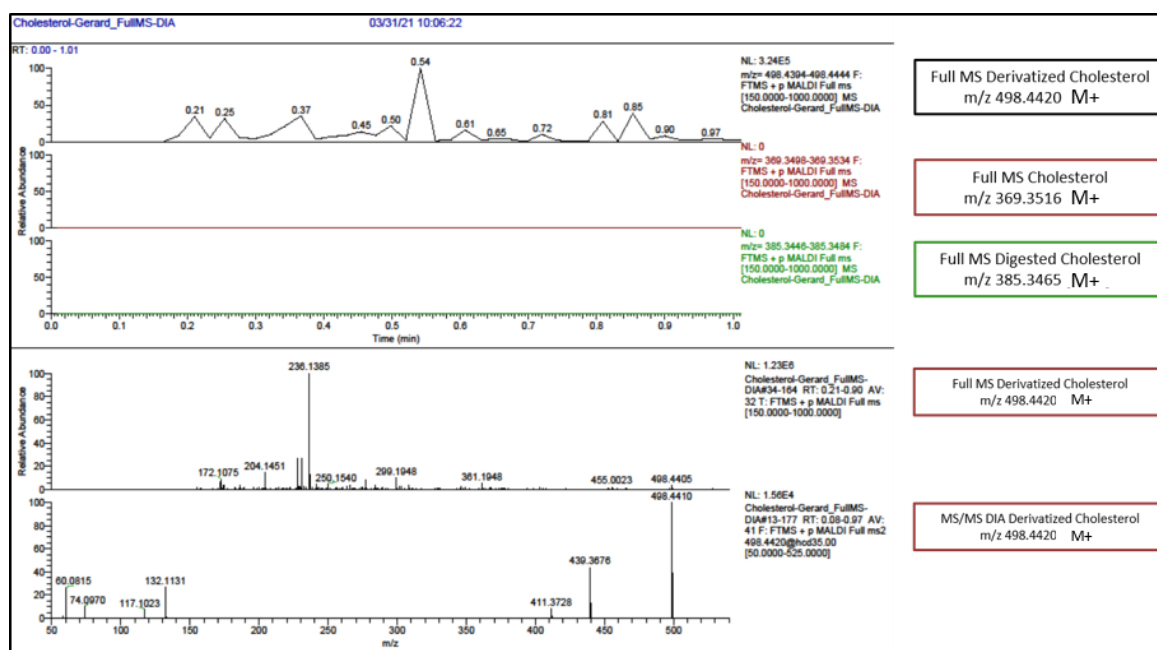


Figure 45. Total Ion Current (TIC), MS, and MS/MS spectra obtained from the analysis of a derivatized Chol spot (0.2 ng/spot).

Figure 43 shows the result obtained with the derivatization of 24SOHC: Panel A: extracted ion current of derivatized 24SOHC with GT, Panel B: extracted ion current of underivatized 24SOHC; Panel C: extracted ion current of oxidated 24SOHC. The obtained results showed how the selected reaction conditions led to the total derivatization of 24SOHC. Panel D and E showed the full scan MS and MS/MS spectra, respectively. As shown in chapter 4.6.2. about the LC-MS method for the analysis of Chol metabolites, 24SOHC and desm presented the same m/z using an ESI source (367.35), due to the loss of water during ionization. Interestingly, after oxidation, 24SOHC and desmosterol gained different m/z (Figure 46), 514.4357 and 496.4268, respectively. For this reason, we decided to investigate further the brain distribution of desmosterol, as a representative Chol precursor, and 24SOHC as the main brain Chol catabolite during the final IMS experiments. The MS/MS spectra did not show any specific fragment for the selected metabolites. The evaluation of the impact of the collision energy (CE) on the fragmentation pattern highlighted how a too high CE led to the formation of common fragments among all steroids (m/z 60.0815, 74.0970, 117.1023, 132.1131).

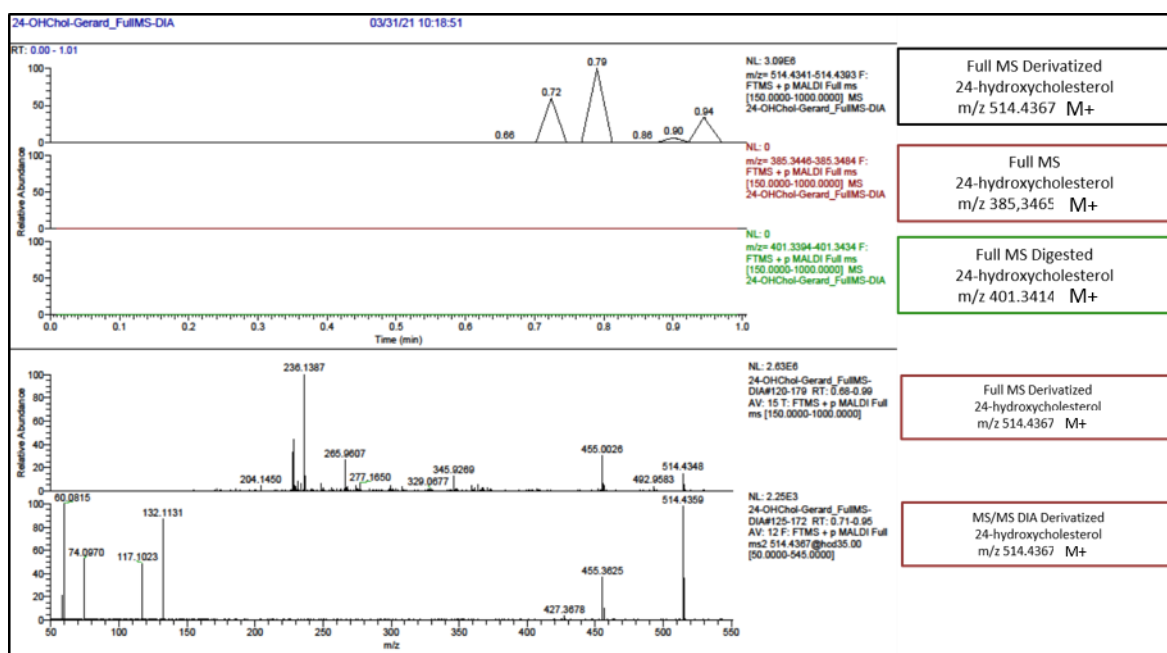


Figure 46. Total Ion Current (TIC), MS, and MS/MS spectra obtained from the analysis of a derivatized 24SOHC spot (0.2 ng/spot)

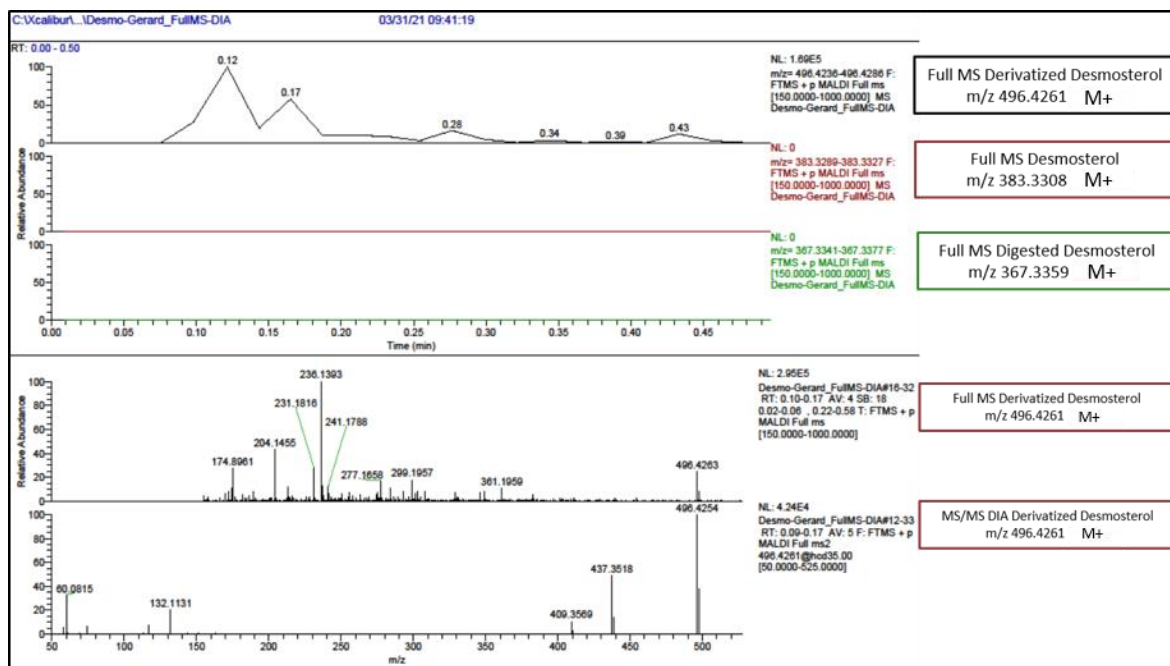


Figure 47. Total Ion Current (TIC), MS, and MS/MS spectra obtained from the analysis of a derivatized desmosterol spot (0.2 ng/spot)

4.13.2. Source parameters optimization

To evaluate the influence of the source setup on the signal of the selected metabolites, we optimized the capillary temperature and the spray voltage by changing one parameter at a time, registering the signal intensity of a derivatized standard of Chol at 0.2 ng/spot concentration as a mean of 20 spectra.

Figure 48 shows the results obtained from the optimization of the spray voltage: the Chol signal increased four times using a Spray voltage of 2 kV.

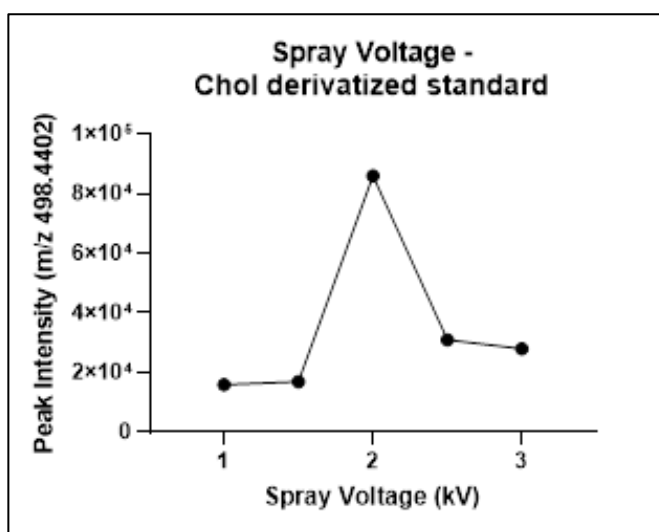


Figure 48. The ramp of spray voltage optimization (kV) using m/z 498.4402 as a reference peak

Figure 49 shows the results obtained for the optimization of the capillary temperature. We acquired a mean mass spectrum of 20 scans and evaluated the signal of derivatized Chol at 0.2 ng/spot concentration. A higher capillary temperature led to a significantly higher signal. Given these results, we chose to set up the source conditions at 2 kV and 350 °C as spray voltage and capillary temperature, respectively, for the imaging mass spectrometry experiments.

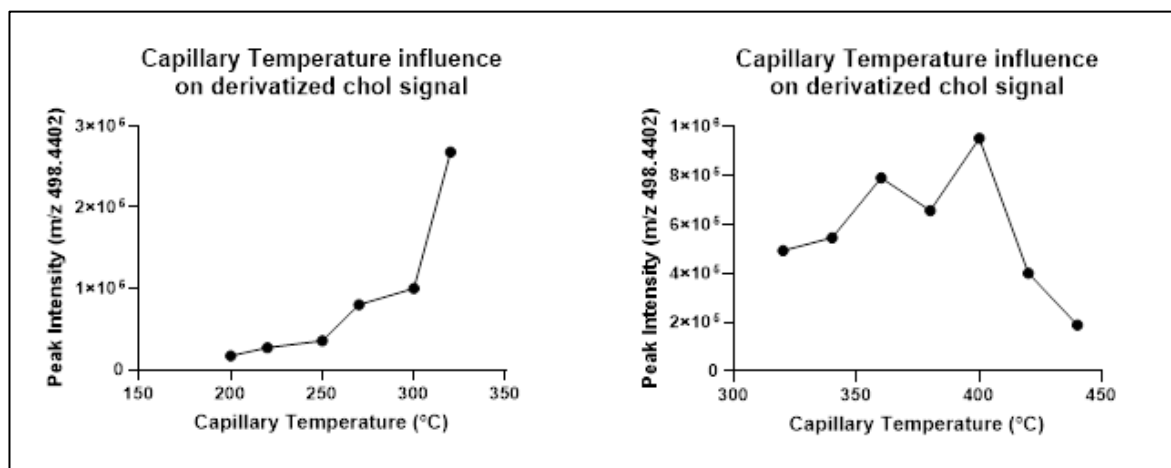


Figure 49. The ramp of capillary temperature optimization using m/z 498.4402 as a reference peak

4.13.3. Imaging experiment on WT and R6/2 mice

The presented preliminary imaging studies were performed using sagittal mouse brain sections with an AP-MALDI-QExactive instrument. GT-tagged Chol gave an intense $[M]^+$ signal dominating the resulting mass spectrum while IS presented a signal lower than 10% (Figure 50).

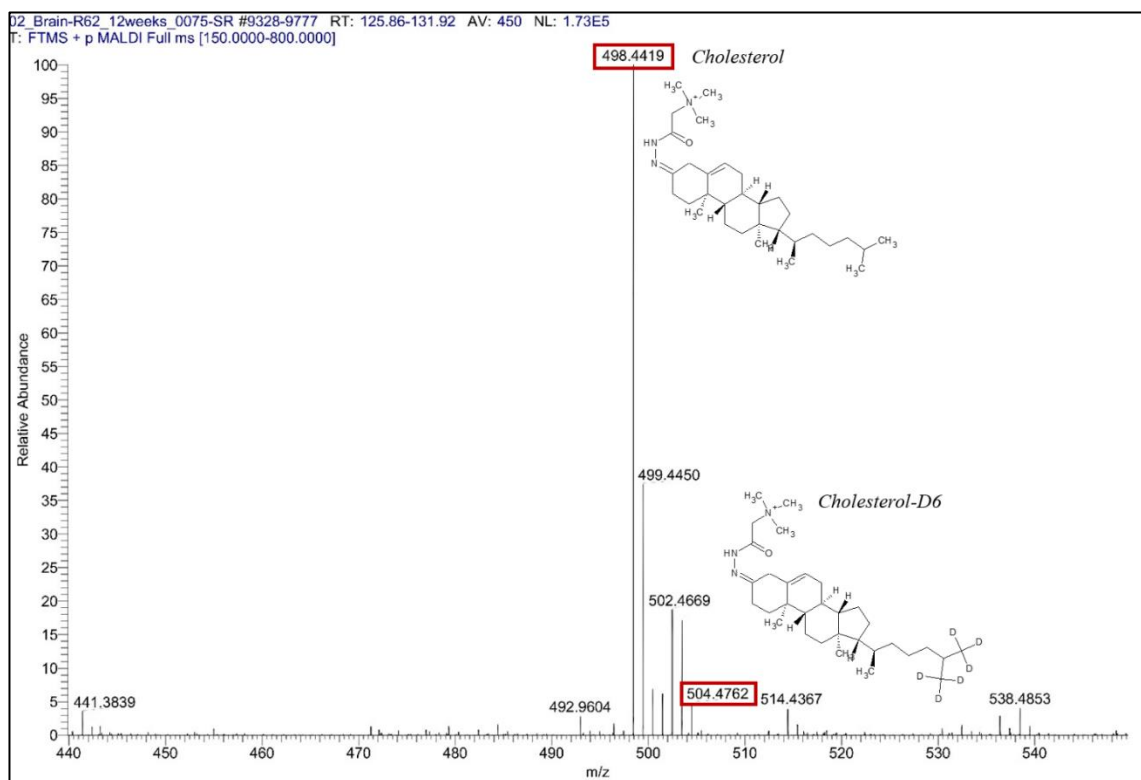


Figure 50. Mean spectra (450 scans) of WT brain slice obtained during an IMS experiment

The brain distribution of the selected Chol metabolites was analyzed in two sagittal brain slices from WT and R6/2 mice, respectively.

The MSI normalized images (Figure 51, 52, 53) showed a similar distribution of all selected m/z in both WT and R6/2 mice. Chol (m/z : 498.4402) presented a mean peak abundance of 1.73×10^5 , while Chol-D6, used as IS, presented a mean peak abundance of 1.76×10^4 (Figure 51).

As previously discussed, 24SOHC gained, after the derivatization step, a different m/z from desmosterol: 514.4357 and 496.4268, respectively. Unfortunately, 514.4357 was the m/z of the main oxidation products of Chol, naturally present in the brain at a higher concentration than 24SOHC, such as 7-ketocholesterol. Figure 52 shows the results of the IMS experiment, highlighting how this m/z had the same spatial distribution of Chol, confirming its origin as an oxidation product. We concluded that MS^3 experiments were essential to distinguish 24SOHC from the Chol oxidation products. Future experiments will include the use of an AP MALDI source on an LTQ Orbitrap XL a high-resolution instrument that includes both an ion-trap and orbitrap analyzers, making it possible to do MS^n experiments. Desmosterol gained, after the derivatization, the same m/z of 7-dehydrochol, leading to a non-specific results during the IMS experiment. Fig 53 obtained from IMS of m/z 496.4268 was representative of both these Chol precursors.

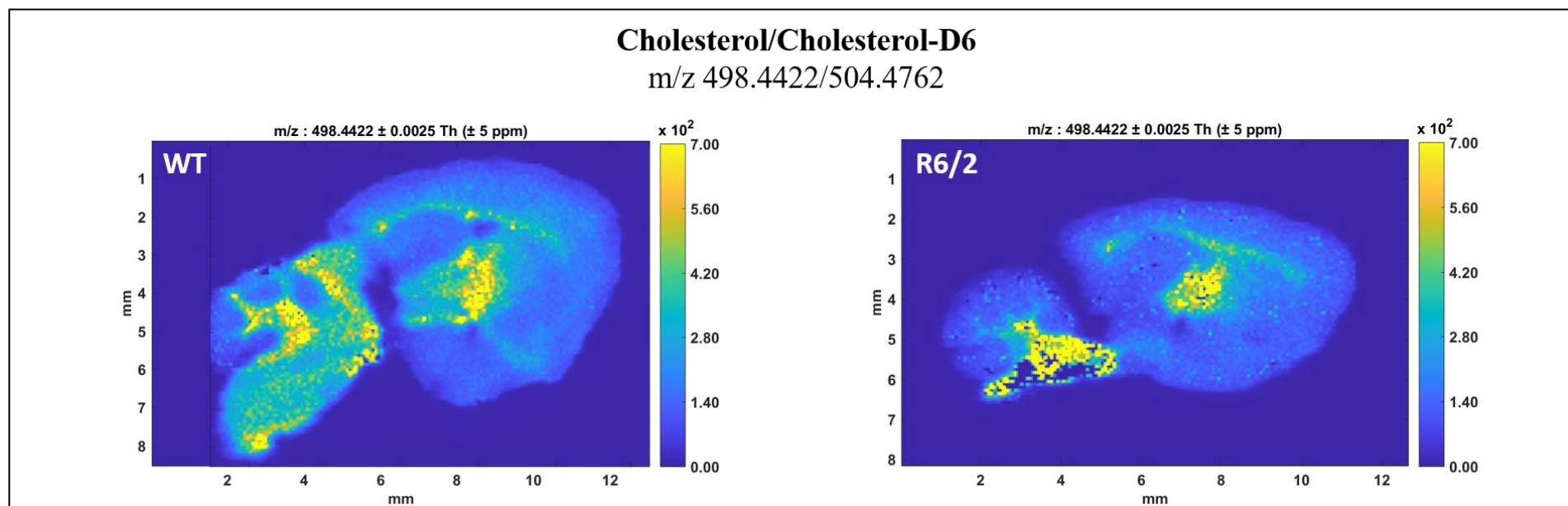


Figure 51. Comparison of IMS analysis of sagittal brain slice from a WT and R6/2 mice, highlighting a lower level of Chol in R6/2 mice. The figures show the Chol distribution and the intensity is proportional to its abundance in the different brain areas (arbitrary units).

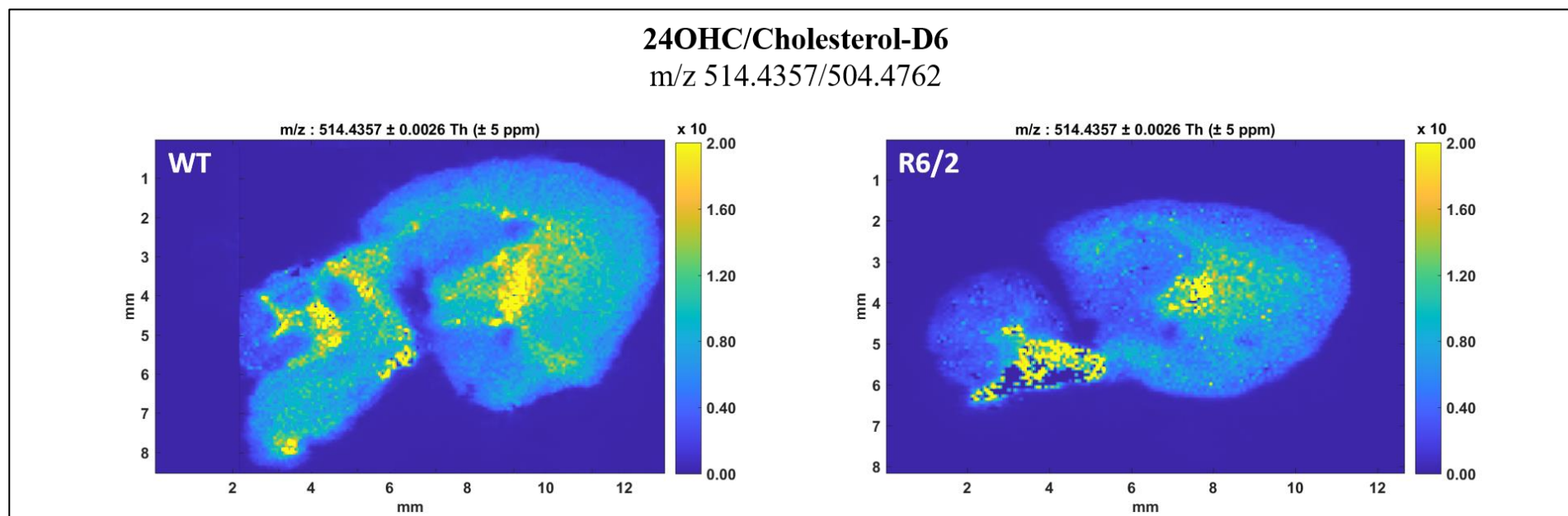


Figure 52. Comparison of IMS analysis of sagittal brain slice from a WT and R6/2 mice, highlighting a lower level of m/z 514.5357 in R6/2 mice. The figures show the distribution and the intensity is proportional to its abundance in the different brain areas (arbitrary units).

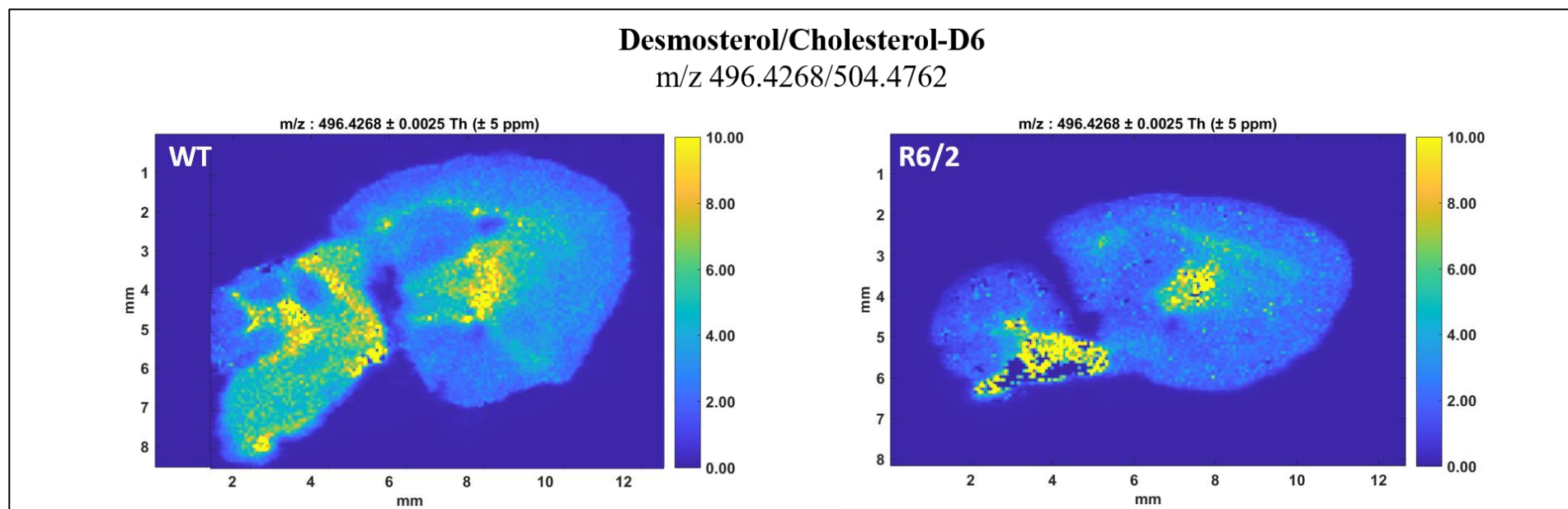


Figure 53. Comparison of IMS analysis of sagittal brain slice from a WT and R6/2 mice, highlighting a lower level of m/z 496.4268 in R6/2 mice. The figures show the distribution and the intensity is proportional to its abundance in the different brain areas (arbitrary units).

4.13.4. Cholesterol Quantitative Imaging Mass Spectrometry

Since the signal of 24SOHC and desmosterol were not specific without MSⁿ experiments, we performed a preliminary experiment of quantitative IMS focusing our attention only on the Chol signal.

To generate a calibration curve, we chose to use increasing amounts of Chol directly spotted on the AP-MALDI target. We assumed that Chol and Chol-D6 have the same matrix effect, as they have the same chemical properties. To generate calibration curves, solutions of increasing Chol concentrations were then manually spotted on the AP-MALDI target (0.2 µL). Although doping brain tissue homogenates with increasing amounts of Chol-D6, as the surrogate analyte, may have been a more accurate approach to generate a calibration curve, we chose the spotting approach directly on the AP-MALDI target, since the ratio of Chol and Chol-D6 matrix effect can be assumed as equal to 1.

The linearity range tested was from 40 ng/spot to 800 ng/spot. For all curves, MSI data were acquired with a spatial resolution of 75 µm. An approximately linear increase in signal was observed with increasing amounts of Chol. Figure 54, Panel A shows the linearity obtained from this preliminary experiment with a good correlation between increasing concentrations and Chol/Chol-D6 signal ratio (r^2 : 0.9783). We used the abovementioned calibration curve to quantify two brain slices from WT and R6/2 mice, respectively. The results obtained are shown in figure 54 Panel B and they were in accordance with the literature, where the concentration of free Chol in brain were from 400 to 600 ng/mm² ⁹⁸. Figure 54 panel C shows the image obtained from the IMS experiment during the acquisition of the calibration curve, highlighting the ROI (region of interest) used for the construction of calibration curves.

The next steps will include the staining of brain slices and the comparison of histological and IMS results. We will focus our attention on the quantitation of free Chol in specific brain areas, such as the striatum, which is the most affected brain area in HD.

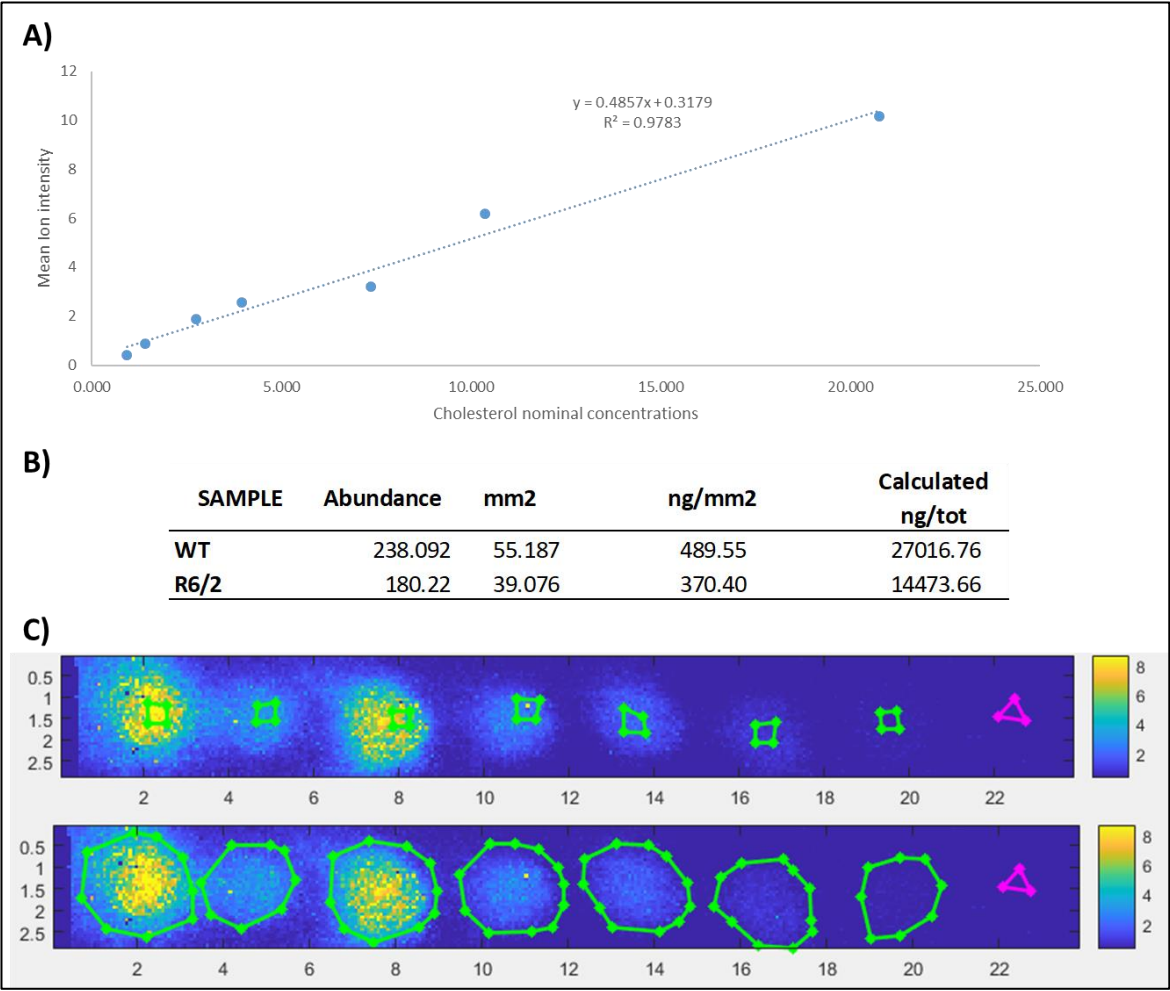


Figure 54 Results obtained from the quantitative IMS experiment of Chol on brain slices from WT and R6/2 mice. Panel A. shows the linearity obtained from the calibration curve. Panel B. shows the quantified Chol level in WT and R6/2 slices expressed as ng/mm2, highlighting a reduction of free Chol level in whole the whole brain area of R6/2 with respect to WT mice. Panel C. shows the results of IMS experiment acquiring Chol standard

5

5. Conclusions

5. CONCLUSIONS

The brain is the organ which is most rich in cholesterol, where it is a structural and functional component of glial and neuronal membranes. Chol is located in specific membrane microdomains, known as lipid rafts, that initiate, propagate, and maintain signal transduction. In the adult brain, Chol levels are maintained by local de novo synthesis because the BBB prevents its uptake from the circulation. Synaptic transmission is sensitive to newly synthesized Chol, so changes in Chol biosynthesis affects vesicle formation, recycling, and fusion, as well as the activity of neurotransmitter receptors.

Several diseases have been linked to dyshomeostasis of brain Chol production and degradation, including HD. HD is a dominantly inherited neurodegenerative disorder caused by an abnormal expansion of cytosine-adenosine-guanine (CAG) repeats in the first exon of the IT15 gene, leading to the formation of a pathological polyQ tract ($Q > 40$) in huntingtin (HTT) protein. This results in the production of a mutant huntingtin (mHTT) protein with an abnormally long polyglutamine repeat. Those with greater than 39 CAG repeats are certain to develop the disease, whilst reduced penetrance is seen between 36 and 39 repeats. Different molecular and cellular dysfunctions have been reported in HD cells and mouse models and in human post-mortem material, (9,10) including alterations of brain Chol biosynthesis (11,12). Chol precursors such as lanosterol, lathosterol, and desmosterol and the enzymatic activity of 3-hydroxy-3-methylglutaryl-coenzyme A reductase (HMGCR) were found downregulated in the brain of several HD animal models, already in the pre-symptomatic stage of the disease, leading to a significantly lower Chol content at later times (13–15). Chol treatment ameliorates neurite outgrowth defects in HD neurons in vitro (16), and brain-permeable nanoparticles loaded with Chol prevent cognitive decline and rescue synaptic dysfunction in HD mice (17), indicating a relationship between neuronal function and exogenous Chol.

Starting from these bases, the presented Ph.D. thesis explored the use of mass spectrometry in the study of HD in an animal model of the disease (R6/2 mice) and the possibility to use the proposed technique for clinical trials.

In particular, in the first part of the Ph.D. we developed and validated, according to EMA guidelines,

an LC-MS method for the quantitation of exogenous administered Chol to evaluate the efficacy of nose-to-brain delivery after Chol loaded liposomes treatment. We performed four different trial, three single dose treatment and one repeated dose treatment. Both the acute treatments highlighted how, in the brain areas, D6-Chol levels increased in the first 24 hours and no decline was observed (remaining stable until 72 hours) suggesting a slow elimination rate from all the brain areas. No differences were observed between the selected brain areas of the two mice genotypes in acute trials, with the only exception of the levels in the striatum of R6/2 transgenic mice 48h after the last administration in the repeated dose treatment. This evidence suggested that R6/2 mice used administered Chol to restore the altered metabolic state in the striatum tissue, that this the most affected tissue by the neurodegeneration in HD. Taken together, our observations confirmed the efficacy of nose-to-brain Chol delivery as a possible strategy to increase Chol availability in the HD brain using a non-invasive approach. In the second part of the Ph.D. project we developed an innovative UPLC-MRM method for the simultaneous quantitation of oxysterols and Chol precursor to investigate the altered metabolic state in the mouse model of the disease. The proposed method included an alkaline hydrolysis reaction optimized in terms of KOH concentration, time and temperature of incubation. The performances of the method were evaluated throughout a validation process and finally compared in terms of calculated concentrations with a commercial kit. The obtained results showed the good reproducibility and accuracy of the method, both using plasma and brain matrices. We investigated the Chol metabolites levels after a chronic treatment with Chol-loaded liposomes.

Interestingly, the treatment with D6-Chol-loaded liposomes partially restored the desmosterol levels, that were significantly lower in R6/2 mice with respect to WT mice.

Moreover, the levels of 24SOHC were significantly different between WT and treated R6/2 mice, suggesting that treated mice used administered Chol to restore the metabolic deficit in Chol synthesis. Taken together all these results suggested that the reduction in brain Chol synthesis mostly involved the astrocytes with a significant reduction of desmosterol levels in R6/2 mice. The significantly lower levels of 24SOHC in treated R6/2 mice with the higher levels of desmosterol suggested that the use of administered Chol helped to maintain the steady state of Chol synthesis.

Starting from a method previously published by Angelini et al. ⁹⁸, we proposed the MSI study of

desmosterol, Chol and 24SOHC. The results obtained highlighted the limits of using an instrument without the capability of doing MSn experiments. The final images obtained were not specific for 24SOHC and desmosterol since they had the same m/z of other Chol metabolites and of other oxidation products of Chol. Finally, we compared the results of quantitative MSI of Chol on WT and R6/2 brain slices and we confirmed that the levels of Chol are lower in transgenic mice. Future MSI studies will include the analysis of more brain slices and a comparison with histological images. The final aim will be the accurate quantitation of free Chol levels in brain slices focusing our attention on each specific area.

In conclusion, we proposed an integrated mass spectrometric approach for the study of HD, starting from a validated LC-MS method for the kinetic study of administered D6-Chol that showed the efficacy of its nose-to-brain delivery using liposomes. In parallel, the validated method for Chol metabolites gave us an important tool to evaluate the altered metabolism in R6/2 mice and HD patients as well. The method showed a good reproducibility and in future it will be integrated with other Chol metabolites and precursor and bile acids, to obtain a more comprehensive targeted lipidomic method. Finally, the integration of the LC-MS results with MSI results will be the final confirmation of the altered Chol metabolism, highlighting the reduced free Chol levels in R6/2 mice. Future experiments will include the use of a mass analyser that allows MSn experiments in order to obtain specific MSI results for the Chol metabolites and an accurate quantitation of the free levels of each one in the specific brain areas.

6. Bibliography

6. BIBLIOGRAPHY

1. MacDonald, M. E. *et al.* A novel gene containing a trinucleotide repeat that is expanded and unstable on Huntington's disease chromosomes. *Cell* **72**, 971–983 (1993).
2. Gil, J. M. & Rego, A. C. Mechanisms of neurodegeneration in Huntington's disease. *Eur. J. Neurosci.* **27**, 2803–2820 (2008).
3. Cattaneo, E. *et al.* Loss of normal huntingtin function: new developments in Huntington's disease research. *Trends Neurosci.* **24**, 182–188 (2001).
4. Cattaneo, E. Dysfunction of wild-type huntingtin in Huntington disease. *News Physiol. Sci. Int. J. Physiol. Prod. Jointly Int. Union Physiol. Sci. Am. Physiol. Soc.* **18**, 34–37 (2003).
5. Ross, C. A. & Tabrizi, S. J. Huntington's disease: from molecular pathogenesis to clinical treatment. *Lancet Neurol.* **10**, 83–98 (2011).
6. Bates, G. P. *et al.* Huntington disease. *Nat. Rev. Dis. Primer* **1**, 15005 (2015).
7. Warby, S. C. *et al.* HTT haplotypes contribute to differences in Huntington disease prevalence between Europe and East Asia. *Eur. J. Hum. Genet. EJHG* **19**, 561–566 (2011).
8. Walker, F. O. Huntington's disease. *Lancet Lond. Engl.* **369**, 218–228 (2007).
9. Myers, R. H. Huntington's disease genetics. *NeuroRx J. Am. Soc. Exp. Neurother.* **1**, 255–262 (2004).
10. Snowden, J. S., Craufurd, D., Griffiths, H. L. & Neary, D. Awareness of involuntary movements in Huntington disease. *Arch. Neurol.* **55**, 801–805 (1998).
11. Wyant, K. J., Ridder, A. J. & Dayalu, P. Huntington's Disease-Update on Treatments. *Curr. Neurol. Neurosci. Rep.* **17**, 33 (2017).
12. Robins Wahlin, T. B. *et al.* High suicidal ideation in persons testing for Huntington's disease. *Acta Neurol. Scand.* **102**, 150–161 (2000).
13. Kirkwood, S. C., Su, J. L., Conneally, P. M. & Foroud, T. Progression of Symptoms in the Early and Middle Stages of Huntington Disease. *Arch. Neurol.* **58**, 273–278 (2001).
14. Valenza, M. & Cattaneo, E. Emerging roles for cholesterol in Huntington's disease. *Trends Neurosci.* **34**, 474–486 (2011).
15. DiFiglia, M. *et al.* Huntingtin is a cytoplasmic protein associated with vesicles in human and rat brain neurons. *Neuron* **14**, 1075–1081 (1995).
16. Damiano, M., Galvan, L., Déglon, N. & Brouillet, E. Mitochondria in Huntington's disease. *Biochim. Biophys. Acta* **1802**, 52–61 (2010).
17. Sharp, A. H. *et al.* Widespread expression of Huntington's disease gene (IT15) protein product. *Neuron* **14**, 1065–1074 (1995).
18. Graham, R. K. *et al.* Levels of mutant huntingtin influence the phenotypic severity of Huntington disease in YAC128 mouse models. *Neurobiol. Dis.* **21**, 444–455 (2006).
19. Halliday, G. M. *et al.* Regional specificity of brain atrophy in Huntington's disease. *Exp. Neurol.* **154**, 663–672 (1998).
20. Vonsattel, J. P. & DiFiglia, M. Huntington disease. *J. Neuropathol. Exp. Neurol.* **57**, 369–384 (1998).

21. Guo, Z. *et al.* Striatal neuronal loss correlates with clinical motor impairment in Huntington's disease. *Mov. Disord. Off. J. Mov. Disord. Soc.* **27**, 1379–1386 (2012).
22. Ross, C. A. *et al.* Huntington disease: natural history, biomarkers and prospects for therapeutics. *Nat. Rev. Neurol.* **10**, 204–216 (2014).
23. Nishat. Huntington's disease (HD) research. *Open Access Government* <https://www.openaccessgovernment.org/huntingtons-disease-hd-research/107601/> (2021).
24. Li, S. H. *et al.* Huntington's disease gene (IT15) is widely expressed in human and rat tissues. *Neuron* **11**, 985–993 (1993).
25. Burg, J. M. van der, Björkqvist, M. & Brundin, P. Beyond the brain: widespread pathology in Huntington's disease. *Lancet Neurol.* **8**, 765–774 (2009).
26. Wild, E., Björkqvist, M. & Tabrizi, S. J. Immune markers for Huntington's disease? *Expert Rev. Neurother.* **8**, 1779–1781 (2008).
27. Björkqvist, M. *et al.* A novel pathogenic pathway of immune activation detectable before clinical onset in Huntington's disease. *J. Exp. Med.* **205**, 1869–1877 (2008).
28. Baig, S. S., Strong, M. & Quarrell, O. W. The global prevalence of Huntington's disease: a systematic review and discussion. *Neurodegener. Dis. Manag.* **6**, 331–343 (2016).
29. Evans, S. J. W. *et al.* Prevalence of adult Huntington's disease in the UK based on diagnoses recorded in general practice records. *J. Neurol. Neurosurg. Psychiatry* **84**, 1156–1160 (2013).
30. Gusella, J. F. *et al.* A polymorphic DNA marker genetically linked to Huntington's disease. *Nature* **306**, 234–238 (1983).
31. Takano, H. *et al.* Close associations between prevalences of dominantly inherited spinocerebellar ataxias with CAG-repeat expansions and frequencies of large normal CAG alleles in Japanese and Caucasian populations. *Am. J. Hum. Genet.* **63**, 1060–1066 (1998).
32. Carrassi, E. *et al.* Epidemiological Study of Huntington's Disease in the Province of Ferrara, Italy. *Neuroepidemiology* **49**, 18–23 (2017).
33. Squitieri, F., Griguoli, A., Capelli, G., Porcellini, A. & D'Alessio, B. Epidemiology of Huntington disease: first post-HTT gene analysis of prevalence in Italy. *Clin. Genet.* **89**, 367–370 (2016).
34. Brignull, H. R., Morley, J. F., Garcia, S. M. & Morimoto, R. I. Modeling polyglutamine pathogenesis in *C. elegans*. *Methods Enzymol.* **412**, 256–282 (2006).
35. Jackson, G. R. *et al.* Polyglutamine-expanded human huntingtin transgenes induce degeneration of *Drosophila* photoreceptor neurons. *Neuron* **21**, 633–642 (1998).
36. Mangiarini, L. *et al.* Exon 1 of the HD gene with an expanded CAG repeat is sufficient to cause a progressive neurological phenotype in transgenic mice. *Cell* **87**, 493–506 (1996).
37. Stack, E. C. *et al.* Combination therapy using minocycline and coenzyme Q10 in R6/2 transgenic Huntington's disease mice. *Biochim. Biophys. Acta* **1762**, 373–380 (2006).

38. Novak, V. *et al.* Enhancement of Vasoreactivity and Cognition by Intranasal Insulin in Type 2 Diabetes. *Diabetes Care* **37**, 751–759 (2014).
39. Beister, A. *et al.* The N-methyl-D-aspartate antagonist memantine retards progression of Huntington's disease. *J. Neural Transm. Suppl.* 117–122 (2004) doi:10.1007/978-3-7091-0579-5_14.
40. Cankurtaran, E. S., Ozalp, E., Soygur, H. & Cakir, A. Clinical experience with risperidone and memantine in the treatment of Huntington's disease. *J. Natl. Med. Assoc.* **98**, 1353–1355 (2006).
41. Dau, A., Gladding, C. M., Sepers, M. D. & Raymond, L. A. Chronic blockade of extrasynaptic NMDA receptors ameliorates synaptic dysfunction and pro-death signaling in Huntington disease transgenic mice. *Neurobiol. Dis.* **62**, 533–542 (2014).
42. Sofi, F., Macchi, C., Abbate, R., Gensini, G. F. & Casini, A. Mediterranean diet and health status: an updated meta-analysis and a proposal for a literature-based adherence score. *Public Health Nutr.* **17**, 2769–2782 (2014).
43. Marder, K. *et al.* Relationship of Mediterranean diet and caloric intake to phenoconversion in Huntington disease. *JAMA Neurol.* **70**, 1382–1388 (2013).
44. MIND diet associated with reduced incidence of Alzheimer's disease - PubMed. <https://pubmed-ncbi-nlm-nih-gov.libezproxy.open.ac.uk/25681666/>.
45. Ehrnhoefer, D. E. *et al.* Preventing mutant huntingtin proteolysis and intermittent fasting promote autophagy in models of Huntington disease. *Acta Neuropathol. Commun.* **6**, 16 (2018).
46. Hofmann, A. F. & Hagey, L. R. Key discoveries in bile acid chemistry and biology and their clinical applications: history of the last eight decades. *J. Lipid Res.* **55**, 1553–1595 (2014).
47. Leoni, V. & Caccia, C. The impairment of cholesterol metabolism in Huntington disease. *Biochim. Biophys. Acta - Mol. Cell Biol. Lipids* **1851**, 1095–1105 (2015).
48. Xu, H., Zhou, S., Tang, Q., Xia, H. & Bi, F. Cholesterol metabolism: New functions and therapeutic approaches in cancer. *Biochim. Biophys. Acta Rev. Cancer* **1874**, 188394 (2020).
49. Carson, J. A. S. *et al.* Dietary Cholesterol and Cardiovascular Risk: A Science Advisory From the American Heart Association. *Circulation* **141**, e39–e53 (2020).
50. Soliman, G. A. Dietary Cholesterol and the Lack of Evidence in Cardiovascular Disease. *Nutrients* **10**, (2018).
51. Russell, D. W. The enzymes, regulation, and genetics of bile acid synthesis. *Annu. Rev. Biochem.* **72**, 137–174 (2003).
52. Dietschy, J. M. & Turley, S. D. Thematic review series: brain Lipids. Cholesterol metabolism in the central nervous system during early development and in the mature animal. *J. Lipid Res.* **45**, 1375–1397 (2004).
53. Maxfield, F. R. & Tabas, I. Role of cholesterol and lipid organization in disease. *Nature* **438**, 612–621 (2005).
54. Björkhem, I. & Meaney, S. Brain cholesterol: long secret life behind a barrier. *Arterioscler. Thromb. Vasc. Biol.* **24**, 806–815 (2004).

55. Chobanian, A. V. & Hollander, W. Body cholesterol metabolism in man. I. The equilibration of serum and tissue cholesterol. *J. Clin. Invest.* **41**, 1732–1737 (1962).
56. Meaney, S. *et al.* Evidence that the major oxysterols in human circulation originate from distinct pools of cholesterol: a stable isotope study. *J. Lipid Res.* **42**, 70–78 (2001).
57. Thelen, K. M., Falkai, P., Bayer, T. A. & Lütjohann, D. Cholesterol synthesis rate in human hippocampus declines with aging. *Neurosci. Lett.* **403**, 15–19 (2006).
58. Pfrieger, F. W. & Ungerer, N. Cholesterol metabolism in neurons and astrocytes. *Prog. Lipid Res.* **50**, 357–371 (2011).
59. Nieweg, K., Schaller, H. & Pfrieger, F. W. Marked differences in cholesterol synthesis between neurons and glial cells from postnatal rats. *J. Neurochem.* **109**, 125–134 (2009).
60. Pfrieger, F. W. Role of cholesterol in synapse formation and function. *Biochim. Biophys. Acta* **1610**, 271–280 (2003).
61. Fünfschilling, U., Saher, G., Xiao, L., Möbius, W. & Nave, K.-A. Survival of adult neurons lacking cholesterol synthesis in vivo. *BMC Neurosci.* **8**, 1 (2007).
62. Petrov, A. M., Kasimov, M. R. & Zefirov, A. L. Brain Cholesterol Metabolism and Its Defects: Linkage to Neurodegenerative Diseases and Synaptic Dysfunction. *Acta Naturae* **8**, 58–73 (2016).
63. Peake, K. B. & Vance, J. E. Normalization of cholesterol homeostasis by 2-hydroxypropyl- β -cyclodextrin in neurons and glia from Niemann-Pick C1 (NPC1)-deficient mice. *J. Biol. Chem.* **287**, 9290–9298 (2012).
64. Koudinov, A. R. & Koudinova, N. V. Essential role for cholesterol in synaptic plasticity and neuronal degeneration. *FASEB J. Off. Publ. Fed. Am. Soc. Exp. Biol.* **15**, 1858–1860 (2001).
65. Xie, C., Lund, E. G., Turley, S. D., Russell, D. W. & Dietschy, J. M. Quantitation of two pathways for cholesterol excretion from the brain in normal mice and mice with neurodegeneration. *J. Lipid Res.* **44**, 1780–1789 (2003).
66. Horton, J. D., Goldstein, J. L. & Brown, M. S. SREBPs: activators of the complete program of cholesterol and fatty acid synthesis in the liver. *J. Clin. Invest.* **109**, 1125–1131 (2002).
67. Cartagena, C. M., Burns, M. P. & Rebeck, G. W. 24S-hydroxycholesterol effects on lipid metabolism genes are modeled in traumatic brain injury. *Brain Res.* **1319**, 1–12 (2010).
68. Suzuki, R., Ferris, H. A., Chee, M. J., Maratos-Flier, E. & Kahn, C. R. Reduction of the cholesterol sensor SCAP in the brains of mice causes impaired synaptic transmission and altered cognitive function. *PLoS Biol.* **11**, e1001532 (2013).
69. Camargo, N. *et al.* High-fat diet ameliorates neurological deficits caused by defective astrocyte lipid metabolism. *FASEB J. Off. Publ. Fed. Am. Soc. Exp. Biol.* **26**, 4302–4315 (2012).
70. Verheijen, M. H. G. *et al.* SCAP is required for timely and proper myelin membrane synthesis. *Proc. Natl. Acad. Sci. U. S. A.* **106**, 21383–21388 (2009).

71. Valenza, M. *et al.* Cholesterol biosynthesis pathway is disturbed in YAC128 mice and is modulated by huntingtin mutation. *Hum. Mol. Genet.* **16**, 2187–2198 (2007).
72. Samara, A. *et al.* Altered expression of 3-beta-hydroxysterol delta-24-reductase/selective Alzheimer's disease indicator-1 gene in Huntington's disease models. *J. Endocrinol. Invest.* **37**, 729–737 (2014).
73. Valenza, M. *et al.* Dysfunction of the cholesterol biosynthetic pathway in Huntington's disease. *J. Neurosci. Off. J. Soc. Neurosci.* **25**, 9932–9939 (2005).
74. Valenza, M. *et al.* Cholesterol Defect Is Marked across Multiple Rodent Models of Huntington's Disease and Is Manifest in Astrocytes. *J. Neurosci.* **30**, 10844–10850 (2010).
75. Fester, L. *et al.* Cholesterol-promoted synaptogenesis requires the conversion of cholesterol to estradiol in the hippocampus. *Hippocampus* **19**, 692–705 (2009).
76. Goritz, C., Mauch, D. H. & Pfrieder, F. W. Multiple mechanisms mediate cholesterol-induced synaptogenesis in a CNS neuron. *Mol. Cell. Neurosci.* **29**, 190–201 (2005).
77. Li, J. Y., Plomann, M. & Brundin, P. Huntington's disease: A synaptopathy? *Trends Mol. Med.* **9**, 414–420 (2003).
78. Levine, M. S., Cepeda, C., Hickey, M. A., Fleming, S. M. & Chesselet, M. F. Genetic mouse models of Huntington's and Parkinson's diseases: Illuminating but imperfect. *Trends Neurosci.* **27**, 691–697 (2004).
79. Schulz, J. G. *et al.* HMG-CoA reductase inhibition causes neurite loss by interfering with geranylgeranylpyrophosphate synthesis. *J. Neurochem.* **89**, 24–32 (2004).
80. Wang, B. & Tontonoz, P. Liver X receptors in lipid signalling and membrane homeostasis. *Nat. Rev. Endocrinol.* **14**, 452–463 (2018).
81. Futter, M. *et al.* Wild-type but not mutant huntingtin modulates the transcriptional activity of liver X receptors. *J. Med. Genet.* **46**, 438–446 (2009).
82. Valenza, M. *et al.* Cholesterol-loaded nanoparticles ameliorate synaptic and cognitive function in Huntington's disease mice. *EMBO Mol. Med.* **7**, 1547–1564 (2015).
83. Birolini, G. *et al.* Striatal infusion of cholesterol promotes dose-dependent behavioral benefits and exerts disease-modifying effects in Huntington's disease mice. *EMBO Mol. Med.* **12**, e12519 (2020).
84. Reese, T. S. & Karnovsky, M. J. Fine structural localization of a blood-brain barrier to exogenous peroxidase. *J. Cell Biol.* **34**, 207–217 (1967).
85. Banks, W. A., Morley, J. E., Niehoff, M. L. & Mattern, C. Delivery of testosterone to the brain by intranasal administration: comparison to intravenous testosterone. *J. Drug Target.* **17**, 91–97 (2009).
86. Pardeshi, C. V. & Belgamwar, V. S. Direct nose to brain drug delivery via integrated nerve pathways bypassing the blood-brain barrier: an excellent platform for brain targeting. *Expert Opin. Drug Deliv.* **10**, 957–972 (2013).
87. Yates III, J. R. A century of mass spectrometry: from atoms to proteomes. *Nat. Methods* **8**, 633–637 (2011).
88. Introduction. in *Mass Spectrometry* 2–13 (Wiley, 2007).

89. Petrović, M., Hernando, M. D., Díaz-Cruz, M. S. & Barceló, D. Liquid chromatography–tandem mass spectrometry for the analysis of pharmaceutical residues in environmental samples: a review. *J. Chromatogr. A* **1067**, 1–14 (2005).
90. Korfmacher, W. A. Foundation review: Principles and applications of LC-MS in new drug discovery. *Drug Discov. Today* **10**, 1357–1367 (2005).
91. Gika, H., Virgiliou, C., Theodoridis, G., Plumb, R. S. & Wilson, I. D. Untargeted LC/MS-based metabolic phenotyping (metabonomics/metabolomics): The state of the art. *J. Chromatogr. B Analyt. Technol. Biomed. Life. Sci.* **1117**, 136–147 (2019).
92. Snyder, N. Investigations Of Bioactivity, Disposition, And Metabolism Of Lipids Through Liquid Chromatography-Mass Spectrometry. (2013).
93. Caprioli, R. M., Farmer, T. B. & Gile, J. Molecular imaging of biological samples: localization of peptides and proteins using MALDI-TOF MS. *Anal. Chem.* **69**, 4751–4760 (1997).
94. Morosi, L. *et al.* Quantitative determination of niraparib and olaparib tumor distribution by mass spectrometry imaging. *Int. J. Biol. Sci.* **16**, 1363–1375 (2020).
95. Görög, S. Advances in the analysis of steroid hormone drugs in pharmaceuticals and environmental samples (2004-2010). *J. Pharm. Biomed. Anal.* **55**, 728–743 (2011).
96. Steven, R. T. & Bunch, J. Repeat MALDI MS imaging of a single tissue section using multiple matrices and tissue washes. *Anal. Bioanal. Chem.* **405**, 4719–4728 (2013).
97. Shariatgorji, M. *et al.* Comprehensive mapping of neurotransmitter networks by MALDI-MS imaging. *Nat. Methods* **16**, 1021–1028 (2019).
98. Angelini, R. *et al.* Visualizing Cholesterol in the Brain by On-Tissue Derivatization and Quantitative Mass Spectrometry Imaging. *Anal. Chem.* **93**, 4932–4943 (2021).
99. Swales, J. G., Hamm, G., Clench, M. R. & Goodwin, R. J. A. Mass spectrometry imaging and its application in pharmaceutical research and development: A concise review. *Int. J. Mass Spectrom.* **437**, 99–112 (2019).
100. Aikawa, H. *et al.* Visualizing spatial distribution of alectinib in murine brain using quantitative mass spectrometry imaging. *Sci. Rep.* **6**, 23749 (2016).
101. Takai, N., Tanaka, Y., Inazawa, K. & Saji, H. Quantitative analysis of pharmaceutical drug distribution in multiple organs by imaging mass spectrometry. *Rapid Commun. Mass Spectrom. RCM* **26**, 1549–1556 (2012).
102. Koeniger, S. L. *et al.* A quantitation method for mass spectrometry imaging. *Rapid Commun. Mass Spectrom. RCM* **25**, 503–510 (2011).
103. Dzeletovic, S., Babiker, A., Lund, E. & Diczfalusy, U. Time course of oxysterol formation during in vitro oxidation of low density lipoprotein. *Chem. Phys. Lipids* **78**, 119–128 (1995).
104. Nagy, K. *et al.* Analysis of sterols by high-performance liquid chromatography/mass spectrometry combined with chemometrics. *Rapid Commun. Mass Spectrom. RCM* **20**, 2433–2440 (2006).
105. Griffiths, W. J. *et al.* Current trends in oxysterol research. *Biochem. Soc. Trans.* **44**, 652–658 (2016).

106. McDonald, J. G., Smith, D. D., Stiles, A. R. & Russell, D. W. A comprehensive method for extraction and quantitative analysis of sterols and secosteroids from human plasma. *J. Lipid Res.* **53**, 1399–1409 (2012).
107. Honda, A. *et al.* Highly sensitive quantification of key regulatory oxysterols in biological samples by LC-ESI-MS/MS. *J. Lipid Res.* **50**, 350–357 (2009).
108. Sidhu, R. *et al.* A validated LC-MS/MS assay for quantification of 24(S)-hydroxycholesterol in plasma and cerebrospinal fluid. *J. Lipid Res.* **56**, 1222–1233 (2015).
109. Jiang, X. *et al.* A sensitive and specific LC-MS/MS method for rapid diagnosis of Niemann-Pick C1 disease from human plasma. *J. Lipid Res.* **52**, 1435–1445 (2011).
110. Lavrynenko, O., Nedielkov, R., Möller, H. M. & Shevchenko, A. Girard derivatization for LC-MS/MS profiling of endogenous ecdysteroids in *Drosophila*. *J. Lipid Res.* **54**, 2265–2272 (2013).
111. DeBarber, A. E. *et al.* Profiling sterols in cerebrotendinous xanthomatosis: utility of Girard derivatization and high resolution exact mass LC-ESI-MS(n) analysis. *J. Chromatogr. B Analyt. Technol. Biomed. Life. Sci.* **879**, 1384–1392 (2011).
112. Soroosh, P. *et al.* Oxysterols are agonist ligands of ROR γ t and drive Th17 cell differentiation. *Proc. Natl. Acad. Sci. U. S. A.* **111**, 12163–12168 (2014).
113. Crick, P. J. *et al.* Quantitative charge-tags for sterol and oxysterol analysis. *Clin. Chem.* **61**, 400–411 (2015).
114. Mendiara, I. *et al.* Determination of total plasma oxysterols by enzymatic hydrolysis, solid phase extraction and liquid chromatography coupled to mass-spectrometry. *J. Pharm. Biomed. Anal.* **150**, 396–405 (2018).
115. Kaza, M., Karaźniewicz-Łada, M., Kosicka, K., Siemiątkowska, A. & Rudzki, P. J. Bioanalytical method validation: new FDA guidance vs. EMA guideline. Better or worse? *J. Pharm. Biomed. Anal.* **165**, 381–385 (2019).
116. Selvaraj, K., Gowthamarajan, K. & Karri, V. V. S. R. Nose to brain transport pathways an overview: potential of nanostructured lipid carriers in nose to brain targeting. *Artif. Cells Nanomedicine Biotechnol.* **46**, 2088–2095 (2018).
117. Khan, A. R., Liu, M., Khan, M. W. & Zhai, G. Progress in brain targeting drug delivery system by nasal route. *J. Controlled Release* **268**, 364–389 (2017).
118. Dhuria, S. V., Hanson, L. R. & Frey, W. H. Intranasal delivery to the central nervous system: mechanisms and experimental considerations. *J. Pharm. Sci.* **99**, 1654–1673 (2010).
119. Villani, C. *et al.* Lovastatin fails to improve motor performance and survival in methyl-CpG-binding protein2-null mice. *eLife* **5**, (2016).
120. Birolini, G. *et al.* Insights into kinetics, release, and behavioral effects of brain-targeted hybrid nanoparticles for cholesterol delivery in Huntington's disease. *J. Control. Release Off. J. Control. Release Soc.* **330**, 587–598 (2021).
121. Lütjohann, D., Lopez, A. M., Chuang, J.-C., Kerksiek, A. & Turley, S. D. Identification of Correlative Shifts in Indices of Brain Cholesterol Metabolism in the C57BL6/Mecp2tm1.1Bird Mouse, a Model for Rett Syndrome. *Lipids* **53**, 363–373 (2018).
122. Gu, H., Liu, G., Wang, J., Aubry, A.-F. & Arnold, M. E. Selecting the correct weighting factors for linear and quadratic calibration curves with least-squares regression algorithm in bioanalytical LC-MS/MS assays and impacts of using

- incorrect weighting factors on curve stability, data quality, and assay performance. *Anal. Chem.* **86**, 8959–8966 (2014).
123. Nunes, V. S., Cazita, P. M., Catanozi, S., Nakandakare, E. R. & Quintão, E. C. R. Decreased content, rate of synthesis and export of cholesterol in the brain of apoE knockout mice. *J. Bioenerg. Biomembr.* **50**, 283–287 (2018).
124. Allen, L. B., Genaro-Mattos, T. C., Porter, N. A., Mirnics, K. & Korade, Z. Desmosterolosis and desmosterol homeostasis in the developing mouse brain. *J. Inherit. Metab. Dis.* **42**, 934–943 (2019).

7.1. List of publications related to the presented Ph.D. project

1. Birolini G, Valenza M, Ottonelli I, Passoni A, Favagrossa M, Duskey JT, et al. Insights into kinetics, release, and behavioral effects of brain-targeted hybrid nanoparticles for cholesterol delivery in Huntington's disease. *J Control Release Off J Control Release Soc.* 10 febbraio 2021;330:587–98.

2. Passoni A, Favagrossa M, Colombo L, Bagnati R, Gobbi M, Diomedede L, et al. Efficacy of Cholesterol Nose-to-Brain Delivery for Brain Targeting in Huntington's Disease. *ACS Chem Neurosci.* 5 febbraio 2020;11(3):367–72.

Efficacy of Cholesterol Nose-to-Brain Delivery for Brain Targeting in Huntington's Disease

Alice Passoni,^{†,‡,§} Monica Favagrossa,^{†,‡,§} Laura Colombo,[†] Renzo Bagnati,^{†,§} Marco Gobbi,[†] Luisa Diomede,^{†,§} Giulia Birolini,^{‡,§} Eleonora Di Paolo,^{‡,§} Marta Valenza,^{‡,§} Elena Cattaneo,^{‡,§} and Mario Salmons^{*,†,§}

[†]Istituto di Ricerche Farmacologiche Mario Negri IRCCS, via Mario Negri 2, 20156 Milan, Italy

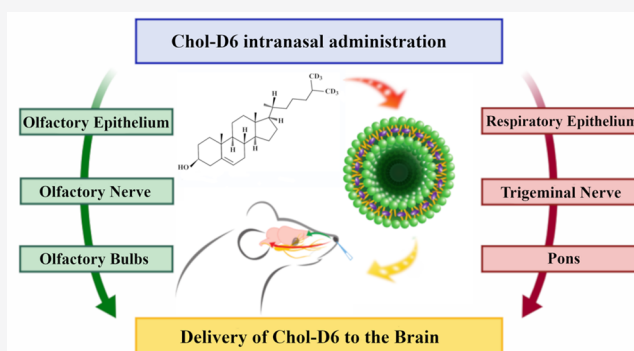
[‡]Department of Biosciences, University of Milan, via G. Celoria 26, 20133, Milan, Italy

[§]Istituto Nazionale di Genetica Molecolare "Romeo ed Enrica Invernizzi," via F. Sforza 35, 20122, Milan, Italy

Supporting Information

ABSTRACT: The current pharmacological treatment of Huntington's disease (HD) is palliative, and therapies to restore functions in patients are needed. One of the pathways affected in HD involves brain cholesterol (Chol) synthesis, which is essential for optimal synaptic transmission. Recently, it was reported that in a HD mouse model, the delivery of exogenous Chol to the brain with brain-permeable nanoparticles protected animals from cognitive decline and rescued synaptic communication, indicating Chol as a therapeutic candidate. We examined whether nose-to-brain delivery, already used in human therapy, could be an alternative, noninvasive strategy to deliver Chol to the adult brain and, in the future, replenish Chol in the HD brain. We gave wild-type (WT) mice a single intranasal (IN) dose of liposomes loaded with deuterium-labeled cholesterol (Chol-D6, to distinguish and quantify the exogenous cholesterol from the native one) (200 μ g Chol-D6/dose). After different intervals, Chol-D6 levels, determined by LC-MS in plasma, striatum, cortex, and cerebellum, reached a steady-state concentration of 0.400 ng/mg between 24 and 72 h. A subsequent acute study confirmed the kinetic profiles of Chol-D6 in all tissues, indicating correspondence between the dose (two doses of 200 μ g Chol-D6/dose) and the calculated brain area concentration (0.660 ng/mg). Finally, in WT mice given repeated IN doses, the average Chol-D6 level after 24 h was about 1.5 ng/mg in all brain areas. Our data indicate the effectiveness of IN Chol-loaded liposomes to deliver Chol in different brain regions, opening the way to future investigations in HD mice.

KEYWORDS: Huntington's disease, brain cholesterol, nose-to-brain delivery, intranasal administration, LC-MS analysis, liposomes



1. INTRODUCTION

The brain is the most cholesterol-rich organ as more than 70% of cholesterol (Chol) is located in myelin sheaths, and the remainder is a structural and functional component of glial and neuronal membranes. Chol is located in specific membrane microdomains, known as lipid rafts, that initiate, propagate, and maintain signal transduction.¹ In the adult brain, Chol levels are maintained by local de novo synthesis because the blood-brain barrier (BBB) prevents its uptake from the circulation.² Synaptic transmission is sensitive to newly synthesized Chol, so changes in Chol biosynthesis affect vesicle formation, recycling, and fusion, as well as the activity of neurotransmitter receptors.^{3–5}

Several diseases have been linked to dyshomeostasis of brain Chol production and degradation, including Huntington's disease (HD). HD is a dominantly inherited neurodegenerative disorder caused by an abnormal expansion of cytosine-adenosine-guanine (CAG) repeats in the first exon of the IT15

gene, leading to the formation of a pathological polyQ tract (Q > 40) in huntingtin (HTT) protein (The Huntington's Disease Collaborative Research Group, 1993). As a consequence, neurons become dysfunctional and eventually die, leading to choreiform movements, cognitive decline, and psychiatric disturbance.^{6–8} Different molecular and cellular dysfunctions have been reported in HD cells and mouse models and in human post-mortem material,^{9,10} including alterations of brain Chol biosynthesis.^{11,12} Chol precursors such as lanosterol, lathosterol, and desmosterol and the enzymatic activity of 3-hydroxy-3-methylglutaryl-coenzyme A reductase (HMGCR) were found downregulated in the brain of several HD animal models, already in the presymptomatic stage of the disease, leading to a significantly lower Chol content at later

Received: October 28, 2019

Accepted: December 20, 2019

Published: December 20, 2019

times.^{13–15} Chol treatment ameliorates neurite outgrowth defects in HD neurons *in vitro*¹⁶ and brain-permeable nanoparticles loaded with Chol prevent cognitive decline and rescue synaptic dysfunction in HD mice,¹⁷ indicating a relationship between neuronal function and exogenous Chol.

Targeting the brain with drugs or molecules that do not pass the BBB (such as Chol) has always been challenging, and noninvasive strategies are attractive. Most treatments for central nervous system (CNS) disorders employ peripheral drug administration, which is limited by the difficulty of drug access to the CNS from the blood. Moreover, drugs given by these routes incur the first-pass metabolism and systemic clearance, which reduce their bioavailability.¹⁸

An alternative strategy for targeting CNS is nose-to-brain delivery, which can overcome the BBB. The neuroepithelium of the olfactory region is the only part of the body where the peripheral environment is in direct contact with the brain.¹⁹ Olfactory and trigeminal nerve pathways mostly mediate drug transport from the nasal cavity to the CNS. Through the olfactory nerve pathway, a drug crosses the cribriform plate and reaches the olfactory bulbs and the deeper part of the brain. Meanwhile, through the trigeminal nerve pathway, the drug is transported mostly to the pons and cerebrum, and to a lesser extent to the frontal and olfactory brain. Pathways involving vasculature, cerebrospinal fluid and lymphatic system all enrich the transport of molecules from the nasal cavity to the CNS.^{20,21}

Thus, the aim of this work was to explore the potential of intranasal (IN) Chol-D6-loaded liposomes as a noninvasive strategy for Chol delivery into the HD brain. We report quantifiable levels of Chol-D6 after acute and repeated IN treatments. We also found that Chol-D6 distributes evenly and accumulates in the brain of WT and HD mice, paving the way for further preclinical investigations. In addition, to quantify the brain distribution of exogenous Chol, we developed a liquid chromatography mass spectrometry (LC-MS)-based method, validated according to the European Medicine Agency (EMA) guidelines,²² in plasma and brain.

2. RESULTS AND DISCUSSION

2.1. Development and Validation of the LC-MS Method. Validation data are reported in detail in the [Supplementary Results](#).

2.2. Acute Treatments of 8-Week-Old WT and HD Mice. To assess the efficacy of IN delivery of Chol into the brain, we initially gave 8-week-old WT mice an acute dose of Chol-D6-loaded liposomes (200 μ g/mouse); animals were then euthanized after 1, 3, 6, 24, 48, and 72 h (3 animals/time-point). Chol-D6 concentrations were measured in plasma and three brain areas ([Figure 1](#)). Plasma concentrations reached a maximum of 2417 ± 313 ng/mL (mean \pm SD) after 24 h, declining to 839 ± 76 ng/mL (mean \pm SD) at 72 h. In the brain areas, Chol-D6 levels rose in the first 24 h but, unlike in plasma, did not decline, and they remained stable until 72 h. These data suggest a slow elimination rate in the brain.

We then ran an acute study to confirm the passage of the BBB and assess the relationship between administered dose and concentrations in plasma and different brain areas in WT and HD mice. Eight-week-old WT and HD mice were treated with two IN doses of 200 μ g/mouse of Chol-D6, 5 h apart (5 mice/time point/genotype), and were euthanized 3, 24, 48, and 72 h after the second dose. Plasma concentrations reached a maximum of 4350 ± 1207 ng/mL (mean \pm SD) and $4760 \pm$

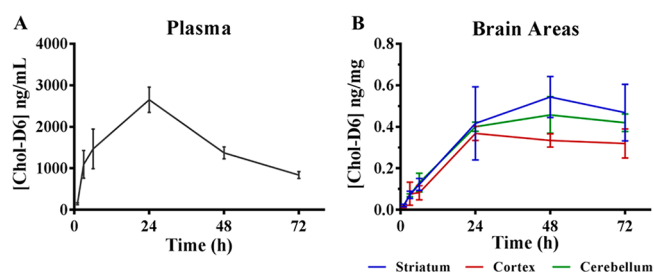


Figure 1. Chol-D6 levels in plasma (gray) (A), striatum (blue), cortex (red) and cerebellum (green) (B) of WT mice after single intranasal doses (connecting lines with error bars, mean \pm SD; $n = 3$ /time point).

703 ng/mL (mean \pm SD) after 24 h in HD and WT mice, respectively. Plasma levels declined with similar kinetic profiles in HD and WT mice to 1698 ± 295 ng/mL (mean \pm SD; $n = 7$) after 72 h. There were no significant differences between WT and HD mice since Chol-D6 had the same time-course profiles ([Figure 2](#)).

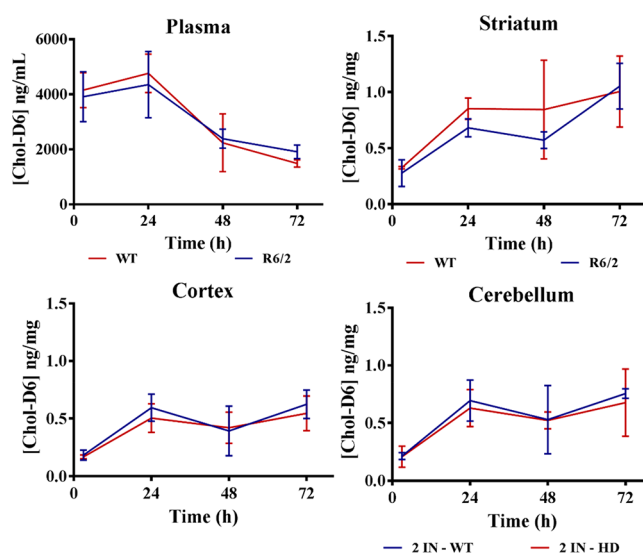


Figure 2. Chol-D6 levels in plasma (A), striatum (B), cortex (C), and cerebellum (D) of WT and HD mice after two intranasal doses, each with 200 μ g/mouse, 5 h apart (means \pm SD; $n = 5$ /time-point/genotype; blue, WT; red, HD).

Finally, we compared Chol-D6 levels at 24 h for single and double IN doses in plasma and brain areas of WT mice. Chol-D6 levels rose at least 61% after two IN doses, suggesting a linear relationship with the dose. Interestingly, Chol-D6 levels in the striatum rose 105% after two doses, confirming the effectiveness of nose-to-brain delivery to the target tissue of HD ([Table 1](#)).

2.3. Repeated Treatment in WT Mice. To assess the accumulation of Chol-D6 in the brain after multiple IN doses, we repeated the treatments of WT mice at 8 weeks of age with Chol-D6-loaded liposomes (200 μ g/dose). Chol-D6 levels in the striatum, cortex, and cerebellum were markedly higher after a single dose, indicating accumulation in the brain ([Figure 3](#)). With this schedule, Chol-D6 reached at least 1.5 ng/mg tissue in all the brain areas. Statistical analysis showed no significant differences in Chol-D6 levels in the brain areas after repeated dosing, confirming homogeneous distribution of Chol-D6 in

Table 1. Chol-D6 Levels 24 h after the Last IN Dose in WT Mice Given One or Two IN Doses

tissues	1 IN	2 IN	% increase 2 IN over 1 IN
plasma (ng/mL)	2650 \pm 305	4760 \pm 703	79.6
striatum (ng/mg)	0.416 \pm 0.176	0.853 \pm 0.095	105.0
cortex (ng/mg)	0.368 \pm 0.034	0.594 \pm 0.118	61.4
cerebellum (ng/mg)	0.400 \pm 0.022	0.694 \pm 0.179	73.5

^a1 IN = one dose, 200 μ g/dose; 2 IN = two doses, 5 h apart, 200 μ g/dose; mean \pm SD.

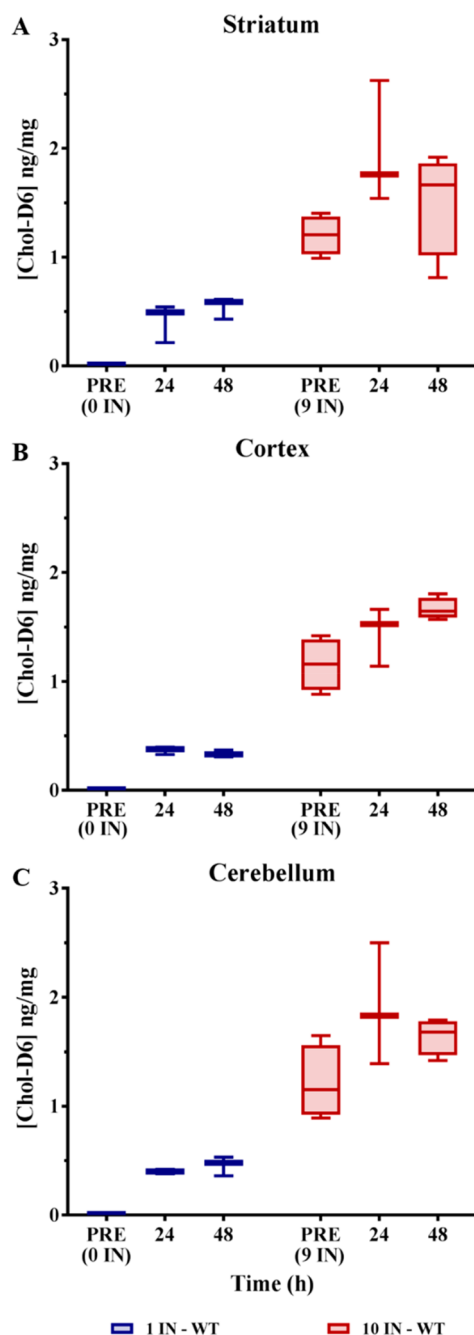


Figure 3. Chol-D6 levels in the striatum (A), cortex (B) and cerebellum (C) in WT mice after acute or repeated intranasal treatments. WT mice were treated every 2 days for 19 days (10 IN). Two days after the ninth dose, four mice/genotype were euthanized before the tenth treatment (PRE 9 IN). The remaining mice received the tenth IN and were euthanized at 24 and 48 h after the treatment.

the whole brain, suggesting both olfactory and trigeminal pathways are involved. The connections between the nasal cavity and the CNS through olfactory and trigeminal neurons have already been described.^{19,21,23} From the nasal olfactory epithelium, drugs are taken up into neuronal cells and transported to the olfactory bulb and the cerebrospinal fluid through the olfactory nerve pathways. The trigeminal nerve innervates both the olfactory and respiratory epithelium and enters the CNS in the pons, leading the distribution of drugs in the rostral brain.^{19,24} These two pathways permit the distribution of drugs to all brain areas. Our observations confirm the efficacy of nose-to-brain Chol delivery as a potential noninvasive approach to increase Chol availability in the HD brain.

3. CONCLUSIONS

To develop a new therapeutic strategy for HD based on Chol delivery to the brain, we set up an experimental approach to investigate the efficacy of exogenous IN Chol. We based our assumption on evidence that Chol biosynthesis is reduced in HD mouse brains^{11,13–15} and that exogenous Chol can rescue the HD phenotypes (ref 17 and unpublished data). Importantly, nose-to-brain delivery is safe and noninvasive and avoids hepatic first-pass metabolism. The nasal route for delivery of drugs that otherwise could not cross the BBB could be beneficial if translatable to clinical practice, and there are already examples in the literature.^{25–28}

In the present study, we also developed and validated according to EMA guidelines, a new LC-MS method to quantify the levels of exogenous Chol-D6 in brain areas and plasma after single or repeated IN doses. Chol-D6 reached measurable levels in the brain and persisted at least 72 h thanks to its slow elimination rate (Figure 1). After two doses HD and WT mice did not present any significant differences in Chol-D6 distribution and accumulation. The final comparison of the two acute treatments showed increases in Chol-D6 in plasma and the brain areas, from 61% in cortex up to 105% in the striatum. These results confirmed the effectiveness of nose-to-brain delivery. The Chol-D6 levels rose most in the striatum, the target tissue of HD (Table 1). Finally, Chol-D6 distributed and accumulated without differences after 10 IN doses in striatum, cortex, and cerebellum (Figure 3), indicating the involvement of both olfactory and trigeminal pathways.

The experimental design in this initial approach provides a detailed view of the effectiveness of the nose-to-brain delivery of Chol. It could also help lay the basis for further preclinical studies for evaluating the therapeutic potential of this approach to supply Chol to neurons affected in HD.

4. MATERIALS AND METHODS

4.1. Standard and Chemicals. Deuterated cholesterol (Chol-D6) (isotopic purity: 97 atom % D), phosphatidylcholine (PC), and β -sitosterol were obtained from Sigma-Aldrich (St Louis, MO, U.S.A.). LC-MS grade acetonitrile and formic acid were from Carlo

Erba, Milan, Italy. LC-MS grade deionized water was obtained from Milli-Ro 60 Water System, Millipore, Milford, MA, U.S.A. Chol-D6 and β -sitosterol, used as the internal standard (IS), were prepared as stock solutions in methanol (MeOH) at 1 mg/mL. The Chol-D6 stock solution was diluted in MeOH to obtain a series of seven working solutions for the construction of calibration curves, validation and sample analysis. The IS stock solution was diluted to 5 μ g/mL in the same organic solvent. All solutions were stored at -20°C until use.

4.2. Liposomes. Chol-D6 was entrapped in oligolamellar, 280–300 nm-wide liposomes, following the dehydration–rehydration method.^{29,30} Briefly, Chol-D6 and PC were dissolved in chloroform at a 1:1 molar ratio. After solvent evaporation, the lipid film was rehydrated with phosphate buffer solution (PBS) and ultracentrifuged at 100 000g for 35 min at 4°C to separate residual lipids. Liposomes were resuspended with 10 mM phosphate-buffered saline, pH 7.4. The concentration of Chol-D6 entrapped in liposomes was determined by HPLC (System Gold instrument – Beckman) equipped with an Eco Cart-LiChrospher 60 RP-select B column (125×3 mm, particle size 5 μm , pore size 60 Å, Merck) at 214 nm. Separation was done with isocratic elution at 100% methanol:isopropanol: NH_4OH (70%:30%, 5 mM) for 12 min. The flow rate was 0.6 mL/min. Entrapment efficacy was $\pm 90\%$, and liposomes were diluted to a final Chol-D6 concentration of 5.6 mg/mL.

4.3. Animal Model and Treatment Schedules. We used an R6/2 colony generated to overexpress the first exon of the human mutant huntingtin gene with approximately 144–150 CAG repeats. The R6/2 line was genotyped by polymerase chain reaction (PCR) on DNA from tail samples at weaning.⁵¹

The IRFMN adheres to the principles set out in the following laws, regulations, and policies governing the care and use of laboratory animals: Italian Governing Law (D.lgs 26/2014; Authorisation n.19/2008-A issued March 6, 2008 by Ministry of Health); Mario Negri Institutional Regulations and Policies providing internal authorization for persons conducting animal experiments (Quality Management System Certificate – UNI EN ISO 9001:2015 – Reg. No. 6121); the NIH Guide for the Care and Use of Laboratory Animals (2011 edition) and EU directives and guidelines (EEC Council Directive 2010/63/UE).

Liposomes were administered to mice by applying 6 μL of a 5.6 mg/mL solution three times to the inner surface of each nostril for a total of 36 μL , corresponding to a final dose of 200 μg of Chol-D6/mouse.³² For the first acute studies, 8-week-old wild-type (WT) mice were euthanized 1, 3, 6, 24, 48, and 72 h after a single IN dose (3 mice/time point). For the acute study, 8-week-old WT and R6/2 mice were given two doses of 200 μg /mouse of Chol-D6, 5 h apart (5 mice/time point/genotype). Mice were euthanized 3, 24, 48, and 72 h from the second IN treatment. For repeated treatments, 8-week-old WT mice received 9 or 10 IN doses, once every 2 days (4 mice/time point). One group of animals was euthanized 2 days after the ninth IN treatment, while the others received the tenth IN dose and were euthanized 24 and 48 h later. Blood samples were collected with the anticoagulant K_3EDTA , and plasma samples were obtained by centrifugation at 2000g for 15 min. Brains were immediately removed and striatum, cortex, and cerebellum were collected separately. All samples were stored at -80°C until LC-MS analysis.

4.4. LC-MS. Chol-D6 levels were determined using a 1200 Series HPLC system (Agilent Technologies, Santa Clara, CA, U.S.A.) interfaced to an API 5500 triple quadrupole mass spectrometer (Sciex, Thornhill, Ontario, Canada). The mass spectrometer was equipped with an atmospheric pressure chemical ionization (APCI) source operating in positive ion and selected reaction monitoring (SRM) mode to measure the product ions obtained in a collision cell from the protonated $[\text{M} - \text{H}_2\text{O}]^+$ ions of the analytes. The transitions identified during the optimization of the method were m/z 375.3–152.1 (quantification transition) and m/z 375.3–167.1 (qualification transition) for Chol-D6; m/z 397.3–147.1 (quantification transition) and m/z 397.3–161.1 (qualification transition) for β -sitosterol as IS. The ion source settings were as follows: nebulized current (NC) 3; curtain gas (CUR) 30; collision gas (CAD) 7; source temperature 400

$^{\circ}\text{C}$; ion source gas 1 (GS1) 60 and gas 2 (GS2) 30. Chol-D6 and β -sitosterol were separated on a Gemini C18 column (50×2 mm; 5 μm particle size), using an isocratic gradient in methanol at 35°C .

4.4.1. Sample Preparation. Plasma. Fifty microliters of plasma was diluted with 200 μL of ethanol containing 200 ng of IS. Samples were vortexed and centrifuged at 13 200 rpm for 15 min; 4 μL aliquots of the supernatants were injected directly into the LC-MS system.

Striatum, Cortex, and Cerebellum. Forty milligrams of each brain area was homogenized in 1 mL of ethanol/water 4:1 (v/v), containing 500 ng of IS. Homogenates were centrifuged for 15 min at 13 200 rpm at 4°C , and the supernatants were injected into the LC-MS apparatus.

4.4.2. Validation. The LC-MS method was validated in mouse plasma and brain tissue following EMA guidelines²² (EMA). Accuracy was determined by expressing the calculated concentration as a percentage of the nominal concentration. Accuracy had to be within 15% of the nominal value for each concentration ($\pm 20\%$ of the nominal value for the lower limit of quantification (LLOQ) as an exception); the precision, expressed by the CV (%), had not to exceed 15% for all concentrations, except 20% for the LLOQ. A freshly prepared calibration curve was analyzed during each validation run.

Calibration Curves. All calibration curves during the validation included one zero point and six calibration points at the concentrations of 50, 100, 250, 500, 1000, 2500, and 5000 ng/mL and 0.030, 0.100, 0.300, 1.00, 3.00, and 10.0 ng/mg of Chol-D6 respectively for plasma and brain samples. The IS concentration was 100 ng/mL in plasma and 0.010 ng/mg in brain homogenates. Responses, expressed as the peak area ratio of the analyte to the IS, were plotted against the corresponding Chol-D6 concentration, and the data were fitted with a linear regression curve. The quality of calibration curves was evaluated from the determination coefficient (r^2) and by comparing the back-calculated concentrations of calibrators with the corresponding nominal values.

Carry-over. The carry-over of the analytical instrumentation was checked by injecting Chol-D6 at the highest concentration (upper limit of quantitation, ULOQ), followed by repeated injections of blank samples. The carry-over was considered absent if the Chol-D6 signal measured in the blank samples immediately after the ULOQ was $< 20\%$ of the LLOQ signal.

Recovery. Recovery was determined by comparing the peak area of Chol-D6 spiked to plasma and brain samples before extraction (C) and the peak area of the analyte spiked to the same samples after extraction (A). The same method was used to calculate the recovery of IS, as follows $\% \text{ Rec} = \text{C/A} \times 100$

4.5. Statistical Analysis. Data were analyzed by ANOVA multiple comparisons and Tukey's tests, using GraphPad v7 (GraphPad Software Inc.). The limit of statistical significance was set at $p < 0.05$.

■ ASSOCIATED CONTENT

● Supporting Information

The Supporting Information is available free of charge at <https://pubs.acs.org/doi/10.1021/acschemneuro.9b00581>.

Supporting material, including tables and figures, describes in detail the validation of the analytical method in plasma and brain samples (PDF)

■ AUTHOR INFORMATION

Corresponding Author

*E-mail: mario.salmona@marionegri.it.

ORCID

Alice Passoni: 0000-0001-6003-5932

Renzo Bagnati: 0000-0002-6535-2686

Luisa Diomede: 0000-0002-2258-0531

Mario Salmona: 0000-0002-9098-9873

Author Contributions

#A.P. and M.F. contributed equally to this paper. M.S., L.C., and E.C. designed the experiments and supervised the scientific work; A.P. and R.B. set up the analytical method, designed the validation experiments and analyzed data; M.F. and L.D. prepared Chol-D6 loaded liposomes; M.V. and G.B. maintained and genotyped the R6/2 colony and contributed to design the *in vivo* experiments; M.F., L.C., E.D.P., and G.B. conducted the *in vivo* experiments; A.P. and M.F. prepared samples for LC-MS analysis and wrote the manuscript; M.G. revised the statistical analysis. All authors reviewed the manuscript.

Notes

The authors declare no competing financial interest.

ACKNOWLEDGMENTS

This paper was supported by a grant of the Italian Ministry of Health entitled “Innovative therapeutic strategy targeting neurons with cholesterol in Huntington disease: from preclinical studies to clinical trial readiness” (RF-2016-02361928), and partially by Telethon (GGP17102).

ABBREVIATIONS

Chol-D6, deuterium-labeled cholesterol
IN, intranasal
HMGCR, 3-hydroxy-3-methylglutaryl-coenzyme A reductase
CNS, central nervous system
LC-MS, liquid chromatography–mass spectrometry
HTT, Huntingtin
HD, Huntington’s disease
BBB, blood-brain barrier
EMA, European Medicine Agency
WT, wild type
LLOQ, lower limit of quantitation
ULOQ, upper limit of quantitation
MeOH, methanol
PBS, phosphate buffer solution

REFERENCES

- (1) Lingwood, D., and Simons, K. (2010) Lipid Rafts as a Membrane-Organizing Principle. *Science* 327 (5961), 46–50.
- (2) Björkhem, I., and Meaney, S. (2004) Brain Cholesterol: Long Secret Life behind a Barrier. *Arterioscler., Thromb., Vasc. Biol.* 24 (5), 806–815.
- (3) Pfrieger, F. W. (2003) Role of Cholesterol in Synapse Formation and Function. *Biochim. Biophys. Acta, Biomembr.* 1610 (2), 271–280.
- (4) Orth, M., and Bellosta, S. (2012) Cholesterol: Its Regulation and Role in Central Nervous System Disorders. *Cholesterol* 2012, 1.
- (5) Zhang, J., and Liu, Q. (2015) Cholesterol Metabolism and Homeostasis in the Brain. *Protein Cell* 6 (4), 254–264.
- (6) Bohanna, I., Georgiou-Karistianis, N., Hannan, A. J., and Egan, G. F. (2008) Magnetic Resonance Imaging as an Approach towards Identifying Neuropathological Biomarkers for Huntington’s Disease. *Brain Res. Rev.* 58 (1), 209–225.
- (7) Rosas, H. D., Salat, D. H., Lee, S. Y., Zaleta, A. K., Pappu, V., Fischl, B., Greve, D., Hevelone, N., and Hersch, S. M. (2008) Cerebral Cortex and the Clinical Expression of Huntington’s Disease: Complexity and Heterogeneity. *Brain* 131 (4), 1057–1068.
- (8) Waldvogel, H. J., Kim, E. H., Tippet, L. J., Vonsattel, J.-P. G., and Faull, R. L. (2014) The Neuropathology of Huntington’s Disease. *Curr. Top. Behav. Neurosci.* 22, 33–80.
- (9) Zuccato, C., Valenza, M., and Cattaneo, E. (2010) Molecular Mechanisms and Potential Therapeutic Targets in Huntington’s Disease. *Physiol. Rev.* 90 (3), 905–981.
- (10) McColgan, P., and Tabrizi, S. J. (2018) Huntington’s Disease: A Clinical Review. *Eur. J. Neurol.* 25 (1), 24–34.
- (11) Valenza, M., Leoni, V., Karasinska, J. M., Petricca, L., Fan, J., Carroll, J., Pouladi, M. A., Fossale, E., Nguyen, H. P., Riess, O., et al. (2010) Cholesterol Defect Is Marked across Multiple Rodent Models of Huntington’s Disease and Is Manifest in Astrocytes. *J. Neurosci.* 30 (32), 10844–10850.
- (12) Karasinska, J. M., and Hayden, M. R. (2011) Cholesterol Metabolism in Huntington Disease. *Nat. Rev. Neurol.* 7 (10), 561–572.
- (13) Valenza, M., Carroll, J. B., Leoni, V., Bertram, L. N., Björkhem, I., Singaraja, R. R., Di Donato, S., Lutjohann, D., Hayden, M. R., and Cattaneo, E. (2007) Cholesterol Biosynthesis Pathway Is Disturbed in YAC128 Mice and Is Modulated by Huntingtin Mutation. *Hum. Mol. Genet.* 16 (18), 2187–2198.
- (14) Valenza, M., Leoni, V., Tarditi, A., Mariotti, C., Björkhem, I., Di Donato, S., and Cattaneo, E. (2007) Progressive Dysfunction of the Cholesterol Biosynthesis Pathway in the R6/2 Mouse Model of Huntington’s Disease. *Neurobiol. Dis.* 28 (1), 133–142.
- (15) Shankaran, M., Di Paolo, E., Leoni, V., Caccia, C., Ferrari Bardile, C., Mohammed, H., Di Donato, S., Kwak, S., Marchionini, D., Turner, S., et al. (2017) Early and Brain Region-Specific Decrease of de Novo Cholesterol Biosynthesis in Huntington’s Disease: A Cross-Validation Study in Q175 Knock-in Mice. *Neurobiol. Dis.* 98, 66–76.
- (16) Valenza, M., Marullo, M., Di Paolo, E., Cesana, E., Zuccato, C., Biella, G., and Cattaneo, E. (2015) Disruption of Astrocyte-Neuron Cholesterol Cross Talk Affects Neuronal Function in Huntington’s Disease. *Cell Death Differ.* 22 (4), 690–702.
- (17) Valenza, M., Chen, J. Y., Di Paolo, E., Ruozi, B., Belletti, D., Ferrari Bardile, C., Leoni, V., Caccia, C., Brilli, E., Di Donato, S., et al. (2015) Cholesterol-Loaded Nanoparticles Ameliorate Synaptic and Cognitive Function in Huntington’s Disease Mice. *EMBO Mol. Med.* 7 (12), 1547–1564.
- (18) Agrawal, M., Saraf, S., Saraf, S., Antimisiaris, S. G., Chougule, M. B., Shoyele, S. A., and Alexander, A. (2018) Nose-to-Brain Drug Delivery: An Update on Clinical Challenges and Progress towards Approval of Anti-Alzheimer Drugs. *J. Controlled Release* 281 (May), 139–177.
- (19) Selvaraj, K., Gowthamarajan, K., and Karri, V. V. S. R. (2017) Nose to Brain Transport Pathways an Overview: Potential of Nanostructured Lipid Carriers in Nose to Brain Targeting. *Artif. Cells, Nanomed., Biotechnol.* 46 (8), 2088–2095.
- (20) Crowe, T. P., Greenlee, M. H. W., Kanthasamy, A. G., and Hsu, W. H. (2018) Mechanism of Intranasal Drug Delivery Directly to the Brain. *Life Sci.* 195 (September 2017), 44–52.
- (21) Pardeshi, C. V., and Belgamwar, V. S. (2013) Direct Nose to Brain Drug Delivery via Integrated Nerve Pathways Bypassing the Blood–Brain Barrier: An Excellent Platform for Brain Targeting. *Expert Opin. Drug Delivery* 10 (7), 957–972.
- (22) EMEA (2015) Guideline on Bioanalytical Method Validation. *Eur. Med. Agency. Comm. Med. Prod. Hum. Use* 44 (July 2011), 1–23.
- (23) Khan, A. R., Liu, M., Khan, M. W., and Zhai, G. (2017) Progress in Brain Targeting Drug Delivery System by Nasal Route. *J. Controlled Release* 268, 364–389.
- (24) Dhuria, S. V., Hanson, L. R., and Frey, W. H. (2010) Intranasal Delivery to the Central Nervous System: Mechanisms and Experimental Considerations. *J. Pharm. Sci.* 99 (4), 1654–63.
- (25) Claxton, A., Baker, L. D., Hanson, A., Trittschuh, E. H., Cholerton, B., Morgan, A., Callaghan, M., Arbuckle, M., Behl, C., and Craft, S. (2015) Long-Acting Intranasal Insulin Detemir Improves Cognition for Adults with Mild Cognitive Impairment or Early-Stage Alzheimer’s Disease Dementia. *J. Alzheimer’s Dis.* 44 (3), 897–906.
- (26) Mischley, L. K., Conley, K. E., Shankland, E. G., Kavanagh, T. J., Rosenfeld, M. E., Duda, J. E., White, C. C., Wilbur, T. K., De La Torre, P. U., and Padowski, J. M. (2016) Central Nervous System

Uptake of Intranasal Glutathione in Parkinson's Disease. *npj Park. Dis.* 2 (1), Article No. 16002.

(27) Novak, V., Milberg, W., Hao, Y., Munshi, M., Novak, P., Galica, A., Manor, B., Roberson, P., Craft, S., and Abduljalil, A. (2014) Enhancement of Vasoreactivity And cognition by Intranasal Insulin in Type 2 Diabetes. *Diabetes Care* 37 (3), 751–759.

(28) Reger, M. A., Watson, G. S., Green, P. S., Baker, L. D., Cholerton, B., Fishel, M. A., Plymate, S. R., Cherrier, M. M., Schellenberg, G. D., Frey II, W. H., and Craft, S. (2008) Intranasal Insulin Administration Dose-Dependently Modulates Verbal Memory and Plasma β -Amyloid in Memory-Impaired Older Adults. *J. Alzheimer's Dis.* 13 (3), 323–331.

(29) De Luigi, A., Colombo, L., Diomede, L., Capobianco, R., Mangieri, M., Miccolo, C., Limido, L., Forloni, G., Tagliavini, F., and Salmona, M. (2008) The Efficacy of Tetracyclines in Peripheral and Intracerebral Prion Infection. *PLoS One* 3 (3), Article No. e1888.

(30) Kirby, C. J., and Gregoriadis, G. (1984) Preparation of Liposomes Containing Factor VIII for Oral Treatment of Haemophilia. *J. Microencapsulation* 1 (1), 33–45.

(31) Mangiarini, L., Sathasivam, K., Seller, M., Cozens, B., Harper, A., Hetherington, C., Davies, S. W., and Bates, G. P. (1996) Exon 1 of the HD Gene with an Expanded CAG Repeat Is Sufficient to Cause a Progressive Neurological Phenotype in Transgenic Mice. *Cell* 87, 493–506.

(32) Hanson, L. R., Fine, J. M., Svitak, A. L., and Faltsek, K. A. (2013) Intranasal Administration of CNS Therapeutics to Awake Mice. *J. Visualized Exp.* 74, 1–7.



Insights into kinetics, release, and behavioral effects of brain-targeted hybrid nanoparticles for cholesterol delivery in Huntington's disease

Giulia Birolini^{a,b,1}, Marta Valenza^{a,b,*,1}, Ilaria Ottonelli^{c,d}, Alice Passoni^e, Monica Favagrossa^e, Jason T. Duskey^{c,f}, Mauro Bombaci^b, Maria Angela Vandelli^c, Laura Colombo^e, Renzo Bagnati^e, Claudio Caccia^g, Valerio Leoni^h, Franco Taroni^g, Flavio Forni^c, Barbara Ruozzi^c, Mario Salmona^e, Giovanni Tosi^c, Elena Cattaneo^{a,b,*}

^a Department of Biosciences, University of Milan, via G. Celoria 26, 20133 Milan, Italy

^b Istituto Nazionale di Genetica Molecolare "Romeo ed Enrica Invernizzi", via F. Sforza 35, 20122 Milan, Italy

^c Nanotech Lab, Te.Far.T.I. Center, Department of Life Sciences, University of Modena and Reggio Emilia, Via G. Campi, 103, 41125 Modena, Italy

^d Clinical and Experimental Medicine PhD Program, University of Modena and Reggio Emilia, via G. Campi 289, 411214 Modena, Italy

^e Istituto di Ricerche Farmacologiche Mario Negri IRCCS, via Mario Negri 2, 20156 Milan, Italy

^f Umberto Veronesi Foundation, 20122 Milan, Italy

^g Unit of Medical Genetics and Neurogenetics, Fondazione I.R.C.C.S. Istituto Neurologico Carlo Besta, Via Celoria 11, 20131 Milan, Italy

^h Laboratory of Clinical Pathology, Hospital of Desio, ASST-Monza, School of Medicine and Surgery, University of Milano-Bicocca, Via Cadore 48, 20900 Monza, Italy

ARTICLE INFO

Keywords:

Huntington
Cholesterol
Nanoparticles
Blood-brain barrier

ABSTRACT

Supplementing brain cholesterol is emerging as a potential treatment for Huntington's disease (HD), a genetic neurodegenerative disorder characterized, among other abnormalities, by inefficient brain cholesterol biosynthesis. However, delivering cholesterol to the brain is challenging due to the blood-brain barrier (BBB), which prevents it from reaching the striatum, especially, with therapeutically relevant doses.

Here we describe the distribution, kinetics, release, and safety of novel hybrid polymeric nanoparticles made of PLGA and cholesterol which were modified with an heptapeptide (g7) for BBB transit (hybrid-g7-NPs-chol). We show that these NPs rapidly reach the brain and target neural cells. Moreover, deuterium-labeled cholesterol from hybrid-g7-NPs-chol is released in a controlled manner within the brain and accumulates over time, while being rapidly removed from peripheral tissues and plasma. We confirm that systemic and repeated injections of the new hybrid-g7-NPs-chol enhanced endogenous cholesterol biosynthesis, prevented cognitive decline, and ameliorated motor defects in HD animals, without any inflammatory reaction.

In summary, this study provides insights about the benefits and safety of cholesterol delivery through advanced brain-permeable nanoparticles for HD treatment.

1. Introduction

Targeting the brain with therapeutic agents is made difficult by the blood-brain barrier (BBB). Current strategies to circumvent this problem include temporary BBB disruption, conjugation of brain-permeable ligands to the drug of interest, intranasal delivery, or direct delivery of molecules into the brain by means of invasive strategies [1]. Among them, nanocarriers [2] decorated on their surface with brain-targeting ligands [3,4] are emerging because of their non-invasiveness. Polymeric nanoparticles (NPs) made of the FDA-approved polymer poly (D,L-

lactide-co-glycolide) (PLGA) and surface-engineered with the g7 glycopeptide (Gly-L-Phe-D-Thr-Gly-L-Phe-L-Leu-L-Ser(O-beta-D-glucose)-CONH₂) are reported to transport molecules into the CNS after their systemic administration in rodents [5]. g7 stimulates membrane curvature and, following endocytosis of the whole carrier at the BBB, it promotes BBB transit by multiple pathways [6]. Previous studies indicate that about 10% of the injected g7-NP reaches the brain [6–11].

This system has been applied to deliver drugs to cope with Huntington's disease (HD), an adult-onset, neurodegenerative genetic disorder caused by a CAG repeat expansion in the gene encoding the

* Corresponding authors at: Department of Biosciences, University of Milan, via G. Celoria 26, 20133 Milan, Italy.

E-mail addresses: marta.valenza@unimi.it (M. Valenza), elena.cattaneo@unimi.it (E. Cattaneo).

¹ Co-first authors.

Huntingtin (HTT) protein. Individuals carrying the mutation develop motor defects, cognitive decline, and psychiatric disturbances. Neuronal dysfunction precedes neurodegeneration, which mainly affects the medium-spiny neurons (MSNs) of the striatum and the cortical neurons [12]. One pathway found to be affected in HD involves brain cholesterol. Peripheral cholesterol is not able to cross the BBB and locally synthesized brain cholesterol is implicated in synapses formation, maintenance and activity, and optimal neurotransmitter release [13,14]. Brain cholesterol biosynthesis and content are reduced across several rodent models of HD [15–20] and altered brain cholesterol homeostasis is also measurable in HD patients starting from pre-symptomatic stages through the circulating level of the brain-specific cholesterol catabolite 24-hydroxycholesterol (24S-OHC) [21,22]. This dysfunction implies a lower availability of newly synthesized cholesterol and its metabolites in the HD brain with detrimental consequences for neuronal and synaptic activities [19,20,23]. Accordingly, strategies aimed at delivering cholesterol to the HD brain proved to be effective [24,25]. In particular, in a first study, systemic injections of PLGA-g7-NPs loaded with cholesterol (PLGA-g7-NPs-cho) were found to prevent synaptic and cognitive defects in a transgenic mouse model of HD [24]. In a subsequent study, cholesterol was infused for 4 weeks into the striatum of HD mice through osmotic mini-pumps, a well-characterized system for controlled drug administration. This led to the identification of the optimal dose of cholesterol needed to restore synaptic and neuropathological features and reverse motor and cognitive abnormalities in HD mice [25]. Recently, the effectiveness of nose-to-brain delivery of cholesterol to the HD brain has also been tested [26]. In the first study with PLGA-g7-NPs-cho, the amount of cholesterol delivered to the brain was sub-optimal compared with the dose identified with osmotic mini-pumps. Although it is difficult to directly compare these systems due to different mechanisms of cholesterol release, it has been estimated that this type of NPs provides the brain with approximately 2 µg of cholesterol in each systemic injection [24], while approximately 13 µg of cholesterol per day was infused into the striatum with mini-pumps, enabling maximum benefit in HD mice after 4 weeks of treatment [25].

The development of a more efficient, non-invasive, brain-targeted cholesterol-based therapy for HD patients requires an optimized generation of NPs with improved pharmaceutical properties. In particular, in this study we tested the therapeutic value of new nanoparticles whose formulation process, structural characteristics, and drug loading capacity have been enhanced.

These NPs, herein named hybrid-g7-NPs-cho, were prepared using a novel formulation that efficiently combines materials (g7-PLGA, PLGA, and cholesterol as starting materials for formulation) [27], using nanoprecipitation (MIX-N) or single emulsion (MIX-SE) with surfactants such as Pluronic F68 in MIX-N and polyvinyl alcohol (PVA) in MIX-SE. This study therefore aimed to investigate the distribution of hybrid-g7-NPs-cho in different brain regions, peripheral tissues, and the circulation, and the kinetics of cholesterol release, the benefits to animals' behavior. Potential side effects which might emerge following chronic treatment in HD mice were also investigated.

2. Method section

2.1. Production and characterization of hybrid-g7-NPs-cho

Starting from already published results [24,27], we produced hybrid NPs using a nanoprecipitation method (N) and simple emulsion (SE). Following previous readouts on the polymer ratio to be used in formulation [28], 1:1 w/w ration between PLGA and Cholesterol was adopted. In details, all hybrid nanoparticles were formulated starting from 50 mg of a mixture of Cholesterol (Sigma-Aldrich, Milan, Italy), PLGA (PLGA R503H Evonik, Essen, Germany) and PLGA-g7 in a weight ratio of 1:0.8:0.2 (25 mg Chol, 20 mg PLGA, 5 mg PLGA-g7).

PLGA-g7 was synthesized via amide formation in the Nanotech Laboratory of the University of Modena and Reggio Emilia, following a

previously described protocol [8,29]. PLGA is a synthetic polymer approved by the US Food and Drug Administration (FDA) and European Medicine Agency (EMA) for biomedical devices. PLGA has a very high biodegradability (Mundargi et al. J. Control. Release 2009): it enters into the Krebs cycle and it is degraded by non-enzymatic hydrolysis leading to the formation of lactic acid, glycolic acid, CO₂ and H₂O. Up to now, no clear data on the degradation rate of PLGA within the brain is available, but the data relating to PLGA clearance in degradation are strongly related to MW and composition of the polymer and in particular the PLGA used in this paper is described to be degrade within a range of 3–4 weeks [30–32]. Pure g7 was purchased from Mimotopes (Clayton, Victoria, Australia).

To obtain MIX-N, Chol and PLGA mixture was dissolved in acetone (4 mL). The organic phase was then added dropwise into 50 mL of a 0.5% (w/v) Pluronic-F68 aqueous solution at 45 °C under magnetic stirring (1300 rpm). After 20 min, the organic solvent was removed at 30 °C under reduced pressure (10 mmHg). The MIX-NPs were recovered and purified three times by an ultracentrifugation process carried out at 14,500 rpm for 10 min (4 °C; Sorvall RC28S, Dupont, Brussels, Belgium) to remove the unformed material and the free surfactant fraction in the solution. The obtained MIX-NPs were re-suspended in 3 mL of a 0.2% (w/v) Pluronic-F68 aqueous solution at room temperature and gently sonicated until completely resuspended.

As cryoprotectant, 150 mg of threosose (Sigma-Aldrich, Milan, Italy) dissolved in 0.5 mL of 0.2% Pluronic-F68 solution were added to the NPs suspension before flash freezing with dry ice and methanol bath. NPs were stored at –20 °C until use.

To obtain MIX-SE, Chol:PLGA mixture were dissolved in dichloromethane (4 mL) and emulsified in 20 mL of 1% (w/v) PVA aqueous solution by sonication (Microson Ultrasonic cell disruptor, Misonix Inc. Farmingdale, NY, USA) (80 W over 1 min) under cooling (5 °C). Then, the O/W emulsion was stirred for at least 3 h (1300 rpm; RW20DZM, IKALabortechnik, Staufen, Germany) at r.t. to allow the solvent evaporation. The MIX-SE were collected and purified by ultracentrifugation as previously described for MIX-N, and stored at 4 °C before the use.

Fluorescently labeled MIX NPs were produced with the same protocol described in 1.1.1, adding 2% in weight of Cy5 derived PLGA and 2% in weight of Bodipy-Cholesterol (Avanti, Alabama, USA). Cy5-PLGA was synthesized in the Nanotech Laboratory of the University of Modena and Reggio Emilia using a protocol published in [29]. The total composition was a mixture of Chol:Chol-Bodipy:PLGA:PLGA-Cy5:PLGA-g7 in weight ratio of 0.96:0.04:0.76:0.04:0.2 (24 mg Chol, 1 mg Chol-Bodipy, 19 mg PLGA, 1 mg PLGA-Cy5, 5 mg PLGA-g7). After centrifugation, NPs were resuspended in an aqueous solution of Pluronic-F68 2% and added of threosose as previously reported before flash freezing.

g7-NPs-d6-Chol were obtained using the same protocol described in paragraph 1.1.1. For the formulation, 50 mg of a mixture of D6 Chol: PLGA:PLGA-g7 in weight ratio of 1:0.8:0.2 (25 mg D6 Chol, 20 mg PLGA, 5 mg PLGA-g7) were used.

2.2. Production of PLGA-g7-NPs loaded with cholesterol

PLGA-g7-NPs-cho were produced as reported in [24], confirming technological and pharmaceutical features as described in Table S1 as shown before.

2.3. Chemico-physical and morphological characterization

100 µL of each type of NPs suspension was freeze-dried (–60 °C, 1 · 10–3 mm/Hg for 48 h; LyoLab 3000, Heto-Holten, Allerød, Denmark) and the yield (Yield%) was calculate as follows:

Yield (%) = [(mg of freeze dried MIX-N or MIX-SE)/(mgPLGA+mg Chol)] × 100.

Mean particle size (Z-Average) and polydispersity index (PDI) of the samples were determined using a Zetasizer Nano ZS (Malvern, UK; Laser 4 mW He–Ne, 633 nm, Laser attenuator Automatic, transmission

100–0.0003%, Detector Avalanche photodiode, Q.E. > 50% at 633 nm). Samples were diluted in MilliQ water at about 0.1 mg/mL. The results were also expressed as intensity distribution, i.e. the size 10% [D(10)], 50% [D(50)] and 90% [D(90)], below which all the MIX NPs are placed. The zeta potential (ζ -pot I) was measured using the same equipment with a combination of laser Doppler velocimetry and phase analysis light scattering (PALS). All data are expressed as means of at least three determinations carried out for each prepared lot (three lots for each sample).

The morphology of the samples was evaluated by atomic force microscopy (AFM) (Park Instruments, Sunnyvale, CA, USA) and scanning transmission electron microscopy (STEM) as reported in [27], confirming the same results as reported in supplementary Fig. S1.

AFM analysis were conducted at about 20 °C operating in air and in non-contact mode using a commercial silicon tip-cantilever (high resolution noncontact “GOLDEN” Silicon Cantilevers NSG-11, NT-MDT, tip radius 10 nm; Zelenograd, Moscow, Russia) with stiffness of about 40 Nm⁻¹ and a resonance frequency around 160 kHz. A drop of each hybrid NPs suspension was diluted with distilled water (about 1:5 v/v) before application on a small mica disk (1 cm × 1 cm).

After 2 min, the excess of distilled water was removed using a paper filter and the sample analyzed. Two kinds of images were obtained: the first is a topographical image and the second is indicated as “error signal”. This error signal is obtained by comparing two signals: the first one representing the amplitude of the vibrations of the cantilever, and the second the amplitude of a reference point. The images obtained by this method show small superficial variations of the samples. Images were processed and analyzed using software from Gwyddion (Department of Nanometrology, Czech Metrology Institute, Brno, Czech Republic).

The internal structure/architecture of the samples was analyzed by scanning transmission electron microscopy (STEM). Briefly, a drop of a water-diluted suspension of the samples (about 0.03 mg/mL) was placed on a 200-mesh copper grid (TABB Laboratories Equipment, Berks, UK), allowed to adsorb, and the suspension surplus was removed by filter paper. All grids were analyzed using a Nova NanoSEM 450 (FEI, Oregon, USA) transmission electron microscope operating at 30 kV using a STEM II detector in Field free mode.

To quantify the amount of cholesterol hybrid-g7-NPs-chol, NPs previously lyophilized to calculate the yield (~1 mg) were dissolved in chloroform (0.3 mL), followed by addition of isopropyl alcohol (0.6 mL) to precipitate the polymer. The mixture was vortexed (15 Hz for 1 min; ZX3, VelpScientifica, Usmate, Italy) and then filtered (polytetrafluoroethylene filter, porosity 0.20 µm, Sartorius). The amount of Chol in the sample was quantified by RP-HPLC using an HPLC apparatus comprised a Model PU980 pump provided with an injection valve with a 50 µL sample loop (Model 7725i Jasco) and an UV detector at 210 nm (UV975, Jasco). Chromatography separation was carried out on a Syncronics C18 (250 × 4.6 mm; porosity 5 µm; Thermo Fisher Scientific, Waltham, MA, USA) at r.t. and with a flow rate of 1.2 mL/min, operating in an isocratic mode using 50:50 v/v acetonitrile:ethanol as mobile phase. The solvents of the mobile phase were filtered through 0.45 µm hydrophilic polypropylene membrane filters (Sartorius) before their use. Chromatographic peak areas of the standard solutions were collected and used for the generation of calibration curves. Linearity was assumed in the range of 50–500 µg/mL ($r^2 = 0.99$). All data are expressed as the mean of at least three determinations.

The chemico-physical properties, concentration and cholesterol amount in g7-NPs used in this work are described in Table S1 along with morphological analysis with AFM and STEM (Fig. S1).

2.4. Colony management

All animal experiments were approved and carried out in accordance with Italian Governing Law (D.lgs 26/2014; Authorization n.581/2019-PR issued July 29, 2019 by Ministry of Health); the NIH Guide for the

Care and Use of Laboratory Animals (2011 edition) and EU directives and guidelines (EEC Council Directive 2010/63/UE).

Our R6/2 colony lifespan was approximately of 12–13 weeks and only males were used to maintain it [33]. Transgenic 6-week-old R6/2 males were mated with wild type females (B6CBAF1/J, purchased from Charles River). CAG repeat length that could affect strain productivity, general behavior, litter size, pup survival, genotype frequency, phenotype was monitored every 6 months with a range between 150 and 180 CAGs.

Mice were weaned and then genotyped at 3 weeks of age (+/- 3 days) and they were housed under standard conditions in enriched cage (22 ± 1 °C, 60% relative humidity, 12 h light/dark schedule, 3–4 mice/cage, with food and water *ad libitum*).

2.5. Mice treatments

For biodistribution studies, cholesterol release study and quantitative analysis, 7-week-old wt or R6/2 mice were treated with 1, 2 or 3 ip injections. For chronic experiments, R6/2 mice were treated with 2 ip injections at week, from 5 to 9 weeks of age. Wt and R6/2 littermates treated with saline solution was used as controls. In all the experiments, mice received 660 µg of cholesterol in each injection.

2.6. Immunohistochemistry and image acquisition

Animals were deeply anesthetized with Avertin 2.5% and transcardially perfused with PFA 4%. Brains, lungs and liver were collected in PFA 4% for 2 h and then in 30% sucrose to prevent ice crystal damage during freezing in OCT. 15 µm-thick brain coronal sections or lung and liver sections were counterstained with the nuclear dye Hoechst 33258 (1:10.000, Invitrogen) and then mounted under cover slips using Vectashield (Vector Laboratories). To study the co-localization of g7-NPs-chol 2.0 with neuronal and glial markers, 15 µm-thick brain coronal sections were incubated with the following primary antibodies for 3 h at RT: rabbit anti-DARPP32 (1:100, Cell Signaling, 2306); mouse anti-NeuN (1:100, Millipore, MAB377); rabbit anti-GFAP (1:250, Dako, Z0334); rabbit anti-IBA1 (1:100, Wako, 019-1971). Anti-rabbit Alexa Fluor 488-conjugated goat secondary antibodies (1:500; Invitrogen) or anti-mouse Alexa Fluor 488-conjugated goat secondary antibodies (1:500; Invitrogen) were used for detection (1 h at RT). Sections were counterstained with the nuclear dye Hoechst 33258 (1:10.000, Invitrogen) and then mounted under cover slips using Vectashield (Vector Laboratories).

Images were acquired the following day with a confocal microscope (Leica SP5). Laser intensity and detector gain were maintained constant for all images and 3-z steps images were acquired at 40×. To quantify hybrid g7-NPs-chol in different tissues, ImageJ software was used to measure the fluorescence of Cy5 ($n = 4$ images/mouse/tissue).

To quantify the released bodipy cholesterol from g7-NPs-chol 2.0, Volocity software was used using the plug-in “find objects” and “calculate object correlation” ($n = 6$ images/mouse/tissue).

2.7. Liquid chromatography-mass spectrometry (LC-MS) analysis for d6-chol

A recently validated method was used [26]. Briefly, 50 µL of plasma was diluted with 200 µL of ethanol containing 200 ng of beta-sitosterol, used as internal standard. Samples were vortexed and centrifuged at 13200 rpm for 15 min and aliquots of the supernatants were injected directly into the LC-MS system. Forty milligrams of each brain area and peripheral tissue were homogenized in 1 mL of ethanol/water 4:1 (v/v), containing 500 ng of internal standard. Homogenates were centrifuged for 15 min at 13200 rpm at 4 °C, and aliquots of the supernatants were injected into the LC-MS system. D6-chol levels were determined using a 1200 Series HPLC system (Agilent Technologies, Santa Clara, CA, U.S.A.) interfaced to an API 5500 triple quadrupole mass spectrometer

(Sciex, Thornhill, Ontario, Canada). The mass spectrometer was equipped with an atmospheric pressure chemical ionization (APCI) source operating in positive ion and multiple reaction monitoring (MRM) mode to measure the product ions obtained in a collision cell from the protonated $[M - H_2O]^+$ ions of the analytes. The transitions identified during the optimization of the method were m/z 375.3–152.1 (quantification transition) and m/z 375.3–167.1 (qualification transition) for D6-cholesterol; m/z 397.3–147.1 (quantification transition) and m/z 397.3–161.1 (qualification transition) for β -sitosterol (IS). D6-cholesterol and β -sitosterol were separated on a Gemini C18 column (50 \times 2 mm; 5 μ m particle size), using an isocratic gradient in 100% methanol at 35 $^\circ$ C.

2.8. Gas chromatography-mass spectrometry (GC–MS) analysis for neutral sterols

To a screw-capped vial sealed with a Teflon-lined septum were added 50 μ L of homogenates together with 500 ng of D4-lathosterol (CDN Isotopes, Canada), 500 ng of D6-desmosterol (Avantipolar Lipids, USA), and 100 ng of D6-lanosterol (Avantipolar Lipids, USA) as internal standards, 50 μ L of butylated hydroxytoluene (BHT) (5 g/L) and 25 μ L of EDTA (10 g/L). Argon was flushed through to remove air. Alkaline hydrolysis was allowed to proceed at room temperature (22 $^\circ$ C) for 1 h in the presence of 1 M ethanolic potassium hydroxide solution under magnetic stirring. After hydrolysis, the neutral sterols (lathosterol, desmosterol and lanosterol) were extracted twice with 5 mL of hexane. The organic solvents were evaporated under a gentle stream of nitrogen and converted into trimethylsilyl ethers with BSTFA-1% TMCS (Ceriliant, USA) at 70 $^\circ$ C for 60 min. Analysis was performed by gas chromatography - mass spectrometry (GC–MS) on a Clarus 600 gas chromatograph (Perkin Elmer, USA) equipped with Elite-5MS capillary column (30 m, 0.32 mm, 0.25 μ m, Perkin Elmer, USA) connected to Clarus 600C mass spectrometer (Perkin Elmer, USA). The oven temperature program was as follows: initial temperature 180 $^\circ$ C was held for 1 min, followed by a linear ramp of 20 $^\circ$ C/min to 270 $^\circ$ C, and then a linear ramp of 5 $^\circ$ C/min to 290 $^\circ$ C, which was held for 10 min. Helium was used as carrier gas at a flow rate of 1 mL/min and 1 μ L of sample was injected in splitless mode. Mass spectrometric data were acquired in selected ion monitoring mode. Peak integration was performed manually. Sterols were quantified against internal standards, using standard curves for the listed sterols.

2.9. Behavioral tests

Mice behavior was evaluated at 9 and 11 weeks of age.

Rotarod test: mice were tested over three consecutive days. Firstly, animals were trained on a rotating bar at 4 rpm for 5 min (apparatus model 47,600, Ugo Basile). One hour later, mice were tested for three consecutive accelerating trials of 5 min with the rotarod speed linearly increasing from 4 to 40 rpm. The latency to fall from the rod was recorded for each trial and averaged.

Activity Cage test: animals were placed in an arena (25 cm \times 25 cm) (2Biological Instrument) and allowed to freely move for an hour in presence of a low-intensity white light source. Movements were assessed by an automated tracking system (Actitrack software, 2Biological Instrument) connected to infrared sensors surrounding the arena. Total distance travelled, mean velocity speed, and numbers of rearings were analyzed. The % of time that mice explored the periphery or the center area of the arena was evaluated as a measure of anxiety-like behavior.

Novel Object Recognition (NOR) test: in the habituation stage, mice were placed into an empty non-reflective arena (44 \times 44 \times 44 cm) for 10 min. In the familiarization stage, two identical objects (A' and A'') were presented to each animal for 10 min. The day after, during the test stage, animals were exposed to one familiar object (A') and a new object (B) for 10 min. All phases of the test were conducted with a low-intensity white light source. The index of discrimination was calculated as (time exploring the novel object – time exploring the familiar object)/(time

exploring both objects) \times 100. Mice exploring less than 7 s. were excluded from the analysis due to their inability to perform the task.

Paw clasping test: animals were suspended by the tail for 30 s and the clasping phenotype was graded according to the following scale: level 0, no clasping; level 1, clasping of the forelimbs only or both fore- and hindlimbs once or twice; and level 2, clasping of both fore- and hindlimbs more than three times or more than 5 s.

Grip strength test: animals were lifted by the tail, lowered towards the grip (Ugo Basile) and gently pulled straight back with consistent force until they released its grip. The forelimb grip force, measured in grams, was recorded. The test was repeated for 5 times, and measures were averaged.

2.10. Bio-Plex

Animals were deeply anesthetized with Avertin 2.5% to collect blood which was centrifuged at 13,000 rpm at 4 $^\circ$ C for 15 min to obtain the plasma. Striatum, cortex, and liver were isolated and frozen. 10 mg of striatum, cortex and liver were homogenized using a tissue grinder in 1 mL of lysing solution according to manufacturer instructions (Bio-Plex® Cell Lysis Kit, Biorad, #171304011). The lysate was frozen at –80 $^\circ$ C, sonicated at 40% for 20 s and centrifuged at 4,500 rcf at 4 $^\circ$ C for 4 min to collect the supernatant. The supernatant was quantified using DC™ Protein Assay Kit I (Biorad, #5000111) and samples were diluted to a final concentration of 500 μ g/mL. To perform the Bio-Plex assay, 150 μ L of assay buffer were added to 150 μ L of samples.

Concerning the plasma, samples were centrifuged at 1,500 rcf at 4 $^\circ$ C for 5 min. 60 μ L of assay buffer and 120 μ L of sample diluent were added to 60 μ L of plasma.

All samples were tested for the following cytokines using the Bio-Plex Pro Mouse Cytokine 23-plex Assay: IL-1 α , IL-1 β , IL-2, IL-3, IL-4, IL-5, IL-6, IL-9, IL-10, IL-12 (p40), IL-12 (p70), IL-13, IL-17A, Eotaxin, G-CSF, GM-CSF, IFN- γ , KC, MCP-1 (MCAF), MIP-1 α , MIP-1 β , RANTES, TNF- α , (Biorad, #M60009RDPD) according to manufacturer instructions and detected using Bioplex™ 200 System (Bio-Rad). The concentration of each cytokine was calculated through calibration curve (individual for each cytokine), determined independently for each experiment, by Bioplex Manager™ software 4.1.

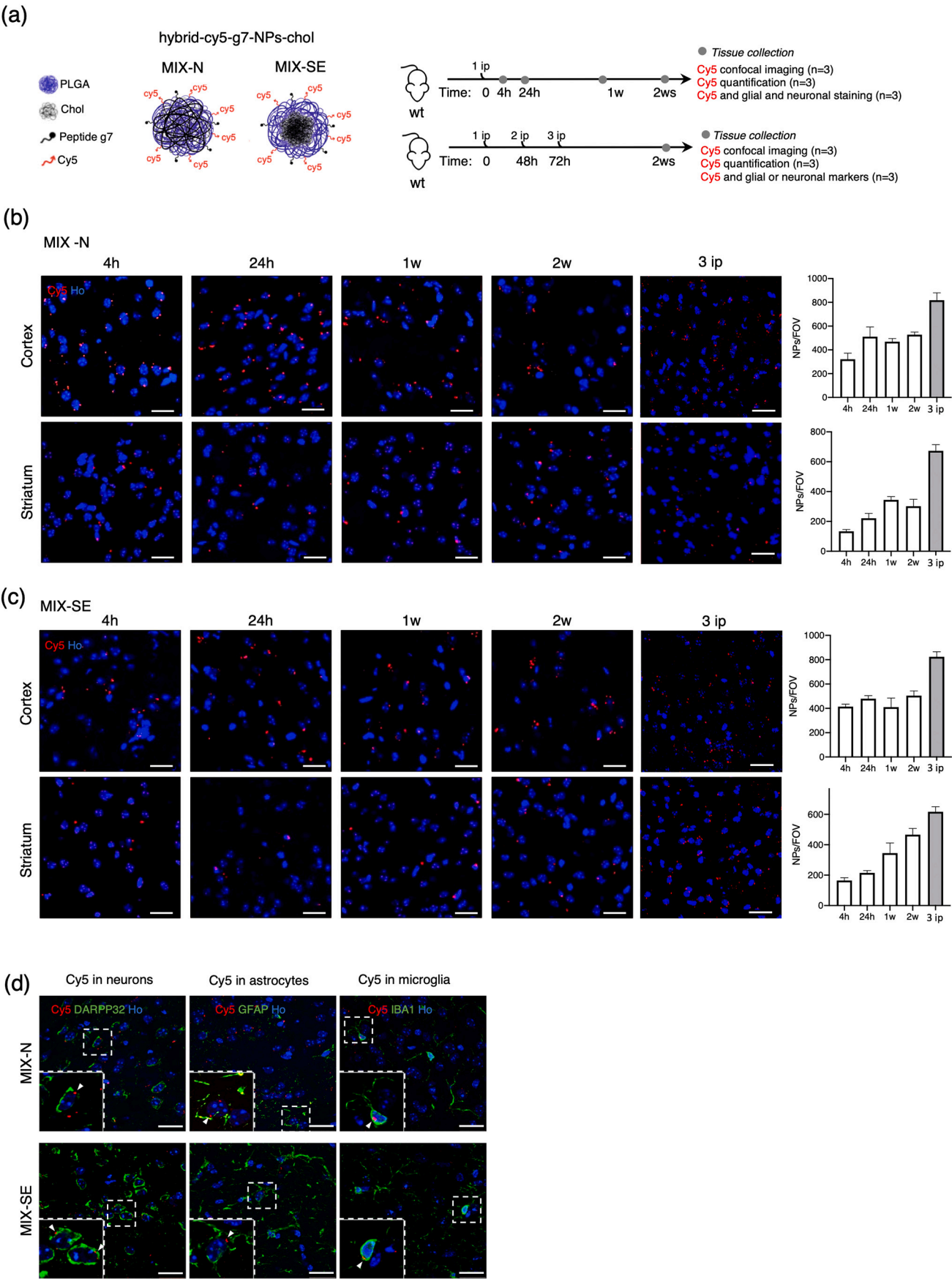
2.11. Statistics

Prism 8 (GraphPad software) was used to perform statistical analyses. G-power software was used to pre-determine group allocation, data collection and all related analyses. For animal studies, mice were assigned randomly, and sex was balanced in the various experimental groups; animals from the same litter were divided in different experimental groups; blinding of the investigator was applied to *in vivo* procedures and all data collection. Grubbs' test was applied to identify outliers. For each set of data to be compared, we determined whether data were normally distributed or not to select parametric or not parametric statistical tests. The specific statistical test used is indicated in the legend of all results figures. Table S3 summarizes all the trials and read-outs performed.

3. Results and discussion

3.1. Localization of hybrid-g7-NPs-cholesterol MIX-N and MIX-SE *in vivo*

The characteristics of both hybrid-g7-NPs-cholesterol MIX-N and MIX-SE were in line with those described in previous studies [24,27] in terms of size, homogeneity, surface charge, cholesterol content, and morphology (Table S1 and Fig. S1). The maximal percentages of cholesterol present in hybrid-g7-NPs-cholesterol MIX-N and MIX-SE were 32.7 \pm 2% and 41.5 \pm 1.5%, respectively, reaching a cholesterol content which is around 40 times higher than that of PLGA-g7-NPs-cholesterol [24]. This drug delivery system is therefore expected to deliver to the HD



(caption on next page)

Fig. 1. (a) Experimental paradigm used in the study. Wild-type (wt) mice ($n = 2$ mice/MIX/time point) were treated with a single or multiple intraperitoneal (ip) injection of hybrid-Cy5-g7-NPs-chol (MIX-N or MIX-SE) and sacrificed at different time points. Brain, liver, and lung were collected for distribution analysis. (b) and (c) Representative confocal images of coronal slices containing cortex and striatum from wt mice that received 1 or 3 ip injections of hybrid-Cy5-g7-NPs-chol (MIX-N in (b) or MIX-SE in (c)) and sacrificed after 4 h, 24 h, 1 week, and 2 weeks with relative quantification. (d) Representative confocal images of immunostaining for DARPP32, GFAP, and IBA1 (green) on coronal sections of brains isolated from wt mice after receiving ip-injected hybrid-Cy5-g7-NPs-chol labeled with Cy5 (red) and sacrificed 2 weeks after the injection. White arrowheads indicate intracellular g7-NPs. Hoechst was used to counterstain nuclei (Ho, blue). Scale bar is 30 μ m. Data are expressed as the number of g7-NPs per field of view \pm standard error of the mean. (For interpretation of the references to colour in this figure legend, the reader is referred to the web version of this article.)

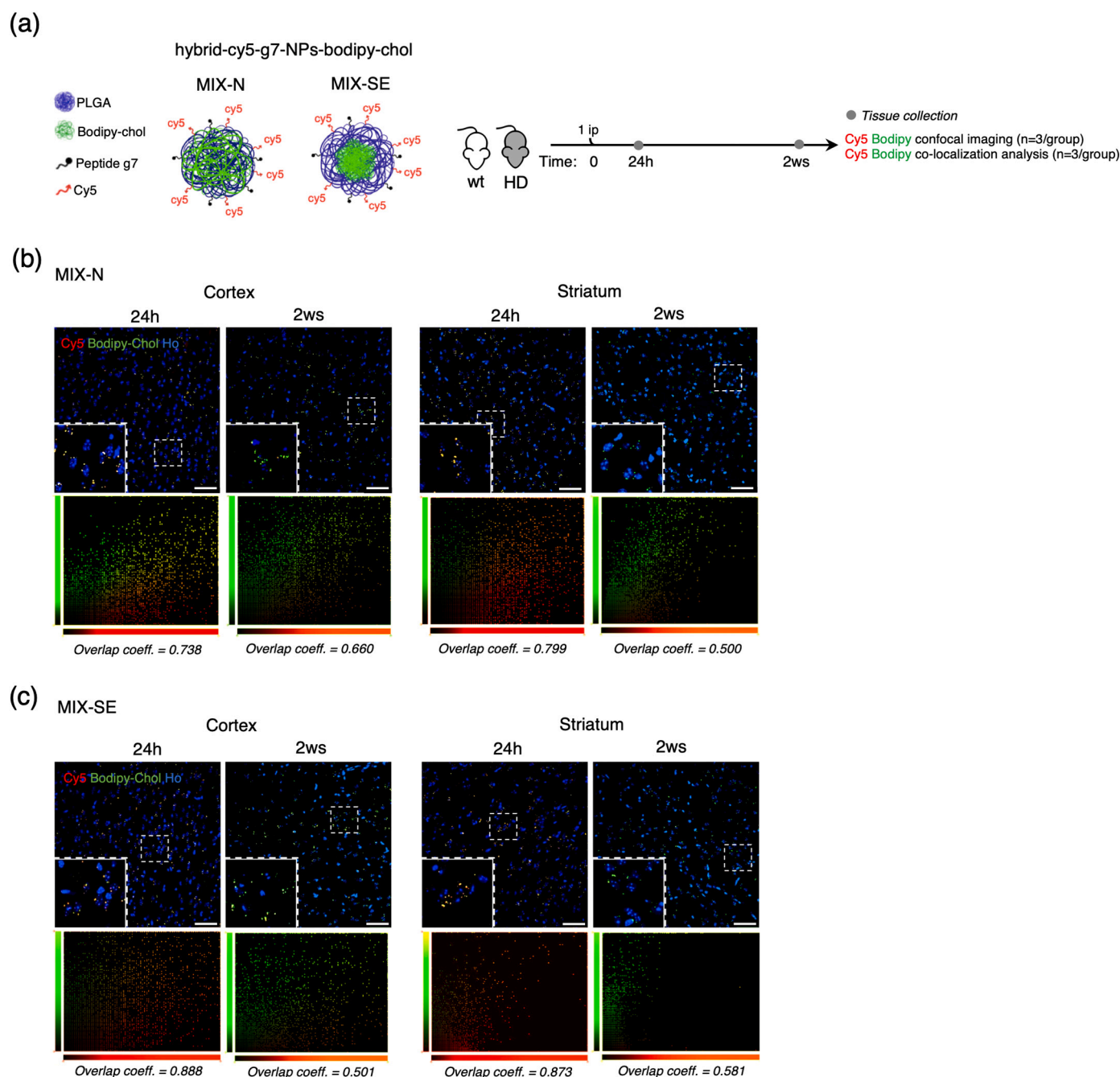


Fig. 2. (a) Experimental paradigm used in the study. Wild-type and R6/2 mice ($n = 3$ mice/genotype/MIX/time point) were treated with a single ip injection of hybrid-Cy5-g7-NPs-bodipy-chol (MIX-N or MIX-SE) and sacrificed at different time points. Brain and liver were collected for the analysis. (b) and (c) Representative confocal images of brain slices from R6/2 mice after ip injection of hybrid-Cy5-g7-NPs-bodipy-chol (MIX-N in (b) or MIX-SE in (c)) and sacrificed after 24 h or 2 weeks and relative co-localization of bodipy-chol and g7-NPs. Hoechst was used to counterstain nuclei (Ho, blue). Scale bar is 50 μ m. (For interpretation of the references to colour in this figure legend, the reader is referred to the web version of this article.)

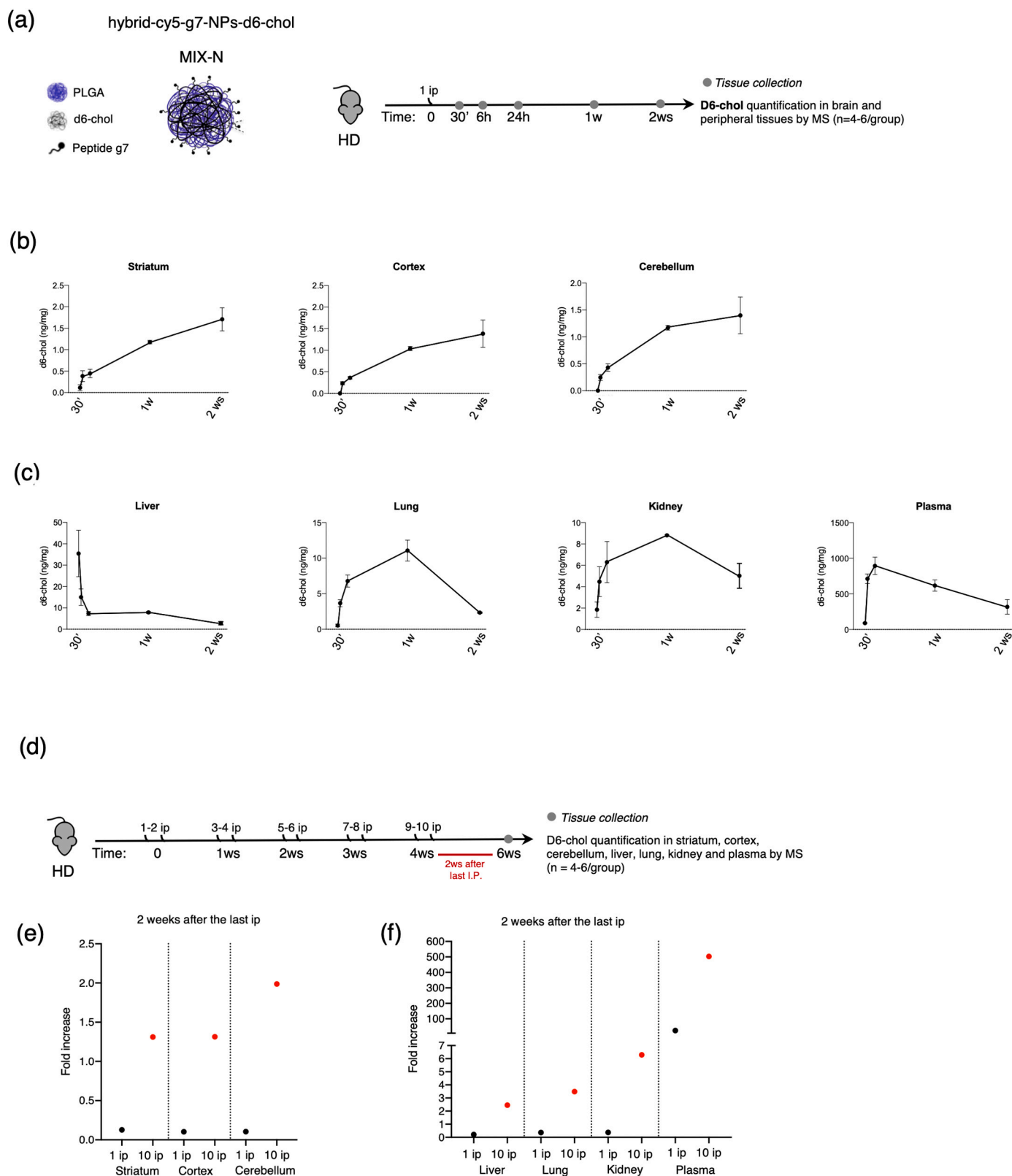


Fig. 3. (a) Experimental paradigm used in the study. R6/2 mice were treated with a single ip injection of hybrid-g7-NPs-d6-chol (MIX-N) and sacrificed at different time points. Striatum, cortex, cerebellum, liver, lung, kidney, plasma, and liver were collected for mass spectrometry analysis ($n = 3$ mice/time point). (b) and (c) Levels of d6-chol in striatum, cortex, cerebellum (b), liver, lung, kidney, and plasma (c) measured by LC-MS. (d) Experimental paradigm used in the study. R6/2 mice were treated with hybrid-g7-NPs-d6-chol (MIX-N) from 5 weeks of age to 9 weeks of age with 2 ip injections/week and sacrificed 2 weeks after the last ip injection. Striatum, cortex, cerebellum, liver, lung, kidney, and plasma were collected for mass spectrometry analysis ($n = 3$ mice). (e) and (f) Levels of d6-chol in striatum, cortex, cerebellum (e), liver, lung, kidney, and plasma (f) measured by LC-MS (red dots). Black dots refer to the measurement represented in Fig. 3B–C. Data are expressed as means \pm standard error of the mean. (For interpretation of the references to colour in this figure legend, the reader is referred to the web version of this article.)

brain a therapeutic dose of cholesterol closer to that identified with the osmotic mini-pumps [25], while being less invasive and more translatable.

The hybrid-g7-NPs-cholesterol MIX-N and MIX-SE were first tested in 7-week-old wild-type (wt) mice to verify their uptake and distribution *in vivo*. To this aim, animals were treated with a single or multiple (3) intraperitoneal (ip) injections of hybrid-g7-NPs-cholesterol MIX-N or MIX-SE labeled with cyanine 5 (Cy5) and sacrificed at different time points (4 h, 24 h, 1 week, 2 weeks) following the last ip injection (Fig. 1(a)). Fluorescence analysis was then performed on brain and peripheral slices to analyze the localization of the Cy5-labeled hybrid-NPs-Chol signals of both MIXs (Fig. 1(b) and (c); Fig. S2). Four hours after a single ip injection, Cy5 signal was detected in the striatum, cortex (Fig. 1(b) and (c)), and hippocampus, as well as in lung and liver (Fig. 1(b) and (c) and Fig. S2(a) and S2(b)), indicating that BBB transit was rapid. Quantification of Cy5 signals revealed that the clearance of both MIXs in peripheral tissues were quite rapid, at least in lung and somewhat less so in liver, since the Cy5 signals decreased markedly 24 h after the ip injection (Fig. S2). Importantly, NPs were accumulating in the brain over time, as evidenced by the Cy5-NPs signal being present at 24 h, 1 week, and 2 weeks after ip injection (Fig. 1(b) and (c); Fig. S2), and strengthening following multiple injections (Fig. 1(b) and (c); Fig. S2). High-magnification confocal images indicated the presence of hybrid-g7-NPs-cholesterol in different neuronal and glial cell types as demonstrated by the colocalization of the signals from Cy5 (NPs) and DARPP32 (marker of striatal medium spiny neurons), GFAP (marker of astrocytes), and IBA1 (marker of microglia) (Fig. 1(d)). Although the biodistributions of MIX-N and MIX-SE were similar, the latter showed higher aggregation in liver, a finding that was more evident after multiple ip injections but which disappeared after 1 week (Fig. S2(b)).

Overall, these results demonstrate that hybrid-g7-NPs-cholesterol rapidly reach the brain and accumulate over time within target cells.

3.2. Cholesterol delivery and intracellular release

To track cholesterol delivery and intracellular release from hybrid-g7-NPs-cholesterol, we performed specific experiments using g7-NPs-cholesterol covalently labeled with Cy5 and loaded with the fluorescent analogue bodipy cholesterol (hybrid-Cy5-g7-NPs-bodipy-cholesterol). Seven-week-old wt and HD mice (R6/2 model) [33] were treated with a single ip injection of hybrid-Cy5-g7-NPs-bodipy-cholesterol MIX-N or MIX-SE and sacrificed at 24 h and 2 weeks after the ip injection (Fig. 2(a)). Following confocal analysis in brain slices, we analyzed the colocalization of red spots (Cy5, NPs) and the green signal (bodipy cholesterol) to evaluate bodipy cholesterol release from the new formulations. We show that 24 h after a single ip injection of hybrid-Cy5-g7-NPs-bodipy-cholesterol, Cy5 and bodipy-cholesterol signals nicely colocalized in striatum and cortex, as indicated by the scatterplot of red and green pixel intensities (Fig. 2(b) and (c)). Importantly, analysis performed 2 weeks after ip injection revealed a partial separation between Cy5 and bodipy-cholesterol signals (Fig. 2(b) and (c)), indicating a slow and progressive release of cholesterol over time. In contrast, cholesterol release in the liver of mice treated with MIX-N was faster than in the brain. In fact, a complete overlap of red and green signal was found 24 h after the ip injection, while 2 weeks after the ip injection all the exogenous cholesterol was released from NPs (Fig. S3). By comparing the overlap coefficient between Cy5 and bodipy signals (Table S2), we found that approximately 30% of bodipy-cholesterol no longer colocalized with Cy5-NPs in cortex and striatum starting from 2 weeks after ip injection, suggesting a progressive release from hybrid-g7-NPs-cholesterol in the brain, in parallel with a reduction in Cy5 signal, probably due to polymer degradation. In contrast, 2 weeks after ip injection, about 90% of bodipy-cholesterol no longer colocalized with Cy5-NPs in the liver (Table S2). No differences in cholesterol release kinetics were found between wt and HD mice, indicating that cholesterol release over-time did not depend on mouse genotype (Table S2). We also conclude that MIX-N and MIX-SE NPs had similar biodistribution profiles and kinetics of cholesterol release. Notably, as MIX-N showed less aggregation in liver and, more importantly, as the surfactant present in

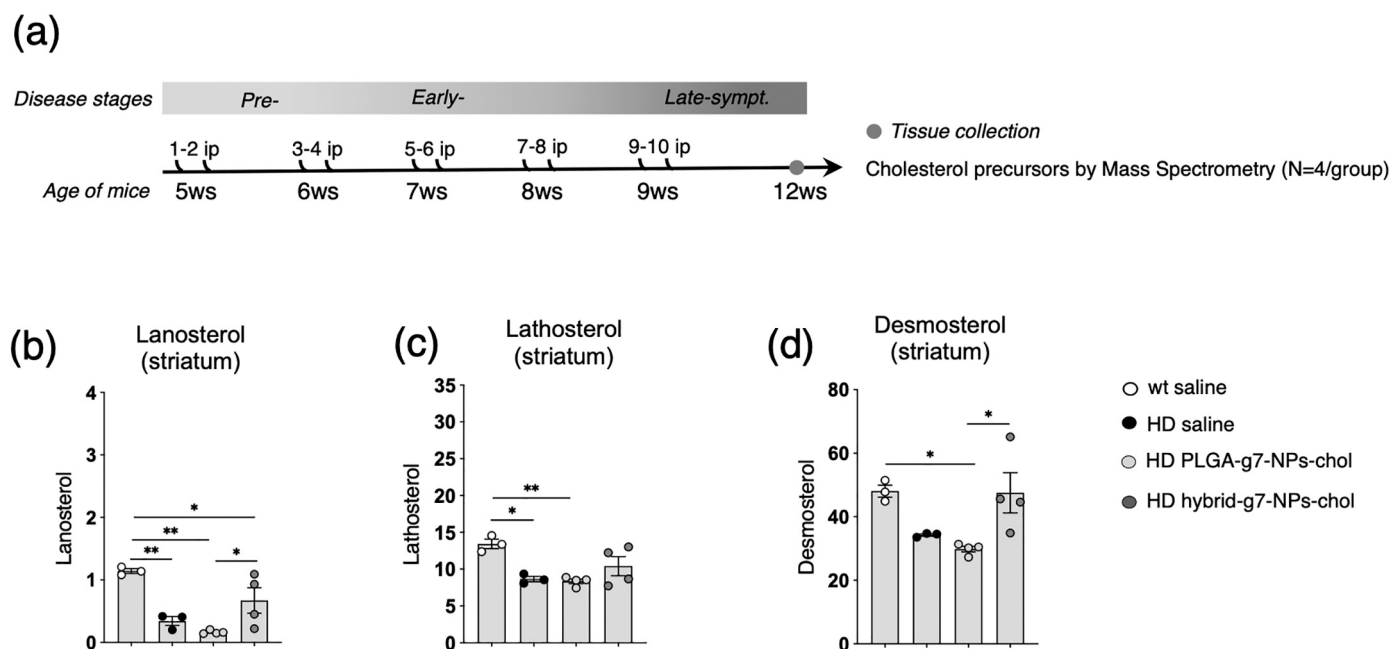


Fig. 4. (a) Experimental paradigm used in the study. R6/2 mice were treated with PLGA-g7-NPs-cholesterol and hybrid-g7-NPs-cholesterol from 5 weeks of age to 9 weeks of age with 2 ip injections/week. Wt and R6/2 littermates were treated with saline solution as controls. Striatum and cortex were collected at 11 weeks of age for mass spectrometry analysis ($n = 3-4$ mice/group). (b), (c), and (d): Lanosterol (b), lathosterol (c), and desmosterol (d) levels measured by GC-MS in the striatum of wt saline, R6/2 saline, R6/2 + PLGA-g7-NPs-cholesterol, and R6/2 + hybrid-g7-NPs-cholesterol mice at 11 weeks of age ($n = 3-4$ mice/group). Data are expressed as means \pm standard error of the mean. Each dot corresponds to the value obtained from each animal. Statistics: one-way ANOVA with Newman-Keuls post-hoc test (* $p < 0.05$; ** $p < 0.01$; *** $p < 0.001$). (For interpretation of the references to colour in this figure legend, the reader is referred to the web version of this article.)

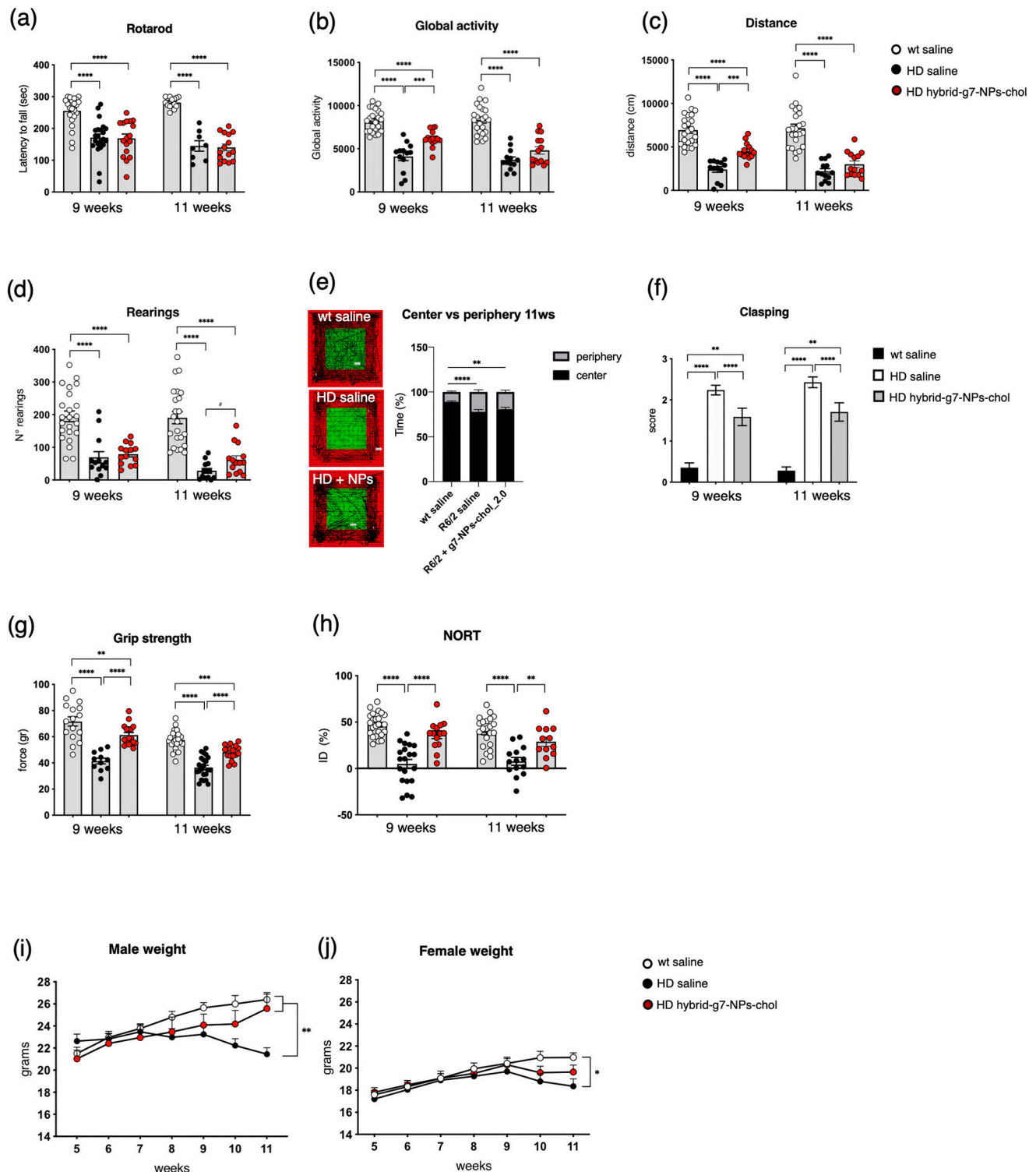


Fig. 5. (a) Latency to falling (seconds) from an accelerating rotarod at 8 and 10 weeks of age in wt saline ($n = 24$ – 25), R6/2 saline ($n = 15$ – 17), and R6/2 + hybrid-g7-NPs-chol ($n = 17$) treated mice. (b), (c), (d), (e) and (f): Global motor activity (b), total distance travelled (c), and number of rearings (d) in an open-field test at 9 and 11 weeks of age in wt saline ($n = 24$ – 25), R6/2 saline ($n = 15$ – 17), and R6/2 + hybrid-g7-NPs-chol ($n = 17$) mice. (e) Representative track plots generated from the open-field test from wt saline ($n = 24$ – 25), R6/2 saline ($n = 15$ – 17), and R6/2 + hybrid-g7-NPs-chol ($n = 17$) mice and relative quantification of the times spent in the center and in the periphery (%) of the arena at 11 weeks of age. (f) Grip strength (grams) at 9 and 11 weeks of age in wt saline ($n = 16$ – 24), R6/2 saline ($n = 11$ – 22), and R6/2 + hybrid-g7-NPs-chol ($n = 17$) mice. (g) Paw clasping at 9 and 11 weeks of age in wt saline ($n = 25$), R6/2 saline ($n = 22$), and R6/2 + hybrid-g7-NPs-chol ($n = 17$) mice. (h) Discrimination index (DI %) in the novel object recognition test of wt saline ($n = 22$ – 23), R6/2 saline ($n = 13$ – 19), and R6/2 + hybrid-g7-NPs-chol ($n = 10$ – 13) mice at 9 and 11 weeks of age. DI above zero indicates a preference for the novel object; DI below zero indicates a preference for the familiar object. (i) and (j) Body weight (grams) of male (i) and female (j) mice at different time points. Data are from three independent trials and shown as scatterplot graphs with means \pm standard error. Each dot corresponds to the value obtained from each animal. Statistics: one-way ANOVA with Newman–Keuls post-hoc test (* $p < 0.05$; ** $p < 0.01$; *** $p < 0.0001$; **** $p < 0.001$) or unpaired Student t -test (# $p < 0.05$; ## $p < 0.01$).

the formulation (Pluronic F68) is approved by the FDA [34], we decided to proceed by testing only this kind of NPs in subsequent studies.

3.3. Kinetics of cholesterol delivery to different organs

Next, to study the kinetics of exogenous cholesterol delivery and to quantify the total amount of cholesterol delivered *in vivo*, we performed two experiments using only MIX-N hybrid-g7-NPs-chol loaded with cholesterol labeled with six deuterium atoms (d6-chol) (hybrid-g7-NPs-d6-chol).

In the first experiment, 7-week-old HD mice were treated with a single ip injection of hybrid-g7-NPs-d6-chol and sacrificed at 30 min, 6 h, 24 h, 1 week, and 2 weeks after the ip injection (Fig. 3(a)). Blood, kidney, lung, liver, cortex, striatum, and cerebellum were collected to measure the amount of d6-chol in the different tissues using liquid chromatography mass spectrometry (LC-MS), starting from 6 h after the ip injection (Fig. 3(b)). We show that starting from 24 h after the treatment, the content of d6-chol increased in the brain tissues over a 2-week period, a finding which is indicative of its slow and progressive release from the NPs (Fig. 3(b)). In contrast, in the liver, d6-chol was rapidly released 30 min after ip injection and rapidly degraded over time. In lung and kidney, NPs were detected around 6 h after the ip injection, the peak of d6-chol release occurred 1 week after the ip injection, after which it was rapidly eliminated (Fig. 3(c)). In plasma, the maximum amount of d6-chol was detected 24 h after the ip injection (Fig. 3(c)). Importantly, this concentration (317,67 ng/mL \pm 635,34) is around 4.000 times lower than the concentration of cholesterol that is present in mouse blood (128 mg/100 mL).

In a second experiment, to quantify cholesterol delivered with the therapeutic regimen of interest, HD mice were treated from 5 to 9 weeks of age with 2 ip injections/week and sacrificed 2 weeks after the last ip injection (Fig. 3(d)). MS analysis revealed that the concentration of d6-chol measured in each tissue following 10 ip injections was around 10 times the concentration of d6-chol measured 2 weeks after a single ip injection (Fig. 3(d) and (e)), indicating that the exogenous cholesterol accumulated in all tissues, even if with different kinetics.

These results demonstrated that the kinetics of cholesterol release differed between brain, plasma, and peripheral tissues and that this delivery system allows a slow release and accumulation of cholesterol in different brain regions where it becomes available to cells over time. Moreover, the fast elimination of cholesterol from blood and peripheral tissues potentially avoids systemic side effects after chronic treatment. Finally, these data combined with the data obtained with bodipy-chol (Fig. 2(b) and (c)), support furtherly the hypothesis that the release of cholesterol from NPs is progressive and slow.

3.4. Enhancement of cholesterol synthesis in the HD mouse brain

We have recently demonstrated that a therapeutically relevant dose of cholesterol delivered to the striatum through osmotic mini-pumps indirectly stimulated endogenous cholesterol synthesis, leading to the reversal of both motor and cognitive abnormalities in HD mice [25]. In contrast, lower doses delivered to the striatum through osmotic mini-pumps [25] or to the brain via PLGA-g7-NPs-chol [24] led to a complete rescue of cognitive decline without significant change in endogenous brain cholesterol biosynthesis or in motor performance.

Since hybrid-g7-NPs-chol [27], with their hybrid structure, are able to carry a larger amount of cholesterol than the previously used PLGA-g7-NPs-chol [24], we sought to test whether the increased amount of cholesterol in hybrid-g7-NPs-chol was sufficient to stimulate endogenous cholesterol synthesis in the diseased brain. As surrogate markers of cholesterol biosynthesis, we quantified cholesterol precursors (lanosterol, lathosterol, desmosterol) by isotopic dilution gas-chromatography mass spectrometry (ID-MS) in the striata of HD mice after a chronic treatment. Accordingly, HD mice from 5 to 9 weeks of age were treated with PLGA-g7-NPs-chol or with hybrid-g7-NPs-chol with 2

ip injections/week and sacrificed 2 weeks after the last ip injection (Fig. 4(a)). As expected, robust deficits of lanosterol, lathosterol, and desmosterol were evident in striatum from HD mice treated with saline compared with wt littermates (Fig. 4(b)–(d)), confirming previous results [16–18,20]. Of note, significant increases in lanosterol and desmosterol levels were found in striatal tissues of HD mice treated with hybrid-g7-NPs-chol compared with those treated with PLGA-g7-NPs-chol (Fig. 4(b)–(d)).

Taken together, these results suggest that the hybrid-g7-NPs-chol transport and release in the brain more cholesterol compared with PLGA-g7-NPs-chol and that the dose is able to enhance endogenous cholesterol biosynthesis in HD mice.

3.5. Effects on cognition, locomotion, and strength

To assess the power of hybrid-g7-NPs-chol to counteract motor and cognitive defects in HD mice, hybrid-g7-NPs-chol were ip injected into R6/2 mice with the same experimental paradigm described in Fig. 4(a) and their motor and cognitive performance were compared with those of R6/2 and wt mice treated with saline solution.

First, we analyzed motor coordination by evaluating the latency of mice to fall when tested on a rotating bar with accelerating speed in the rotarod test. Starting from 8 weeks of age, HD mice exhibited a progressive deterioration in motor coordination, as shown by the shorter latency to fall compared with wt controls. Systemic and chronic administration of hybrid-g7-NPs-chol did not rescue this defect in HD mice (Fig. 5(a)).

To further test the animals' motor abilities, we analyzed spontaneous locomotory activity in the activity cage test. During disease progression, HD mice showed a severe hypokinetic phenotype as demonstrated by reduced global activity, total distance travelled, and number of rearings compared with wt mice, at both 9 and 11 weeks of age. At 9 weeks, HD mice treated with hybrid-g7-NPs-chol had greater global activity and total distance travelled compared with HD mice treated with saline, even if they did not reach the performance observed in wt mice. Moreover, these differences were lost at 11 weeks of age, suggesting that the amount of cholesterol delivered in the brain was not sufficient to counteract motor deficits at a late symptomatic time point, when the HD phenotype worsens (Fig. 5(b) and (c)). When we looked at the number of rearings, no rescue was measured in HD mice treated with hybrid-g7-NPs-chol (Fig. 5(d)). As a measure of anxiety-like behavior, the time that mice spent exploring the periphery or center area of the arena during the activity cage test was also evaluated (Fig. 5(e)). HD animals spent more time in the periphery compared with wt mice, indicating anxiety-related behavior. Cholesterol delivery did not rescue this phenotype (Fig. 5(e)).

As a marker of disease progression, we measured hind-limb clasping with the paw clasping test, a test widely used to measure neurological features in several mouse models of neurodegeneration. In HD mice treated with hybrid-g7-NPs-chol, this phenotype was ameliorated (Fig. 5(f)).

To study neuromuscular functions and strength, we determined the force developed by the mice using the grip-strength test. Muscular strength was reduced in HD mice from 9 weeks of age and it was completely rescued by hybrid-g7-NPs-chol at both 9 and 11 weeks of age (Fig. 5(g)).

Furthermore, we found that 44% of the analyzed R6/2 animals treated with saline suffered from epileptic seizures, while only 18% of R6/2 mice injected with hybrid-g7-NPs-chol were affected.

Finally, to evaluate cognitive function we performed the novel object recognition (NOR) test. As expected, long-term memory declined during disease progression in HD mice, with a marked impairment in the ability to discriminate novel and familiar objects at 11 weeks of age. HD mice treated with hybrid-g7-NPs-chol performed similarly to wt mice, indicating that this treatment completely prevented cognitive decline in these animals (Fig. 5(h)). Weight loss was observed in R6/2 mice

Table 1

Inflammatory response of HD mice following systemic and chronic injection of hybrid g7-NPs-cho.

Analyte	Striatum		Cortex		Liver		Plasma	
	Fold-change		Fold-change		Fold-change		Fold-change	
	Mean \pm SEM	p-value	Mean \pm SEM	p-value	Mean \pm SEM	p-value	Mean \pm SEM	p-value
IL-1a	1010 \pm 0,025	0,9348	0,927 \pm 0,033	0,3884	0,976 \pm 0,111	0,8622	0,212 \pm 0,032	0,0078 **
IL-1b	1055 \pm 0,200	0,8435	0,747 \pm 0,134	0,3254	1088 \pm 0,184	0,7466	0,920 \pm 0,381	0,8608
IL-2	1415 \pm 0,076	0,0081 **	0,708 \pm 0,013	0,1058	1159 \pm 0,179	0,4831	0,398 \pm 0,081	0,0467 *
IL-3	1012 \pm 0,298	0,9739	0,771 \pm 0,097	0,2840	1031 \pm 0,038	0,7151	N/D	
IL-4	0,632 \pm 0,110	0,5871	1472 \pm 0,499	0,4103	0,744 \pm 0,182	0,4333	0,429 \pm 0,184	0,3575
IL-5	1264 \pm 0,165	0,5834	1276 \pm 0,561	0,6831	0,924 \pm 0,158	0,7211	0,330 \pm 0,085	0,1610
IL-6	1061 \pm 0,132	0,7723	1019 \pm 0,102	0,9132	0,889 \pm 0,133	0,5446	N/D	
IL-9	0,789 \pm 0,143	0,4046	0,836 \pm 0,145	0,5136	0,900 \pm 0,112	0,6095	N/D	
IL-10	1020 \pm 0,291	0,9593	0,677 \pm 0,123	0,1301	1109 \pm 0,354	0,8100	1175 \pm 0,002	0,1610
IL-12 (p40)	1666 \pm 0,435	0,2450	0,667 \pm 0,176	0,3861	1843 \pm 0,113	0,1025	0,921 \pm 0,236	0,8124
IL-12 (p70)	0,944 \pm 0,242	0,8601	0,798 \pm 0,138	0,3859	0,803 \pm 0,116	0,4620	N/D	
IL-13	0,950 \pm 0,072	0,5667	0,835 \pm 0,069	0,2902	0,977 \pm 0,097	0,8460	1099 \pm 0,152	0,5886
IL-17	1345 \pm 0,414	0,5198	0,892 \pm 0,125	0,2902	1194 \pm 0,104	0,3108	1345 \pm 0,414	0,5198
Eotaxin	1695 \pm 0,359	0,1447	0,447 \pm 0,078	0,0228 *	0,958 \pm 0,215	0,8927	0,809 \pm 0,195	0,5637
G-CSF	0,943 \pm 0,203	0,8490	0,914 \pm 0,153	0,6571	1001 \pm 0,120	0,9970	0,987 \pm 0,148	0,9529
GM-CSF	1025 \pm 0,222	0,9314	1060 \pm 0,220	0,8302	1090 \pm 0,080	0,4218	0,724 \pm 0,188	0,2956
ING-gamma	1413 \pm 0,272	0,2607	0,899 \pm 0,102	0,5404	1155 \pm 0,184	0,4968	0,749 \pm 0,322	0,7225
KC	1337 \pm 0,302	0,3446	1340 \pm 0,169	0,1438	0,988 \pm 0,313	0,9742	0,489 \pm 0,086	0,1494
MCP-1	0,947 \pm 0,375	0,9216	0,907 \pm 0,196	0,8058	1657 \pm 0,414	0,2082	1365 \pm 0,689	0,7636
MIP-1a	1133 \pm 0,326	0,7593	0,816 \pm 0,138	0,4708	1065 \pm 0,126	0,6874	0,525 \pm 0,222	0,5987
MIP-1b	1511 \pm 0,186	0,1488	0,731 \pm 0,137	0,3533	0,920 \pm 0,192	0,7806	0,614 \pm 0,452	0,4762
Ranteg	1010 \pm 0,075	0,9520	1020 \pm 0,134	0,9271	0,882 \pm 0,087	0,5915	0,998 \pm 0,231	0,9954
TNF-a	1173 \pm 0,276	0,6227	0,854 \pm 0,249	0,6447	1100 \pm 0,352	0,8135	0,851 \pm 0,371	0,8106

Data expressed as fold-change (HD mice treated with hybrid-g7-NPs-cho vs HD mice treated with saline solution)

starting from a late time point (10 weeks of age). Remarkably, this parameter was rescued in male R6/2 mice treated with hybrid-g7-NPs-cho (Fig. 5(i) and (j)).

Collectively, these results indicate that the dose of cholesterol delivered and released in the brain with chronic treatment was sufficient to prevent cognitive decline over time and ameliorate some motor defects at 9 weeks of age. However, the fast and aggressive phenotype of this HD mouse model did not allow us to evaluate the long-term effect of this treatment when all cholesterol is released from the NPs, which may require several weeks.

3.6. Assessment of markers of inflammation, a possible side effect

To explore any eventual side effects of chronic administration of hybrid-g7-NPs-cho, we next sought to analyze the inflammation status of treated mice. Cytokines, chemokines, and growth factors are cell-signaling proteins that mediate a wide range of physiological responses including immunity and inflammation, and are also associated with a spectrum of neurodegenerative diseases [35,36]. Through the simultaneous detection of 23 analytes in a single well of a 96-well microplate, we analyzed the inflammation status of striatum, cortex, liver, and plasma from HD mice treated with saline or with hybrid-g7-NPs-cho. In general, we did not observe gross changes in the levels of the analytes analyzed, except for an increase in IL-2 in the striatum and a decrease in eotaxin in cortex and in IL-1a and IL2 in plasma of R6/2 mice treated with hybrid-g7-NPs-cho compared with R6/2 mice treated with saline (Table 1). These findings suggest that chronic treatment with hybrid-g7-NPs-cho is safe in R6/2 mice. Moreover, observation of the mice during chronic administration regimens did not reveal any cases of mortality in the treated and control groups and no signs of abnormal behavioral reactions and general clinical symptoms were detected.

Overall, these results suggest that chronic administration of hybrid-g7-NPs-cho does not lead to side effects in HD mice.

4. Conclusion

Previous studies pointed out the benefits of strategies aimed at delivering cholesterol to the HD brain [24,25], but defining the dose of

cholesterol that reaches the brain is critical to a complete understanding of the power and limits of the approach. With the aim of developing a new and non-invasive strategy closer to clinical application, hybrid-g7-NPs-cho were produced with improved chemical and physical properties and increased cholesterol content [27]. Here, we characterized hybrid-g7-NPs-cho *in vivo* in a transgenic mouse model of HD. We demonstrated that hybrid-g7-NPs-cho are taken up and reach different cell types in the brain, and that they accumulate over time and are able to release cholesterol, which becomes available for neuronal functions. Importantly, NPs are rapidly degraded in the plasma and in peripheral tissues without a detectable inflammatory response. These systems can be optimized further in order to transport not only cholesterol but other molecules that can be useful in treating HD and other brain pathologies, or even used with different routes of administration [26]. Finally, we highlighted the utility of cholesterol as a model drug with which to define delivery systems based on NPs.

Author contributions

M.V., G.T., B.R. and E.C. conceived the study (Conceptualization); G. B. performed immunostaining experiments and provided confocal images and quantification (Methodology, Investigation, Formal analysis); G.B. and M.V. performed *in vivo* experiments (Methodology, Investigation, Formal analysis); G.T., B.R., F.F. and M.A.V. conceptualized and developed NPs (Conceptualization, Methodology); J.T.D. and I.O. produced and characterized chemico-physical features of NPs (Methodology, Investigation); C.C., V.L. and F.T. performed GC-MS analysis and analyzed the data (Methodology, Investigation, Formal analysis); A.P., M.F., L.C., R.B. and M.S. performed LC-MS analysis for d6-cho and analyzed the data (Methodology, Investigation, Formal analysis); G.B., M.V. and M.B. performed bioplex analysis (Methodology, Investigation, Formal analysis); M.V. and E.C. oversaw and coordinated responsibility for all research activities and their performance and provided experimental advice throughout the work (Supervision and Project administration); E.C. secured the funding, the collaborations and the execution of the entire project (Funding acquisition); M.V., G.B., and E.C. wrote the paper (Writing - Original draft, Writing - Review & Editing); all the authors edited and reviewed the paper (Writing - Review & Editing).

Acknowledgments

The authors acknowledge the technical assistance of Dr. Chiara Cordiglieri, responsible of the INGM Imaging Facility (Istituto Nazionale Genetica Molecolare – INGM, Milan, Italy) and Centro Interdipartimentale Grandi Strumenti UNIMORE for AFM and SEM-FEG images. This research was supported by Telethon Foundation (GGP17102) to E.C., by Italian Ministry of Health (RF-2016-02361928) to M.S. and E.C., by MAECI Progetti di Grande Rilevanza Scientifica Italy-USA (MAE00691612020-06-26), PORFESR Emilia Romagna “Mat2Rep”, IMI2 grant “IM2PACT” to G.T., and Fondazione Umberto Veronesi Fellowship Grant to J.T.D.

Appendix A. Supplementary data

Supplementary data to this article can be found online at <https://doi.org/10.1016/j.jconrel.2020.12.051>.

References

- [1] H. Gao, Progress and perspectives on targeting nanoparticles for brain drug delivery, *Acta Pharm. Sin.* B 6 (2016) 268–286.
- [2] M. Germain, F. Caputo, S. Metcalfe, G. Tosi, K. Spring, A.K.O. Åslund, A. Pottier, R. Schifferers, A. Ceccaldi, R. Schmid, Delivering the power of nanomedicine to patients today, *J. Control. Release* 326 (2020) 164–171.
- [3] D. Hersh, Evolving drug delivery strategies to overcome the blood brain barrier, *Curr. Pharm. Des.* 22 (2016) 1177–1193.
- [4] C. Saraiva, C. Praça, R. Ferreira, T. Santos, L. Bernardino, Nanoparticle-mediated brain drug delivery: overcoming blood-brain barrier to treat neurodegenerative diseases, *J. Control. Release* 235 (2016) 34–47.
- [5] A.V. Vergoni, G. Tosi, R. Tacchi, M.A. Vandelli, A. Bertolini, L. Costantino, Nanoparticles as drug delivery agents specific for CNS: in vivo biodistribution, *Nanomedicine* 5 (2009) 369–377.
- [6] G. Tosi, R.A. Fano, L. Bondioli, L. Badiali, R. Benassi, F. Rivasi, B. Ruozzi, F. Forni, M.A. Vandelli, Investigation on mechanisms of glycopeptide nanoparticles for drug delivery across the blood-brain barrier, *Nanomedicine* 6 (2011) 423–436.
- [7] L. Costantino, F. Gandolfi, G. Tosi, F. Rivasi, M.A. Vandelli, F. Forni, Peptide-derivatized biodegradable nanoparticles able to cross the blood-brain barrier, *J. Control. Release* 108 (2005) 84–96.
- [8] G. Tosi, L. Costantino, F. Rivasi, B. Ruozzi, E. Leo, A.V. Vergoni, R. Tacchi, A. Bertolini, M.A. Vandelli, F. Forni, Targeting the central nervous system: In vivo experiments with peptide-derivatized nanoparticles loaded with Loperamide and Rhodamine-123, *J. Control. Release* 122 (2007) 1–9.
- [9] G. Tosi, et al., NIR-labeled nanoparticles engineered for brain targeting: in vivo optical imaging application and fluorescent microscopy evidences, *J. Neural Transm.* 118 (2011) 145–153.
- [10] G. Tosi, A. Vilella, R. Chhabra, M.J. Schmeisser, T.M. Boeckers, B. Ruozzi, M. A. Vandelli, F. Forni, M. Zoli, A.M. Grabrucker, Insight on the fate of CNS-targeted nanoparticles. Part II: Intercellular neuronal cell-to-cell transport, *J. Control. Release* 177 (2014) 96–107.
- [11] A. Vilella, G. Tosi, A.M. Grabrucker, B. Ruozzi, D. Belletti, M.A. Vandelli, T. M. Boeckers, F. Forni, M. Zoli, Insight on the fate of CNS-targeted nanoparticles. Part I: Rab5-dependent cell-specific uptake and distribution, *J. Control. Release* 174 (2014) 195–201.
- [12] C. Zuccato, M. Valenza, E. Cattaneo, Molecular mechanisms and potential therapeutic targets in Huntington's disease, *Physiol. Rev.* 90 (2010) 905–981.
- [13] D.H. Mauch, et al., CNS synaptogenesis promoted by glia-derived cholesterol, *Science* 294 (2011) 1354–1357.
- [14] H.A. Ferris, et al., Loss of astrocyte cholesterol synthesis disrupts neuronal function and alters whole-body metabolism, *Proc. Natl. Acad. Sci. U. S. A.* 114 (2017) 1189–1194.
- [15] M. Valenza, et al., Dysfunction of the cholesterol biosynthetic pathway in Huntington's disease, *J. Neurosci.* 25 (2005) 9932–9939.
- [16] M. Valenza, V. Leoni, A. Tarditi, C. Mariotti, I. Björkhem, S. Di Donato, E. Cattaneo, Progressive dysfunction of the cholesterol biosynthesis pathway in the R6/2 mouse model of Huntington's disease, *Neurobiol. Dis.* 28 (2007) 133–142.
- [17] M. Valenza, J.B. Carroll, V. Leoni, L.N. Bertram, I. Björkhem, R.R. Singaraja, S. Di Donato, D. Lutjohann, M.R. Hayden, E. Cattaneo, Cholesterol biosynthesis pathway is disturbed in YAC128 mice and is modulated by huntingtin mutation, *Hum. Mol. Genet.* 16 (2007) 2187–2198.
- [18] M. Valenza, et al., Cholesterol defect is marked across multiple rodent models of Huntington's disease and is manifest in astrocytes, *J. Neurosci.* 30 (2010) 10844–10850.
- [19] M. Valenza, E. Cattaneo, Emerging roles for cholesterol in Huntington's disease, *Trends Neurosci.* 34 (2011) 474–486.
- [20] M. Shankaran, et al., Early and brain region-specific decrease of de novo cholesterol biosynthesis in Huntington's disease: a cross-validation study in Q175 knock-in mice, *Neurobiol. Dis.* 98 (2017) 66–76.
- [21] V. Leoni, et al., Plasma 24S-hydroxycholesterol and caudate MRI in pre-manifest and early Huntington's disease, *Brain* 131 (2008) 2851–2859.
- [22] V. Leoni, et al., Plasma 24S-hydroxycholesterol correlation with markers of Huntington disease progression, *Neurobiol. Dis.* 55 (2013) 37–43.
- [23] J.M. Karasinska, M.R. Hayden, Cholesterol metabolism in Huntington disease, *Rev. Nat. Rev. Neurol.* 7 (2011) 561–572.
- [24] M. Valenza, et al., Cholesterol-loaded nanoparticles ameliorate synaptic and cognitive function in Huntington's disease mice, *EMBO Mol. Med.* 7 (2015) 1547–1564.
- [25] G. Birolini, et al., Striatal infusion of cholesterol promotes dose-dependent behavioral benefits and exerts disease-modifying effects in Huntington's disease mice, *EMBO Mol. Med.* (2020) 1–20.
- [26] A. Passoni, et al., Efficacy of cholesterol nose-to-brain delivery for brain targeting in Huntington's disease, *ACS Chem. Neurosci.* 11 (2020) 367–372.
- [27] D. Belletti, A.M. Grabrucker, F. Pederzoli, I. Menerath, M.A. Vandelli, G. Tosi, T. J. Duskey, F. Forni, B. Ruozzi, Hybrid nanoparticles as a new technological approach to enhance the delivery of cholesterol into the brain, *Int. J. Pharm.* 543 (2018) 300–310.
- [28] L. Rigon, et al., Targeting brain disease in MPSII: preclinical evaluation of IDS-loaded PLGA nanoparticles, *Int. J. Mol. Sci.* 20 (2019) 1–15.
- [29] J.T. Duskey, I. Ottonelli, F. Da Ros, A. Vilella, M. Zoli, S. Kovachka, F. Spyrikis, M. A. Vandelli, G. Tosi, B. Ruozzi, Novel peptide-conjugated nanomedicines for brain targeting: in vivo evidence, *Nanomedicine* 28 (2020) 102226.
- [30] H.K. Makadia, S.J. Siegel, Poly Lactic-co-Glycolic Acid (PLGA) as biodegradable controlled drug delivery carrier, *Polymers (Basel)* 3 (2011) 1377–1397.
- [31] D.J. Hines, D.L. Kaplan, Poly (lactic-co-glycolic acid) controlled release systems: experimental and modeling insights, *Crit. Rev. Ther. Drug Carrier Syst.* 30 (2013) 257–276.
- [32] S. Rezvantalab, et al., PLGA-based nanoparticles in Cancer treatment, *Front. Pharmacol.* 9 (2018) 1260.
- [33] L. Mangiarini, et al., Exon 1 of the HD gene with an expanded CAG repeat is sufficient to cause a progressive neurological phenotype in transgenic mice, *Cell* 87 (1996) 493–506.
- [34] A. Pitto-Barry, N.P.E. Barry, Pluronic® block-copolymers in medicine: from chemical and biological versatility to rationalisation and clinical advances, *Polym. Chem.* 5 (2014) 3291–3297.
- [35] B.N.P. Rocha, G.D. Colpo, A.L. Teixeira, E.F. Stimming, Clinical trials for Huntington disease, *Pract. Neurol.* (2020) 69–74.
- [36] T. Nagatsu, M. Mogi, H. Ichinose, A. Togari, Cytokines in Parkinson's disease, *J. Neural Transm. Suppl.* (2000) 143–151.

7.2. Conference proceedings related to the presented Ph.D. project

[1] Lanno A., Favagrossa M., Colombo L., Salmona M., Bagnati R., **Passoni A.** “Development and validation of an innovative UHPLC-MS method for monitoring the cholesterol synthetic pathway in biological samples” AMYC BIOMED, 2021. *Remote poster.*

[2] **Passoni A.**, Siciliano A.M., Lanno A., Favagrossa M., Colombo L., Salmona M., Bagnati R., Davoli E. “An integrated MS strategy using high-resolution AP-MALDI-imaging and UHPLC-MRM to investigate brain cholesterol metabolism in Huntington’s Disease mouse model” 69th Annual Conference on Mass Spectrometry and Allied Topics, 2021. *Remote poster and congress proceedings.*

[3] **Passoni A.**, Siciliano A.M., Lanno A., Favagrossa M., Colombo L., Salmona M., Bagnati R., Davoli E. “AP-MALDI-MSI: new approach to image the brain cholesterol metabolism in Huntington’s Disease mouse model” OURCON2021 The International Mass Spectrometry Imaging Conference, 2021 *Remote poster.*

[4] Lanno A., Bagnati R., **Passoni A.** “An innovative UHPLC-MRM method for monitoring the cholesterol synthetic pathway in biological samples” in Proceedings of the 9th MS J day 2021, Ed. F. Fanti, R. Pascale, V. Lazazzara, G. Ventura, F. Vincenti, ISBN: 978-88-94952-06-3, 30, 2021, Rome. *Congress proceedings.*

[5] **Passoni A.** “MRM approach in clinical and preclinical research: Huntington’s disease” [2020, Shimadzu 50 MS day] *Oral.*

[6] **Passoni A.**, Favagrossa M., Colombo L., Bagnati R., Salmona M. “Mass spectrometric quantitation of intranasal cholesterol delivery in a mouse model of Huntington’s disease” [4th International Mass Spectrometry School”, 15-20 September, Sitges - Spain] *Poster.*

[7] **Passoni A** “Mass spectrometric quantitation of intranasal cholesterol delivery in a mouse model of Huntington’s disease” [2019, I giovani e la spettrometria di massa – 7 MS J Day, Bolzano / 2019, Validation Day – Pozzuoli] *Oral*.

7.3. List of publications (2018-2022)

1. Violatto MB, Pasetto L, Casarin E, Tondello C, Schiavon E, Talamini L, et al. Development of a Nanoparticle-Based Approach for the Blood-Brain Barrier Passage in a Murine Model of Amyotrophic Lateral Sclerosis. *Cells*. 10 dicembre 2022;11(24).
2. Sainas S, Giorgis M, Circosta P, Poli G, Alberti M, **Passoni A**, et al. Targeting Acute Myelogenous Leukemia Using Potent Human Dihydroorotate Dehydrogenase Inhibitors Based on the 2-Hydroxypyrazolo[1,5-a]pyridine Scaffold: SAR of the Aryloxyaryl Moiety. *J Med Chem*. 13 ottobre 2022;65(19):12701–24.
3. Fracasso C, **Passoni A**, Brambilla L, Mantegazza R, Rossi S, Gobbi M, et al. A Validated HPLC-MS/MS Method for Quantification of Fingolimod and Fingolimod-Phosphate in Human Plasma: Application to Patients with Relapsing–Remitting Multiple Sclerosis. *Appl Sci*. gennaio 2022;12(12):6102.
4. Houshmand M, Vitale N, Orso F, Cignetti A, Molineris I, Gaidano V, et al. Dihydroorotate dehydrogenase inhibition reveals metabolic vulnerability in chronic myeloid leukemia. *Cell Death Dis*. 30 giugno 2022;13(6):576.
5. Ongaro A, Violatto MB, Casarin E, Pellerani I, Marchini G, Ribaudo G, et al. The mode of dexamethasone decoration influences avidin-nucleic-acid-nano-assembly organ biodistribution and in vivo drug persistence. *Nanomedicine Nanotechnol Biol Med*. febbraio 2022;40:102497.
6. Palladini J, Bagnati R, **Passoni A**, Davoli E, Lanno A, Terzaghi E, et al. Bioaccumulation of PCBs and their hydroxy and sulfonated metabolites in earthworms: Comparing lab and field results. *Environ Pollut Barking Essex* 1987. 15 gennaio 2022;293:118507.
7. Lucchetti J, Fumagalli F, Olivari D, Affatato R, Fracasso C, De Giorgio D, et al. Brain Kynurenine Pathway and Functional Outcome of Rats Resuscitated From Cardiac Arrest. *J Am Heart Assoc*. 7 dicembre 2021;10(23):e021071.

8. **Passoni A**, Mariani A, Comolli D, Fanelli R, Davoli E, De Paola M, et al. An integrated approach, based on mass spectrometry, for the assessment of imidacloprid metabolism and penetration into mouse brain and fetus after oral treatment.
9. Pinessi D, Resovi A, Sangalli F, Morosi L, Zentilin L, Borsotti P, et al. Tumor vascular remodeling by thrombospondin-1 enhances drug delivery and antineoplastic activity. *Matrix Biol J Int Soc Matrix Biol.* settembre 2021;103–104:22–36.
10. Sainas S, Giorgis M, Circosta P, Gaidano V, Bonanni D, Pippione AC, et al. Targeting Acute Myelogenous Leukemia Using Potent Human Dihydroorotate Dehydrogenase Inhibitors Based on the 2-Hydroxypyrazolo[1,5-a]pyridine Scaffold: SAR of the Biphenyl Moiety. *J Med Chem.* 13 maggio 2021;64(9):5404–28.
12. Regoni M, Cattaneo S, Mercatelli D, Novello S, **Passoni A**, Bagnati R, et al. Pharmacological antagonism of kainate receptor rescues dysfunction and loss of dopamine neurons in a mouse model of human parkin-induced toxicity. *Cell Death Dis.* 10 novembre 2020;11(11):963.
13. Feo ML, Bagnati R, **Passoni A**, Riva F, Salvagio Manta D, Sprovieri M, et al. Pharmaceuticals and other contaminants in waters and sediments from Augusta Bay (southern Italy). *Sci Total Environ.* 15 ottobre 2020;739:139827.
14. Resovi A, Borsotti P, Ceruti T, **Passoni A**, Zucchetti M, Berndt A, et al. CCN-Based Therapeutic Peptides Modify Pancreatic Ductal Adenocarcinoma Microenvironment and Decrease Tumor Growth in Combination with Chemotherapy. *Cells.* 13 aprile 2020;9(4).
15. Matteo C, Dovrtelova G, Di Clemente A, Frapolli R, **Passoni A**, Ceruti T, et al. HPLC-MS/MS measurement of lidocaine in rat skin and plasma. Application to study the release from medicated plaster. *J Chromatogr B Analyt Technol Biomed Life Sci.* 1 febbraio 2020;1138:121942.

16. Bagnati R, Terzaghi E, **Passoni A**, Davoli E, Fattore E, Maspero A, et al. Identification of Sulfonated and Hydroxy-Sulfonated Polychlorinated Biphenyl (PCB) Metabolites in Soil: New Classes of Intermediate Products of PCB Degradation? *Environ Sci Technol*. 17 settembre 2019;53(18):10601–11.
17. Sainas S, Temperini P, Farnsworth JC, Yi F, Møllerud S, Jensen AA, et al. Use of the 4-Hydroxytriazole Moiety as a Bioisosteric Tool in the Development of Ionotropic Glutamate Receptor Ligands. *J Med Chem*. 9 maggio 2019;62(9):4467–82.
18. Violatto MB, Casarin E, Talamini L, Russo L, Baldan S, Tondello C, et al. Dexamethasone Conjugation to Biodegradable Avidin-Nucleic-Acid-Nano-Assemblies Promotes Selective Liver Targeting and Improves Therapeutic Efficacy in an Autoimmune Hepatitis Murine Model. *ACS Nano*. 23 aprile 2019;13(4):4410–23.
19. Lucchetti J, Fracasso C, Balducci C, **Passoni A**, Forloni G, Salmona M, et al. Plasma and Brain Concentrations of Doxycycline after Single and Repeated Doses in Wild-Type and APP23 Mice. *J Pharmacol Exp Ther*. gennaio 2019;368(1):32–40.
20. Raitano G, Goi D, Pieri V, **Passoni A**, Mattiussi M, Lutman A, et al. (Eco)toxicological maps: A new risk assessment method integrating traditional and in silico tools and its application in the Ledra River (Italy). *Environ Int*. ottobre 2018;119:275–86.

8. Acknowledgements

8. ACKNOWLEDGEMENTS

At the end of my thesis I would like to thank all those people who made this thesis possible.

*First of all, a grateful thank to **Dr. Mario Salmona** and all the collaborators to give me the opportunity to have an active role in the analytical part of this important project on Huntington 's disease.*

*I would to express my gratitude to my supervisor **Dr. Renzo Bagnati** for the encouragement and the analytical support he provided me during the elaboration of my thesis. A special thanks to **Dr. Enrico Davoli**, head of Mass Spectrometry Lab, for all the precious suggestions for my career and to encourage me to spent part of the Ph.D. abroad.*

*My sincere thanks to **all my colleagues at Mario Negri Institute**. I have been very privileged to get to know and to collaborate with them.*

*Most of all I would like to express my heartfelt gratitude to **my family** for offering me their affection, encouragement and continuous support without which this work would not have been possible.*

